

Spin-flip Raman scattering in low-dimensional semiconductors

Dissertation

presented to the Faculty of Physics of the
TU Dortmund University, Germany,
in partial fulfillment of the requirements
for the degree of

Doktor rer. nat.

by
Jörg Debus



Dortmund, March 2012

Accepted by the Faculty of Physics of the TU Dortmund University, Germany.

Day of the oral examination: 12th April 2012

Examination board:

Prof. Dr. Dmitri R. Yakovlev

Prof. Dr. Victor F. Sapega

Prof. Dr. Bernhard Spaan

Dr. Ilya A. Akimov

Contents

| | |
|--|-----------|
| Motivation | 1 |
| 1 Theoretical Background | 5 |
| 1.1 Characteristics of Low-Dimensional Semiconductors | 5 |
| 1.1.1 Band Structure - Group Theoretical Approach | 5 |
| 1.1.2 Carrier Wave Function in a Quantum Dot | 9 |
| 1.1.3 Impact of Quantum Confinement on the Electron g Factor | 13 |
| 1.2 Inelastic Light Scattering in Semiconductors | 15 |
| 1.2.1 Preliminaries | 15 |
| 1.2.2 Inelastic Scattering of Electrons | 20 |
| 1.2.3 Spin-Flip Raman Scattering | 24 |
| 2 Experimental Methods | 29 |
| 2.1 SFRS: What is Experimentally Required? | 29 |
| 2.2 Spin-Flip Raman Scattering Setup | 34 |
| 2.3 Time-Resolved Photoluminescence Setup | 38 |
| 3 Exchange Interactions Providing SFRS in a CdTe Quantum Well | 41 |
| 3.1 Experimental Details | 42 |
| 3.2 Optical Tuning of Resident Carrier Concentration | 43 |
| 3.3 SFRS in Neutral and Charged Excitons | 45 |
| 3.3.1 SFRS in Faraday Geometry | 45 |
| 3.3.2 Dependence on Geometry, Temperature and Laser Power | 51 |
| 3.4 Discussion of Scattering Mechanisms | 56 |
| 3.4.1 SFRS at the Exciton Resonance | 58 |
| 3.4.2 SFRS at the Trion Resonance | 63 |
| 3.5 Conclusion | 67 |
| 4 Spin-Flip Raman Scattering in (In,Ga)As/GaAs Quantum Dots | 69 |
| 4.1 Characterization of Electron Spin-Flip Raman Scattering | 70 |
| 4.1.1 Symmetry-Dependent Scattering Mechanism | 70 |

| | | |
|----------|---|------------|
| 4.1.2 | Magnetic Field Dependence of the Raman Shift | 75 |
| 4.1.3 | Electron g Factor Dispersion | 77 |
| 4.2 | Coupling of Ground and Excited Electron States | 78 |
| 4.3 | Optically Induced Electron-Nuclear Hyperfine Interaction | 83 |
| 4.4 | Conclusion | 86 |
| 5 | Indirect Band-Gap (In,Al)As/AlAs Quantum Dots | 89 |
| 5.1 | Fine Structure of Γ -X Mixed Exciton | 90 |
| 5.1.1 | Γ -X Mixing of Conduction Band States | 91 |
| 5.1.2 | SFRS on Γ -X Mixed Exciton | 94 |
| 5.1.3 | Characteristics of the g Factors | 100 |
| 5.1.4 | Theoretical Simulation of SFRS Spectrum | 103 |
| 5.2 | Recombination Dynamics of the Indirect Exciton | 106 |
| 5.2.1 | Sample Characteristics | 107 |
| 5.2.2 | Time-Resolved Photoluminescence | 111 |
| 5.2.3 | Exciton Lifetime Distribution | 114 |
| 5.2.4 | Impact of Interface Sharpness | 116 |
| 5.3 | Spin Dynamics of the Indirect Exciton | 119 |
| 5.4 | Conclusion | 123 |
| 6 | Summary | 127 |
| 7 | Outlook: SFRS and Beyond | 129 |
| 7.1 | Many-Body Effects and Inter-Dot Coupling in Direct Band-Gap QDs . . . | 129 |
| 7.2 | Spin Dynamics and Valley Mixing in (In,Al)As/AlAs Quantum Dots . . . | 131 |
| 7.3 | NV ⁻ Centers in Diamond | 131 |
| | Bibliography | 135 |
| | Symbols and Abbreviations | 155 |
| | List of Figures | 159 |
| | List of Tables | 161 |
| | Curriculum Vitae | 163 |
| | Acknowledgments | 167 |

Motivation

The question whether a gas might be magnetically birefringent [...] was raised at a seminar. The next morning I awoke early, too early to go to the lab. As it was too cold to get out of bed, I lay there thinking about the seminar question and had the idea for the experiment. When I got to the lab, I recruited Gerlach as a collaborator. He was a skilful experimentalist, while I was not. In fact, each part of the apparatus that I constructed had to be remade by Gerlach.

We were never able to get the apparatus to work before midnight. When finally all seemed to function properly, we had a strange experience. After venting to release the vacuum, Gerlach removed the detector flange. But he could see no trace of the silver atom beam and handed the flange to me. With Gerlach looking over my shoulder as I peered closely at the plate, we were surprised to see gradually emerge two distinct traces of the beam. Several times we repeated the experiment, with the same mysterious result. Finally we realized what it was. [...] My salary was too low to afford good cigars, so I smoked bad cigars. These had a lot of sulfur in them, so my breath on the plate turned the silver into silver sulfide, which is jet black so easily visible. It was like developing a photographic film. [1]

Otto Stern

The Stern-Gerlach experiment in the early 1920s, demonstrating the space quantization of the electron spin for the first time, marks the beginning of the studies on spin effects in the solid-state physics [2]. However, at that time the quantized angular momentum *spin* was not identified as an intrinsic property of the electron. Not only the splitting of the silver atom beam sending through an inhomogeneous magnetic field, but also the splitting of atomic spectral lines in an external magnetic field, discovered by P. Zeeman already in 1897 [3], prompted several physicists to work on a quantum mechanical explanation of these phenomena. W. Pauli suggested a classically indescribable ambivalence of the quantum theoretical properties of the electron [4], afterwards, in the year 1925 G. E. Uhlenbeck and S. Goudsmit postulated the existence of the electron spin [5]. Decisive developments in the understanding of spin related effects were followed, such as Dirac's formulation of the quantum mechanics of many-electron systems [6] and Pauli's connection between spin and statistics [7]. Besides the study of spin fundamentals, another intrinsic property of the electron, its electric charge, gained in importance in the technical science by the invention of the electronic solid-state transistor [8]. Nowadays, almost every electronic device takes advantage of semiconductor-based transistors as logic switches to process information. Modern technologies demand a fast transfer and processing of information, hitherto, the electronic solid-state transistor fulfills respective requirements, whereby its miniaturization plays a major role. The current usage of non-planar transistor structures with sizes of about 20 nanometers [9, 10] upholds Moore's law declaring an exponential growth in the microprocessor chip performance as a function of time [11]. Nevertheless, the development of the integrated-circuit technology based on the electric charge has to face its slowdown.

A paradigm shift has already been initiated by developing the research field of spin electronics (spintronics), where the advantages of both the intrinsic charge and spin are combined or spin-only applications are designed. A prominent example of utilizing both properties is the giant magneto-resistance effect resulting from spin-dependent scattering of electrons propagating through thin metallic films [12, 13]. A promising candidate for a device based on the electron spin as information carrier is the spin field-effect transistor which has been proposed by S. Datta and B. Das at the end of 1989 [14]. Semiconductors and their low-dimensional variants have been established as basis materials thus giving rise to the semiconductor-based spintronics. The *semiconductor spintronics* aims at the full control over the quantum mechanical nature of the spin [15]. Indeed, the spin transistor can be expected to have very fast dynamics and low power dissipation, but the accomplishment of a sufficient number of quantum operations requires electron spin lifetimes exceeding 100 microseconds – at room temperature [16]. While the precession frequency of the electron spin (ranging between 10^3 and 10^6 MHz) limits the possible speed of coherent semiconductor spintronic applications [17], the spin lifetime describes the time during which a spin can serve as information carrier until reaching its thermal equilibrium. Long electron spin lifetimes in semiconductors have already been achieved [18, 19]. In that context, different ways to realize the topmost aim of the semiconductor spintronics have been suggested, for instance, the spin can be transferred from the optically controllable electron to the long-lived nuclear spin system acting as spin memory. Accordingly, one can create an electron spin polarization surviving as long as the underlying Overhauser field with persistence times of about one hour [20].

Despite the successful study of a variety of spin phenomena, fundamental questions are challenging the semiconductor spintronics. The dimension of the semiconductor is a crucial parameter: low-dimensional semiconductor structures whose miniaturization ends in zero-dimensional *quantum dots* offer promising properties for spin-based applications. As an example, the three-dimensional spatial confinement of a quantum dot protects the electron spin from relaxation. The number of perturbing interactions within a quantum dot is reduced [21], nevertheless, the limitation of the quantum state lifetime or the loss of coherence cannot fully be avoided. An implementation of an electron into a highly symmetric surrounding, or the utilization of the symmetry itself to control the quantum nature of the spin, as in the case of the exchange symmetry [22], may provide a further step toward the realization of quantum computing. Moreover, the optical properties of low-dimensional semiconductors are characterized by the bound electron-hole pairs known as excitons which, in turn, can capture an additional carrier thus forming a charged exciton denoted as trion. That three-carrier complex can also be regarded as research object affecting spin studies positively [23, 24]. Most studies are focused on the electron while minor importance is attributed to the hole, however, the type of the carrier and its state of coupling are relevant for the semiconductor spintronics [25]. Principally, the challenges for achieving novel spin effects or improving existent spin phenomena are based on *interaction*, namely interactions between carriers themselves as well as a carrier and a second system, e.g., the nuclear spin system or a lattice vibration (phonon) leading to a scattering process and thus to spin decoherence.

The spin properties of the confined carriers and interaction processes in low-dimensional semiconductors can suitably be characterized by the resonant *spin-flip Raman scattering* technique. It is predicated on the inelastic light scattering under involvement of a carrier whose spin orientation is reversed. The change in the spin state is accom-

panied by a variation in the energy of the carrier which is acquired via spectroscopic instruments. The splitting of the spin states, which is defined by the g factor of the carrier under study [26], is typically induced by a strong external magnetic field. Since the spin-flip Raman scattering sensitively responds to different external parameters like the magnetic field, temperature, geometry, or exciting light, properties of the carrier spin and interaction process can be studied for diverse scenarios. The Raman spectroscopy is used in a wide range of research fields, such as surface-enhanced Raman scattering for biological applications [27], in-situ characterizations of polymer structures in the chemical and mechanical engineering [28], or spin-flip Raman scattering in bulk semiconductor structures [29]. The application of the spin-flip Raman scattering technique to low-dimensional semiconductors is very limited, particularly, it has not yet been used to characterize the exciton and its constituents in quantum dots. Essential features of low-dimensional semiconductors are overviewed in the Chapter 1, it also includes a description of the theoretical basics of inelastic light scattering. Details on the experimental setup are given in the Chapter 2.

The investigation of fundamental interactions between confined carriers attaches key importance in the semiconductor physics. One essential type of interactions in low-dimensional semiconductors is the exchange interaction between localized spins of electrons and/or holes. In the Chapter 3, the spatially isotropic and anisotropic spin exchanges in exciton and trion complexes are characterized for a quantum well structure. It is shown, for instance, that the anisotropic electron-hole exchange interaction depends on their angle-dependent g factors, and the strength of the anisotropic exchange is linked to the localization degree of the carriers. Furthermore, the efficiency of the electron and hole spin-flip scattering can be tuned by an additional nonresonant excitation that represents a method to identify the type of resident carrier and emphasizes differences between the negatively and positively charged excitons. Among the described spin-flip scattering mechanisms one can find a process whose origin has not been explained up to now: why is a single electron or hole spin-flip Raman scattering process in a neutral exciton observable for a crossed circular polarization in Faraday geometry, though it is forbidden by selection rules?

Not only the anisotropic exchange is a spin-nonconserving interaction, but also the coupling between ground and excited electron states can be accompanied by the relaxation of the spin angular momentum conservation, it is outlined by a novel optical resonance excitation for quantum dot ensembles in the Chapter 4. Hereby, the idea of an exciton-cyclotron resonance observed in semiconductor quantum wells is transferred to the fully quantized level spectrum of the quantum dots. For both types of interactions, the reduction in the local symmetry results in spin-flip scattering; it is considerably dependent on the tilting of the sample growth axis with respect to the magnetic field direction. In addition to the symmetry dependence, the competition between the magnetic field confinement and the potential confinement of the quantum dots is indicated. Moreover, it is illustrated that the Overhauser field can directly be measured by the spin-flip Raman shift demonstrating a new method to study electron-nuclear effects in quantum dot ensembles.

A novel quantum dot structure is presented in the Chapter 5. The undoped (In,Al)As/AlAs quantum dots with indirect band gap and type-I band alignment provide indirect-in-momentum-space excitons with remarkable dynamical properties: their

radiative recombination time and spin lifetime exceed hundreds of microseconds. These indirect excitons are promising candidates for semiconductor spintronic applications. By tailoring the composition profile and size of the quantum dots not only the exciton recombination dynamics can be controlled, but also a mixing between electron levels from direct and indirect valleys can be obtained. Due to the level mixing the indirect exciton is optically addressable, thus being specified by the spin-flip Raman scattering technique. The g factor tensor components of the electron, hole, and exciton indicate a high quantum dot symmetry, where spin-orbit interaction and valence band mixing are negligible. The experimental results of the exciton recombination dynamics as well as the spin structure characteristics are compared to theoretical predictions.

Fundamental spin interactions of carriers confined in low-dimensional semiconductors are characterized with regard to their dependence on the local structure symmetry as well as the type and excitation state of the carrier complex by using the resonant spin-flip Raman scattering technique. Accordingly, the studies outline problems of the semiconductor spintronics, but also ways to identify and monitor them, and present a promising structure to make a step toward the realization of spin-based applications.

Chapter 1

Theoretical Background

Characteristics of low-dimensional semiconductors and inelastic light scattering in semiconductors are the main topics of the chapter *Theoretical Background*. As the experimental results refer to optical properties of two- and particularly zero-dimensional semiconductor structures, the theoretical details presented in the following bridge these subjects. The semiconductor band structure is described with respect to dimensionality and crystal symmetry, also the features of the electron g factor depending on the quantum confinement are studied. Once in a while the focus is directed to the zero-dimensional quantum dots (QDs); the carrier wave functions spatially confined in the three dimensions are discussed in Subsection 1.1.2 explicitly. Due to the QD confinement the density of the electron states takes the form of a sharp δ -function and the electrons and holes have discrete energy levels [30, 31]. Besides the characteristics of the low-dimensional semiconductors, the physics of light scattering is highlighted. The different types of light scattering, applied in diverse scientific fields, can be reduced to a distinguishing feature related to the question: is the light scattering elastic or inelastic? Since most information can be extracted from inelastic scattering processes, the focus is placed on the inelastic Raman scattering. Basic rules of carrier scattering as well as the spin-flip Raman scattering (SFRS) are described in Section 1.2. The spin-flip Raman scattering will turn out to be a sophisticated tool to study the basic properties of low-dimensional semiconductor structures.

1.1 Characteristics of Low-Dimensional Semiconductors

1.1.1 Band Structure - Group Theoretical Approach

The discussion of optical properties of a semiconductor structure requires the knowledge of the electronic band structure. It is closely related to the crystallographic symmetry. In Fig. 1-1 (a) the band structure of a crystal with zincblende lattice is shown as the dependence of the energy E on the absolute wave vector $|\mathbf{k}| = k$ in the one-electron picture. It illustrates the band structure of a bulk III-V semiconductor with direct band gap, like GaAs or InAs. In the region around the center of the Brillouin zone ($k = 0$, Γ -point) the parabola-shaped conduction band is twofold spin-degenerate and the two valence subbands are fourfold and twofold degenerate; energy and k -related deviations due to the absence of an inversion center in the zincblende crystal are neglected

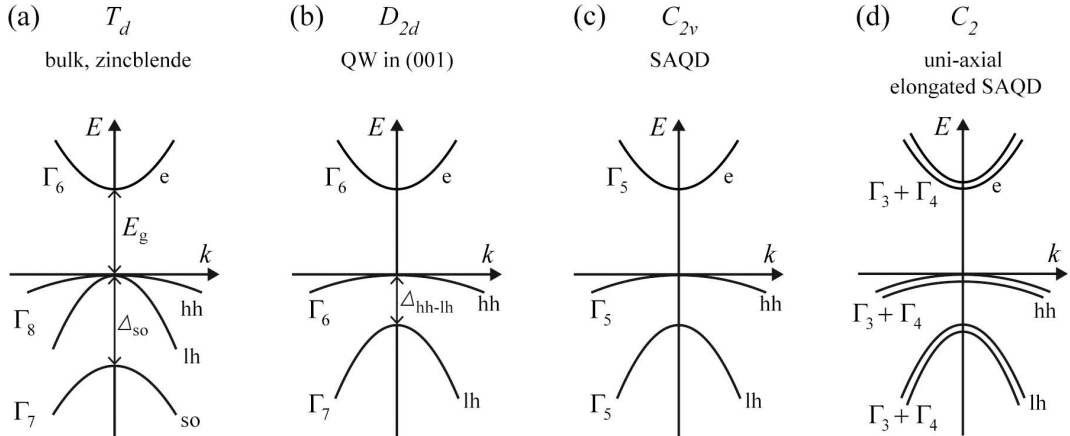


Figure 1-1: Electronic band structures for different point group symmetries shown in the vicinity of the Brillouin zone-center. The conduction band and valence subbands are indicated by the group-specific irreducible representation Γ_i . For the sake of clarity the energies are given on an arbitrary scale, spin splittings at $k \neq 0$ and nonparabolic effects are omitted. For the self-assembled quantum dots (SAQD) the heavy-light hole splitting as well as the spin-dependent splittings are solely schematically depicted.

[32, 33, 34]. The subbands possess different curvatures leading to different effective masses m^* . Within a generalized picture of anisotropic energy dispersions [30], the inverse effective mass can be expressed as a second-rank tensor in terms of the second derivative of the energy dispersion: $[(m^*)^{-1}]_{\alpha,\beta} = \hbar^{-2} \partial_{k_\alpha k_\beta}^2 E(\mathbf{k})$. Here, α and β denote the spatial coordinates x , y , or z , and \hbar is the reduced Planck constant. Away from the Γ -point the bands are nonparabolic which results from the spin-orbit interaction of an energetically higher with a lower lying subband [35]. At $k = 0$ the bottom of the conduction band and the top of the valence band are split by the band gap energy E_g . The Fermi energy of an undoped semiconductor lies by definition within the band gap. Thus, in the crystal ground state the valence band is completely filled, while the conduction band is empty.

The bulk zincblende crystal is characterized by the symmetry of the tetrahedral point group T_d [36]. In T_d the spin part χ_s of the hole (h) wave function is described by the basis functions of the irreducible representation Γ_6 with spin projections of $\pm 1/2$ [37]. Since the hole wave function has an orbital angular momentum of $l = 1$ (like an atomic p-state), its spatial part χ_h transforms like Γ_5 [38]. The symmetry of the total wave function $\Psi_h = \chi_h \cdot \chi_s$ is defined by the direct product $\Gamma_5 \otimes \Gamma_6 = \Gamma_7 + \Gamma_8$. Due to spin-orbit coupling the initially sixfold degenerate valence band edge splits into the fourfold degenerate Γ_8 - and twofold degenerate Γ_7 -states. The Γ_8 -states split into the twofold Kramers' degenerate* heavy-hole (hh) and light-hole (lh) subbands for $k \neq 0$. The Γ_7 -states, which are denoted as spin-orbit split-off band (so-band), are decoupled from the Γ_8 -quadruplet in III-V semiconductors; for example, in GaAs they are separated

*Kramers' degeneracy [39] means that the invariance under time reversal causes a degeneracy of energy states in the presence of an electric field. Hence, a simultaneous reversal of the wave vector and spin does not change the energy at any point of the Brillouin zone: $E(\mathbf{k}, \uparrow) = E(-\mathbf{k}, \downarrow)$. While in a free atom the spin-orbit interaction can lift the degeneracy of states having the same orbital wave function but opposite spins, this spin splitting is not allowed in solids with inversion symmetry.

by an energy $\Delta_{\text{so}} = 0.34$ eV [40]. Thus, the so-band will be neglected in the further considerations. By comparison, the splitting $\Delta_{\text{hh-lh}}$ between the heavy- and light-hole states typically amounts to tens of meV. Neglecting the so-band the hole can be described as a particle with total angular momentum of $j_{\text{h}} = 3/2$, where the hh and lh states have angular momentum projections of $j_{z,\text{hh}} = \pm 3/2$ and $j_{z,\text{lh}} = \pm 1/2$, respectively.

The band structure of crystals having a lower symmetry than T_d can be derived in the similar way as described above. While the symmetry of two-dimensional quantum wells grown on a (001)-oriented substrate belongs to the D_{2d} group, lens-shaped self-assembled quantum dots are typically described in terms of the C_{2v} group. In the case of an elongation in the xy -plane, e.g. along the (110)-direction, the symmetry is further lowered to C_2 which only consists of the identity operation and a twofold rotation about the z -axis. The spin degeneracy of the valence band states (and also conduction band states) is lifted in the low symmetry C_2 where the hh and lh subbands are split into the Γ_3 - and Γ_4 -levels. The band structures are schematically illustrated in the Figs. 1-1 (b)-(d). The valence band structures for the different symmetries are given by the following relations; note, the two lowest conduction band levels are represented by the second factor of each direct product.

$$D_{2d} : \quad \Gamma_5 \otimes \Gamma_6 = \Gamma_6(\text{hh}) + \Gamma_7(\text{lh}), \quad (1.1)$$

$$C_{2v} : \quad (\Gamma_2 + \Gamma_4) \otimes \Gamma_5 = \Gamma_5(\text{hh}) + \Gamma_5(\text{lh}), \quad (1.2)$$

$$C_2 : (\Gamma_1 + \Gamma_2) \otimes (\Gamma_3 + \Gamma_4) = \underbrace{\Gamma_3 + \Gamma_4}_{\text{hh}} + \underbrace{\Gamma_3 + \Gamma_4}_{\text{lh}}. \quad (1.3)$$

How can the wave function of a bound electron-hole pair, namely an exciton, be evolved? Principally, it is determined by the product of the electron (e) and hole wave functions as well as the envelope (env) function describing the relative motion of the electron and hole. The possible symmetries of the exciton (Ex) are governed by the direct product of the symmetries of the electron, hole, and envelope functions:

$$\Gamma_{\text{Ex}} = \Gamma_{\text{e}} \otimes \Gamma_{\text{h}} \otimes \Gamma_{\text{env}}. \quad (1.4)$$

The envelope function for the ground state always transforms like Γ_1 [38]. Choosing the T_d point group as an example, the exciton is formed with the electron in the Γ_6 conduction band and the hole in the Γ_8 valence band:

$$\Gamma_{\text{Ex},T_d} = \Gamma_6 \otimes \Gamma_8 \otimes \Gamma_1 = \Gamma_3 + \Gamma_4 + \Gamma_5. \quad (1.5)$$

While the spin-singlet state Γ_5 can be reached from the ground state by an electric dipole transition, the Γ_3 - and Γ_4 -states with parallel electron and hole spins are dipole forbidden thus indicating the nonradiative (dark) exciton states. For the other symmetries the energetically lowest exciton wave functions read

$$\Gamma_{\text{Ex},D_{2d}} = \Gamma_6 \otimes \Gamma_6 \otimes \Gamma_1 = \Gamma_1 + \Gamma_2 + \Gamma_5, \quad (1.6)$$

$$\Gamma_{\text{Ex},C_{2v}} = \Gamma_5 \otimes \Gamma_5 \otimes \Gamma_1 = \Gamma_1 + \Gamma_2 + \Gamma_3 + \Gamma_4, \quad (1.7)$$

$$\Gamma_{\text{Ex},C_2} = (\Gamma_3 + \Gamma_4) \otimes (\Gamma_3 + \Gamma_4) \otimes \Gamma_1 = 2\Gamma_1 + 2\Gamma_2. \quad (1.8)$$

In D_{2d} symmetry the transition to the doublet state Γ_5 is dipole allowed for the electric field vector perpendicular to the growth axis of the quantum well, while the singlet levels

Γ_1 and Γ_2 are dipole forbidden [41]. In the case of the C_{2v} symmetry the dipole allowed states belong to the irreducible representations Γ_2 and Γ_4 , while the dark excitons are described by the representations Γ_1 and Γ_3 [42]. If the quantum dot is elongated or stressed along one of the in-plane directions, the symmetry is reduced to C_2 . The direct product of the single-particle states Γ_3 and Γ_4 designates the bright excitons to the representation Γ_1 . In that way, the group theoretical approach provides selection rules, nevertheless, it does not yield information about the magnitude of the splittings or the ordering of the bands.

In order to develop explicit expressions for the different conduction and valence band states, Bloch's theorem [43] will be applied to quantized band edge states with the total angular momentum j as good quantum number. The theorem allows to characterize the electrons in a periodic crystal potential in the band n with wave vector \mathbf{k} by a wave function $\Psi_{\mathbf{k}}^n(\mathbf{r}) = \exp(i\mathbf{k} \cdot \mathbf{r}) u_{\mathbf{k}}^n(\mathbf{r})$. The Bloch function $u_{\mathbf{k}}^n$ has the same periodicity as the crystal potential. The states are described by two quantum numbers: the total angular momentum and its projection onto the quantization axis z . The Bloch states of the conduction band with $j = 1/2$ and $j_z = \pm 1/2$ take the form

$$|u_{1/2}\rangle = |s\rangle|\uparrow\rangle \quad \text{and} \quad |u_{-1/2}\rangle = |s\rangle|\downarrow\rangle, \quad (1.9)$$

where $|s\rangle$ denotes the coordinate part of the s-type Bloch amplitude which is invariant under symmetry transformations of the crystal [35]. Since the valence band Bloch states have orbital p-symmetry, the coupling between the orbital momentum $l = 1$ and spin $s = 1/2$ within the frame of the Clebsch-Gordan theory has to be considered. For the hh ($j_z = \pm 3/2$) and lh ($j_z = \pm 1/2$) states the Bloch amplitudes with $j_h = 3/2$ read

$$\begin{aligned} |u_{3/2}\rangle &= -\frac{1}{\sqrt{2}}|x+iy\rangle|\uparrow\rangle \quad , \quad |u_{-3/2}\rangle = \frac{1}{\sqrt{2}}|x-iy\rangle|\downarrow\rangle, \\ |u_{1/2}\rangle &= -\frac{1}{\sqrt{6}}(|x+iy\rangle|\downarrow\rangle - 2|z\rangle|\uparrow\rangle), \\ |u_{-1/2}\rangle &= \frac{1}{\sqrt{6}}(|x-iy\rangle|\uparrow\rangle + 2|z\rangle|\downarrow\rangle). \end{aligned} \quad (1.10)$$

Here $|x\rangle$, $|y\rangle$, and $|z\rangle$ are the p-type coordinate parts of the Bloch amplitudes which transform like the spatial coordinates x , y , and z . Due to the presence of the $|z\rangle$ part in the lh Bloch states, the electric dipole allowed interband transitions are not only circularly but also linearly polarized (see Subsection 1.2.3).

The closing remarks of this Subsection treat the competing effects of quantum confinement and Coulomb-induced electron-hole correlations for an electron and a hole confined in a quantum dot. According to Heisenberg's uncertainty principle the confinement of a particle into an area with length Δx introduces an uncertainty in the momentum p_x given by $\Delta p_x \sim \hbar/\Delta x$ [44, 45]. For an electron-hole pair confined in a QD two length scales are characteristic: the size of the quantum dot estimated by the length $R = \sqrt{\hbar/(\mu\omega)}$ [46], and the effective Bohr radius $a_B^* = \epsilon\hbar^2/(\mu e^2)$. Here, $\mu = m_e^*m_h^*/(m_e^* + m_h^*)$ marks the reduced mass of the electron-hole pair with the effective masses of the electron and hole, ϵ the dielectric constant of the QD material, and e the elementary charge. The relation between both length scales defines the strong and weak confinement regimes. In the weak confinement regime with $R \gg a_B^*$ the quantum energy of localization $\hbar\omega = \hbar^2/(\mu R^2) \sim R^{-2}$ can be neglected against the Coulomb

attraction $\sim R^{-1}$ [47], therefore, an electron-hole pair is strongly correlated. By comparison, in the strong confinement regime with $R \ll a_{\text{B}}^*$ the electron-hole pair is weakly correlated and occupies the pair of lowest energy single-particle states [48]. The stronger confinement of an electron and a hole in a quantum dot increases the direct Coulomb interaction as the electron-hole separation is reduced. At the same time, their kinetic energy is also enhanced. However, the increase in the direct Coulomb coupling does not imply that Coulomb effects gain more significance. They are more likely defined by the extent to which the electron and hole can correlate to form an exciton [48]. Additionally, the short-range electron-hole exchange interaction scaled by R^{-3} can play an essential role in determining the electron-hole pair level structure [49].

1.1.2 Carrier Wave Function in a Quantum Dot

Analytical derivations of the electron and hole wave function in a quantum dot are commonly based on the separation of the vertical (z) and in-plane (x, y) motion, thus allowing the usage of a single-band approximation being in line with the generalized Kohn-theorem[†]. In contrast to the electron, the hole ground state has a nonzero orbital angular momentum giving rise to spin-orbit coupling induced mixing between the light- and heavy-hole states at $k = 0$ [52]. The mixing between the heavy-hole and light-hole states forbids to describe the valence band within the single-band approximation [53]. Furthermore, the spin-orbit interaction between the subbands of the valence band considerably increases with a decrease in the dot dimensions [54]. However, certain factors, for example, the strain[‡] present in the (lens-shaped) self-assembled quantum dots, increase the splitting between the subbands of the light- and heavy-holes, and, in turn, weaken the intersubband interaction. Accordingly, the single-band approximation for valence band holes is justified, and the confined QD states of a hole can be described in a way similar to that of the electron states, only with different effective masses and depth of the confining potential [56, 57, 58].

The QD confinement along the growth direction z can be assumed to be stronger than in the xy -plane. Therefore, the basis function of the localized single electron or hole is separable into an in-plane and a perpendicular part:

$$\Psi_{\text{e,h}}(\mathbf{r}) = \chi_{\text{e,h}}(x, y) \cdot f_{\text{e,h}}(z). \quad (1.11)$$

The subband function $f_{\text{e,h}}(z)$ is a linear combination of plane waves $\exp(\pm ik_{\text{e,h}}z)$ inside the quantum dot, in the surrounding wetting layer it exponentially decays as $\exp(-k'_{\text{e,h}}z)$ [59]. The confining potential in the vertical direction can be supposed as a rectangular quantum well provided by the band offset between the QD and barrier material[§]. The

[†]Originally, W. Kohn has demonstrated that in a two-dimensional electron system with translational symmetry, a perturbing electric field only connects Hamiltonian eigenstates whose energies are separated by the cyclotron energy [50]. Hence, the cyclotron mass is not influenced by electron interactions. The generalized Kohn-theorem states that a many-electron system exhibits a single-electron response even for a parabolic quantum dot confinement [51].

[‡]The strain fields in and around, for instance, self-assembled (In,Ga)As/GaAs QDs depend on the dot geometry, average (In,Ga)As composition, and the In/Ga distribution profile. A result of these strain fields are piezo-electric fields of varying sizes [55].

[§]Due to the larger effective mass the hole is more confined in the vertical direction. This electron-hole asymmetry reduces the overlap of the electron and hole wave functions.

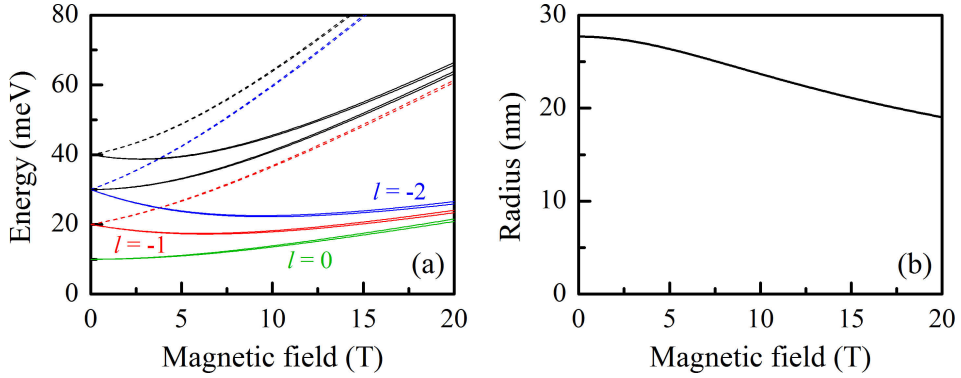


Figure 1-2: (a) Fock-Darwin states of a single electron in an (In,Ga)As QD with $m_e^* = 0.062m_0$ and a lateral confinement energy $\hbar\omega_0 = 10$ meV. The states $|n = 0, l \leq 0, s_{z,e} = \pm 1/2\rangle$ are marked by colored solid lines. The states with positive orbital angular momentum and $n = 0$ are indicated by dashed lines. The levels with $n = 1$ are shown by black lines. The ground state $|0, 0, +1/2\rangle$ has the lowest energy due to the negative electron g factor $g_e = -0.6$. (b) Magnetic field dependence of the effective size (radius) of the FD state $|0, 0\rangle$.

rotational symmetry of the Hamiltonian with respect to the z -axis allows the wave functions $\chi_{e,h}(x, y)$ to be separated into a radial and an angular part. Since the lateral confinement potential can be approximated by a cylindrical symmetry with a parabolic profile, the functions $\chi_{e,h}$ satisfy the Schrödinger equation for a two-dimensional (2D) harmonic oscillator. In consideration of a self-assembled quantum dot with 2D parabolic confinement $V_0(\rho) = 1/2m^*\omega_0^2\rho^2$ in a magnetic field with $\mathbf{B} \parallel \mathbf{z}$, the effective Hamiltonian[¶] of an electron or a hole is written in terms of the azimuthal ϕ and radial ρ coordinates [60, 61]:

$$\hat{H} = -\frac{\hbar^2}{2m^*} \left(\rho^{-1} \frac{\partial}{\partial \rho} \rho \frac{\partial}{\partial \rho} + \rho^{-2} \frac{\partial^2}{\partial \phi^2} \right) - \frac{i}{2} \hbar \omega_c \frac{\partial}{\partial \phi} + \frac{1}{8} m^* \omega_c^2 \rho^2 + \mu_B g S_z B + V_0(\rho). \quad (1.12)$$

Here, m^* is the in-plane effective mass, $\omega_c = |e|B/m^*$ the cyclotron frequency, $\mu_B = 5.7884 \cdot 10^{-5}$ eV/T the Bohr magneton, g the effective g factor, and S_z describes the z -component of the carrier effective spin. The latter parameter is defined as $S_{z,e} = s_{z,e} = \pm 1/2$ for the electron and as $S_{z,hh} = -1/3 j_{z,hh}$ or $S_{z,lh} = -j_{z,lh}$ for the hole with total angular momentum projections $j_{z,hh} = \pm 3/2$ or $j_{z,lh} = \pm 1/2$ [62]. The spin-orbit coupling term $\hat{H}_{so} \sim (\nabla V_{ep} \times \mathbf{p}) \cdot \boldsymbol{\sigma}$ with the momentum operator \mathbf{p} and the Pauli matrix $\boldsymbol{\sigma}$ in the presence of an electric potential V_{ep} is neglected. \hat{H}_{so} comprises the structure inversion asymmetry of the confinement potential (Rashba term) and bulk inversion asymmetry of the crystal lattice (Dresselhaus term) [63, 64]. Furthermore, deviations from the parabolic potential ($\sim \rho^4$ or asymmetries with $\omega_{c,x} \neq \omega_{c,y}$) as well as Coulomb interaction between identically charged carriers are omitted; both can be essential for quantum dot structures with – at least – two interacting electrons [51, 65, 66]. Exchange-based interactions or interactions between carriers localized in different quantum dots are also disregarded.

[¶]The parameters m^* , ρ , ϕ , ω_c , g , and S_z , being different for the electron and hole, are not marked by subscripts.

The energy eigenfunction of Hamiltonian (1.12) takes the form

$$\chi_{n,l}(\phi, \rho) = \frac{1}{\sqrt{\pi}} \exp(i l \phi) R_{n,l}(\rho), \quad (1.13)$$

where $n \in \mathbb{N}_0$ is the radial quantum number and $l \in \mathbb{Z}$ the angular momentum component along z . The radial wave function is determined by

$$R_{n,l}(\rho) = \sqrt{\frac{n!}{(n+|l|)!}} \exp\left(-\frac{\rho^2}{2l_\Omega^2}\right) \frac{\rho^{|l|}}{l_\Omega^{|l|+1}} L_n^{|l|}(\rho^2/l_\Omega^2) \quad (1.14)$$

with the effective length $l_\Omega = \sqrt{\hbar/(m^*\Omega)}$, $\Omega = \sqrt{\omega_0^2 + \omega_c^2}/4$, and the generalized Laguerre polynomials^{||} $L_n^{|l|}$. These eigenstates of a noninteracting single particle are called Fock-Darwin (FD) states [67, 68]. The magnetic field evolution of the energy spectrum for a real confinement potential is similar to the lowest part of the FD spectrum [56]. The eigenenergies are given by

$$E_{n,l} = (2n + |l| + 1)\hbar\Omega + \frac{1}{2}\hbar l \omega_c + \mu_B g S_z B. \quad (1.15)$$

Since for dipole allowed transitions only electrons and holes with the same set of quantum numbers can recombine, the FD spectrum of an electron-hole pair can simply be defined as the sum of the electron and hole energies [69]:

$$E_{n,l}^{\text{eh}} = (2n + |l| + 1)\hbar(\Omega_e + \Omega_h) + \frac{1}{2}\hbar l(\omega_{c,e} + \omega_{c,h}) + \mu_B B(g_e S_{z,e} + g_h S_{z,h}). \quad (1.16)$$

An exemplary electron FD spectrum is shown in Fig. 1-2 (a) for an (In,Ga)As quantum dot. For the electron states with nonzero orbital angular momentum the energy has a minimum in relatively low magnetic fields due to the reduction in the effective length. The electrons become more localized around the QD center where the confinement potential has a minimum. The energy increase at higher fields is attributed to the increasing kinetic energy of the cyclotron motion. For vanishing confinement potential ($\omega_0 \rightarrow 0$) or large magnetic field strength ($\omega_c \gg \omega_0$) the Landau solution is obtained. In this limit the energy $E_{n,l}$ tends to $[n + (|l| - l)/2 + 1/2]\hbar\omega_c$. Thus, the energies of the positive l states would be independent of l without a confinement potential. With a confinement potential, however, the energies increase with l . This is the key difference between the behavior of free and confined electrons [70]. Moreover, the parameter l_Ω which indicates the effective length of the system decreases with increasing magnetic field and increases with the angular momentum. The size of a FD state, which can be estimated by the squared radius [71]

$$R^2 \sim l_\Omega^2(2n + |l| + 1), \quad (1.17)$$

is characterized by the similar magnetic field dependence, as shown in Fig. 1-2 (b). In addition to that, the confinement and magnetic length can be defined by $l_0 = \sqrt{\hbar/(m^*\omega_0)}$ and $l_c = \sqrt{\hbar/(m^*\omega_c)}$, respectively.

^{||}The generalized (or associated) Laguerre polynomials are given by $L_n^{|l|}(x) = \frac{e^x x^{-|l|}}{n!} \frac{d^n(e^{-x} x^{n+|l|})}{dx^n}$. The first two polynomials take the form $L_0^{|l|}(x) = 1$ and $L_1^{|l|}(x) = 1 - x + |l|x$.

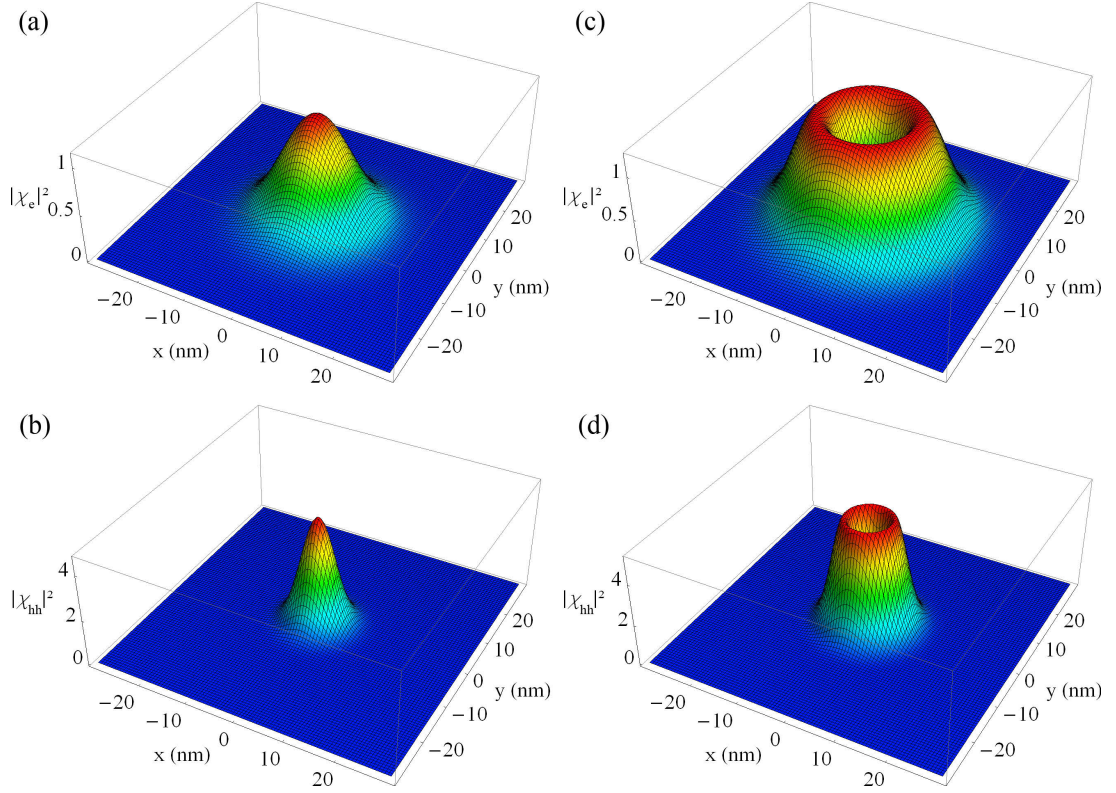


Figure 1-3: Probability distributions of the electron and heavy-hole wave functions $\chi(x, y)$ in an (In,Ga)As quantum dot for a magnetic field of 8 T. The ground-state wave functions of the electron and heavy-hole are illustrated in (a) and (b), respectively. In (c) and (d) the relations $|\chi_e|^2$ and $|\chi_{hh}|^2$ for the first-excited state are shown. The following parameters are used: $m_e^* = 0.062m_0$, $m_{hh}^* = 0.34m_0$, $\hbar\omega_0 = 10$ meV.

The probability densities $|\chi(x, y)|^2$ of the electron and heavy-hole ground and excited states are shown in the Figs. 1-3 (a)-(d) for an (In,Ga)As quantum dot. As illustrated in the panels (a) and (b), the ground state $|n = 0, l = 0\rangle$ of both the electron and heavy-hole is solely described by a radial-symmetric Gaussian distribution, as characteristic for a s-type wave function [72]. In the case of the first-excited states with $l = \pm 1$, the Gaussian function is modulated by a coefficient linear in the radial coordinate ρ , and thus the wave function probability tends to zero at the center of the xy -plane, see Figs. 1-3 (c) and (d). In comparison to the electron, the probability distribution of the heavy-hole wave function is more strongly centered in the xy -plane owing to the larger effective mass. Note, it is assumed that the electrons and heavy-holes have the same lateral confinement energy of 10 meV. The presented wave function probabilities indicate that s- and p-like distributions only slightly overlap. In real quantum dots different elongations in the in-plane directions and distribution alignments in the z -direction dependent on the composition profile as well as dot size and shape might play an important role [55, 73]. In self-assembled QDs the confinement length l_0 for both types of carriers can be assumed to be equal [57, 58]. However, the hole wave functions in the in-plane direction might be more delocalized than the electron ones, since the electrons and holes differently respond to band-offset potentials, strain, and composition fluctuations.

1.1.3 Impact of Quantum Confinement on the Electron g Factor

In low-dimensional semiconductor structures the g factors of the electron as well as hole deviate from their bulk values. The discrepancy can be attributed to the following reasons: (i) the confinement potential changes band parameters, particularly the band gap energy [74]. (ii) The electron g factor becomes anisotropic in a system with reduced symmetry [75]. Hence, off-diagonal g factor tensor components deviate from zero. For instance, in the T_d symmetry the g factor is isotropic, while a further symmetry reduction to D_{2d} leads to different transverse and longitudinal g factors ($g_{x,x} = g_{y,y} \neq g_{z,z}$). In low-symmetry systems off-diagonal tensor components (e.g., $g_{x,y} = g_{y,x} \neq 0$) must also be considered [59]. (iii) Since the g factor values in the quantum layer and its surrounding material are different, any interlayer redistribution and modification of the electron wave function causes a change in the g factor and its anisotropy [74]. (iv) Strain effects induced by the lattice mismatch between the different materials in a semiconductor heterostructure, and/or (v) the discrete energy spectrum itself quenching the orbital angular momentum can modify the electron and hole g factors [76]. These mutually dependent aspects can further be related to, e.g., the quantum structure width, mixing between ground states, coupling with excited carrier states, nonparabolicity of the conduction band [77], interface-related electric fields [78], or corrections due to electron-hole exchange interaction. All these reasons can contribute to the behavior of the carrier g factor in a low-dimensional semiconductor structure.

The electron g factor (or Landé factor) characterizes the Zeeman splitting of the electron spin levels in a magnetic field. The Zeeman term of the electron Hamiltonian is given by

$$\hat{H}_Z = \frac{1}{2}\mu_B \sum_{\alpha,\beta} \sigma_\alpha g_{\alpha,\beta} B_\beta, \quad (1.18)$$

where the Pauli spin matrices σ_α , g factor tensor $g_{\alpha,\beta}$ and magnetic field vector components B_β are functions of the spatial coordinates $\alpha, \beta = x, y, z$. In the most general case the second-rank tensor $g_{\alpha,\beta}$ contains nine linearly independent components. In a system with uniaxial symmetry, the linearly independent components are reduced to $g^\parallel = g_{z,z}$ and $g^\perp = g_{x,x} = g_{y,y}$ with z being the quantization axis. Accordingly, the Zeeman splitting ΔE_Z of the spin sublevels only includes the longitudinal and transverse g factor values, whereby, the magnetic field vector \mathbf{B} and the spatial \mathbf{z} -vector enclose an angle θ :

$$\Delta E_Z = \mu_B |\mathbf{B}| \sqrt{(g^\parallel \cos \theta)^2 + (g^\perp \sin \theta)^2}. \quad (1.19)$$

Based on the second-order $\mathbf{k} \cdot \mathbf{p}$ perturbation theory the Zeeman Hamiltonian for the conduction band electrons can be expressed as [59]

$$\hat{H}_Z = \frac{1}{2}\mu_B \sum_{\gamma} B_{\gamma} \left(g_0 \sigma_{\gamma} - \frac{2i}{m_0} \sum_{n \neq c} \sum_{\alpha, \beta} \delta_{\alpha, \beta, \gamma} \frac{p_{c,n}^{\alpha} p_{n,c}^{\beta}}{E_c - E_n} \right).$$

Here, $g_0 \approx 2.0023$ is the free electron Landé factor [79], $p_{c,n}$ the momentum matrix element between the Γ -point electron states in the conduction band c and the band n for a specific spin momentum projection $s_{z,e} = \pm 1/2$, E_c and E_n are the electron energies at the conduction band bottom in the lower or higher band $n \neq c$ at the Γ -point, and $\delta_{\alpha,\beta,\gamma}$ the unit antisymmetric third-rank tensor. For an electron occupying the lowest

conduction band Γ_6 in a semiconductor with tetrahedral T_d symmetry, the g factor is isotropic and determined by the coupling matrix elements $\langle c|p_{x,y}|n\rangle$ and $\langle n|p_{y,x}|c\rangle$ with the x - and y -components of the momentum operator [80]:

$$g_e = g_{z,z} = g_0 \left(1 + \frac{1}{im_0} \sum_{n \neq c} \frac{\langle c|p_x|n\rangle \langle n|p_y|c\rangle - \langle c|p_y|n\rangle \langle n|p_x|c\rangle}{E_c - E_n} \right). \quad (1.20)$$

Since the upper valence bands Γ_8 and Γ_7 mainly contribute to g_e , the electron g factor equation takes the following form originally calculated by Roth, Lax, and Zwerdling [81]:

$$g_e = g_0 \left[1 - \frac{E_p}{3} \frac{\Delta_{so}}{E_g(E_g + \Delta_{so})} \right] + \Delta g_e. \quad (1.21)$$

The band gap energy is described by E_g , E_p is the energy of the matrix element of the conduction and valence band coupling**, Δ_{so} is the spin-orbit splitting of the valence band ground state, and Δg_e includes contributions from the remote conduction and valence bands. Alternatively, the electron g factor can be expressed in terms of the electron effective mass m_e^* :

$$g_e = g_0 \left[1 - \frac{\Delta_{so}}{3E_g + 2\Delta_{so}} \left(\frac{m_0}{m_e^*} - 1 \right) \right]. \quad (1.22)$$

Note, the calculation of the electron effective mass additionally requires the consideration of the upper conduction bands Γ_7 and Γ_8 , as demonstrated by Hermann and Weisbuch [80]. By comparison, the electron g factor particularly depends on the band gap as well as the spin-orbit splitting of the topmost valence band.

In strongly confined systems, like in quantum wells or quantum dots, the index n refers not only to different bands but also to subbands. The assumption of a purely isotropic electron g factor has to be abandoned. As an example, the relative anisotropy of the electron g factor in an unstrained quantum well can be estimated by [59]:

$$\frac{g_e^\perp - g_e^\parallel}{g_e^\perp} \approx \frac{3}{2} \frac{(E_{lh} - E_{hh})(E_g + \Delta_{so})E_p}{E_g[E_p\Delta_{so} - 3E_g(E_g + \Delta_{so})]}. \quad (1.23)$$

The confinement energies in the lowest heavy-hole and light-hole subbands are denoted by E_{hh} and E_{lh} , respectively. If the quantum well consists of two semiconductor materials with mismatched lattice constants, strain-induced band shifts must be taken into account. Accordingly, both the confinement and strain induce the splitting of the heavy- and light-hole states. The longitudinal and transverse g factors of an electron in an InAs/GaAs heterostructure are shown as a function of the band gap energy in Fig. 1-4 (a). The band gap strongly influences g_e ; the absolute values of both g factors decrease with increasing energy, whereby, the relation $|g_e^\perp| < |g_e^\parallel|$ is valid.

Theoretical calculations of the electron g factor tensor for low-symmetry QDs can hardly be found in the literature [76]. In the case of spherical QDs the isotropic electron g factor has been evaluated from the numerical solution of a $8 \times 8 \mathbf{k} \cdot \mathbf{p}$ Hamiltonian [75].

** E_p is also called Kane parameter and is written in the form $E_p = 2m_0\hbar^{-2}P^2 = 2/m_0 p_{c,v}^2$.

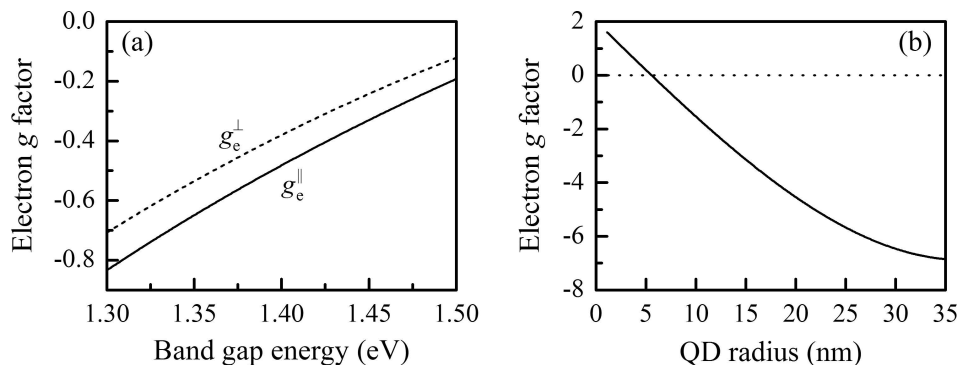


Figure 1-4: (a) Calculated energy dependence of the electron g factor for an InAs/GaAs heterostructure based on the Eqs. (1.21) and (1.23) using parameters from Table 1-1. The heavy-hole energy E_{hh} is set as zero-level, the light-hole split-off energy is approximated by -10 meV. (b) Electron g factor dependent on the radius of a spherical $\text{In}_{0.25}\text{Ga}_{0.75}\text{As}$ quantum dot. The estimation is based on Eq. (1.24), where $f(r)$ is expanded in series until third order, the constant C is set to unity, and E is approximated by a few meV [75].

In that case the electron g factor can be expressed by

$$g_e = g_0 + (g_A - g_0)w_A + (g_B - g_0)w_B + (g_B - g_A)V(R)f^2(r). \quad (1.24)$$

The volume of the spherical quantum dot is described by $V(R) = 4/3\pi R^3$, the function $f(r)$ is given by $C/r \sin(k_{A,B}r)$ with a coefficient C and $k = \sqrt{2m_{A,B}E/\hbar^2}$ [75], $w_{A,B}$ is equal to the integral $\int f^2(r)dr$, and $g_{A,B}$ are calculated with Eq. (1.21) for the QD materials A and B. Here, E denotes the electron energy with respect to the bottom of the conduction band. While the second and third terms of Eq. (1.24) refer to volume contributions, the last term can be regarded as an interface contribution. Exemplarily, the electron g factor as a function of the radius of a spherical $\text{In}_{0.25}\text{Ga}_{0.75}\text{As}$ quantum dot is shown in Fig. 1-4 (b). Parameters listed in Table 1-1 are used for this calculation. The evolution qualitatively demonstrates that the electron g factor remarkably depends on the spatial extension of the quantum dot; g_e decreases with increasing QD radius.

1.2 Inelastic Light Scattering in Semiconductors

1.2.1 Preliminaries

A scattering process is inelastic if the nature or the internal state of the particles involved is changed. Inelastic light scattering is a process in which a photon interacts with an elementary quantized excitation inside an optical medium. Hereby, the photon changes its energy and/or propagation direction. In a bulk semiconductor one can distinguish between scattering processes where carriers, phonons, or static imperfections or inhomogeneities (Rayleigh scattering) are involved. This general classification can be expanded, thus, the term *carriers* previously mentioned embraces not only (free) electrons or holes, but also different kinds of bound excitation complexes like excitons, or quasi-particles like magnons or plasmons. In the case of phonon induced light scattering a difference between

Table 1-1: Material parameters for bulk GaAs, AlAs, InAs, and CdTe. The band gap energy E_g is listed for the Γ - and X-point of the Brillouin zone. The hole effective masses are related to the (001)-direction. The characteristic Kohn-Luttinger Hamiltonian parameters γ_i , the calculated quantity $\kappa_{\text{KL}} = -1/3\gamma_1 + 2/3\gamma_2 + \gamma_3 - 2/3$, and q_{KL} are designated in the table [81, 82]. The longitudinal heavy-hole g factors for AlAs, InAs, and CdTe are determined by $g_{\text{hh}}^{\text{bulk}} = -6\kappa_{\text{KL}}$ [83, 84]. The electron hyperfine constant and nuclear spin are summed up for each structure without composition weighting by use of $A_{\text{hf}}^{\text{In}} = 47 \mu\text{eV}$ with nuclear spin $I = 9/2$, $A_{\text{hf}}^{\text{Ga}} = 44 \mu\text{eV}$ and $A_{\text{hf}}^{\text{As}} = 46 \mu\text{eV}$ with $I = 3/2$ [85, 86].

| Parameter | GaAs | AlAs | InAs | CdTe |
|--|--------------------|--------------------|--------------------|--------------------|
| E_g^Γ (eV) | 1.519 ^a | 3.099 ^a | 0.417 ^a | 1.606 ^b |
| E_g^X (eV) | 1.981 ^a | 2.24 ^a | 1.433 ^a | 3.29 ^c |
| Δ_{so} (eV) | 0.341 ^d | 0.28 ^a | 0.38 ^d | 0.92 ^d |
| E_p (eV) | 28.8 ^a | 21.1 ^a | 21.5 ^a | 16.7 ^e |
| g_e^{bulk} | -0.44 ^f | 1.52 ^g | -14.9 ^g | -1.68 ^h |
| $g_{\text{hh}}^{\text{bulk}}$ | 1.05 ⁱ | -0.3 | -45.2 | -2.1 |
| m_e^*/m_0 | 0.067 ^j | 0.15 ^a | 0.026 ^j | 0.093 ^j |
| m_{hh}^*/m_0 | 0.34 ^k | 0.41 ^l | 0.34 ^l | 0.48 ^l |
| m_{lh}^*/m_0 | 0.09 ^k | 0.16 ^k | 0.03 ^m | 0.13 ^l |
| a_B (nm) | 11.2 ⁿ | 2.0 ^p | 35 ^p | 7 ⁿ |
| γ_1^a | 6.98 | 3.76 | 20.0 | 4.11 ^q |
| γ_2^a | 2.06 | 0.82 | 8.5 | 1.08 ^q |
| γ_3^a | 2.93 | 1.42 | 9.2 | 1.95 ^q |
| κ_{KL} | 1.31 | 0.05 | 7.5 | 0.35 ^q |
| q_{KL}^r | 0.04 | 0.03 | 0.04 | — |
| $\sum A_{\text{hf}}I$ (μeV) | 135 | — | 281 | — |

References: ^a [87], ^b [88], ^c [89], ^d [36], p. 75; ^e [90], ^f [91], ^g [92], ^h [93], ⁱ [94], ^j [36], p. 71; ^k [95], ^l [96], ^m [97], ⁿ [36], p. 282; ^p [98], ^q [99], ^r [41], p. 80.

acoustic (Brillouin or Mandelstam-Brillouin) and optical (Raman) phonon scattering can be drawn*.

In the following the physical basics of light scattering are explained with an electric dipole oscillator exposed to an external electric field $E(t)$ varying periodically in time t at a specific frequency ω_i . Within this simple model the elastic and inelastic scattering contributions are outlined. The electric dipole with eigenfrequency ω_d is characterized by the dipole moment $P(t)$ which satisfies the equation of motion for an externally perturbed oscillator

$$\ddot{P}(t) + \omega_d^2 P(t) = \gamma(t)E(t). \quad (1.25)$$

The coupling between the incident monochromatic light wave $E(t) = E_i \cos(\omega_i t)$ of amplitude E_i and the electric dipole is described by $\gamma(t)$. It presumably consists of the sum of

*The discovery of inelastic light scattering from molecules was awarded to C. V. Raman [100, 101, 102] by the Nobel Prize Committee in 1930 thus coining the term *Raman scattering*. While C. V. Raman and his colleague K. S. Krishnan studied different kinds of liquids or their dust-free vapors by use of collimated sun light and complementary light filters, at the same time G. S. Landsberg and L. I. Mandelstam [103, 104] performed scattering experiments on quartz crystals illuminated by light of a mercury lamp. Landsberg and Mandelstam published their results denoted as combinatorial scattering of light about one week later in 1928 than Raman and Krishnan [105].

a constant γ_0 and time varying part $\gamma_t \cos(\Omega t)$ with modulation frequency $\Omega \ll \omega_d$ [59]. The solution of the inhomogeneous linear differential equation (1.25) with the second derivative of $P(t)$ with respect to t is obtained in the form

$$P(t) = \frac{\gamma_0 E_i}{\omega_d^2 - \omega_i^2} \cos(\omega_i t) + \frac{\gamma_t E_i}{\omega_d^2 - (\omega_i \pm \Omega)^2} \cos(\omega_i \pm \Omega)t. \quad (1.26)$$

Due to the external light perturbation the dipole moment $P(t)$ performs oscillations at the initial frequency ω_i and the combined frequencies $\omega_i \pm \Omega$. Correspondingly, the secondary light wave with frequency ω_i is caused by elastic scattering, while inelastic scattering processes give rise to the emission of waves with the modulated frequencies $\omega_i \pm \Omega$. In a real system the modulation energy $\hbar\Omega$ can be the phonon energy or the energy spacing between two eigenstates of the system [59]. Note, when ω_i of the external field is equal to the intrinsic frequency ω_d , resonance occurs and particularly the first term is indeterminate. By applying L'Hospital's rule it can be demonstrated that in resonance the oscillation amplitude linearly increases in time [106].

The secondary waves with the frequencies $\omega_s = \omega_i \pm \Omega$ belong to the two general types of Raman scattering, namely the Stokes and anti-Stokes process. The Stokes (anti-Stokes) scattering corresponds to the generation (annihilation) of an elementary excitation. In Fig. 1-5 (a) a Stokes process is described by a Feynman diagram. In both cases the energy and momentum are conserved:

$$\hbar\omega_s = \hbar\omega_i \pm \hbar\Omega, \quad (1.27)$$

$$\boldsymbol{\kappa}_s = \boldsymbol{\kappa}_i \pm \mathbf{q}. \quad (1.28)$$

Here, the incident and scattered photons are described by the wave vectors $\boldsymbol{\kappa}_i$ and $\boldsymbol{\kappa}_s$, respectively. The wave vector of the generated or annihilated excitation is denoted as \mathbf{q} . Besides the conservation of energy and momentum related to the homogeneity of time and space, the rotation invariance as a result of the isotropy of space governs the conservation of angular momentum[†]. For a photon the angular momentum quantum number takes the values ± 1 . Linearly polarized light carries zero angular momentum (on average) due to the equal superposition of both states with opposite helicities [108]. Since not all excitations involved in the scattering process transfer angular momentum, the total angular momentum j_m of the local system, that comprises the entity of particles participating in the scattering, will be considered. The conservation law of the angular momentum for Stokes and anti-Stokes processes then reads

$$j_s = j_i \pm j_m. \quad (1.29)$$

Furthermore, the possibility of a Raman scattering process can be determined by the parity selection rule. In general, if the inversion operator \hat{P} is a symmetry operation of a state $|\Psi\rangle$, specified by $\hat{P}|\Psi\rangle = e^{i\delta}|\Psi\rangle$, the parity will be conserved. The low-dimensional compound semiconductors under study are supposed to have inversion asymmetry leading

[†]Following Noether's theorem [107], conservation laws are related to symmetry properties of the studied system. The operator $\hat{O}_\alpha(\Delta\alpha)$ should describe a specific symmetry transformation of the variable α applied on the system wave function Ψ . The change in its initial state is given by $\Delta\alpha$. If the observable ϱ of α is conserved, the new state will only differ from the initial one by a phase factor $e^{i\varrho\Delta\alpha}$ thus defining a conservation law. The full relation reads $\hat{O}_\alpha(\Delta\alpha)|\Psi\rangle = e^{i\varrho\Delta\alpha}|\Psi\rangle$.

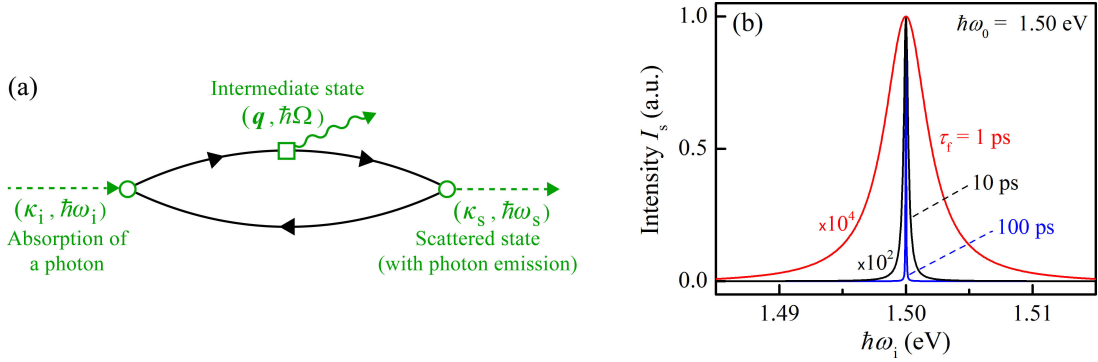


Figure 1-5: (a) Feynman diagram of a Stokes scattering process illustrates the three-step scattering principle. Firstly, a photon is absorbed and creates an electron-hole pair. The intermediate step consists of the change in the electron-hole pair state via scattering with an elementary excitation. At final stage, the electron-hole pair recombines under emission of a scattered photon. (b) Secondary emission intensity calculated after Eq. (1.33) for parallel geometry ($e_i \parallel e_s \parallel \mathbf{d}$) for constant incident intensity $I_i \propto |E_i|^2$. The lifetime of the excited state τ_f characterizes the width as well as the amplitude of the almost Lorentzian-like resonance curve. A long lifetime sharpens the spectral intensity curve, the total intensity remains unchanged.

to crystal fields which break the parity selection rule [109].

How strict are these conservation laws? The energy conservation is the topmost criterion for the allowance of a scattering process. The conservation of energy is governed by the fundamental principle of time-translation invariance expressing the homogeneity of time. Since the energy of a state is not subjected to a unique universal uncertainty principle due to the lack of a universal time operator [110], an energy can exactly be determined – in principle[‡]. On the contrary, the absence of translation symmetry lifts the wave vector conservation represented by (1.28). In low-dimensional structures the crystal momentum is not a good quantum number for the wave vector component along the direction of the size quantization. Thus, in quantum dots with three-dimensional confinement any component of the wave vector is not conserved. Furthermore, under resonance condition the optical absorption in the scattering medium is described by a complex refractive index. As discussed in Ref. [113], a range $\Delta\mathbf{q}$ of phonon wave vectors can then be excited, whereby, $\Delta\mathbf{q}$ is defined by the extinction coefficients at the incident and scattered frequencies. While the wave vector conservation is a rather weak criterion for quantum structures, the preservation of the angular momentum defines a more valid selection rule for the scattering process. Particularly, the optical excitation and recombination of an electron-hole pair is determined by the angular momentum conservation and, in turn, polarization selection rules based on the electric dipole approximation, as it will be discussed in Subsection 1.2.3. The total angular momentum of the whole scattering process and thus the underlying property of the isotropy of space can, however, be violated by, e.g., anisotropic interactions.

[‡]If the theoretical considerations about the time-energy uncertainty are judged by the experimental observations which demonstrate a finite width of detected signals, the uncertainty relation $\Delta t \Delta E \gtrsim \hbar$ cannot be discarded. Note, in a more general way the uncertainty principle is formulated by the Heisenberg-Robertson commutation [111], or the entropic uncertainty relation [112].

The consideration of angular momentum conservation in a scattering process may raise the question whether a phonon could transfer a finite orbital angular momentum? The phonon as a quantized lattice vibration is a quasi-particle without spin, and it can change the momentum \mathbf{k} of an electron significantly. The possibility of the transfer of the orbital angular momentum $\Delta l = \Delta j = \pm 1$ in an electron-phonon scattering process has been reported [114]. By assuming the possibility of angular momentum transfer via (spherical) phonons [115], virtual states can be constructed to realize radiative dipole allowed transitions. For instance, an electron in an initially excited p-state can recombine with a ground state hole after electron-phonon spin-flip scattering with additional orbital angular momentum transfer. The transfer of an angular momentum via a phonon will not be regarded in the following Raman scattering processes.

Before turning to the discussion of inelastic light scattering, characteristic terms of a scattering process must be defined. The most relevant parameter is the scattering cross section ζ which sets the number of scattered photons N_s in relation to the incident photons N_i , integrated over all directions and frequencies: $\zeta = N_s/N_i$. In experiments one only detects photons which are scattered into a cone with a solid angle $\Delta \mathcal{Y}$ along a specific direction and within a scattered frequency range $\Delta \omega_s$ centered on ω_s . In that case the scattering event is described by the differential scattering cross section $d^2\zeta/d\mathcal{Y}d\omega_s$. In literature further parameters are often used, for example, the scattering efficiency η_s , scattering rate w_{fi} , scattering or transition probability $|M_{fi}|^2$, or scattering amplitude A_s . They are proportional to each other, their interdependence reads [36, 38, 116]:

$$\frac{d^2\eta_s}{d\mathcal{Y}d\omega_s} = \frac{\omega_s}{\omega_i A} \frac{d^2\zeta}{d\mathcal{Y}d\omega_s} = \frac{\omega_s}{\omega_i A} \frac{w_{fi}}{\rho_{j,i}} = \frac{2\pi\omega_s}{\hbar\rho_{j,i}\omega_i A} |M_{fi}|^2 \delta(\Delta E). \quad (1.30)$$

Here, A is the area of the incident photon beam, the flux of the incident photons is denoted by $\rho_{j,i}$, and the δ -function accounts for the conservation of energy $\Delta E = E_i - E_f \pm \hbar\Omega$. The expression for the scattering rate w_{fi} of a system between state $|i\rangle = |\Psi_i\rangle$ and $|f\rangle = |\Psi_f\rangle$ in Eq. (1.30) is based on Fermi's golden rule [117]:

$$w_{fi} = \frac{2\pi}{\hbar} |M_{fi}|^2 \delta(E_i - E_f \pm \hbar\Omega). \quad (1.31)$$

The scattering matrix element is given by

$$M_{fi} = \langle f | \hat{H}_s | i \rangle = \int \Psi_f^*(\mathbf{r}) \hat{H}_s \Psi_i(\mathbf{r}) dr. \quad (1.32)$$

The Hamiltonian \hat{H}_s describes the interaction inducing the scattering process where an elementary excitation of energy $\hbar\Omega$ is involved. The square of the scattering amplitude which describes the intensity I_s of the scattered light is directly proportional to the scattering rate: $I_s \propto |A_s|^2 \propto w_{fi}$. Since the time-independent scattering operator \hat{H}_s connects the initial and final states via $|\Psi_f(\mathbf{r}, t)\rangle = \hat{H}_s |\Psi_i(\mathbf{r}, t)\rangle$, the scattering matrix element is the central quantity of the quantum scattering physics[§].

[§]Also, the scattering operator \hat{H}_s is postulated to follow the fundamental properties of Hamiltonian operators formulated by Kato [118, 119]: (i) the scattering operator is self-adjoint, correspondingly, its matrix is Hermitian ($M_{fi} = M_{if}^\dagger$). (ii) The scattering operator is unitary ($\hat{H}_s \hat{H}_s^\dagger = \hat{H}_s^\dagger \hat{H}_s = \mathbf{1}$) expressing the probability conservation law. (iii) The scattering states are asymptotically convergent, thus, the scattering amplitudes can be calculated definitely.

In the end of the Subsection, the contributions to the resonant secondary emission, namely the resonant photoluminescence and resonant Rayleigh scattering, will be described. Consider a two-level quantum system consisting of a ground $|g\rangle$ and an excited $|f\rangle$ state which are energetically separated by $\hbar\omega_0$. An incident photon with specific frequency ω_i , wave vector $\boldsymbol{\kappa}_i$, and polarization unit vector \mathbf{e}_i is absorbed and creates an exciton. In the second step, the exciton is annihilated under emission of a photon with ω_s , $\boldsymbol{\kappa}_s$, and \mathbf{e}_s . The secondary emission intensity is given by

$$I_s \propto |M_{fg}|^2 \delta(\omega_s - \omega_i) \propto \left| \frac{(\mathbf{e}_s^* \cdot \mathbf{d}_{fg})(\mathbf{e}_i \cdot \mathbf{d}_{fg})}{\omega_0 - \omega_i - i\Gamma} E_i \right|^2 \delta(\omega_s - \omega_i), \quad (1.33)$$

where \mathbf{d}_{fg} is the dipole-moment matrix element for the optical transition from $|g\rangle$ to $|f\rangle$, and E_i the amplitude of the incident wave. The damping parameter Γ corresponds to $(2\tau_f)^{-1}$ with the lifetime τ_f of the excited state. The ground state lifetime is supposed to tend to infinity. The damping term[¶] avoids the appearance of a singularity at the fully resonant condition of $\omega_i = \omega_0$. In Fig. 1-5 (b) the impact of the lifetime on the intensity I_s , namely its width and amplitude, is depicted. The process above can be attributed to resonant photoluminescence described by a two-step process with real states. Nevertheless, the secondary radiation depends on the incident frequency: its frequency is shifted by ω_i . Accordingly, the secondary emission can also be considered as light scattering. For the coincidence of both frequencies $\omega_i = \omega_s$, namely the resonant Rayleigh scattering, the photocreated exciton interacts elastically where only the wave vector is transferred.

The resonant secondary emission has both the resonance scattering as well as resonant PL character. The interaction which happens between the optical absorption and radiative recombination determines its spectral properties. However, information about this interaction is obtained indirectly, since the experimental analysis is solely based on the incident and emitted/scattered photons [122]. One property of resonance (Rayleigh or Raman) scattering is the type of the intermediate state which is defined as virtual state in the traditional way [59]. On the contrary, the (resonant) PL is based on the participation of real excited states only. Moreover, the resonance Raman scattering is coherent with the exciting beam, as distinguished from the photoluminescence, see Chapter 4 in Ref. [123]. Since the resonance scattering is an instantaneous two-photon direct process, the time-resolved characteristics can be expected to differ from that of the PL [124]. Furthermore, a correlation between the incident and scattered \mathbf{k} -vectors is characteristic for the resonant Raman scattering, however, in low-dimensional structures the wave vector is not conserved. Hence, this feature distinguishing both contributions to the resonant secondary emission in nonspecular directions is not applicable. In what follows, the resonant Raman scattering processes will be separated from the resonant PL.

1.2.2 Inelastic Scattering of Electrons

Two main inelastic scattering processes which are relevant for the experimentally observed spin-flip Raman scattering will be discussed in the following: (i) the inelastic scattering

[¶]The positive damping parameter is originally introduced to ensure convergence within the second-order time-dependent perturbation theory [120, 121]. Concretely, the integral expression of the second-order correction $M^{(2)}$ is damped at infinity by $\lim_{t \rightarrow \infty} \exp(-\Gamma t) \rightarrow 0$.

between the electromagnetic radiation field and an electron as well as (ii) the acoustic phonon-electron scattering. The three-step scattering principle forms the basis of these processes: an incident photon creates an electron-hole pair, afterwards, the electron is scattered by an acoustic phonon. Finally, the electron-hole pair recombines under emission of a scattered photon. A Feynman diagram of the three-step scattering is depicted in Fig. 1-5 (a).

According to the three-step Feynman diagram three Hamiltonians have to be considered: the electron-radiation interaction \hat{H}_{e-R} , electron-phonon interaction \hat{H}_{e-ph} , and unperturbed \hat{H}_0 Hamiltonians [125]. The latter describes the free photon, phonon and electron and is given by

$$\hat{H}_0 = \sum_{\kappa, \mathbf{e}} \hbar\omega_{\kappa} \left(\hat{c}_{\kappa, \mathbf{e}}^{\dagger} \hat{c}_{\kappa, \mathbf{e}} + \frac{1}{2} \right) + \sum_{\mathbf{q}} \hbar\Omega(\mathbf{q}) \left(\hat{b}_{\mathbf{q}}^{\dagger} \hat{b}_{\mathbf{q}} + \frac{1}{2} \right) + \sum_{n, \mathbf{k}} E_{n, \mathbf{k}} \left(\hat{a}_{n, \mathbf{k}}^{\dagger} \hat{a}_{n, \mathbf{k}} + \frac{1}{2} \right). \quad (1.34)$$

Here, $\hat{a}_{n, \mathbf{k}}$ and $\hat{a}_{n, \mathbf{k}}^{\dagger}$ are the electron annihilation and creation operators acting on the band state which is characterized by the wave vector \mathbf{k} , the quantum number n , and the energy $E_{n, \mathbf{k}}$. The annihilation operators for the photons and phonons are represented by $\hat{c}_{\kappa, \mathbf{e}}$ and $\hat{b}_{\mathbf{q}}$, respectively. The wave vector κ and polarization vector \mathbf{e} describe the light with frequency ω_{κ} . The phonon has the frequency Ω and the wave vector \mathbf{q} . The polarization vector is oriented perpendicularly to the photon propagation direction and parallelly to the electric field vector.

(i) The electron-radiation interaction Hamiltonian can be expressed as

$$\hat{H}_{e-R} = \underbrace{\frac{2\pi\hbar e^2}{m_0 V \sqrt{\nu(\omega_i)\nu(\omega_s)\omega_i\omega_s}}}_{=: A_{e-R}} \hat{c}_{\kappa_i} \hat{c}_{\kappa_s}^{\dagger} \sum_{\mathbf{k}, s, s'} \iota_{s, s'} \hat{a}_{\mathbf{k}+\Delta\mathbf{k}, s}^{\dagger} \hat{a}_{\mathbf{k}, s}. \quad (1.35)$$

Hereby, the photon energies $\hbar\omega_{i, s}$ are not necessarily smaller than the difference between the unperturbed energy of a conduction band level and the energy of another band (resonant scattering). The electron is scattered within the same band by changing its spin and momentum. The emitting volume is described by V , and its refractive index is ν . The matrix ι can be written as a linear combination of the 2×2 unit matrix \hat{I} and the Pauli matrix $\boldsymbol{\sigma}$ considering the upper valence bands Γ_8 and Γ_7 of a zincblende structure:

$$\iota = B(\mathbf{e}_i \cdot \mathbf{e}_s^*) \hat{I} - iC(\mathbf{e}_i \times \mathbf{e}_s^*) \cdot \boldsymbol{\sigma}. \quad (1.36)$$

The explicit expressions for the coefficients B and C can be found in Ref. [59]. The substitution of ι into the Eq. (1.35) leads to

$$\hat{H}_{e-R} = A_{e-R} \hat{c}_{\kappa_i} \hat{c}_{\kappa_s}^{\dagger} \left[B(\mathbf{e}_i \cdot \mathbf{e}_s^*) \sum_{\mathbf{k}, s} \hat{a}_{\mathbf{k}+\Delta\mathbf{k}, s}^{\dagger} \hat{a}_{\mathbf{k}, s} - iC(\mathbf{e}_i \times \mathbf{e}_s^*) \sum_{\mathbf{k}, s, s'} \boldsymbol{\sigma}_{s, s'} \hat{a}_{\mathbf{k}+\Delta\mathbf{k}, s'}^{\dagger} \hat{a}_{\mathbf{k}, s} \right]. \quad (1.37)$$

The first term only describes a change in the electron momentum for parallel-orientated polarization vectors of the incident and scattered light, while the second term accounts for the electron spin-dependent scattering. On the one hand, the spin orientation and momentum are scattered:

$$\mathbf{k}, \pm 1/2 \rightarrow \mathbf{k} + \Delta\mathbf{k}, \mp 1/2 \quad \propto (\mathbf{e}_i \times \mathbf{e}_s^*)_x \pm i(\mathbf{e}_i \times \mathbf{e}_s^*)_y. \quad (1.38)$$

Hereby, the in-plane components of the polarization cross product are relevant. On the other hand, along the quantization z -axis the spin of the electron is conserved and only its wave vector is contributed by the transferred wave vector $\Delta\mathbf{k}$ which can solely be equal to the photon wave vector $\boldsymbol{\kappa}$:

$$\mathbf{k}, s \rightarrow \mathbf{k} + \Delta\mathbf{k}, s \quad \propto (\mathbf{e}_i \times \mathbf{e}_s^*)_z. \quad (1.39)$$

According to the electron-photon interaction Hamiltonian, an electron spin-flip scattering process is performed in oblique geometries. Note, the previous derivations were originally done for spin-density excitations which do not differ from spin-flip processes in absence of a magnetic field [126]. Under application of a magnetic field \mathbf{B} along \mathbf{z} , resulting in a splitting of the electron spin states, the transferred energy in a spin-flip scattering process from s to $-s$ amounts to $|g_e\mu_B B|$.

(ii) Next, the second interaction Hamiltonian will be discussed. It is based on the interaction between an electron and acoustic phonon deformation potential. The general Hamiltonian of the electron-phonon interaction is linear in the phonon operator and bilinear in the electron operator [127]:

$$\hat{H}_{\text{e-ph}} = \sum_{n', n, \mathbf{k}, \mathbf{q}} S_{n', n}(\mathbf{q}) \hat{a}_{n', \mathbf{k}+\mathbf{q}}^\dagger \hat{a}_{n, \mathbf{k}} (\hat{b}_{\mathbf{q}} + \hat{b}_{-\mathbf{q}}^\dagger). \quad (1.40)$$

Here, $S_{n', n}$ is the matrix element for the electron-hole-pair phonon coupling depending on the quantum numbers n and n' , and \mathbf{q} is the phonon wave vector. The matrix element is defined by the phonon coupling potential $V_q \propto \sqrt{q} D_{\text{dp}}$ for the electron and hole, where D_{dp} is the deformation potential constant [125, 128]. The longitudinal acoustic phonons dominantly contribute to the electron-phonon scattering, since their deformation potential exceeds that of the transverse acoustic phonons which primarily produce shear strain [129]. According to Eq. (1.40), the phonon scatters the electron from the state n to n' ; this energy change can be accompanied by a reversal of its spin orientation. Hence, the electron-phonon scattering is regarded as an inelastic spin-flip scattering mechanism.

The differential scattering cross section per unit length and solid angle is given by

$$\frac{d^2\zeta}{d\mathcal{T}d\omega_s} = \frac{\omega_s^2 V}{4\pi^2 \hbar^2 c^4} \nu(\omega_i) \nu^3(\omega_s) |w_{\text{fi}}(\omega_s, \mathbf{e}_s; \omega_i, \mathbf{e}_i)|^2. \quad (1.41)$$

Including intermediate electron-hole pair states $|\zeta\rangle$ and $|\zeta'\rangle$ with lifetime broadenings $\Gamma_{\zeta, \zeta'}$ and energies similar to Eq. (1.16), the scattering rate can be written as

$$w_{\text{fi}} = \sum_{\zeta, \zeta'} \frac{\langle f | \hat{H}_{\text{e-R}}(\omega_s) | \zeta \rangle \langle \zeta | \hat{H}_{\text{e-ph}} | \zeta' \rangle \langle \zeta' | \hat{H}_{\text{e-R}}(\omega_i) | i \rangle}{(\hbar\omega_s - E_\zeta + i\Gamma_\zeta) (\hbar\omega_i - E_{\zeta'} + i\Gamma_{\zeta'})}. \quad (1.42)$$

This form of the scattering rate in the lowest order perturbation theory neglecting non-resonant contributions can be evaluated from the three-step Feynman diagram. Notably, for acoustic phonon scattering via the short-ranged deformation potential the differential scattering cross section is proportional to the square of the magnetic field strength [125].

Another contribution to the acoustic phonon scattering is given by the piezo-electric

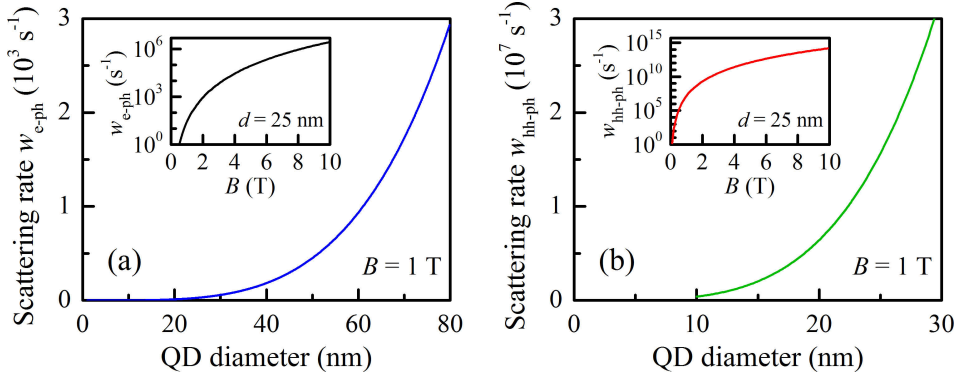


Figure 1-6: Calculated scattering rates for the electron (a) and heavy-hole (b) spins induced by acoustic phonon coupling in a cylindrical GaAs-based QD. In the main panels the dependence of the scattering rates on the QD diameter d are illustrated at a constant magnetic field strength of 1 T. The insets show the scattering rates as a function of the magnetic field for $d = 25$ nm. While for w_{e-ph} the height of the dot is set to 5 nm, the spin scattering rates of the heavy-hole are calculated for $h_{\text{QD}} = 10$ nm and $d \geq h_{\text{QD}}$. The following parameters are used (partly from [133]): $\rho_m = 5.316$ g/cm³, $v_{\text{ph}} = 3860$ m/s, $|g_e| = 0.55$, $\xi_{14} = 1.2 \times 10^9$ V/m, $E_g = 1.4$ eV, $\Delta_{\text{hh-lh}} = 10$ meV, $D'_{\text{dp}} = 5.4$ eV, $D''_{\text{dp}} = 1.98$ eV, $E_{0,0} - E_{0,1} = 10$ meV.

interaction in noncentrosymmetric structures. While the deformation potential^{||} combines the relative displacement of an atom with the energy shift of a band, the piezo-electric effect describes the coupling of a carrier with a varying electric field induced by lattice distortions. Hereby, the carrier-phonon coupling potential V_q is proportional to $q^{-1/2}\xi$ with the piezo-electric tensor ξ [130]. The piezo-electric coupling dominates for phonons with small wave vectors (long wavelength region) against the deformation potential coupling.

Finally, the relaxation rates of an electron or a hole spin in a quantum dot induced by acoustic phonon scattering will be described. The rate of spin-flip transitions between the Zeeman levels of the lowest electron states in a cylindrical QD with a fixed height of $h_{\text{QD}} = 5$ nm and a diameter d due to piezo-electric phonon coupling is given by [131]

$$w_{e-ph} = \frac{8\pi\hbar^2 K_e}{\rho_m v_{\text{ph}}^5} \left(\frac{\Delta_{\text{so}} \xi_{14}}{\sqrt{2m_e^* E_g E_g E_p (E_{0,0} - E_{0,1})^2}} \right)^2 (\mu_B g_e B)^5 d^4. \quad (1.43)$$

Here, ξ_{14} is the nonvanishing piezo-electric tensor element in a zincblende structure, ρ_m the mass density of the studied material, v_{ph} the sound velocity, and $K_e = 0.91 \times 10^3$ a numerical factor. By comparison, the heavy-hole scattering rate affected by the deformation potential is defined by [132]

$$w_{\text{hh-ph}} = \frac{3\pi}{8\hbar^2 \rho_m v_{\text{ph}}^7} \frac{\gamma_2^2 V_{\text{hh}}}{m_0^2 m_{\text{hh}}^* \Delta_{\text{hh-lh}}^2} \frac{K_{\text{hh}} K_{\text{ph}} (D'_{\text{dp}}{}^2 + D''_{\text{dp}}{}^2)}{(2h_{\text{QD}})^4} (3\kappa_{\text{KL}} \mu_B B)^5 (eB)^2 d^4. \quad (1.44)$$

^{||}Deformation potential scattering is also possible for optical phonons; via the Fröhlich interaction longitudinal optical phonons are coupled to carriers. It originates from the Coulomb interaction between the electric field of the optical phonon and the charge of the carrier.

Here, the GaAs-parameters $\gamma_2 = 2.1$ and $\kappa_{\text{KL}} = 1.3$ of the Kohn-Luttinger Hamiltonian are used, see Table 1-1. The numerical factors $K_{\text{hh}} = 1.882$ and $K_{\text{ph}} = 32/35$ for the longitudinal acoustic phonon, and an energy $V_{\text{hh}} = 59.2$ meV characterizing the heavy-hole confinement in z -direction are included into the calculations.

In the Figs. 1-6 (a) and (b) the scattering rates for the electron and heavy-hole are shown as a function of the QD diameter and magnetic field strength. While the scattering rate is proportional to d^4 in both cases of the electron and heavy-hole, the spin relaxation rate for an electron is four orders of magnitude smaller due to its smaller effective mass. Thus, the spin-flip inducing interaction between a heavy-hole and an acoustic phonon is very efficient. As illustrated in both insets of the Figs. 1-6 (a) and (b), at $B = 10$ T the electron-phonon scattering time $w_{\text{e-ph}}^{-1}$ is about a few μs , while $w_{\text{hh-ph}}^{-1}$ is in the sub-ps range. The scattering rate increases by a B^7 -dependence for the heavy-hole. The high scattering rate of the heavy-hole spin corresponds to a very efficient coupling to acoustic phonons. Furthermore, the scattering rates for the electron and heavy-hole differ in their dependence on low temperatures (not shown here). While $w_{\text{hh-ph}}$ is rather unaffected by the temperature, the electron spin transition rates increase with temperature [134]. The temperature and, particularly, magnetic field dependence of the electron spin scattering via an acoustic phonon will be relevant for the study of the exciton spin dynamics in (In,Al)As quantum dots, see Section 5.3.

1.2.3 Spin-Flip Raman Scattering

In spin-flip Raman scattering (SFERS) the spin of a carrier is reversed via a scattering event. A SFERS process is typically initiated by the inelastic scattering of an incident photon. The photon excites an electron-hole pair, whereby, the photon energy is in resonance with the electron-hole transition. The spin of the electron, hole, or both carriers involved in the scattering process reverses, as described by Eq. (1.38). A single carrier spin-flip corresponding to an intraband transition can be induced by, for example, a phonon or carrier-carrier interaction. The energy is conserved, while the conservation of the wave vector and/or total angular momentum can be lifted. The final interband transition (e-h pair recombination) follows the electric dipole selection rules.

The observation of a spin-flip Raman line is linked to the magnitude of the transferred energy $\hbar\Omega$ and, in turn, to the energy difference between the states with oppositely orientated spins. In an externally unperturbed semiconductor this difference is typically rather small being below the detection limit. An external magnetic field B can enhance the splitting of the spin states to an experimentally accessible degree of magnitude. Furthermore, the presence of a magnetic field can lift restrictions imposed by selection rules thus making possible SFERS processes. It can also increase the scattering efficiency, since the magnetic confinement can enhance the exciton oscillator strength owing to the shrinkage of its in-plane wave function [135]. The energy splitting, namely the spin-flip Raman shift ΔE_{sf} , is defined by the Zeeman term of the scattered carrier with Landé factor g_s :

$$\Delta E_{\text{sf}} = g_s \mu_B B. \quad (1.45)$$

Accordingly, the SFERS spectroscopy provides the direct measurement of the g factors of the electron, holes and excitons in low-dimensional semiconductors. Angle-dependent measurements with respect to the magnetic field orientation and sample quantization

axes allow to determine the g factor tensor components; an example of an anisotropic electron g factor is described by the Eq. (1.19).

The origin of a SFRS process is not necessarily revealed by the shift of the respective Raman line only. For instance, equal g factors of the electron and hole forbid a definite assignment. Also, the magnetic field dependence of the Raman shift ΔE_{sf} can show deviations from the linear Zeeman behavior, as it will be demonstrated in Subsection 3.3.1. By means of the width of the SFRS line the lifetime of the intermediate scattering state can be estimated thus yielding further information about the spin-flip Raman scattering mechanism. The temperature dependence of the Raman intensity can be used to describe the localization energy of the scattered particle complex. Another possibility to determine the type of SFRS is represented by the tuning of the resonant excitation energy E_{R} , since it affects the scattering efficiency and the Raman shift.

Besides these examples the polarization characteristics of the SFRS line play a key role in the definite designation of the scattering mechanism. In Faraday geometry with parallel alignment of the magnetic field direction and sample growth axis ($\mathbf{B} \parallel \mathbf{z}$) the SFRS mechanism is evaluated from the circularly polarized SFRS spectra by analyzing the selection rules for electric dipole transitions**. The electric dipole selection rules for states $|j, j_z; l, s_z\rangle$, characterized by the quantum numbers of the total angular momentum j , its projection j_z , orbital angular momentum l and the spin projection s_z , are given by

$$\Delta j = 0, \pm 1 \quad , \quad \Delta j_z = 0, \pm 1 \quad \text{and} \quad \Delta l = \pm 1. \quad (1.46)$$

The interband transitions with $\Delta j_z = \pm 1$ are circularly polarized, while the transitions without transfer of total angular momentum are linearly polarized. In the case of the heavy-hole exciton the excitation into the optically active $|j_z\rangle = |s_{z,e}, j_{z,\text{hh}}\rangle = |\pm 1\rangle = |\mp 1/2, \pm 3/2\rangle$ states occurs by the absorption of right- or left-handed circularly (σ^\pm) polarized light. The optical excitation into the $|\mp 2\rangle = |\mp 1/2, \mp 3/2\rangle$ states is forbidden in the dipole approximation.

The differential scattering cross section provides further insight into the electron- or hole-SFRS mechanism. According to Eq. (1.37), in the backscattering Faraday geometry for low-dimensional semiconductors the differential scattering cross section is defined by

$$\frac{d^2\zeta}{d\mathcal{T}d\omega_s} \propto |(\mathbf{e}_i \times \mathbf{e}_s^*) \times \mathbf{B}|^2. \quad (1.47)$$

SFRS experiments are typically performed in the backscattering geometry, where the propagation directions of the incident (z) and scattered (\bar{z}) light are opposite. Then, a polarization configuration with σ_i polarized incident and σ_s polarized scattered light is denoted by the term $z(\sigma_i, \sigma_s)\bar{z}$ [136]. In that geometry, the cross product of the polarization vectors of the incident and scattered photons with the magnetic field vector only differs from zero if \mathbf{B} has a nonzero component perpendicular to the light propagation

**The Hamiltonian of a carrier interacting with the quantized electro-magnetic field contains the scalar product of the vector potential $\mathbf{A}(\mathbf{r})$ and carrier momentum \mathbf{p} , where the vector potential can be expressed in terms of $\hat{c}\exp(i\boldsymbol{\kappa}\mathbf{r})\mathbf{e}_\kappa$ [30]. From the ultra-violet to the near-infrared range, the light wavelength is much larger than the spatial extension of the confined carrier wave function ($\boldsymbol{\kappa} \cdot \mathbf{r} \ll 1$). Thus, the multipole expansion of the exponential factor can be interrupted after the first term, i.e. $\exp(i\boldsymbol{\kappa}\mathbf{r}) \approx 1$. The spatial variation of the electro-magnetic field is negligible in contrast to the polarization described by the unit vector \mathbf{e}_κ . The scalar product reduces to terms similar to $\hat{c}\mathbf{e}_\kappa \cdot \mathbf{p}$.

direction [59]. In the backscattering process the photon angular momentum either remains unchanged ($\Delta l = 0$) or changes by $\Delta l = \pm 2$. Therefore, in that geometry the Raman scattering, which induces a single spin-flip of an electron ($|\Delta s_{z,e}| = 1$) or a hole ($|\Delta j_{z,hh}| = 3$, $|\Delta j_{z,lh}| = 1$), is principally forbidden. However, this selection rule can be bypassed: for instance, a tilted magnetic field lifts the restrictions of the selection rules, as in the case of a mixing between light-hole and heavy-hole states induced by, e.g., strain. An oblique orientation of the magnetic field with $B_x, B_y \neq 0$ creates a mixing between the optically bright and dark excitons. As the heavy-hole does not have a magnetic moment perpendicular to z in a high-symmetric structure, the mixing is established via the transverse electron g factor [137]. A longitudinal field induced mixing is symmetry-forbidden. In structures with lower symmetry, e.g. C_{2v} in (001)-grown QDs, at zero magnetic field the light-hole and heavy-hole states are mixed due to strain [41, 138, 139]. The Bir-Pikus Hamiltonian describes the effect of strain on the valence band structure, see e.g. Ref. [140]. While the longitudinal magnetic field has no influence on the valence band mixing, in transverse B -field geometry the magnetic coupling of the hole can be described by the Hamiltonian terms $J_{x,h}^3 B_x + J_{y,h}^3 B_y$ and $J_{x,h}^3 B_y + J_{y,h}^3 B_x$. Moreover, anisotropic exchange interaction between identically charged carriers or between an electron and a hole, based on a symmetry reduction of the crystal field, provides SFRS of a single carrier. Principally, if a perturbation lowers the symmetry of the electron-hole pair complex, the light scattering involving the spin of a carrier becomes allowed. A low-probable carrier-nucleus coupling can also lift the selection rules. Note, the simultaneous spin-flip of an electron and a hole in an e-h pair complex via acoustic phonons is allowed by Eq. (1.47).

In the following an example of exchange-based SFRS of an acceptor-bound hole in p-type GaAs/(Al,Ga)As quantum wells (QWs) will be outlined. Experimentally, a heavy-hole spin-flip Raman line has been observed in the parallel polarization configurations $z(\sigma^+, \sigma^+)z$ and $z(\sigma^-, \sigma^-)z$ for resonant excitation at the high-energy side of the QW emission spectrum in Faraday geometry [141, 142]. The SFRS line shift corresponds to the heavy-hole Zeeman term $g_{hh}\mu_B B$. Since the polarization states of the incident and scattered photons are equal, the photogenerated exciton keeps its total angular momentum during the scattering process ($|s_{z,e}, j_{z,hh}\rangle = |s'_{z,e}, j'_{z,hh}\rangle$). Thus, the photogenerated heavy-hole does not change its spin state, but induces via anisotropic exchange interaction the reversal of the spin of a heavy-hole bound to an acceptor. The anisotropic exchange is attributed to a spatial separation of the localization centers of both the photo-exciton and acceptor-bound hole. This difference reduces the symmetry of the coupled carrier complex, hence, the selection rules defined by Eqs. (1.46) or (1.47) are relaxed. The mathematical description of the anisotropic exchange coupling can basically be extracted from the matrix element of the Coulomb interaction between the exciton and acceptor-hole. It contains the Coulomb term (effective repulsion) between both holes and the quantum mechanical correction – the exchange term:

$$V_{\text{Coul}} \propto \iint d\mathbf{x}_1 d\mathbf{x}_2 \frac{\psi_{j_h}^*(\mathbf{x}_1)\psi_{j'_h}(\mathbf{x}_1)}{|\mathbf{x}_1 - \mathbf{x}_2|} \int d\mathbf{x}_e \Psi_{j_{\text{Ex}}}^*(\mathbf{x}_e, \mathbf{x}_2)\Psi_{j_{\text{Ex}}}(\mathbf{x}_e, \mathbf{x}_2), \quad (1.48)$$

$$V_{\text{xch}} \propto - \iint d\mathbf{x}_1 d\mathbf{x}_2 \frac{\psi_{j_h}^*(\mathbf{x}_1)\psi_{j'_h}(\mathbf{x}_2)}{|\mathbf{x}_1 - \mathbf{x}_2|} \int d\mathbf{x}_e \Psi_{j_{\text{Ex}}}^*(\mathbf{x}_e, \mathbf{x}_2)\Psi_{j_{\text{Ex}}}(\mathbf{x}_e, \mathbf{x}_1). \quad (1.49)$$

The exchange integral principally represents the difference between a quasi-classical and quantum mechanical description of a many-particle problem, and it is not related to a real

physical interaction [143]. Nevertheless, one can explain the present exchange interaction in the way that the change in the positions \mathbf{x}_1 and \mathbf{x}_2 for the acceptor-bound hole wave function ψ and the photo-exciton wave function Ψ with fixed electron position \mathbf{x}_e is accompanied by a mutual exchange of the initial and final spin states. This kind of non-phonon light scattering represents a spin-flip Raman scattering mechanism perturbing the strict optical selection rules in the dipole approximation in a system with reduced symmetry [41].

Chapter 2

Experimental Methods

The spin-flip Raman scattering (SFRS) spectroscopy is a technique to directly determine the g factors of the electron and holes in semiconductors. In the spintronics and quantum information processing based on optical spin manipulation, for instance, the spin initialization by optical pumping [144] or the coherent spin rotation with ultrashort laser pulses [24] require the knowledge about the electron and hole g factors as they define the energy levels of quantum bits. Not only the energy and spin level structure but also spin interactions between quantum confined carriers can be characterized. Considering the original publication by C. V. Raman from 1928 [100], or one of the first SFRS experiments on bound electrons and holes in CdS by Thomas and Hopfield [145], or even surface-enhanced resonance Raman scattering in the biotechnology [146], the main idea of Raman scattering is simply related to the comparison between the energies of the incident and scattered photons. This energy difference, denoted as Raman shift, is one of the key parameters. Moreover, the intensity and spectral width of the SFRS signal depending on different external perturbations like the temperature, optical excitation polarization or magnetic field yield useful information on the spin-flip scattering mechanism. However, the experimental realization of SFRS in low-dimensional semiconductors is not simple, since it requires sophisticated equipment. The major experimental requirements are described with respect to the properties of SFRS in the Section 2.1. Afterwards, the basic SFRS setup and its extensions providing two-color Raman experiments are presented. Since the (In,Al)As/AlAs quantum dots have been studied by not only SFRS spectroscopy but also time-resolved photoluminescence (PL) determining the exciton dynamics, the description of the time-resolved PL setup completes the Chapter about the experimental methods.

2.1 SFRS: What is Experimentally Required?

Spin-flip Raman scattering of an electron and/or a hole should be observable in every semiconductor, that is laser-excited with an energy being resonant with the bound electron-hole complex, under application of a magnetic field noticeably lifting the spin degeneracy of the electron and/or hole. This a-priori-like statement and, correspondingly, the SFRS feasibility are linked to external parameters like the temperature, geometry of experiment, as well as energy and polarization of the exciting light, which are depicted in the Fig. 2-1. For instance, the probability of spin-flip Raman scattering is minimized by

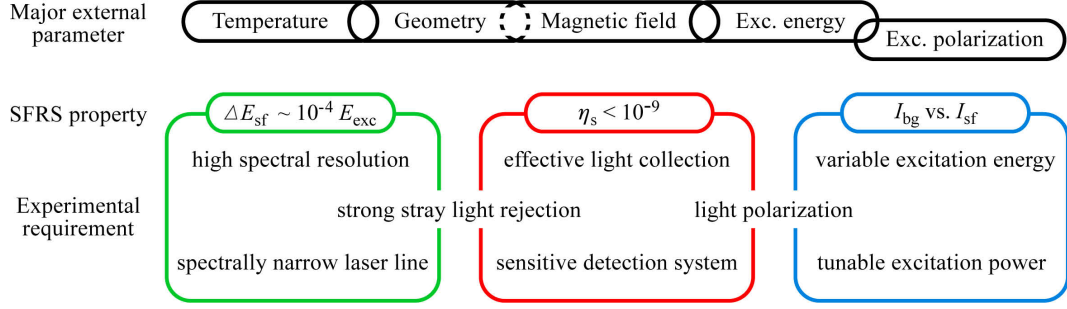


Figure 2-1: Schematic overview of experimental parameters affecting the properties and observation of SFRS in low-dimensional semiconductors. As the excitation polarization is less important for the SFRS feasibility, it is symbolically shifted below the other external parameters.

a thermal energy exceeding the binding energy of the scattering exciton complex, while it is enhanced in a tilted magnetic field geometry where the symmetry of the complex is reduced*. The excitation energy satisfying the resonance condition is also a major external parameter. By comparison, a specific light polarization is not fundamentally necessary to obtain a SFRS signal. Even though the external parameters would have been chosen to fulfill fundamental conditions, one has to overcome further obstacles in order to observe a SFRS signal:

- (i) The efficiency η_s of such inelastic light scattering ranges between 10^{-9} and 10^{-12} [59, 113].
- (ii) The Raman shift ΔE_{sf} is about four orders of magnitude smaller than the excitation energy E_{exc} . The SFRS line appears as a weak satellite in close vicinity of the laser line.
- (iii) The resonant excitation causes a photoluminescence background with intensity I_{bg} potentially obscuring the SFRS line.

These three SFRS properties demand different experimental requirements. They are shown in Fig. 2-1, and will be discussed in the following.

(i) Apart from the intrinsically low spin-flip Raman scattering efficiency, the light scattered from the sample can only be collected partially, since the sample located inside a cryostat is optically accessible through small-sized windows. The light collimation can be established via a long-focused lens (a) positioned outside the cryostat, or a short-focused lens construction (b) inside the cryostat sample chamber[†]. These two possibilities are illustrated in the Fig. 2-2. In order to compare the light gathering power of both lens systems, the intensity I_L of the collected light is estimated by the f -number N_f or,

*In accordance with the electric dipole selection rules a SFRS process will also be possible at zero magnetic field, if the respective spin states are nondegenerate. From experimental point of view the energy transferred in that inelastic scattering process is in most cases too small to be ascertainable.

[†]Instead of the short-focused lens construction, a second type of Raman-holder consisting of a concave mirror as light collimation element is also used.

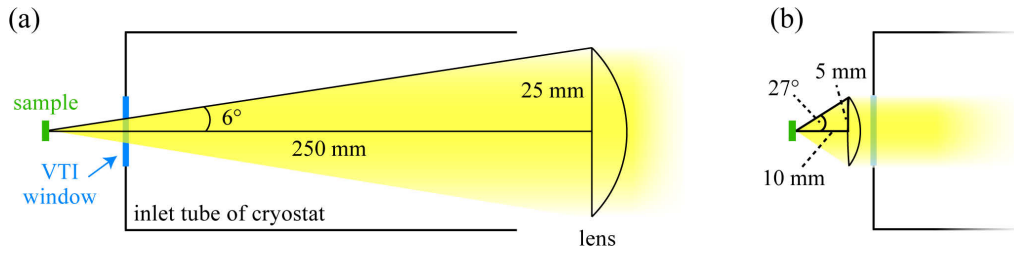


Figure 2-2: Schematically illustrated comparison between the standard and specially designed ways of collimation of light emitted from a sample located in a cryostat-magnet system. (a) Normally, the emitted light which has passed through the VTI (variable temperature insert) window is collimated with a large-diameter plano-convex lens positioned in front of the cryostat. A lens with a focal length of 250 mm and diameter of 50 mm yields an aperture half-angle of about 6° . (b) The Raman-holder, placed inside the VTI of the cryostat, provides a five times larger numerical aperture.

correspondingly, the numerical aperture N_A [147]:

$$I_L \propto N_f^{-2} = \left(\frac{f}{D}\right)^{-2} = (2N_A)^2 = (2\nu \sin \vartheta)^2. \quad (2.1)$$

In the case (b), the sample is in the focal plane of a plano-convex lens with a diameter of $D = 10$ mm and focal length of $f = 10$ mm; the f -number is equal to $N_f = 1$. The numerical aperture is based on the half-angle ϑ of the light cone originating from the sample area illuminated by the laser. By use of a refractive index $\nu_{\text{air}} = 1.00$ for the medium[‡] between the sample and lens and an evaluated half-angle $\vartheta = 27^\circ$ the numerical aperture amounts to $N_A = 0.45$. In the case (a) where the lens with $f = 250$ mm and $D = 50$ mm defines the dimensions of the gathered light cone, the f -number is 5 and the half-angle is not larger than 6° . Therefore, the light intensity I_L is about 25 times weaker for the long-focused lens system compared to I_L for the compact lens construction, denoted as Raman-holder in the following. The latter one, in turn, attributes a specific focal length f_1 to the lens in front of the spectrometer entrance slit. Since the triple-spectrometer (Princeton Instruments, TriVista 555) is characterized by an input f -number $N_f = 5.9$ [153] and the parallel beam of scattering light has a diameter $D_L \approx 15$ mm including a slight divergence, the effective focal length should be $f_1 \approx 90$ mm. A misalignment of its focus influences the gathered light intensity. A Gaussian beam with diameter D_L possesses a minimal diameter $D'_L = 4\lambda f_1 / (\pi D_L)$ in the

[‡]The light gathering power of a lens is enhanced by a decrease in the f -number or an increase in the numerical aperture. As N_A linearly depends on the refractive index of the medium, the usage of liquid helium having a refractive index of $\nu = 1.03$ improves the light collection [148]. Additionally, the reflections from the different interfaces are reduced by the liquid helium as its refractive index is more similar to the high refractive indices of the lens (BK7 - borosilicate crown glass, $\nu = 1.52$) [149], VTI window (quartz, $\nu = 1.54$) [150], and sample surface (e.g. GaAs, $\nu = 3.26$) [151]. The overall intensity after transmission through the VTI window can be approximated by the different Fresnel reflection coefficients $[(\nu_1 - \nu_2)/(\nu_1 + \nu_2)]^2$ for normal light incidence [147]: in comparison to air the liquid helium enhances the intensity by about 10 %. Hereby, light absorption and scattering are neglected. Moreover, the light emission becomes more efficient by means of graded-index coatings grown on top of the sample thus reducing Fresnel reflections [152].

focal plane after propagating through the focusing lens [154]. Considering wavelengths λ in the near-infrared or visible range the diameter D'_L is $(5 \pm 1) \mu\text{m}$. A misaligned focus leads to an increase in the beam diameter possibly exceeding the slit width[§] and, in turn, to a truncation of the beam profile and a reduction in the gathered intensity of the scattered light. Note, the previous considerations are valid for an ideal point source which emits light along the optical axis.

Besides the way of light collimation, the efficiency of the final detection system comprising the spectrometer and photon detector is essential to observe a weak SFRS line. The upper limit of its light throughput is governed by the first-order diffraction efficiency of the gratings. The plane non-blazed holographic gratings used with a density of 1800 grooves/mm have an average efficiency of about 45% at 800 nm. For the triple-spectrometer the light transmission is further reduced by a factor of two due to the absorption of the mirror surfaces in each Czerny-Turner stage [155]. Owing to this light attenuation, a sensitive detector with a high quantum efficiency and large signal-to-noise ratio is necessary. The front-illuminated charge-coupled device (CCD) detector (Princeton Instruments, Spec-10:2K/LN) composed of Si-photodiodes has a quantum yield of 40% at 800 nm[¶]. The signal-to-noise ratio of this liquid-nitrogen cooled CCD camera combined with a 100 kHz readout-amplifier is mainly determined by the shot noise of the signal, while the readout noise and particularly thermal noise are negligible [156].

The polarization of the scattered light is a further parameter influencing the efficiency of the SFRS detection. On the one hand, the grating efficiency is different for light polarized parallel (p-polarized, transverse electric) or perpendicular (s-polarized, transverse magnetic) to the grating grooves. According to solutions of the Helmholtz-equation with different boundary conditions for p- and s-polarized waves [157], for wavelengths smaller (larger) than the blazed wavelength the diffraction efficiency for p(s)-polarized light is higher than for s(p)-polarized light. The overall sum of efficiencies is equal to one due to the conservation of energy. As the SFRS experiments are in the near-infrared spectral region and the used gratings are optimized for the visible wavelength range, the light incident on the spectrometer should be s-polarized to gain the highest diffraction efficiency. On the other hand, the crossing of the polarizer and analyzer attenuates the laser light intensity significantly. Thus, the spectral overlapping between the laser stray light and the weak SFRS line is reduced, provided that the SFRS process is allowed in the crossed-linear polarization configuration. Also, the PL background can be weakened for a specific circular polarization, while the SFRS line intensity I_{sf} might be enhanced.

(ii) Not only the low SFRS intensity, but also the small Raman shift ΔE_{sf} demands a strong stray light suppression. Aside from the spectrometer settings, the efficiency of the stray light suppression is influenced by the laser light reflected from the sample surface, the elastically scattered light, and background stray light resulting from imperfections in the optics and scattering off walls and dust inside the spectrometer [36]. A SFRS line which differs a few hundreds of μeV (a few cm^{-1}) from the Rayleigh line will be screened by stray light if it is suppressed insufficiently. A double-spectrometer (Jobin Yvon, U1000) offers a stray-light rejection ratio r_r as small as 10^{-14} [158]. In the case

[§]A typical width of the entrance slit is $20 \mu\text{m}$ using the subtractive mode of the triple-spectrometer, in the additive mode it does not exceed $100 \mu\text{m}$.

[¶]The Peltier-cooled GaAs-based photomultiplier tube (PMT, Hamamatsu, R943-02) loses its sensitivity at about 930 nm. At 800 nm the quantum efficiency is approximately 12%.

of the triple-spectrometer the ratio approximately amounts to 10^{-12} . A rejection ratio $r_r \leq r_r^* = 10^{-12}$ can be translated into the minimally observable Raman shift via the empiric equation

$$\Delta E_{\text{sf,min}} [\text{cm}^{-1}] \approx 1 - 0.1 \left(\frac{10^{-12}}{r_r} \right)^{\frac{1}{|\delta|+1}}$$

with the difference δ between the exponents of the rejection ratios r_r and r_r^* . By means of the triple-spectrometer SFRS line shifts of $\Delta E_{\text{sf,min}} \approx 0.9 \text{ cm}^{-1}$ can be observed. The double-spectrometer can resolve line shifts down to about 0.5 cm^{-1} .

The SFRS detection also depends on the spectral resolution of the spectrometer. According to the Rayleigh criterion two peaks are spectrally resolved when one peak maximum coincides with the minimum of the other peak [147]. The best possible separation of adjacent spectral lines is quantified by the dimensionless resolving power. It linearly depends on the grating width and is inversely proportional to the wavelength. A more practical quantity is the spectral resolution I_{sr} as it includes instrumental factors leading to a broadening in the width of the recorded line. Besides aberrations and diffractive effects, the spectral resolution is mainly determined by the alignment and quality of the spectrometer optics as well as the finite widths of the entrance and exit slits. The detected SFRS line profile is also contributed by the natural and laser line widths. The triple-spectrometer in the additive mode with 1800 g/mm gratings and slit widths of $10 \mu\text{m}$ provides a full width at half maximum (FWHM) of 0.44 cm^{-1} (13 pm)^{||} of the spectral line at 546.07 nm of a low-pressure calibration mercury lamp. This FWHM is taken as the achievable spectral resolution. By comparison, the double-spectrometer yields a FWHM of 0.16 cm^{-1} (5 pm); the natural width of the spectral line is about 1 pm. In the near-infrared wavelength range the spectral resolution of the triple-spectrometer is also approximately $I_{\text{sr}} = 0.4 \text{ cm}^{-1}$, evaluated from the line width of the continuous-wave Ti:Sapphire laser (Tekhnoscan, T&D-scan)** which is about 0.03 cm^{-1} [159]. Note, an increase in the slit widths until $25 \mu\text{m}$ does not change the line profile significantly, but the light throughput is enhanced. The influence of the spectral resolution, laser line width, and stray light rejection on a SFRS spectrum is demonstrated in Fig. 2-3. In comparison to a reference spectrum shown in panel (a) where two SFRS lines are visible, if one of the three experimental SFRS requirements is not fulfilled, both SFRS lines are not distinguishable from the high background as illustrated in panel (b). Hereby, a spectrally broad laser line has two effects on the SFRS spectrum: spectrally approaching the laser line is more strongly restricted, and the SFRS line itself can be broadened.

(iii) The competition between the PL background and the SFRS line is a further obstacle in the spin-flip Raman scattering spectroscopy. As already mentioned in (i), the polarization characteristics of I_{bg} and I_{sf} may differ, hence, the choice of an appropriate polarization can enhance the ratio between the SFRS intensity and PL background. A different dependence of both intensities on the optical power density offers another possibility to identify the SFRS line with respect to the PL background. In addition to that, the change in the excitation energy can result in a reduced screening of the SFRS

^{||}The wavelength λ [nm] is converted into the absolute wavenumber by k [1/cm] = $10^7/\lambda$. A wavelength difference is expressed as relative wavenumber using the equation $\Delta k = [1/\lambda - 1/(\lambda + \Delta\lambda)] 10^7$. The relative wavelength of a spectral peak is given by $\Delta\lambda = [1/(k - \Delta k) - 1/k] 10^7$.

**A thick Fabry-Perot interferometer (also called *etalon*) with high reflectance, inserted into the laser resonator, reduces the laser line width [154].

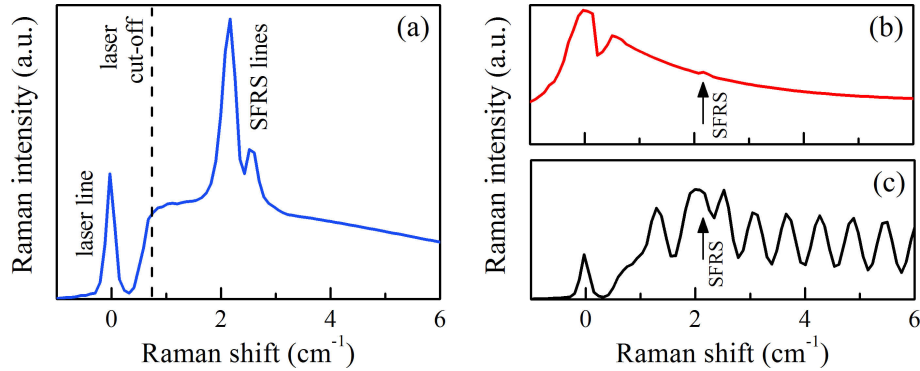


Figure 2-3: Simulated SFRS spectra for fulfilled and unsatisfied experimental requirements determining the SFRS observation. (a) In the case of a spectrally narrow laser line, an efficient stray light rejection, and a high spectral resolution, two different spin-flip scattering processes manifest themselves in sharp lines differing from the laser line by their Raman shifts. The simulated SFRS spectrum refers to a measurement with the triple-spectrometer in subtractive mode combined with a CCD camera. (b) If one of the experimental conditions is not accomplished, the SFRS lines cannot be distinguished from the background. The more intensive SFRS line, marked by the arrow, may appear as slight background deviation. (c) Despite fulfilled SFRS conditions an oscillatory PL background might disturb the SFRS spectrum making impossible a SFRS line identification.

line. By resonantly exciting an edge of the PL band the SFRS intensity can be improved with regard to the PL. Moreover, the anti-Stokes regime is often exempt from a PL background. Only in the case of a multi-peak PL spectrum, the study of the anti-Stokes SFRS might be interfered by photoluminescence.

Another effect which can in some cases obscure the SFRS line is an oscillatory PL background, as exemplarily demonstrated in Fig. 2-3 (c). If the widths of the PL oscillations are similar to the SFRS line width, a definite SFRS identification will be impossible. What are the reasons for such artificial oscillations? The front-illuminated CCD camera does not show an etalon-like behavior [154], and imperfections in the holographic gratings causing Rowland ghost signals owing to periodic errors in the groove spacing or satellites (*grass* background due to randomly misplaced grooves) are negligible [160]. The oscillatory PL behavior can be attributed to interferences of the emitted light in the vacuum window of the CCD camera or/and in the layered structure of the semiconductor sample. Although the different thicknesses of the window and semiconductor layers allow to identify their contributions to the oscillations, their separation from SFRS lines is not possible. The usage of a CCD window with an anti-reflection coating approximately halves the amplitude of the oscillations. Moreover, the emission of the Ti:Sapphire laser may have an oscillatory fluorescence background. A condensate film (e.g., of frozen gases) on a vacuum window of the cryostat can also cause the interference fringes.

2.2 Spin-Flip Raman Scattering Setup

How is the experimental setup arranged to fulfill the SFRS requirements? The SFRS setup is divided into the excitation, sample, and detection segments. The excitation

path of the basic SFRS setup is marked by [i] in the Fig. 2-4. In general terms, the semiconductor sample, studied at cryogenic temperatures and in an external magnetic field, is optically excited with a single laser beam, and the induced inelastic scattering process is analyzed with a spectrometer and photon detector. First of all, the setup of the single-beam SFRS experiment will be described. It is followed by the presentation of the setup extensions corresponding to the excitation paths [ii] and [iii] in the Fig. 2-4. Typical experimental parameters used for the SFRS measurements are listed in the Table 2-1.

The optical excitation of the sample is provided by the continuous-wave Ti:Sapphire laser (Tekhnoscan, T&D-scan) pumped by the second harmonic (532 nm, 2.33 eV) of a Nd:YVO₄ laser (Coherent, Verdi V10). The tunable Ti:Sapphire laser covers a wavelength range from 690 to 1050 nm (1.18 to 1.80 eV). A fiber-coupled wavelength meter device (Coherent Wavemaster, or HighFinesse WS/6) measures the actual wavelength. As described in the Section 2.1, the laser line width is about 0.03 cm⁻¹ (2.3 pm) at the central wavelength. After passing through a longpass colored glass filter (CF), which absorbs the green background light of the pumping laser, the Ti:Sapphire laser beam is directed to an iris diaphragm (ID). It selects the central part of the beam cross section, and is used as a reference for the laser spot position. The intensity of the laser beam is then attenuated by a gradient neutral filter (VF) as well as by the combination of an achromatic half-wave plate ($\lambda/2$) and a Glan-Thompson prism (GTP). The half-wave plate rotates the polarization direction of the incoming linearly polarized laser light, while the light transmitted through the polarizer is vertically linear polarized: by rotating the half-wave plate the intensity of light passing the polarizer can be regulated. During an intensity-sensitive measurement demanding a stable laser power, the power is monitored with a power meter (PM) which detects the beam reflected from a glass plate (GP). The power density P_{exc} at the sample is varied from 0.03 to 12 W/cm². A Glan-Thompson prism, ensuring a definite vertical-linear polarization, prefaces a $\lambda/4$ retardation plate which converts the linear polarization of the laser beam to a circular polarization.

The millimeter-sized sample (S) is mounted at a Raman-holder located inside the sample chamber (VTI) of a cryostat with a superconductive split-coil magnet (Cryogenic Limited). The sample is exposed to low temperatures ranging from 1.3 to 10 K and high magnetic fields up to 10 T. The orientation of the sample can be varied with respect to the magnetic field direction: the sample holding element can be set to a specific angular position between $\theta = 0^\circ$ and 45° . By a 90° -rotation of the cryostat-magnet system (CMS) angles between $\theta = 45^\circ$ and 90° can be established. The frontside of the sample is illuminated from the backside of the cryostat. There are two types of Raman-holders differing in the way of light collimation via either a lens (L) or a concave mirror (CM) which have focal lengths of 10 mm. In the Fig. 2-4 and inset (a) the Raman-holder based on the concave mirror is shown. The lens L1 directly focuses the laser beam through a hole in the center of the mirror onto the sample. The sample is fixed at a small brass-plate by silver conductive varnish. The plate can be wedge-shaped to provide the angle θ between the magnetic field direction and the surface normal of the sample. The light emitted/scattered from the sample is eventually collimated by the annular area of the concave mirror. In the alternative case of the lens-based Raman-holder, the lens L1 focuses the laser light via an intermediate small-sized silver mirror (SM) onto the sample, see the inset (b) in Fig. 2-4. Hereby, the sample is set into the focal plane ($f = 10$ mm) of a small-diameter lens (L) that provides a parallel light

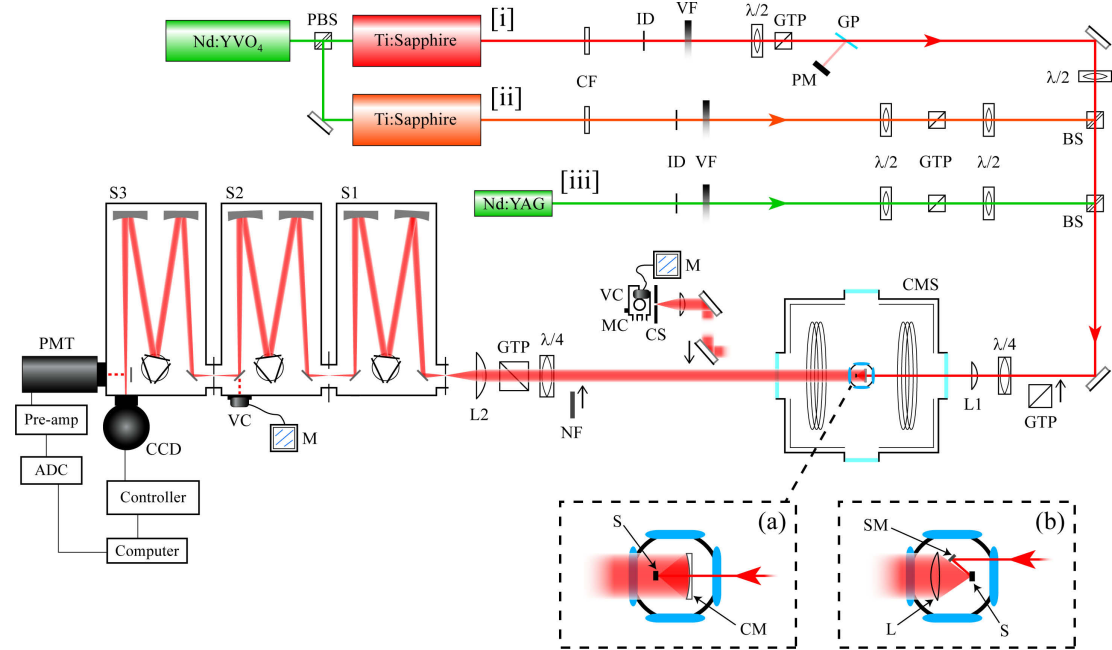


Figure 2-4: Scheme of the SFRS setup including the basic segment [i] for resonant excitation and the paths [ii] or [iii] for a two-color SFRS experiment. In the insets (a) and (b) the two different Raman-holders are depicted in a magnified way. The dashed red lines (in spectrometer scheme) indicate the alternative light paths if the positions of the respective mirrors are changed. The abbreviations are explained in the main text.

beam propagating to the spectrometer, as in the case of the concave mirror construction. The concave mirror-based Raman-holder has several advantages: firstly, the polarization plane of the incident light is not rotated by a mirror. Secondly, the concave mirror does not show the Faraday effect* in a parallel magnetic field, as does the collimating lens L . Thirdly, the wave vector of the exciting light can be parallel to the growth axis of the sample as well as the magnetic field direction. However, the mirror-based Raman-holder is limited to small-sized samples ($3 \text{ mm} \times 3 \text{ mm}$). And, the piece of sample cannot be mounted in a fully stress-free way by using a black paper envelope.

The spectrometer and photon detectors form the detection segment. Before the light is focused by the lens $L2$ onto the entrance slit of the first stage ($S1$) of the spectrometer, the polarization is analyzed and the illumination position on the sample can be controlled. The parallel light beam can be directed via two mirrors to a lens generating an intermediate image in the plane of a cross slit (CS). For that purpose, one of the plane mirrors is inserted into the detection path, as indicated by the respective black arrow in the Fig. 2-4. To avoid an exceeding magnification of the image showing the illuminated sample area the focal length of the lens is short ($f \lesssim 50 \text{ mm}$). The intermediate image is resolved by a microscope (MC) combined with a video camera (VC) and monitor (M).

*The Faraday effect describes the rotation of the polarization plane when linearly polarized light passes through a medium in a direction parallel to the applied magnetic field [161]. The polarization plane of a laser beam ($\lambda = 563 \text{ nm}$) propagating through the five Faraday windows of the cryostat under tilted incidence of about 15° is rotated by $\theta_{\text{fara}} = 2.3^\circ \pm 0.1^\circ$ per tesla.

Table 2-1: Typical experimental parameters for SFRS measurements using the triple-spectrometer in the subtractive(+CCD) or additive(+PMT) mode. The grating configurations starting from the first stage are 1800/1800/1800 in the additive and 900/900/1800 in the subtractive mode, in units of g/mm. Besides the focal length characterizing the light dispersion, the slit widths, magnetic field strength, temperature, optical excitation density and approximate laser spot diameter on the sample surface are listed.

| Mode | f (m) | slit widths (μm) | B (T) | T (K) | P_{exc} (W/cm ²) | d_{spot} (mm) |
|-------------|------------|----------------------------------|------------|------------|--|---------------------------|
| Additive | 1.5 | ≤ 100 | ≤ 10 | ≤ 6 | ≈ 1.5 | 0.5 |
| Subtractive | 0.5 | 20/10000/20 | | | | |

Furthermore, the circular polarization of the scattered photons is studied by a large-diameter quarter-wave plate ($D = 30$ mm). A polarizer is set to generate s-polarized light in order to achieve the highest diffraction efficiency. The triple-spectrometer can operate in two different modes: in the additive mode all three stages contribute to the positive light dispersion. Using slit widths smaller than approximately $100 \mu\text{m}$, this mode combined with the PMT as detector offers a high spectral resolution and efficient stray light rejection. An achromatic lens whose focal plane coincides with the exit slit provides a full illumination of the PMT photocathode. In the subtractive mode the first and second stages operate as a tunable sharp bandpass filter, where the second grating cancels the dispersive action of the first grating. This mutually dependent action of the gratings is schematically depicted in the Fig. 2-4 by the grating turrets rotated oppositely. This kind of stray light rejection reduces the danger of overwhelming light incidence, therefore, a CCD camera gathering light over a broad spectral range can be used. The spectral resolution is solely defined by the third stage (S3). In comparison to the CCD camera, the disadvantage of the PMT usage is the time consuming acquisition of a spectrum[†]. The PMT photocathode is protected from the intensive laser light by a neutral filter (NF) which has to be manually inserted into the detection path during the laser line measurement. Moreover, the illumination of the second grating is monitored with a video camera installed at the front output of S2. In that way, the focusing of the entire optical system can be checked.

The excitation segment of the basic SFRS setup, denoted by [i] in the Fig. 2-4, can be extended by additional laser sources to perform two-color SFRS experiments. In addition to the resonant excitation, the sample is illuminated by nonresonant light emitted from the lasers [ii] or [iii][‡]. Both laser beams are profiled with comparable equipment in the same manner as in the case [i]. In a two-color SFRS experiment the simultaneous illumination of the sample requires the spatial coincidence of both laser spots on the sample surface. A nonpolarizing beamsplitter (BS) couples the additional laser beam into the main excitation path. The overlapping of the laser spots is checked with the intermediate image of the illuminated sample area, as described in the previous

[†]The average background noise of the PMT is about five counts per second. It is set by the discriminator of the preamplifier (Advanced Research Instruments Corporation, F-100T) ensuring an optimal signal-to-noise ratio.

[‡]If both Ti:Sapphire lasers are used, the pumping beam is split by a polarizing beamsplitter (PBS) combined with a half-wave plate which defines the split ratio.

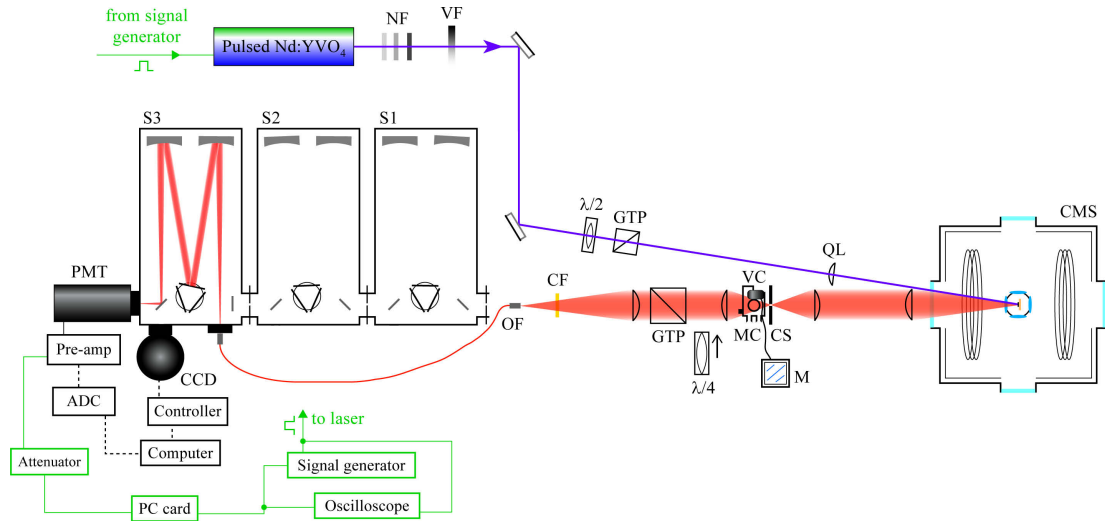


Figure 2-5: Scheme of the time-resolved PL setup. The connections between the electronic devices of the detection systems for stationary and transient PL are marked by dashed black-colored and solid green-colored lines, respectively.

paragraph. Two Ti:Sapphire laser beams are applied for studies of the electron-nuclear hyperfine interaction in (In,Ga)As/GaAs quantum dots (QDs). The second harmonic of a neodymium doped yttrium aluminum garnet laser (Nd:YAG, Laser 2000, LCS-DTL-317) combined with the main Ti:Sapphire laser is used, for instance, to optically modify the SFRS in the CdTe/(Cd,Mg)Te quantum well.

2.3 Time-Resolved Photoluminescence Setup

The exciton photoluminescence and its polarization properties in (In,Al)As/AlAs QDs are studied in the stationary and time-resolved regime for nonresonant excitation. For that purpose, a PL setup consisting of a pulsed laser excitation synchronized with a time-resolved detection system is required. It should offer the possibilities to apply an external magnetic field, vary the temperature as well as set the polarization of the incident laser beam and analyze the polarization of the light emitted from the QD sample. In the Fig. 2-5 the time-resolved PL setup is schematically illustrated, its description is followed in the next paragraphs.

The second (532 nm, 2.33 eV) or third harmonic (355 nm, 3.49 eV) of a Q-switched Nd:YVO₄ laser (Newport Spectra-Physics, J40-BL6S) with a pulse duration of 5 ns is used. The laser power is varied by neutral glass filters (NF), a continuously variable neutral filter (VF), and a $\lambda/2$ retardation plate combined with a Glan-Thompson prism (GTP). The sample is excited with linearly polarized light. A tilted light incidence without any high-reflective optical element assures an excitation with definite polarization. A quartz lens (QL) with 300 mm focal length directs the laser beam to the sample. In order to reduce the power density the focal plane of the quartz lens does not coincide with the sample surface. The diameter of the defocused laser spot on the sample surface is typically larger than 1 mm.

The QD sample stress-free enveloped in black paper is installed at a holder made of brass. The sample is immersed in either pumped liquid helium or helium gas; the temperature ranges from 1.6 to 30 K. The PL experiments are performed in the Faraday geometry where the magnetic field is directed along the QD growth axis. The strength of the magnetic field varies between 0 and 10 T. The emitted light is collimated in the standard manner with an achromatic lens ($f = 250$ mm, $D = 50$ mm) located outside the cryostat. By means of an intermediate image of the illuminated sample area the laser spot position is checked; a video camera (VC) and monitor (M) connected to a microscope (MC) enhance this controllability. A cross slit (CS) selects the homogeneously illuminated sample region, the slit aperture is about $400 \mu\text{m} \times 400 \mu\text{m}$. The generation of the intermediate image and its coupling into the main detection path are established via two quartz lenses with focal lengths of 190 mm. Before focusing the PL onto the entrance aperture of an optical fiber (OF), the polarization of the PL can be analyzed by a $\lambda/4$ retardation plate and Glan-Thompson prism. Furthermore, a colored filter OG550 (CF) absorbs the laser light reflected from the sample surface and cryostat windows. The last lens has the same properties like the first collimation lens. The light transmission through the fiber is optimized for the visible and near-infrared spectral range. The fiber input and output are screened from room light in order to improve the ratio between the usually weak PL and background signal. The fiber output is directly coupled to the third stage (S3) of the triple-spectrometer, whereby, the entrance slit width is approximately $150 \mu\text{m}$ and the side exit slit is almost completely opened (≈ 2.5 mm). The nonresonant time-resolved PL experiments do not require a high spectral resolution or stray light rejection, it is more essential to maximize the light throughput.

The GaAs-based PMT operating in the time-correlated photon-counting mode detects the light dispersed by a 900 g/mm grating. The amplified PMT signal is sent to an event-time-digitizer computer card (FAST ComTec, P7889) providing single photon counting with a minimum time resolution of 100 ps[§]. Note, the response time of the preamplifier is limited to 1 ns and the full width at half maximum of the laser pulse is about 5 ns. The photon counting (PC) card operations are synchronized via a signal generator (Tektronix, AFG3102) with the laser pulses. The timing sequences are monitored with an oscilloscope (Tektronix, TDS2012). The signal generator works as master clock that temporally delays both the laser pulse and starting pulse for the PC card without external triggering. Without intentional delay setting the laser pulse is detected 250 ns after the start of the photon counting. This internal delay is caused by the finite lengths of the BNC connection cables, amplification and digitalization processes as well as the finite speed of light (propagation of 1 m takes about 3.3 ns). The electronic jitter in the time domain is not larger than 10 ns, correspondingly, it approximately amounts to the twofold width of the laser pulse. The pulse repetition frequency is varied between 1 and 100 kHz. The time resolution of the detection system is set to values ranging between 1.6 and 200 ns. Besides the time-resolved PL measurements, basic characterizations of the time-integrated exciton PL influenced by the (lattice) temperature or external magnetic field are studied with the CCD camera covering a broad spectral range.

[§]After the amplification of the PMT signal and its conversion into a TTL output, an attenuator (Kay Electronics, 431C) reduces the amplitude of the TTL signal to approximately 1 V. This additional damping prevents a damage of the sensitive PC card. The width of the TTL pulse is not influenced by the attenuator consisting of Ohmic resistors only.

Chapter 3

Exchange Interactions Providing SFRS in a CdTe Quantum Well

The dynamics of carrier spins in low-dimensional semiconductor structures attract remarkable interests due to the possibilities of spin storage, transfer and information processing [162, 163, 164, 165]. For spintronic and quantum information applications, the understanding of the fundamental interactions between confined carrier spins is essential, since these interactions determine the information transfer, spin relaxation and, in turn, spin decoherence [166]. One main type of interactions between two localized carrier spins is the exchange interaction [167, 168, 169]. The exchange interaction between carriers is attributed to the carrier-carrier Coulomb interaction as well as to the antisymmetric character of their wave function. Hereby, a distinction is drawn between isotropic and anisotropic exchange interaction. While the isotropic one conserves the total spin of both carriers involved, the anisotropic exchange leads to spin relaxation and information losses being a major drawback for quantum applications. In that context, not only the electron-hole exchange relaxation, but also the exchange interaction between identically charged carriers (electrons or holes) play a significant role [170, 171]. The main focus has been directed on the exchange interaction between donor-bound electrons [172, 173, 174]. The anisotropic exchange interactions between an exciton and a resident electron or hole localized by potential fluctuations in quantum wells (QWs) have not been studied yet.

The resonant spin-flip Raman scattering (SFRS) technique offers the possibility to study basic interactions between carrier spins in semiconductor nanostructures [142, 175, 176]. By means of SFRS the g factors of the carriers are measured directly, thus supporting the identification of the type of scattered carrier. In nonmagnetic CdTe-based quantum wells the SFRS technique has been used to measure the electron and exciton g factors [74, 177, 178]. Their dependencies on the quantum well confinement and on the splitting between the light-hole and heavy-hole states have been determined. While the exciton-SFRS is realized via the simultaneous spin-flips of its hole and electron, the single spin-flip of the electron or hole in highly symmetric low-dimensional structures (e.g. D_{2d}) is forbidden by the optical selection rules. The Raman scattering mechanisms of the electron and hole spin-flip for resonant probing of the neutral or charged excitons have not been discussed so far.

This Chapter focuses on the electron- and heavy-hole-SFRS induced via exchange interactions in a CdTe/Cd_{0.63}Mg_{0.37}Te quantum well. The Raman scattering processes

of the electron and heavy-hole spins are compared for the resonant excitation of the neutral as well as positively and negatively charged excitons. The charge state of the exciton is tuned by additional above-barrier illumination. It will be demonstrated that the spin-flip scattering of a single electron or hole in a neutral exciton becomes allowed when the symmetry of the carrier complex is reduced. As a result of the lifting of the angular momentum conservation, electrons and/or holes can mutually interact via anisotropic exchange. Also, a magnetic field tilted with respect to the QW growth axis can provide an electron- or a hole-SFRS process. The scattering via an acoustic phonon and direct (isotropic) exchange interaction can accompany the symmetry-breaking mechanisms. The strength of the electron-hole and hole-hole anisotropic exchange interactions, and the role of the electron and hole localization for the SFRS are discussed.

The Chapter is organized as follows: in Sec. 3.1 the characteristics of the studied sample and of the experimental setup are specified. In Sec. 3.2 the optical tuning of the resident carrier concentration is described. The photoluminescence of the neutral and charged excitons and its dependence on the magnetic field are shown. In Subsec. 3.3.1 the circular polarization properties of the electron- and heavy-hole-SFRS in the Faraday geometry are described. The magnetic field dependence of both SFRS lines and their resonance profiles are demonstrated. In Subsection 3.3.2 it is illustrated how the line shift and intensity of the SFRS processes vary with the angle between the magnetic field direction and the QW growth axis. Moreover, the impacts of the lattice temperature and the power density of the above-barrier illumination on the electron- and hole-SFRS intensities are shown. The Sec. 3.4 is introduced by the discussion which SFRS processes are allowed by the electric dipole selection rules in the Faraday geometry without light-heavy-hole mixing. In the Subsections 3.4.1 and 3.4.2, the spin-flip scattering mechanisms of the electron and heavy-hole are discussed for resonant excitation of either neutral or charged exciton states. The Chapter is concluded in Sec. 3.5.

3.1 Experimental Details

The studied CdTe/Cd_{0.63}Mg_{0.37}Te quantum well structure (#090505AC), grown by molecular beam epitaxy on a (100)-oriented GaAs substrate, consists of one 20-nm-thick CdTe quantum well with adjacent 120-nm-thick and, respectively, 150-nm-thick Cd_{0.63}Mg_{0.37}Te barriers [179]. Although the sample is nominally undoped, the QW contains resident holes due to residual impurities in the barriers. The concentration of the resident holes is about 10^{10} cm^{-2} being evaluated from magnetorefectivity spectra of the charged excitons [180]. The concentration and even type of the resident carriers can be tuned by additional illumination with photon energies exceeding the band gap of the Cd_{0.63}Mg_{0.37}Te layers of 2.26 eV. The photocreated electrons are collected from the Cd_{0.63}Mg_{0.37}Te layers into the CdTe QW, as illustrated in Fig. 3-1 (a). The holes remain in the barriers being captured by surface states or trapped centers [180]. Depending on the intensity of the above-barrier illumination with a photon energy of $E_a = 2.33 \text{ eV}$, the achievable density of the two-dimensional electron gas is a few 10^{10} cm^{-2} . Under below-barrier excitation electron-hole pairs are only generated in the CdTe QW and thus the density of the resident carriers is not changed. Such optical tuning of the resident carrier concentration is very suitable for a comparative study of the negatively and positively charged excitons in the same structure due to avoiding technological and growth uncer-

tainties. Note, without above-barrier illumination the concentration of the resident holes is approximately one order of magnitude larger than the one of the resident electrons. Due to the coexistence of resident holes and electrons the formation of positively and negatively charged excitons is possible. Nevertheless, the notation used in the following refers to the positive T^+ trion only. And, instead of *charged exciton* the term *trion* will be used [181].

The SFRS experiments were performed at high magnetic fields up to 10 T and at low temperatures ranging from 1.3 to 9 K. For the resonant excitation of the neutral and charged exciton states a tunable continuous-wave (CW) Ti:Sapphire laser was used. Its power density on the sample was about 0.5 W/cm^2 . The additional above-barrier illumination was provided by the second harmonic of a CW Nd:YAG laser with a photon energy of 2.33 eV. Its power density P_a was varied between 10^{-4} and 15 W/cm^2 . Both beams of the resonant excitation and above-barrier illumination were directed to a position joint on the sample by use of a nonpolarizing beamsplitter mounted on a precisely adjustable stage. The experimental setup is schematically shown in the Fig. 2-4 [iii]. The spatial overlap of the laser spots has been checked by an intermediate image using a video camera connected to a monitor. The diameters of the laser spots were typically 0.5 mm. The circular polarization of the exciting photons was defined by a Glan-Thompson prism combined with a quarter-wave retardation plate. The corresponding polarization optics were used for the analysis of the circular polarization degree of the light scattered from the sample. The scattering light was dispersed by the triple-spectrometer and detected by either the Si-based CCD camera or the GaAs PMT. While in the additive mode the scattering light was detected with the PMT, the CCD camera was used with the spectrometer operating in the subtractive mode.

The Raman spectra were measured in the backscattering geometry. The incident and scattered light, propagating in opposite directions, were directed along the structure growth axis (z -axis). The magnetic field \mathbf{B} was applied either along (Faraday geometry, $\mathbf{B} \parallel \mathbf{z}$) or perpendicular (Voigt geometry, $\mathbf{B} \perp \mathbf{z}$) to the structure growth axis. The circular polarization characteristics of the SFRS spectra are described by the notation $z(\sigma^\eta, \sigma^\gamma)\bar{z}$ or the abbreviated expression $(\sigma^\eta, \sigma^\gamma)$ [136]. Here, z and \bar{z} designate the directions and σ^η and σ^γ the circular polarizations of the incident and scattered light, respectively. The sign of η and γ is determined by the sign of the photon angular momentum projection on the propagation direction of the incident light. For angular dependent SFRS measurements delivering information about the components of the g factor tensor, the angle θ between the magnetic field direction and the z -axis was varied in the range from 0° to 90° . Since in the tilted geometries the optical selection rules are lifted, the polarization was changed from the circularly polarized to the cross-linearly polarized configuration. Also, in that way the laser stray light was reduced to minimum.

3.2 Optical Tuning of Resident Carrier Concentration

The photoluminescence (PL) of the neutral and charged excitons in the CdTe/Cd_{0.63}Mg_{0.37}Te QW is shown in the Fig. 3-1 (b) for a magnetic field of $B = 7 \text{ T}$ and a temperature of $T = 1.8 \text{ K}$. The PL line at higher energies is related to the recombination of heavy-hole (hh) excitons. The second line which is shifted to lower energy from the exciton (Ex) is attributed to trion recombination. The below-barrier excitation with

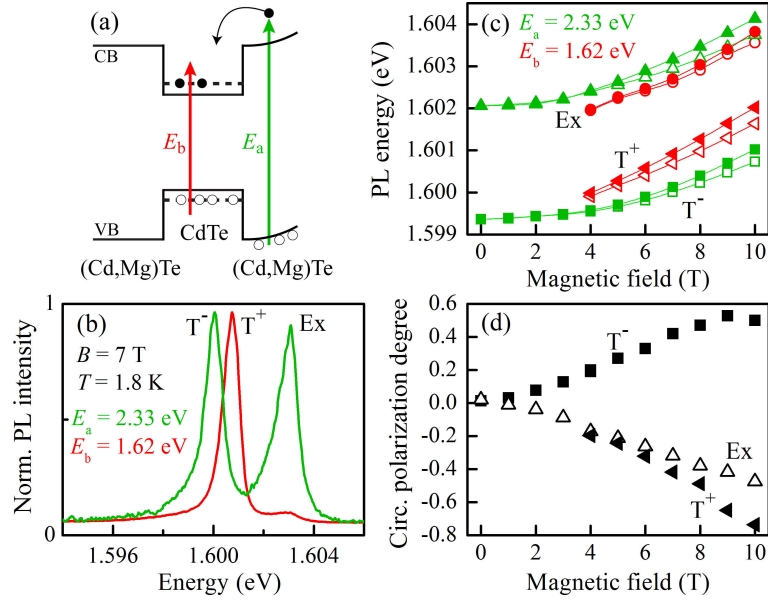


Figure 3-1: (a) Band structure of the studied CdTe/(Cd,Mg)Te QW. Pairs of electrons (closed circles) and holes (open circles) can be created by above-barrier or below-barrier illumination with photon energies of $E_a = 2.33$ eV and $E_b = 1.62$ eV, respectively. (b) Left-handed circular-polarized PL spectra for linearly polarized above- and below-barrier excitation at $B = 7$ T and $T = 1.8$ K in Faraday geometry. The optical power densities amount to $P_a = 0.05$ W/cm² and $P_b = 0.8$ W/cm². The spectra contain neutral (Ex) and charged (T^\pm) exciton lines. (c) B -field dependence of the exciton PL energies for both excitation energies. In high magnetic fields the Zeeman splittings of the right-handed (closed symbols) and left-handed (open symbols) circular-polarized PL are observed. (d) Magnetic field induced circular polarization degree ρ_c of the neutral, positively and negatively charged exciton PL. According to the optical selection rules a positive ρ_c can be assigned to negative trions, while $\rho_c < 0$ is characteristic for positive trions.

an energy $E_b = 1.62$ eV, provided by the CW Ti:Sapphire laser, results in an intensive positive trion (T^+) line compared to the exciton one. When the sample is excited by laser light with $E_a = 2.33$ eV the type of the resident carriers is tuned from holes to electrons [179, 182]. Here, the negative trion (T^-) line shifts to lower energies compared to the T^+ one, while the exciton PL energy only changes slightly. The intensity ratio between the exciton and trion lines changes, especially the exciton PL is enhanced with illumination thus reflecting the depletion of the resident hole concentration.

In Fig. 3-1 (c) the magnetic field dependent energies of the circular-polarized PL of the exciton and trions are illustrated for both below- and above-barrier excitation. By below- or above-barrier illumination the positive and negative trion PL is selectively excited. The difference in their PL energies is attributed to the different binding energies of the T^- and T^+ trions*. The exciton PL also depends on both excitation energies. The

*The binding energies (at 4 T) of the negative and positive trions are $E_B^{T^-} = 2.8$ meV and $E_B^{T^+} = 1.6$ meV, respectively. The trion binding energy is mainly determined by the confinement conditions: in QWs the trion stability is enhanced by the reduced dimensionality due to the localization of the trion wave function along the growth direction. The smaller binding energy of the T^+ trion can be explained by a stronger effective hole-hole Coulomb repulsion compared to the electron-electron one [183]. Furthermore, the slight decrease of $E_B^{T^+}$ with increasing magnetic field is attributed to a reduced overlapping between

spatial separation between electrons in the CdTe layer and holes in the Cd_{0.63}Mg_{0.37}Te layers, caused by the above-barrier excitation, induces electric fields inside the QW. As a result, the conduction and valence bands are bent and the exciton PL energies are blue-shifted.

Moreover, the PL lines shift to higher energies with increasing magnetic field strength. The splitting between the left-handed σ^- (open symbols) and right-handed σ^+ (closed symbols) circularly polarized PL lines becomes larger. The magnetic field dependence of the PL energy is mainly described by the diamagnetic [184] and Zeeman shift:

$$E_{\text{PL}}^{\pm}(B) = E_{\text{g}}^* + \frac{e^2 \langle \rho_1^2 \rangle}{8\mu} B^2 \pm \frac{1}{2} g_{\text{PL}} \mu_{\text{B}} B. \quad (3.1)$$

Here, E_{g}^* denotes the effective band gap energy including the binding energy of the carrier complex, μ_{B} the Bohr magneton, e the elementary charge, μ the reduced mass, $\langle \rho_1^2 \rangle$ the spatial extension of the wave function in the lateral direction (perpendicular to the magnetic field), and g_{PL} the effective g factor of the neutral or charged exciton. A fit[†] of the σ^+ polarized exciton PL energy (green-colored solid triangles) yields a lateral extension of the exciton wave function of $\langle \rho_{1,\text{Ex}}^2 \rangle = 35 \text{ nm}^2$.

In Fig. 3-1 (d) the magnetic field dependencies of the circular polarization degree of the exciton and trion PL are shown. The circular polarization degree ρ_{c} of the PL intensities I^{\pm} for σ^+ and σ^- polarized light is calculated with the equation $\rho_{\text{c}} = (I^+ - I^-)/(I^+ + I^-)$. As in the studied QW the electron and heavy-hole g factors have a negative sign [179, 182, 185], the emission from the singlet states of the T⁺ and T⁻ trions is characterized by opposite circular polarizations. A negative circular polarization degree is attributed to T⁺ trions and holes are the resident carriers in the QW, as in the case of below-barrier illumination. Under above-barrier illumination ρ_{c} is positive, which corresponds to T⁻ emission and resident electrons. Therefore, the type of the resident carriers in the CdTe QW can be inverted by the above-barrier illumination. The inversion from the p-doped to the n-doped regime depends not only on the excitation energy but also on the excitation density. The inversion is achieved when the concentration of the resident electrons exceeds the background concentration of the holes. Note, a coexistence regime of resident holes and resident electrons localized at different sites separated spatially in the QW plane can also be established [179].

3.3 SFRS in Neutral and Charged Excitons

3.3.1 SFRS in Faraday Geometry

In Fig. 3-2 the SFRS Stokes-spectra for the parallel (σ^+, σ^+), (σ^-, σ^-) and crossed (σ^+, σ^-), (σ^-, σ^+) circular polarization configurations are shown. They were measured at $B = 9 \text{ T}$ and $T = 1.8 \text{ K}$ in the Faraday geometry ($\mathbf{B} \parallel \mathbf{z}$). The excitation energies

the magnetically confined electron wave function and the two heavy-hole wave functions acting as centers with heavy masses.

[†]The B -field dependence of $E_{\text{PL,Ex}}^+$ is fitted by the Eq. (3.1) with a fixed reduced mass $\mu = m_{\text{e}}^* m_{\text{hh}}^*/(m_{\text{e}}^* + m_{\text{hh}}^*) = 0.078 m_0$ using the effective masses listed in the Table 1-1. The effective g factor of the exciton takes the value $g_{\text{PL,Ex}} = 1.0 \pm 0.3$.

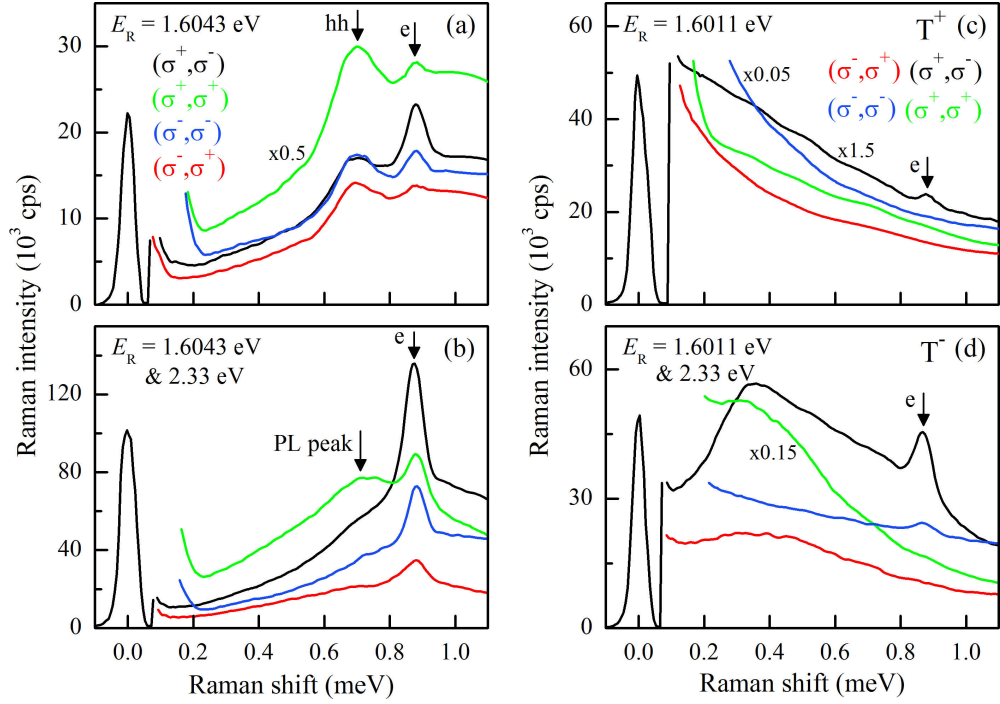


Figure 3-2: SFRS Stokes-spectra in Faraday geometry at $B = 9$ T and $T = 1.8$ K for parallel and crossed circular polarizations measured at the exciton and trion resonances. (a) The exciton is resonantly excited with an energy of $E_R = 1.6043$ eV. The laser line is at zero Raman shift. The intensity of the (σ^+, σ^+) polarized SFRS spectrum is scaled by a factor of 0.5 for better visibility. (b) The sample is simultaneously illuminated with above-barrier photons, $P_a = 0.04$ W/cm². Electron and heavy-hole spin-flip Raman lines as well as the broad exciton PL peak are marked by arrows. (c) The excitation of the positive trion yields an electron-SFRS in the (σ^+, σ^-) polarization. (d) At the T^- resonance the e-SFRS is also detected in the co-polarized (σ^-, σ^-) configuration. Due to the above-barrier illumination the peak of the trion PL is shifted to lower energies. The PL peak can be seen at a Raman shift of about 0.4 meV.

$E_R = 1.6043$ eV or $E_R = 1.6011$ eV are in resonance with the high-energy side of the exciton or trion PL, compare Fig. 3-1 (c). The SFRS spectra measured at the exciton resonance are depicted in the Figs. 3-2 (a) and (b), while the spectra in the panels (c) and (d) are obtained at the trion resonances.

As illustrated in the Fig. 3-2 (a), for the resonant excitation of the exciton two SFRS lines are observed on the PL background. Their Raman shifts of about 0.89 meV and 0.70 meV, displaying the Zeeman splittings, correspond to the longitudinal g factors of $|g_e^{\parallel}| = 1.71 \pm 0.01$ and $|g_{hh}^{\parallel}| = 1.34 \pm 0.02$. These longitudinal g factor values can be assigned to the electron and heavy-hole [74, 177, 179]. The e- and hh-SFRS lines are detected for both crossed and parallel circular polarizations. While the e-SFRS is dominant in the (σ^+, σ^-) configuration, the heavy-hole spin-flip is most intensive in the co-polarized state (σ^+, σ^+) . The ratios of the SFRS intensities I_{sf} for the polarization configurations $(\sigma^+, \sigma^-) : (\sigma^+, \sigma^+) : (\sigma^-, \sigma^-) : (\sigma^-, \sigma^+)$ at $E_R = 1.6043$ eV are given by

$$\text{Ex-resonance: } \begin{cases} \text{e-SFRS:} & 1 : 0.31 : 0.39 : 0.15, \\ \text{hh-SFRS:} & 0.27 : 1 : 0.33 : 0.28. \end{cases} \quad (3.2)$$

The intensities of the e-SFRS line in the co-polarized configurations are about 2/3 smaller than in the (σ^+, σ^-) one, while $I_{\text{sf}}(\sigma^-, \sigma^+)$ is only 1/7 of $I_{\text{sf}}(\sigma^+, \sigma^-)$ for Stokes shifted lines. The hh-SFRS has its highest intensity for the (σ^+, σ^+) polarization. The relative intensities of the hh-SFRS line demonstrate a 1 to 3 ratio. Note, the intensity ratios are expected to depend on the excitation energy; SFRS resonance profiles are described later.

The above-barrier illumination changes the intensities of both SFRS lines, as it is illustrated in Fig. 3-2 (b). The e-SFRS line is enhanced by about one order of magnitude, while the hh-SFRS line vanishes. The intensity ratios of the e-SFRS lines for the different polarization configurations are 1 : 0.36 : 0.42 : 0.20. In comparison to the ratios given in Eq. (3.2), the above-barrier illumination does not significantly change the relative intensities for the different configurations.

In Fig. 3-2 (c) the SFRS spectra for the resonant excitation of the high-energy side of the positive trion PL are depicted. They strongly differ from the corresponding SFRS spectra measured at the exciton resonance: only for the (σ^+, σ^-) polarization a SFRS line is present. Its Raman shift of 0.89 meV identifies it as an electron-SFRS. Its intensity is about four times weaker than that at the exciton resonance. A Raman scattering process inducing a spin-flip of a heavy-hole is not detected in the Faraday geometry.

In Fig. 3-2 (d) the SFRS Stokes-spectra under simultaneous above-barrier illumination are shown. At the T^- resonance the intensity of the e-SFRS line in the crossed circular polarization (σ^+, σ^-) is enhanced. Moreover, a σ^- polarized resonant excitation results in σ^- polarized scattered light belonging to the electron spin-flip. The circularly polarized SFRS spectra indicate that the absolute intensities of the e-SFRS are different for the resonant probing of the negative and positive trions, respectively. As in the case of the T^+ trion, the hh-SFRS is absent.

In the Fig. 3-3 (a) the anti-Stokes spectra measured at the exciton resonance are shown for the four polarization configurations. In the anti-Stokes regime, where the scattered photons have a higher energy than the incident ones, the e-SFRS line is most intensive for (σ^-, σ^+) . It is inverted to the polarization configuration in the Stokes regime. Moreover, the e-SFRS is present in the (σ^+, σ^+) configuration together with the hh-SFRS. The SFRS of the heavy-hole is dominant for (σ^+, σ^+) in both the Stokes as well as anti-Stokes regime. The inversion of the circular polarization configurations is also demonstrated by the e-SFRS at the T^- resonance, as shown in the Fig. 3-3 (b). The Raman line of the electron spin-flip is σ^+ polarized for the excitation with σ^+ or σ^- polarized light. The scattering intensities are more than one order of magnitude weaker than that in the Stokes regime.

The SFRS Stokes-spectra for $B = 4$ T at the exciton resonance without and with above-barrier illumination are depicted in the Figs. 3-3 (c) and (d). In absence of the additional illumination the relative intensities of the broad SFRS line in the different polarization configurations are 0.82 : 1 : 0.86 : 0.39. These intensity ratios and the large line width of about 0.11 meV suggest that the SFRS lines of the electron and heavy-hole overlap. In the (σ^+, σ^-) configuration the SFRS line (black curve) becomes narrower. It is mainly contributed by the electron-SFRS, since the e-SFRS at 9 T is also dominant for this crossed circular polarization. Accordingly, its Raman shift is smaller than the one of the hh-SFRS line. The difference of 0.012 meV in their Raman shifts is within the measuring accuracy.

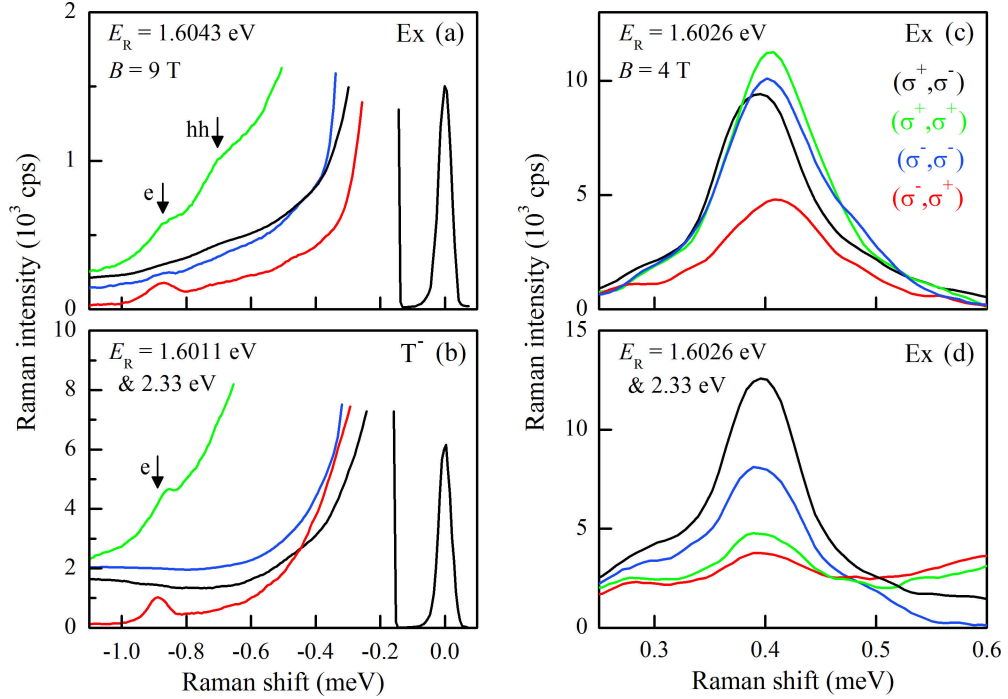


Figure 3-3: Circularly polarized SFRS anti-Stokes spectra in Faraday geometry for $B = 9$ T at the exciton (a) and T^- trion (b) resonance. In (c) and (d) the SFRS Stokes-spectra for $B = 4$ T at the exciton resonance without and with above-barrier illumination are shown. Note, the spectra measured at 4 T only contain the SFRS lines.

When the above-barrier illumination is applied, see Fig. 3-3 (d), the SFRS lines for each polarization have the same width as the SFRS line in the (σ^+, σ^-) configuration shown in the Fig. 3-3 (c). Their Raman shifts coincide, and the relative intensities of $1 : 0.27 : 0.49 : 0.18$ are similar to the e-SFRS intensity ratios described in Eq. (3.2). Therefore, the SFRS lines in Fig. 3-3 (d) and the (σ^+, σ^-) one in panel (c) are caused by the Raman scattering of the electron spin. By use of the above-barrier illumination the e-SFRS can be separately studied from the hh-SFRS. Moreover, the comparable intensity ratios of the e-SFRS at 4 and 9 T illustrate that the scattering mechanism does not change with the magnetic field strength.

The dependence of the electron and heavy-hole spin-flip Raman shift on the magnetic field is depicted for the Faraday geometry in Fig. 3-4 (a). Specific excitation conditions have been chosen in order to avoid an overlap of both SFRS lines disturbing the determination of their Raman shifts: at an excitation energy of 1.6043 eV the hh-SFRS line is detected in the (σ^+, σ^+) configuration. Under above-barrier illumination only the electron-SFRS is observed for (σ^+, σ^-) polarization. The e-SFRS line (closed squares) linearly shifts with increasing magnetic field strength B , as described by the Zeeman term $|g_e^{\parallel}| \mu_B B$. The linear behavior of the e-SFRS shift as well as the absolute value of the Raman shift are very similar for resonant excitation of the exciton and trion[‡]. In low

[‡]The absolute longitudinal electron g factor probed at the exciton resonance is 0.4% smaller than the one at the trion resonance.

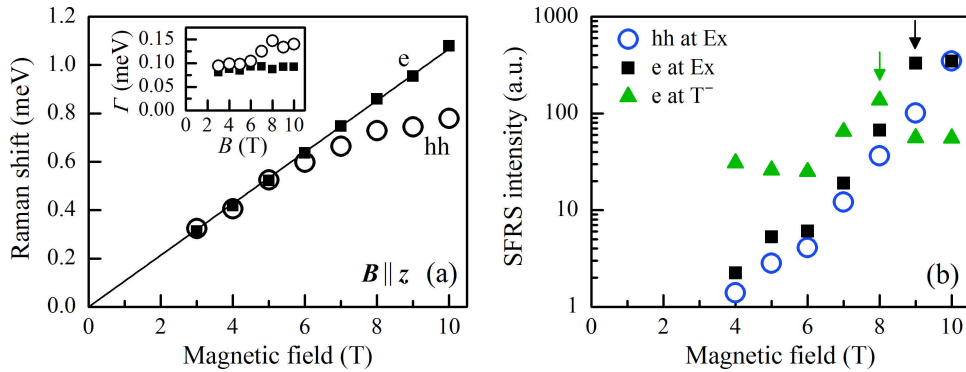


Figure 3-4: Magnetic field dependence of the spin-flip Raman shifts and intensities of the electron and heavy-hole in Faraday geometry at $T = 1.8$ K. (a) The e-SFRS line (closed squares) linearly shifts with the magnetic field, as illustrated by a linear fit (solid line). The hh-Raman shift (open circles) deviates from the linear behavior for $B > 5$ T. In the inset the FWHM of the electron- and heavy-hole-SFRS lines is shown as a function of the magnetic field. (b) The intensities of the e- and hh-SFRS lines probed at the exciton resonance strongly depend on the magnetic field. The e-SFRS line intensity at the T^- resonance only slightly increases with increasing B -field. The arrows mark the magnetic fields where the SFRS intensities are resonant. The errors of the Raman shift, width, and intensity do not exceed the sizes of the corresponding symbols.

magnetic fields ($B \leq 5$ T) the shift of the hh-SFRS line (open circles) coincides with that of the electron. Here, their Zeeman splittings and, correspondingly, their longitudinal g factors are about equal. For magnetic fields exceeding 5 T the hh-SFRS shift deviates from the linear evolution tending to saturation. Since in such high magnetic fields the mixing of the heavy-hole and light-hole states becomes essential [182], the reduced hh-SFRS shift can be approximated by a Zeeman term comprising a mixed longitudinal g factor of the heavy-hole and light-hole. A light-hole g factor being smaller than $|g_{hh}^{\parallel}|$ reduces the Zeeman splitting and, correspondingly, the SFRS line shift. Despite the contribution from the light-holes, the SFRS line will further be denoted as hh-SFRS line.

The magnetic field dependence of the e- and hh-SFRS line widths are demonstrated in the inset of Fig. 3-4 (a). The full width at half maximum (FWHM) Γ of the hh-SFRS line increases from 0.09 meV at 3 T to about 0.14 meV at 10 T. Particularly for $B > 6$ T the line width becomes broader. In that B -field range the shift of the hh-SFRS line also shows a deviation. By comparison, the e-SFRS line slightly broadens with increasing magnetic field. It is not limited by the laser line width which is about half of the e-SFRS line width ranging about 0.08 meV. The broadening is caused by the g factor dispersion. In the case of two slightly different g factors g_1 and g_2 the distance, i.e. broadening ($|g_1 - g_2|\mu_B B$), between their overlapping lines linearly increases with the magnetic field. Another reason for broadening are well width fluctuations that influence the light-hole admixture to the heavy-hole states. The rather strong increase in Γ of the hh-SFRS line at large B -fields might be caused by the light-hole admixture.

Apart from the Raman shift and line width, the intensities of the e- and hh-SFRS lines depend on the magnetic field strength, as illustrated in the Fig. 3-4 (b). The linear evolutions in the half-logarithmic representation demonstrate that the e- and hh-SFRS intensities probed at the exciton resonance increase exponentially with B . The increase

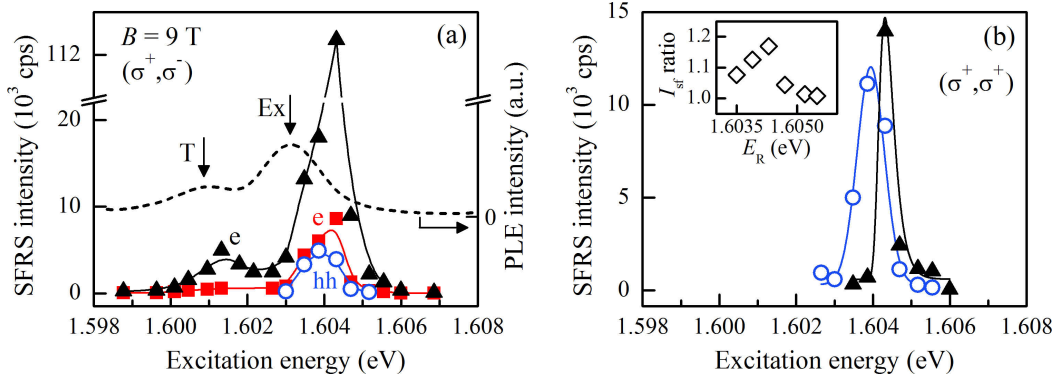


Figure 3-5: SFRS resonance profiles of the electron and heavy-hole in Faraday geometry at $B = 9$ T. (a) For the (σ^+, σ^-) configuration the intensity evolution of the electron spin-flip Raman line is measured with (black triangles) and without (red squares) above-barrier illumination. The heavy-hole-SFRS (blue circles) is obtained for resonant excitation of the exciton. A PLE spectrum for $B = 9$ T, detected at 1.5977 eV, is shown by the dashed line. It is similar to an absorption spectrum. The exciton and trion peaks are marked by vertical arrows. (b) SFRS resonance profiles for the electron and heavy-hole measured in the (σ^+, σ^+) configuration. In the inset the e-SFRS intensity ratio $I_{\text{sf}}(\sigma^+, \sigma^-)/I_{\text{sf}}(\sigma^+, \sigma^+)$ is shown as a function of the excitation energy E_R .

in the SFRS intensity is attributed to the shrinkage of the exciton Bohr radius and to the increase in its oscillator strength with increasing B -field [141]. The e-SFRS intensity at the T^- resonance increases slightly, see the green-colored triangles. The almost constant e-SFRS intensity indicates that the scattering efficiency is only weakly affected by the enhanced magnetic confinement.

The e-SFRS lines show a sudden increase in their intensities, as marked by the arrows in the Fig. 3-4 (b): at $B = 9$ T for the resonant excitation of the exciton and at 8 T for probing of the T^- trion. At these magnetic fields the energy of the incident or scattered photon (incoming or outgoing channel) coincides with an interband transition. Hence, a resonance occurs where one term of the denominator of the SFRS intensity, which can be estimated by the Eq. (1.42), vanishes. In the next paragraphs it will be shown that the outgoing channel is most effective for the SFRS in the CdTe QW.

The changes in the intensity of the SFRS lines by varying the excitation energy across the exciton and trion resonances are shown in Fig. 3-5 (a) for the crossed circular polarization (σ^+, σ^-) . These resonance profiles describe the spectral dependence of the probability of electron- or heavy-hole-SFRS. The resonance profiles of the e-SFRS (red squares) and hh-SFRS (blue circles) without above-barrier illumination as well as the e-SFRS (black triangles) under the above-barrier illumination are measured in the Faraday geometry at $B = 9$ T. All three SFRS lines have their maximal intensity at about $E_R = 1.6043$ eV. Both e-SFRS lines show a second maximum at 1.6013 eV which is about five times smaller than the respective high-energy maximum. The hh-SFRS is absent across the entire trion resonance. The resonance profiles indicate that the e-SFRS intensities for resonant excitation of the exciton or trion states are enhanced by the above-barrier illumination. The positions of the resonance profile maxima are not changed by the application of E_a .

In addition to the SFRS resonance profiles, a photoluminescence excitation (PLE) spectrum for $B = 9$ T and $T = 1.8$ K was measured. It is shown as dashed line in the Fig. 3-5 (a). The PLE peaks of the exciton and trion do not coincide with the SFRS resonance profile maxima. The SFRS intensities are maximal at the high-energy edges of both PLE peaks. At these energies the weakly localized states are probed [186]. Moreover, the shift in the resonance profiles to higher energies of about 1 meV, which corresponds to the electron Zeeman splitting at 9 T, demonstrates that the SFRS is more efficient for the outgoing channel. Hereby, the energy of the scattered photons coincides with the exciton or trion transition.

The spectral dependence of the e- and hh-SFRS intensities in the co-polarized configuration (σ^+, σ^+) is depicted in the Fig. 3-5 (b). Only in resonance with the weakly localized exciton both SFRS lines are observed. The hh-SFRS shows a resonance profile spectrally similar to that in (σ^+, σ^-), while the width of the e-SFRS resonance profile is narrower. At excitation energies exceeding 1.6045 eV its intensity becomes comparable to the e-SFRS intensity in the crossed polarized configuration. As illustrated in the inset of Fig. 3-5 (b), the ratio $I_{\text{sf}}(\sigma^+, \sigma^-)/I_{\text{sf}}(\sigma^+, \sigma^+)$ of the e-SFRS is about unity at high excitation energies. In this region of less localized excitons the e-SFRS line intensity in (σ^+, σ^+) does not decrease as strong as in the (σ^+, σ^-) configuration.

3.3.2 Dependence on Geometry, Temperature and Laser Power

Further details on the electron and heavy-hole g factor tensors as well as the SFRS processes are revealed by the dependence of the SFRS line shifts on the angle between the magnetic field direction and z -axis. In Fig. 3-6 the angular evolutions of the electron- and heavy-hole-SFRS are illustrated for $B = 7$ T. At the exciton resonance, the e-SFRS line (closed squares) is weakly shifted with the increase in the angle θ from the Faraday geometry ($\theta = 0^\circ$) to the Voigt geometry ($\theta = 90^\circ$). On the contrary, the hh-SFRS line (solid circles) shows a strongly anisotropic behavior. The Raman shift can be described by different longitudinal and transverse g factor values. In analogy to the Eq. (1.19), the dependence of the g factor on the tilting angle θ is expressed by the equation

$$g(\theta) = \sqrt{(g^{\parallel} \cos \theta)^2 + (g^{\perp} \sin \theta)^2}. \quad (3.3)$$

Fits of the spin-flip Raman shifts $\Delta E_{\text{sf}}(\theta) = g(\theta)\mu_{\text{B}}B$ by means of Eq. (3.3) yield the following g factor tensor components of the electron and heavy-hole[§]:

$$\begin{aligned} g_{\text{e}}^{\parallel} &= -1.70 \pm 0.01 & , & & g_{\text{e}}^{\perp} &= -1.62 \pm 0.01, \\ g_{\text{hh}}^{\parallel} &= -1.56 \pm 0.01 & , & & |g_{\text{hh}}^{\perp}| &= 0.15 \pm 0.02. \end{aligned}$$

Due to the nonlinear magnetic field dependence of the hh-SFRS line in the Faraday geometry, as demonstrated in the Fig. 3-4 (a), the longitudinal heavy-hole g factor derived above is valid for $B = 7$ T only. At fields lower than $B = 6$ T the longitudinal g factors of the electron and heavy-hole are about equal. Note, the evaluated electron g factors are valid for the whole field range.

[§]The g factor signs cannot directly be evaluated from the SFRS experiments, but they are known for the studied QW [182].

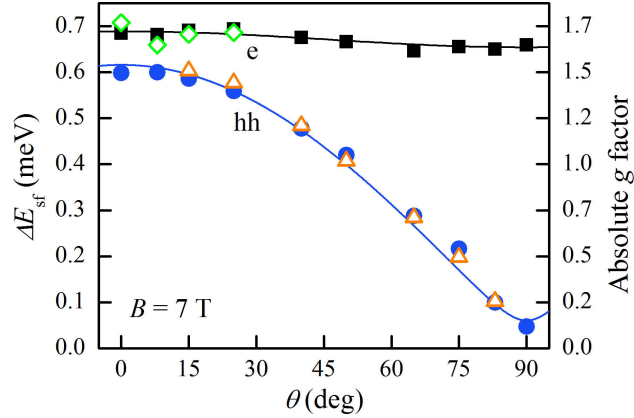


Figure 3-6: Angular dependence of the spin-flip Raman shifts at $B = 7$ T and $T = 1.8$ K. By resonantly exciting the exciton the electron-SFRS (closed squares) shows a slight anisotropy, while the Raman shift of the heavy-hole line (closed circles) strongly depends on the tilting of the magnetic field direction. In the case of resonant excitation of the Γ^+ trion, the electron- and heavy-hole-SFRS processes (open symbols) demonstrate both a spectral as well as an intensity dependence on the angle θ . The latter dependence is implicitly shown by the appearance or, respectively, disappearance of data points with increasing tilting angle. The e- and hh-SFRS are spectrally shifted with θ equivalently as in case of the exciton resonance. For $\theta > 25^\circ$ the e-SFRS line disappears, and only the spin of the hh is flipped. The error of the Raman shift does not exceed the symbol size.

Moreover, the longitudinal g factor of the exciton can be estimated. The use of the definition $g_{\text{Ex}} = g_{\text{hh}} - g_{\text{e}}$ for the bright exciton leads to $g_{\text{Ex}}^{\parallel} = 0.14$ at $B = 7$ T. It considerably deviates from the imprecise $g_{\text{PL,Ex}}$ which has been determined in the Sec. 3.2. The magnitude of its transverse g factor is uncertain due to the indeterminate sign of g_{hh}^{\perp} . Nevertheless, the deviation of g_{hh}^{\perp} from zero is highlighted by the SFRS spectrum measured at the exciton resonance in Voigt geometry[¶], see the black curve in Fig. 3-7 (a). Here, the hh-SFRS line partially appears in the close vicinity of the laser line. Under above-barrier illumination the SFRS spectrum (red curve) solely contains the e-SFRS line. Note, the ratios between the e-SFRS line maxima and the PL background are weaker than the corresponding ratios in the Faraday geometry, compare the Figs. 3-2 (a) and (b).

The angular dependence of the SFRS probed at the positive trion resonance manifests itself in a strong variation in the SFRS intensities. In the Faraday geometry the resonant excitation of the positive trion yields an electron-SFRS line, marked by the green-colored open diamonds in Fig. 3-6, while a heavy-hole spin-flip is absent. In a tilted geometry with an angle exceeding $\theta \approx 15^\circ$ the spin-flip of both an electron as well as a heavy-hole can be identified from their partially overlapping SFRS lines. A corresponding SFRS spectrum

[¶]The deviation of g_{hh}^{\perp} from zero depends on different aspects [187]: the transverse hh g factor can be described by the anisotropic parameter q_{KL} of the Kohn-Luttinger (or Bir-Pikus) Hamiltonian. It depends on the penetration of the hh wave function into the barrier material, and the spin-orbit splitting. Also, strain induced in-plane mixing of the lh and hh states is included. Furthermore, g_{hh}^{\perp} is affected by \mathbf{k} -induced admixture of light-hole to the heavy-hole states. Moreover, an anisotropy of the electron-hole exchange in n-doped QWs and an anisotropic lateral localizing potential can modify the transverse hh g factor.

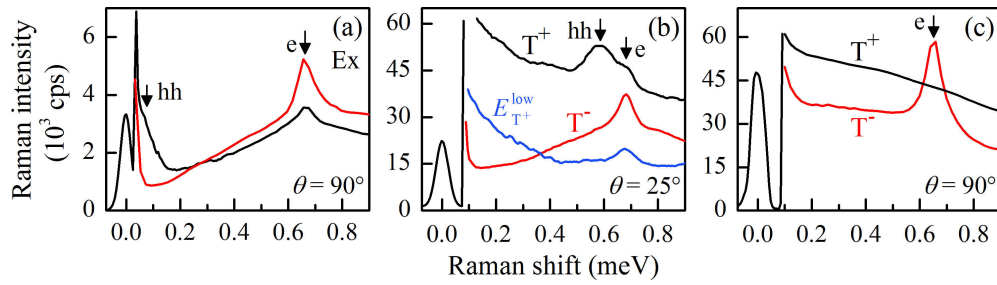


Figure 3-7: SFRS spectra in Voigt geometry ($\theta = 90^\circ$) and in tilted geometry ($\theta = 25^\circ$) at $B = 7$ T and $T = 1.8$ K without (black curves) and with (red curves) above-barrier illumination. (a) The hh-SFRS line is partially visible at the edge of the laser line for resonant excitation of the exciton. Under above-barrier illumination the hh-SFRS line is not present. (b) In resonance with the T^+ trion ($E_R = 1.6007$ eV) at an angle of $\theta = 25^\circ$ the lines of the hh- and e-SFRS are observed. The above-barrier illumination with $P_a = 0.04$ W/cm² leads to a suppression of the hh-SFRS line, while the e-SFRS intensity is increased, as demonstrated by the red curve. The hh-SFRS line also disappears when the excitation energy is reduced to $E_{T^+}^{\text{low}} = 1.6000$ eV, see the blue curve. (c) In Voigt geometry at the T^+ resonance the e-SFRS is absent.

for $\theta = 25^\circ$ is illustrated by the black curve in the Fig. 3-7 (b). By comparison, the SFRS spectrum under above-barrier illumination only demonstrates the electron spin-flip at $\Delta E_{\text{sf}} = 0.68$ meV. The intensity of the e-SFRS line decreases with increasing angle and vanishes for $\theta > 25^\circ$. The SFRS line attributed to the heavy-hole becomes stronger, and demonstrates the similar angle-dependent behavior like the hh-SFRS line at the exciton resonance, as seen by the open triangles in Fig. 3-6. The angle dependencies imply that both SFRS processes, probed at the T^+ trion, have different scattering probabilities and are based on SFRS mechanisms which are differently affected by the orientation of the magnetic field. The e-SFRS at the positive trion resonance remains disappeared in the Voigt geometry, as demonstrated in the Fig. 3-7 (c). However, under illumination for resonantly exciting the T^- trion the e-SFRS line with rather high intensity is observed, it is marked by the vertical arrow.

Apart from the angle dependence of the e- and hh-SFRS at the T^+ resonance, the hh-SFRS also depends on the excitation energy varied across the trion resonance. The spectrum containing both SFRS lines is measured for $E_R = 1.6007$ eV. When the energy is changed to $E_{T^+}^{\text{low}} = 1.6000$ eV the hh-SFRS disappears, as shown by the blue curve in the Fig. 3-7 (b). Thus, the hh-SFRS is very sensitive to the localization degree of the carrier complex. It might be also possible for such low excitation energies that a heavy-hole bound to an acceptor or a donor-bound exciton is involved in the Raman scattering process.

In Fig. 3-8 the intensities of the electron- and heavy-hole-SFRS lines are shown as a function of the lattice temperature varied from 1.3 to 9 K. The measurements were done in Faraday geometry at $B = 9$ T. The SFRS processes induced in the exciton complex by the energy $E_{\text{Ex}}^{\text{mid}} = 1.6035$ eV are indicated by open symbols, while the closed squares refer to the e-SFRS at the higher energy $E_{\text{Ex}}^{\text{high}} = 1.6043$ eV. The e- and hh-SFRS lines are strongly sensitive to the temperature: they are most intensive at temperatures below 2 K, whereby their absolute intensities differ from each other considerably. For $T = 5$ K the intensities are at least twice smaller than that at 2 K, whereas at 9 K they are

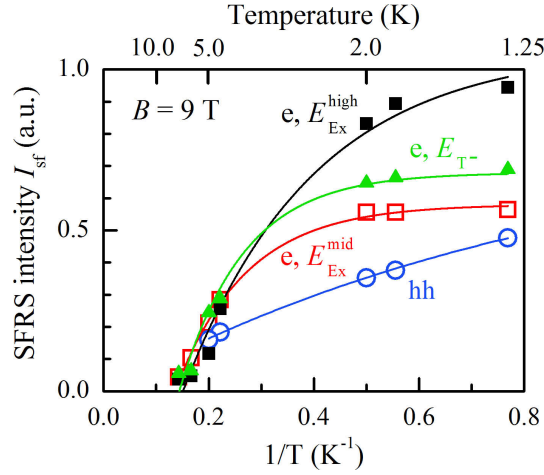


Figure 3-8: Temperature dependence of the electron- and heavy-hole-SFRS intensities for resonant excitation of the exciton and T^- trion at $\theta = 0^\circ$ (Faraday geometry). The exponential fits after Eq. (3.4), from which the activation energies of the SFRS processes are evaluated, are illustrated by lines. The e-SFRS is probed in resonance with both the exciton at $E_{Ex}^{mid} = 1.6035$ eV or $E_{Ex}^{high} = 1.6043$ eV as well as the negative trion at $E_{T^-} = 1.6011$ eV, the polarization configuration is (σ^+, σ^-) . The line intensity of the hh-SFRS in the exciton for (σ^+, σ^+) polarization does not show a saturating plateau thus indicating a small activation energy.

almost disappeared. The temperature-dependent SFRS intensities follow the Arrhenius-like exponential equation

$$I_{sf} = I_0 \exp\left(\frac{\epsilon}{k_B T}\right), \quad (3.4)$$

where I_0 is the intensity amplitude, k_B the Boltzmann constant, and ϵ the activation energy of the corresponding SFRS process. The hh-SFRS is described by an activation energy of only 0.1 meV, since its temperature dependence does not have a regime of stable intensity. By comparison, the fittings of the e-SFRS data yield activation energies of 0.3 meV for E_{Ex}^{high} and 0.8 meV for E_{Ex}^{mid} . Although the absolute intensity of the high-energy e-SFRS is large, its activation energy is about three times smaller than that for E_{Ex}^{mid} . The activation energies of the e-SFRS processes are smaller for larger excitation energies where less localized states are excited. Moreover, ϵ for E_{Ex}^{mid} is similar to $\epsilon = 0.7$ meV probed at the negative trion resonance, see the green-colored triangles and curve in Fig. 3-8. Since the exciton binding energy in CdTe QWs is about 12 meV and that of a trion is about 2-3 meV [185, 188], ϵ cannot be attributed to the binding energy. On the contrary, the energies ϵ for the exciton and negative trion rather coincide with the FWHM of their PL lines which do not exceed 0.9 meV, see Fig. 3-1 (b). The localization potential of the QW as well as the QW width and barrier-alloy fluctuations define the line width of the PL. Therefore, the activation energy can be assumed to describe the localization energy of the corresponding carrier complex.

In the following the impact of the power density P_a of the above-barrier illumination on the SFRS processes will be highlighted. The power dependence of the electron- and heavy-hole-SFRS intensities is illustrated in the Fig. 3-9 (b). Their tendencies are characteristic of the crossed and parallel circular polarizations. They will be compared

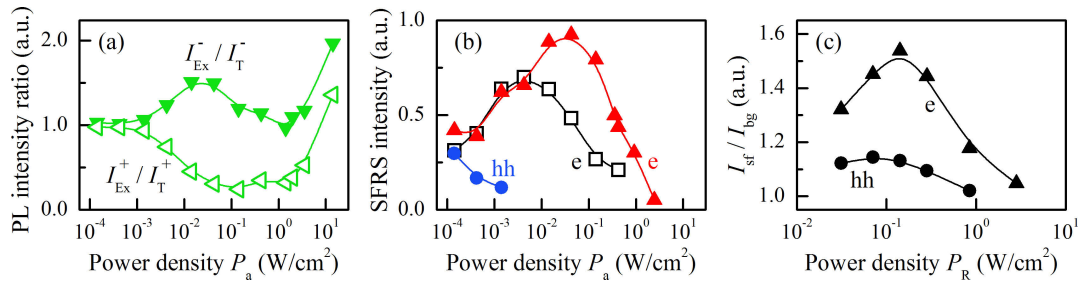


Figure 3-9: Dependence of the SFRS and PL intensities on the power density of the above-barrier illumination in Faraday geometry, $B = 9$ T and $T = 1.8$ K. (a) Intensity ratios of the σ^+ or σ^- polarized PL of the exciton (Ex) and trion (T), excited only by $E_a = 2.33$ eV. (b) Enhancement and quenching of the electron- and heavy-hole-SFRS processes by the above-barrier illumination. The power density of the resonant laser is $P_R = 0.5$ W/cm^2 . The e-SFRS for resonant excitation of the trion ($E_R = 1.6011$ eV) is marked by the open squares, the other experimental data are taken at the exciton resonance ($E_R = 1.6037$ eV). (c) Dependence of the e- and hh-SFRS intensity in relation to the PL background intensity I_{bg} on the power density of the resonant excitation.

with the PL intensities of the exciton I_{Ex} and trion I_{T} , since their PL mirrors the optical tuning of the resident carrier concentration by the above-barrier illumination. The ratios between the circularly polarized exciton and trion PL are shown in the Fig. 3-9 (a). In what follows, the comparison is attributed to the regimes of low, intermediate, and high power densities.

At low power densities $P_a < 10^{-3}$ W/cm^2 the PL intensity ratios $I_{\text{Ex}}/I_{\text{T}}$ are similar to unity for σ^+ and σ^- polarization. Here, the concentration of the resident holes of about 10^{10} cm^{-2} exceeds the number of photogenerated electrons in the QW. The electron-SFRS intensity approximately remains at the level as without above-barrier illumination. However, the hh-SFRS sensitively responds to P_a : the increase from 10^{-4} to 10^{-3} W/cm^2 leads to a decrease of its intensity by three times.

For intermediate power densities between 10^{-3} and 0.1 W/cm^2 the PL ratio for the σ^+ polarization decreases, while the ratio $I_{\text{Ex}}^-/I_{\text{T}}^-$ rises above unity, in agreement with the circular polarization degrees shown in the Fig. 3-1 (d). The concentration of the resident electrons becomes larger than the concentration of the holes, hence, the type of the resident carriers changes from p- to n-type. As depicted in Fig. 3-9 (b), in this power-density regime the hh-SFRS vanishes, while the e-SFRS intensities are considerably enhanced. The intensity dependence of the e-SFRS reaches its maximum at $P_a \approx 0.05$ W/cm^2 for the resonant excitation of the exciton (red triangles) and at about 0.005 W/cm^2 at the T^- resonance (open squares).

At high power densities $P_a > 0.1$ W/cm^2 the PL intensity ratios increase and at about 5 W/cm^2 they rise strongly. The e-SFRS intensities decrease and are fully suppressed at about 1 W/cm^2 . At high power densities the injected electrons lead to heating effects, and the trion oscillator strength decreases due to electron delocalization. These effects reduce the lifetime of the scattering states and, in turn, the intensity of the electron-SFRS line. Note, by use of a below-barrier illumination with an energy of 1.88 eV the SFRS of the electron (and also hh) cannot be enhanced in intensity. For similar power

densities as used for the above-barrier illumination its intensity remains at the level as without additional illumination, and for larger power densities it is suppressed. These preliminary results require further experimental studies.

The change in the e- and hh-SFRS intensity by varying the power density P_R of the resonant excitation is shown in Fig. 3-9 (c). The SFRS intensity is normalized by the intensity of the PL background. In contrast to the P_a -dependence, both the e-SFRS and hh-SFRS intensity distributions probed at the exciton resonance depend on P_R in a similar way: for $P_R = 0.2 \text{ W/cm}^2$ the intensities are maximal, and for power densities exceeding 1 W/cm^2 the SFRS lines can hardly be separated from the PL background.

3.4 Discussion of Scattering Mechanisms

The SFRS mechanism can be evaluated from the circularly polarized Raman spectra, measured in Faraday geometry, by analyzing the selection rules for electric dipole transitions. In the electric dipole approximation the change in the total angular momentum is $\Delta j = 0$ or ± 1 . The transitions are circularly polarized when the projection of the total angular momentum j_z on the quantization axis in z -direction changes by ± 1 . In the case of resonant probing of a heavy-hole exciton, the optical excitation of the states $|j_z\rangle = |s_{z,e}, j_{z,hh}\rangle = | + 1\rangle = | - 1/2, + 3/2\rangle$ and $| - 1\rangle = | + 1/2, - 3/2\rangle$ by the absorption of σ^+ or, respectively, σ^- polarized light is allowed. Here, $s_{z,e}$ and $j_{z,hh}$ designate the projections of the electron spin and heavy-hole angular momentum. On the contrary, the optical excitation into the (dark) exciton states $| + 1/2, + 3/2\rangle$ or $| - 1/2, - 3/2\rangle$ is forbidden in the electric dipole approximation.

In the following the electric dipole selection rules are checked for SFRS processes in three types of exciton complexes: a neutral exciton (i), a negative (ii) and positive (iii) trion. For a (100)-grown QW the symmetry can be described by the irreducible representation D_{2d} , see details in the Section 1.1.1. Here, the heavy-hole subbands are separated from the light-hole ones. It is assumed that a high magnetic field applied along the growth axis of the QW lifts the spin degeneracy of the electron and heavy-hole states. It is further supposed that the incident light is σ^+ polarized. The possible SFRS processes in the three types of complexes are illustrated by the schemes (i), (ii), and (iii) in Fig. 3-10. A description of each scheme is given in the following.

- (i) The incident photon creates an exciton in the state $| + 1\rangle = | - 1/2, + 3/2\rangle$ which does not interact with a resident carrier. A single spin-flip of either the electron or heavy-hole leads to a dark exciton state of $| + 2\rangle = | + 1/2, + 3/2\rangle$ or $| - 2\rangle = | - 1/2, - 3/2\rangle$, respectively. Hence, Raman scattering of a single spin in an exciton is not observable. However, the simultaneous reversal of the electron and heavy-hole spins is allowed; this exciton spin-flip scattering process is induced by an acoustic phonon, as depicted in the Fig. 3-10 (i). Accordingly, the exciton is scattered from $| - 1/2, + 3/2\rangle$ into the state $| + 1/2, - 3/2\rangle$. The annihilation of this exciton yields a scattered photon having an opposite circular polarization than the incident one, i.e. σ^- polarization in the considered example. Therefore, the SFRS line of the exciton is observable in the $(\sigma^\eta, \sigma^{-\eta})$ configuration. The Raman shift is given by the exciton Zeeman splitting: $\Delta E_{sf} = \Delta E_{Ex}$.
- (ii) For resonant excitation of a negative singlet trion the resident electron occupies

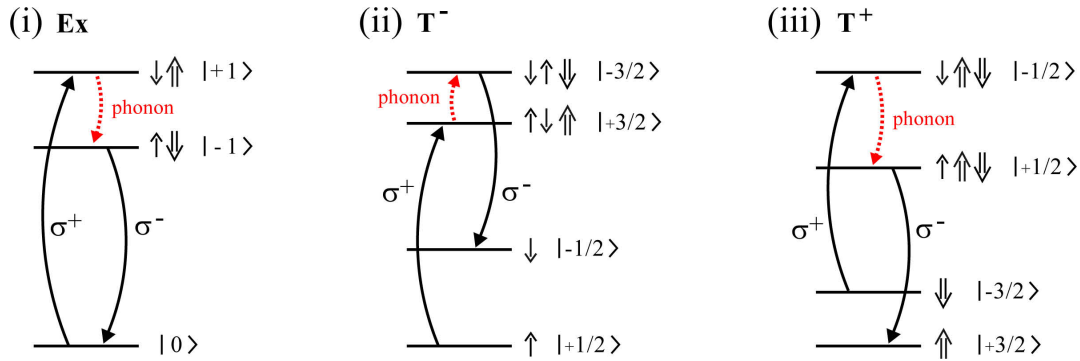


Figure 3-10: Model schemes of electric dipole allowed SFRS Stokes-processes in an exciton, a negative and positive trion. The Faraday geometry, and separated light-hole and heavy-hole states are considered. The resonant excitation is σ^+ polarized. (i) For an exciton noninteracting with a resident carrier, only the SFRS of the exciton itself is allowed via acoustic phonon scattering. (ii) In the negative trion the heavy-hole spin is scattered by an acoustic phonon. The difference between the incident and scattered photon energies is $\hbar\omega_i - \hbar\omega_s > 0$ thus defining a Stokes process, see Subsection 1.2.1. (iii) In the positive trion the unpaired electron spin interacts with an acoustic phonon. The trion Raman shifts are equal to $\Delta E_e + \Delta E_{hh}$.

the spin-up and the photo-electron the spin-down state, the heavy-hole is in the $j_{z, hh} = +3/2$ state; the trion is initially in the state $|+1/2, -1/2, +3/2\rangle$. The total angular momentum projection is $j_z = +3/2$, as it is shown in Fig. 3-10 (ii). Here, the single spin-flip of an electron is forbidden by Pauli's exclusion principle. Only an isotropic flip-flop exchange interaction between both electrons in the singlet state is possible. Actually, it does not change the spin configuration of the trion complex. Note, in the traditional way of explaining resonant Raman scattering via virtual states the inclusion of the flip-flop of both electron spins is demanded (see Section 1.2.1), although in the trion the two electrons with superposed wave functions are indistinguishable. Only the unpaired heavy-hole in the T^- trion can flip its spin via acoustic phonon scattering. Hence, the trion is scattered from $|+1/2, -1/2, +3/2\rangle$ into the state $|+1/2, -1/2, -3/2\rangle$. The final recombination leads to σ^- polarized light, whereby, a spin-down electron is left. The polarization configuration is $(\sigma^\eta, \sigma^{-\eta})$, and the Raman shift is equal to $\Delta E_{sf} = \Delta E_e + \Delta E_{hh}$. The trion Raman shift practically coincides with that of the exciton. Since the sign of $\Delta E_{e(hh)}$ depends on the sign of the electron (heavy-hole) g factor, $\Delta E_{e(hh)}$ can be either positive or negative.

- (iii) In analogy to the negative trion the resonant probing of the positive trion $| -1/2, -3/2, +3/2\rangle$ solely yields a SFRS process of the unpaired carrier spin. Accordingly, the electron spin is scattered from $s_{z,e} = -1/2$ to $s_{z,e} = +1/2$ via an acoustic phonon. A flip-flop between the two heavy-hole spins might be induced by direct exchange interaction. In the end, the annihilation of the $|+1/2, -3/2, +3/2\rangle$ trion results in σ^- polarized light in accordance with the electric dipole selection rules.

In the Faraday geometry the Raman scattering which induces a single spin-flip of either an electron or a heavy-hole in an exciton is principally forbidden by the electric

Table 3-1: Properties of the different SFRS lines for resonant excitation of the exciton (E_{Ex}) and trion (E_{T}) states. The properties refer to the Stokes regime and Faraday geometry, except for the hh-SFRS in the positive trion. The above-barrier illumination is denoted by E_{a} . Besides the activation energy ϵ determined by the temperature dependence, the dominant circular polarization configuration ($\sigma^\eta, \sigma^\gamma$) is designated. The latter is abbreviated by $(\eta\gamma)$. The geometries in which the SFRS line is observed are marked by the tilting angle θ . The main SFRS mechanisms are listed, they refer to anisotropic exchange interaction (\hat{H}_{xch}), direct exchange interaction between electrons ($\hat{H}_{\text{d}}^{\text{e-re}}$), and interaction with an acoustic phonon (\hat{H}_{ac}). Note, the value $\epsilon = 0.3$ meV for the hh-SFRS at E_{T} is uncertain due to temperature fluctuations during the specific experiment.

| SFRS | Excitation | ϵ (meV) | $(\eta\gamma)$ | Geometry | Mechanism |
|------|---------------------------------|------------------|----------------|---|---|
| e | $E_{\text{Ex}} (+E_{\text{a}})$ | 0.8 | $(+-)>(++)$ | $0^\circ \leq \theta \leq 90^\circ$ | $\hat{H}_{\text{ac}} + \hat{H}_{\text{xch}}^{\text{e-h}}$ |
| hh | E_{Ex} | 0.1 | $(++)>(+ -)$ | $0^\circ \leq \theta \leq 90^\circ$ | $\hat{H}_{\text{xch}}^{\text{h-h}}$ |
| e | E_{T} | < 0.1 | $(+-)$ | $0^\circ \leq \theta \lesssim 25^\circ$ | $\hat{H}_{\text{d}}^{\text{e-re}} + \hat{H}_{\text{xch}}^{\text{e-hh}}$ |
| hh | E_{T} | (0.3) | \ | $\theta \gtrsim 15^\circ$ | $\text{lh} \leftrightarrow \text{hh} + \theta \neq 0^\circ$ |
| e | $E_{\text{T}} + E_{\text{a}}$ | 0.7 | $(+-), (--)$ | $0^\circ \leq \theta \leq 90^\circ$ | $\hat{H}_{\text{d}}^{\text{e-re}} + \hat{H}_{\text{xch}}^{\text{e-hh}}$ |

dipole selection rules. Only an exciton-SFRS based on the simultaneous spin-flip of the electron and heavy-hole can be expected. Possibilities to bypass the electric dipole selection rules will be evaluated from the experimental observations. For instance, if a resident carrier is in the vicinity of the photogenerated exciton the angular momentum conservation can be relaxed due to a reduction in symmetry of the excitonic complex. Thus, anisotropic flip-stop-like exchange interaction between identically charged carriers is possible. It will be discussed in Subsection 3.4.1. Moreover, it will be shown that the anisotropic flip-stop-like exchange interaction between the electron and heavy-hole in an exciton plays a major role as a spin-flip scattering mechanism. Furthermore, the tilting of the magnetic field direction with respect to the QW growth axis leads to a mixing of the electron states and hole states. Therefore, single spin-flip Raman processes become allowed. By comparison, in Faraday geometry the strain-induced mixing between the light-hole and heavy-hole states results in linearly polarized SFRS lines satisfying the electric dipole selection rules; in tilted geometries it contributes to the elliptical polarization of the scattered light.

In the Table 3-1 the characteristics of the experimentally observed SFRS lines are summarized. The type of the SFRS process is described with respect to the resonant excitation energy which is in resonance with either the exciton or trion. Additionally, the simultaneous application of the above-barrier illumination is indicated. The activation energy as well as the dominant circular polarization configuration are specified. Moreover, the mechanism of the SFRS process is described by the corresponding Hamiltonian operator. Note, the properties summarized in the Table 3-1 are related to the Faraday geometry, only for the hh-SFRS at E_{T} the data refer to a tilted geometry.

3.4.1 SFRS at the Exciton Resonance

SFRS lines of a heavy-hole and an electron are present in the experimentally obtained spectra for the resonant excitation of the exciton. In contrast to the model scheme (i), an exciton-SFRS line has not been observed, most probably due to the small longitudinal

exciton g factor. The hh -SFRS is most intensive in the (σ^+, σ^+) configuration across the entire exciton resonance, as noted in the Table 3-1. The e -SFRS is dominant for the (σ^+, σ^-) polarization. Their experimental intensities in the different circular polarization configurations are given in Eq. (3.2). The above-barrier illumination does not influence the intensity ratios of the circularly polarized e-SFRS lines; it enhances their absolute intensities with equal probability. On the contrary, the hh-SFRS line is suppressed already at small power densities of the above-barrier illumination, see Fig. 3-9 (b). In the following the Raman scattering mechanisms of the electron spin-flip and, thereafter, the heavy-hole one at the exciton resonance will be discussed.

Electron-SFRS. According to Eq. (3.2) the Stokes scattered light of the electron spin-flip is elliptically polarized in Faraday geometry: both for σ^+ and σ^- polarized excitation the e-SFRS line is observed in the Stokes regime for parallel and opposite circular polarizations. As indicated by the nonlinear magnetic field dependence of the heavy-hole-SFRS line shift, see Fig. 3-4 (a), light-hole and heavy-hole states are mixed. In the case of valence band mixing induced by local QW deformations or its asymmetric interface potential [138, 140, 189], the lowest energy hole states take the form

$$|\Psi_h^\pm\rangle \propto |\pm 3/2\rangle - \beta |\mp 1/2\rangle, \quad (3.5)$$

where the mixing coefficient β is equal to the ratio w_{lh}/w_{hh} of probabilities for the hole to be light or heavy. From the relative intensities of the e-SFRS noted in Eq. (3.2) the mixing coefficient can be estimated to about $\beta = 0.28$. By comparison, the hh-SFRS line intensities yield a similar mixing coefficient of 0.29. This 1 to 3 ratio coincides with the typical probability of transitions to light-hole ($j_{z,lh} = \pm 1/2$) and heavy-hole ($j_{z,hh} = \pm 3/2$) states. Therefore, the full explanation of the polarization characteristics of the e-SFRS line at the exciton resonance requires the inclusion of the lh-hh mixing.

The electron-SFRS line at the exciton resonance is explained in terms of a fourth-order Raman process in additional consideration of lh-hh mixing. The SFRS process is schematically depicted in the Fig. 3-11 (a). The e-SFRS is initiated by the creation of a $| -1/2, \Psi_h^+ \rangle$ exciton addressed with σ^+ or σ^- polarized light. At the second stage, the electron flips its spin from $| -1/2 \rangle$ to $| +1/2 \rangle$ via the interaction with an acoustic phonon. It is described by the Hamiltonian $\hat{H}_{ac} = S_{\uparrow\downarrow} \hat{a}_\uparrow^\dagger \hat{a}_\downarrow \hat{b}^\dagger$, where $S_{\uparrow\downarrow}$ describes the electron-phonon coupling matrix element depending on the electron spin momentum projections, \hat{a}_\downarrow and \hat{a}_\uparrow^\dagger are the electron annihilation and creation operators, and \hat{b}^\dagger is the phonon creation operator. The phonon energy $\hbar\Omega_{ac}$ is equal to the electron Zeeman splitting $g_e^\parallel \mu_B B$. At this stage, the difference in the total angular momentum of the exciton $|1/2, \Psi_h^+ \rangle$ is either $\Delta j_z = 2$ or zero. In order to obtain circular-polarized scattered photons, the photogenerated hole has to reverse its spin state. Since the emission of the acoustic phonon has reduced the energy of the complex, the photo-hole has to flip its spin without change in energy.

After the phonon-induced electron spin-flip the exciton in the state $|1/2, \Psi_h^+ \rangle$ should be additionally shifted in energy by the exciton exchange energy δ_0 designating the bright-dark exciton splitting. Accordingly, the e-SFRS line shift should be given by $g_e^\parallel \mu_B B + \delta_0$. Only in the case of fast hole spin relaxation with $\hbar/\tau_{s,h} > \delta_0$, the Raman shift does not depend on the exciton exchange energy. In the CdTe-based QWs the exchange splitting ranges between 0.05 and 0.1 meV [190]. In order to satisfy the condition above, the spin relaxation time $\tau_{s,h}$ of the hole in the neutral exciton has to be shorter than 10 ps.

From the literature, only the spin dephasing time of resident holes in the studied CdTe QW is known [179]. The radiative exciton recombination time is about 20-30 ps [190]. By assuming the latter one as upper limit of $\tau_{s,h}$, the condition $\hbar/\tau_{s,h} > \delta_0$ is not fully fulfilled. However, the studied exciton possesses a spatially asymmetric wave function due to spatially shifted localization centers of the electron and hole, as will be shown later. Accordingly, the hole spin can relax very fast due to anisotropic exchange interaction with the electron spin. In turn, only the energy of the electron Zeeman splitting contributes to the Raman shift in agreement with the experimental results.

At the third stage, an anisotropic exchange interaction between the $s_{z,e} = 1/2$ electron and hole in the state $|\Psi_h^+\rangle$ changes the hole spin state from $|\Psi_h^+\rangle$ to $|\Psi_h^-\rangle$ while leaving $s_{z,e}$ invariant. This anisotropic flip-stop-like exchange interaction promotes the hole into a virtual state whose energy coincides with the energy of the $|\Psi_h^+\rangle$ spin state. The initial hole state and the virtual one are degenerate, they do not differ by the Zeeman splitting energy. The virtual state is not an eigenstate of the exciton, but it serves as an intermediate state in the coherent Raman scattering process. It instantaneously provides the annihilation of the $|1/2, \Psi_h^-\rangle$ exciton under emission of scattered light which is mostly σ^- and partially σ^+ polarized. The energy difference between the incident and scattered photons is equal to the electron Zeeman splitting $g_e^{\parallel} \mu_B B$.

The anisotropic flip-stop-like exchange interaction results from spatially shifted wave function probability densities of the electron and hole. The centers ρ_e and ρ_h of their in-plane localization areas do not coincide. The presence of the in-plane direction $\rho_e - \rho_h$ lowers the symmetry of the exciton complex. Since the projection of the angular momentum on the axis defined by $\rho_e - \rho_h$ is not preserved, the restrictions imposed by the angular momentum conservation are lifted. This symmetry reduction allows an anisotropic exchange interaction which flips the hole spin while leaving the electron spin invariant. Correspondingly, it is called flip-stop-like exchange interaction [141, 142, 191]. The Hamiltonian of the flip-stop-like e-h exchange interaction is described by

$$\hat{H}_{\text{xch}}^{\text{e-h}} = (\Delta_h \sigma_+^h + \Delta_h^* \sigma_-^h) \sigma_z^e. \quad (3.6)$$

Here, Δ_h and Δ_h^* are complex coefficients, and the Pauli matrices σ_z^e and $\sigma_{\pm}^h = (\sigma_x \pm i\sigma_y)/2$ act on the electron or, respectively, light-hole and heavy-hole states in the basis $1/\sqrt{2}|x - iy\rangle|\downarrow\rangle$, $-1/\sqrt{2}|x + iy\rangle|\uparrow\rangle$, $1/\sqrt{6}(|x - iy\rangle|\uparrow\rangle + 2|z\rangle|\downarrow\rangle)$, and $-1/\sqrt{6}(|x + iy\rangle|\downarrow\rangle - 2|z\rangle|\uparrow\rangle)$. The anisotropic exchange requires a symmetry reduction due to spatially different probability densities of the in-plane electron and hole wave functions. The weak wave function overlap is indicated by the small activation energy $\epsilon = 0.8$ meV of the exciton complex, compare Fig. 3-8. One can conjecture that the e-SFRS is observed for excitons with nonspherical symmetry.

The mechanism of the e-SFRS at the exciton resonance previously discussed has no alternative. An influence of a resident hole or electron can be excluded, since the polarization characteristics of the e-SFRS line do not depend on the above-barrier illumination. If a resident hole excited the photo-hole into the virtual state via anisotropic exchange interaction, the application of the above-barrier illumination would solely suppress the e-SFRS. If a resident electron participated in the e-h exchange, the intensity of the e-SFRS line would be very weak in absence of the above-barrier illumination. An anisotropic exchange interaction between a resident electron and the exciton would also result in a strong co-polarization of the scattered light. The complex of exciton and

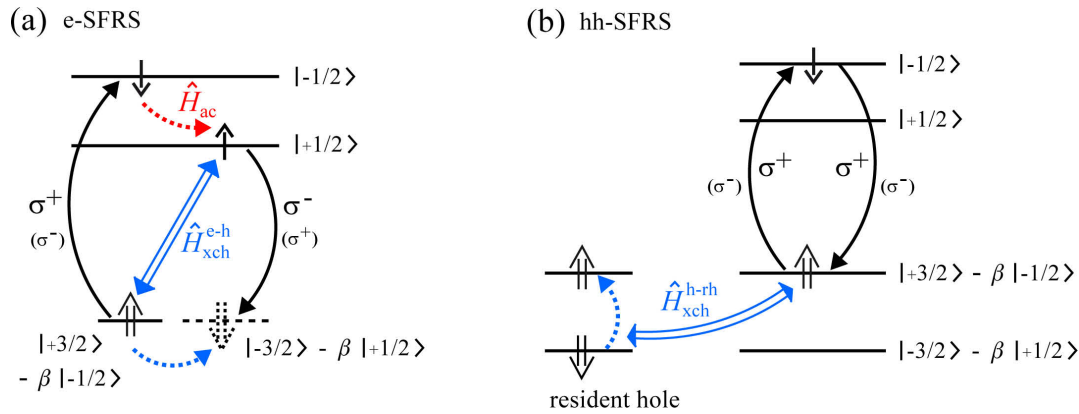


Figure 3-11: Schemes of the e-SFRS and hh-SFRS Stokes-processes at the exciton resonance in Faraday geometry, illustrated in the single-particle picture. (a) Fourth-order process describing the electron-SFRS line in the differently circular-polarized configurations. The intermediate states are based on the scattering of the electron with an acoustic phonon, and the anisotropic exchange interaction between the electron and hole. (b) Third-order hh-SFRS process based on the anisotropic exchange between the photogenerated and resident hole. A radiative transition is marked by the curved single-line arrow. The blue-colored double-line arrow notes an anisotropic flip-stop-like exchange interaction.

resident electron would be more asymmetric, thus, the localization energy would be as small as ϵ for the hh-SFRS at the exciton resonance.

Furthermore, two other processes which might be thought to be responsible for the dominant (σ^+, σ^-) polarization of the e-SFRS can be excluded. (1) After the spin-flip of the photo-electron via an acoustic phonon, it can recombine with a resident heavy-hole whose spin is orientated opposite to the spin of the photo-hh. The emitted light is σ^- polarized and its energy could be reduced by the electron Zeeman splitting only. Nevertheless, this process is not a coherent SFRS process, it only leads to resonant PL. Also, it would sensitively depend on the concentration of the resident holes. (2) If the e-SFRS is solely based on an isotropic exchange interaction between the electron and heavy-hole, the scattered photon will be σ^- polarized. But, the energy of the scattered photon will be the sum of the electron and heavy-hole Zeeman splittings: $|g_e^\parallel + g_{hh}^\parallel| \mu_B B$.

The enhancement of the absolute e-SFRS intensity by the above-barrier illumination is caused by an increase in the exciton lifetime. As shown by Koudinov et al. [192], the SFRS intensity depends on the third power of the lifetime τ_{Ex} or, respectively, the homogeneous line width Γ_{Ex} of the exciton state: $I_{sf} \propto \Gamma_{Ex}^{-3} \propto \tau_{Ex}^3$. Due to the background concentration of holes the excitons can be trapped into positive trion states. This trion formation is the dominant nonradiative decay mechanism for excitons. The trion formation time τ_T is about a few ps, while the exciton lifetime approaches 30 ps. Hence, the line width of the exciton will be broadened and, in turn, the SFRS intensity decreases. The above-barrier illumination leads to a reduction in the resident hole concentration thus making the formation of positive trions less probable. Correspondingly, the lifetime of the exciton states is increased resulting in an increase in the overall electron-SFRS intensity. The increase in the SFRS intensity requires that the scattering time τ_s of the acoustic phonon and spin-spin exchange exceeds the trion formation time, and the entire

e-SFRS must occur within the exciton lifetime: $\tau_T < \tau_s < \tau_{\text{Ex}}$. At high optical power densities of the above-barrier illumination the SFRS intensity will be reduced again, as depicted in Fig. 3-9 (b). Note, the trion formation time and/or exciton lifetime only influence the SFRS intensity, while the width of the SFRS line is affected by τ_s .

A further property of the e-SFRS in the exciton can be extracted from the resonance profiles: they illustrate that at high excitation energies of about 1.605 eV the intensity of the e-SFRS line in the (σ^+, σ^+) configuration becomes comparable to $I_{\text{sf}}(\sigma^+, \sigma^-)$, see inset of Fig. 3-5 (b). And, the SFRS resonance profile in the co-polarized configuration becomes narrower, see Figs. 3-5 (a) and (b). The change in the SFRS intensity ratio can be explained by an energy dependence of the e-SFRS mechanism. The anisotropic exchange interaction between a resident and the photogenerated electron can lead to the relative intensity enhancement of the co-polarized scattered light. At high excitation energies the probability of probing a complex of a residual electron and an exciton less localized in the lateral QW plane is increased. Note, a weaker localization of the exciton complex is also expressed by the lower energy $\epsilon = 0.3$ meV probed at high excitation energy, see Fig. 3-8. Therefore, it can be assumed that in this energy range two SFRS processes are present: the electron spin-flips are performed in both the isolated exciton as well as the resident electron-exciton complex. Alternatively, the SFRS intensity change and the narrowing of the SFRS resonance profile can be described by an energy-dependent variation of the light-hole admixture into the hole state, in consideration of isolated excitons only. According to the valence band mixing, the heavy-hole part accounts for the (σ^+, σ^-) configuration, while the σ^+ polarized scattering light is contributed by the light-hole. Since the effective in-plane mass of the light-hole can become comparable to that of the heavy-hole with increasing excitation energies [186, 193], the localization potential and also the lh-hh mixing coefficient β might be affected so that the exciton receives a more significant light-hole character.

Heavy-Hole-SFRS. The SFRS of the heavy-hole at the exciton resonance is the result of a third-order scattering process. Since the hh-SFRS line intensities are elliptically polarized with a light-hole admixture of 29%, the lh-hh mixing must be taken into account^{||}. The scheme of the hh-SFRS is illustrated in the Fig. 3-11 (b). In the case of Stokes scattering a circularly polarized photon creates a $| -1/2, \Psi_{\text{h}}^+ \rangle$ exciton. Due to the strong sensitivity of the hh-SFRS to the above-barrier illumination, a resident hole (rh) is assumed to be neighbored to the photogenerated exciton. The wave function of the resident hole which is localized by QW width or alloy fluctuations is spatially shifted from the wave function of the photo-hole. Due to the spatially separated in-plane localization centers of the photo-hole and the neighboring resident hole the anisotropic exchange interaction between both holes becomes probable, as in the case of the e-SFRS process discussed previously. Note, the low activation energy $\epsilon = 0.1$ meV indicates that the envelope functions of the photo-exciton and resident hole weakly overlap, in turn, their density probabilities are strongly separated in space. Accordingly, the photo-hole induces a spin-flip of the resident hole from $|\Psi_{\text{rh}}^- \rangle$ to $|\Psi_{\text{rh}}^+ \rangle$ via the anisotropic flip-stop-like exchange interaction. This interaction is illustrated by the blue-colored double-line

^{||}For the (σ^-, σ^-) polarization the relative intensity of the hh-SFRS is also about 0.3, although this configuration has the lowest probability. The circular polarization degree of the resident holes is about 30% at $B = 9$ T. Thus, the hole spin polarization also contributes to the hh-SFRS polarization characteristics.

arrow in Fig. 3-11 (b). In analogy to Eq. (3.6), the interaction Hamiltonian $\hat{H}_{\text{xch}}^{\text{h-rh}}$ is given by $\hat{H}_{\text{xch}}^{\text{h-rh}} = (\Delta_{\text{rh}}\sigma_+^{\text{rh}} + \Delta_{\text{rh}}^*\sigma_-^{\text{rh}})\sigma_z^{\text{h}}$.

At the final stage of the hh-SFRS process, the photo-exciton $|s_{z,e}, \Psi_{\text{h}}^+\rangle$ annihilates by emitting light having the same circular polarization as the incident light. Due to the lh character of the exciton it is σ^+ and partially σ^- polarized. In comparison to the incident light, the energy of the scattering light is reduced by the Zeeman energy of the resident hole ($\Delta E_{\text{sf}} = \Delta E_{\text{rh}}$). Altogether, the observation of the hh-SFRS in the Stokes regime requires that the electron occupies the $| - 1/2\rangle$ state, and the rh has to change its spin state from the lower to the upper Zeeman level, thus providing a low-energy scattered photon. In the case of the anti-Stokes process the transition of the resident hole from the upper to the lower state contributes the Zeeman energy to the exciton complex.

The strength of the anisotropic hole-hole exchange interaction can be estimated by the localization degrees of the resident hole and exciton. According to Ref. [191], the exchange energy is expressed in terms of the localization radius a_{rh} of the resident hole captured by potential fluctuations, the surface area δS defining the exciton-localization dimension in the xy -plane of the QW, the QW width L_z , and the permittivity ε of CdTe. The exchange energy can then be described by [191]

$$E_{\text{h-rh}} \approx \frac{e^2 a_{\text{rh}}^2}{\varepsilon L_z \delta S}. \quad (3.7)$$

The localization radius of the resident hole is small in comparison to the lateral extension of the photo-exciton and, in turn, to the localization radius of the photo-hole. By using the values $\varepsilon = 8.91\varepsilon_0$ [194], $L_z = 20$ nm, $a_{\text{rh}} \approx 0.1$ nm and $\delta S \approx 35$ nm²,** the exchange energy is approximately $E_{\text{h-rh}} \approx 0.03$ meV. The calculated value is similar to the localization energy ϵ evaluated from the hh-SFRS temperature dependence.

The energies of the anisotropic exchange interactions between the holes $E_{\text{h-rh}}$ and the electron and hole $E_{\text{e-h}}$ can be estimated from the corresponding energies ϵ . Both the localization energy of the scattering complex as well as the exchange energy depend on the overlapping of the carrier wave functions. By considering ϵ as the upper limit for the effective strength of the exchange interaction between the two carriers, $E_{\text{e-h}}$ falls below 0.8 meV and $E_{\text{h-rh}}$ can be estimated to be less than 0.1 meV. According to these estimations the magnitude of the anisotropic exchange interaction between the electron and hole exceeds the energy of the anisotropic exchange between the two holes.

3.4.2 SFRS at the Trion Resonance

In addition to the resonant excitation of the exciton without above-barrier illumination, the **hh-SFRS** is observed for resonant probing of the positive trion. As noted in Table 3-1, at the exciton resonance the hh-SFRS line is detected in each polarization configuration, while it is absent in the Faraday geometry at the T⁺ trion resonance. The hh-SFRS line only appears in tilted geometries with an angle $\theta \gtrsim 15^\circ$. It is in agreement

**The localization radius is estimated by the Bohr radius of the hole which is given by $a_{\text{rh}} = \varepsilon \hbar^2 / (m_{\text{hh}}^* e^2)$ with the heavy-hole effective mass $m_{\text{hh}}^* = 0.48m_0$. Since the diamagnetic shift $e^2 \langle \rho_{\text{I}}^2 \rangle / (8\mu) B^2$ is proportional to the lateral extension of the exciton wave function, $\delta S \approx \langle \rho_{\text{I,Ex}}^2 \rangle$ is taken from the fitting of the magnetic field dependence of the exciton PL energy.

with the model scheme (iii), shown in Fig. 3-10, that predicts only an exciton-SFRS in Faraday geometry. Actually, the absence of the hh-SFRS in the Faraday geometry indicates that the T^+ trion complex is spherically symmetric. Thus, an anisotropic spin exchange interaction bypassing the conservation of angular momentum is not possible in the positive trion complex; the reversal of spin of one of the holes is blocked by Pauli's exclusion principle. Accordingly, only in a tilted magnetic field the spin-flip scattering of the heavy-hole is observable.

The tilting of the magnetic field direction with respect to the QW growth axis leads to a mixing of the electron states. They are mixed by the in-plane component of the magnetic field vector, and can be described by [145]:

$$\Psi_e^\pm = \cos(\theta/2)|\pm 1/2\rangle \pm \sin(\theta/2)|\mp 1/2\rangle. \quad (3.8)$$

The mixing of the two lowest electron spin states is established via the transverse electron g factor. The lh-hh mixing is affected by the coupling of \mathbf{B} to a nonzero in-plane magnetic moment of the heavy-hole due its transverse g factor $g_{hh}^\perp \neq 0$. Therefore, in tilted geometries the probability of the mixing between the light-hole and heavy-hole states differs from that in Faraday geometry, where it is mainly induced by strain. Correspondingly, the lh-hh mixing coefficient depends on the tilting angle θ . The hole wave functions take the form of Eq. (3.5) where the mixing coefficient is substituted by $\beta'(\theta)$.

As depicted in the Fig. 3-12 (a), incident light which is vertical-linearly polarized is supposed to excite the positive trion into the state $|\Psi_e^-, \Psi_h^-, \Psi_h^+\rangle$, whereby, the resident hole initially occupies the $|\Psi_h^+\rangle$ state. Due to the mixed conduction band states, the spherical symmetry of the complex, and the occupation of both hole spin states, neither the electron nor the holes need to change their spin states to realize a hh-SFRS process. The final stage of this two-order SFRS process is governed by the annihilation of the trion $|\Psi_e^-, \Psi_h^-, \Psi_h^+\rangle$, whereby, a hole in the $|\Psi_h^-\rangle$ state is left. The energy difference between the incident and scattered light is determined by the hole Zeeman splitting. Note, both holes can interact via direct exchange interaction described by the Heisenberg-like Hamiltonian $\hat{H}_d^{h-rh} = J_{h-rh} (\sigma_x^h \sigma_x^{rh} + \sigma_y^h \sigma_y^{rh})$. Here, J_{h-rh} is the exchange integral and $\sigma_{x,y}$ are the Pauli matrices of the two holes. The mutual spin-flip scattering could be necessary – even in this spherically symmetric complex – to distinguish between resonant PL and the resonant SFRS process, see the discussion in Subsection 1.2.1.

In absence of the above-barrier illumination the resonant excitation of the trion also yields an **electron-SFRS**. In Faraday geometry it is detected for the (σ^+, σ^-) polarization with rather weak intensity. Due to residual electrons, also in absence of the above-barrier illumination, the e-SFRS can take place in a negative trion. An electron spin-flip in the positive trion would require the scattering of the photo-hole into an energetically equivalent virtual state with opposite spin, as in the case of the exciton complex. The presence of the resident heavy-hole in the T^+ trion forbids the excitation of that virtual state, since the hole spins have to be anti-correlated^{††}.

The application of the above-barrier illumination enhances the intensity of the e-

^{††}The disappearance of the e-SFRS and almost simultaneous appearance of the hh-SFRS at about $\theta = 25^\circ$ may give rise to the assumption that both SFRS processes are in competition, and at larger angles the hh-SFRS becomes more efficient. If both SFRS processes were correlated, they would take place in the positive trion complex. However, an e-SFRS in the positive trion is forbidden.

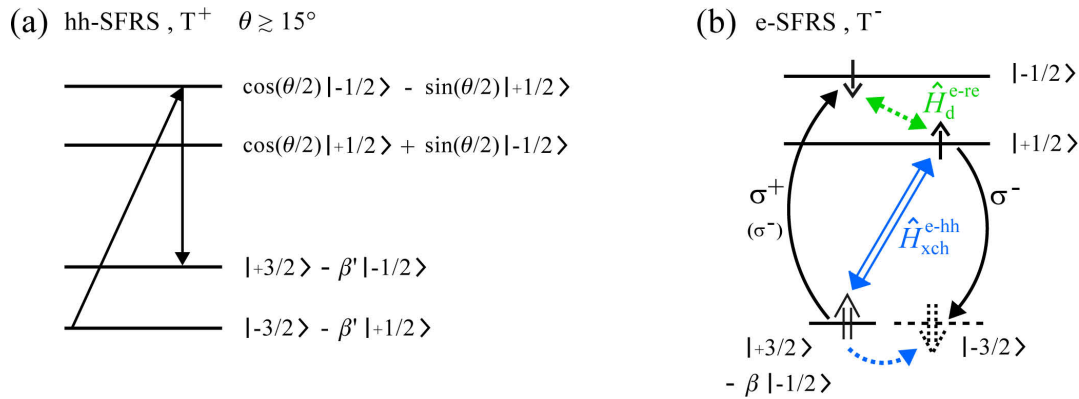


Figure 3-12: Schemes of the hh- and e-SFRS Stokes-processes in the positive and negative trion, respectively. (a) In resonance with T^+ trion, at tilting angles $\theta \gtrsim 15^\circ$ the hh-SFRS is possible due to the mixing of the electron states. (b) The electron-SFRS process in the negative trion in Faraday geometry consists of a direct flip-flop exchange between the two electron spins, and the anisotropic e-hh exchange interaction. The photo-hole is scattered into the virtual heavy-hole state $|-3/2\rangle$. The e-SFRS line is present in the (σ^\pm, σ^\mp) configurations.

SFRS line, and leads to its observation in the (σ^+, σ^-) and (σ^-, σ^-) configurations, as noted in Table 3-1. The above-barrier illumination makes the e-SFRS more stable against the increase in the lattice temperature. While the e-SFRS line probed without above-barrier illumination disappears at elevated tilting angles, it is observable over the whole angular range when the additional illumination is applied. It will be demonstrated that the electron-SFRS is performed in the negative trion via the same scattering mechanism with and without above-barrier illumination, and that the scattering intensity is influenced by the angle dependence of the anisotropic e-h exchange interaction as well as the number of additional resident electrons provided by the above-barrier illumination.

Moreover, the observation of the e-SFRS probed at the T^- trion in the Faraday geometry, its strong dependence on the above-barrier illumination, and the presence of anisotropic e-h exchange interaction (as the only SFRS mechanism) demonstrate that the negative trion complex is not spherically symmetric, in contrast to the T^+ trion. Therefore, the isotropic exchange between the two electrons is necessary to realize the e-SFRS. The small activation energy of 0.7 meV of the negative trion complex, being similar to that of the exciton complex, also evidences that the T^- complex is not spherically symmetric. Thus, an electron can interact via anisotropic exchange interaction with the hole. Assuming a fully symmetric negative trion where the electron spins form a singlet, an electron-SFRS will only be observable if the hole spin relaxes very fast. However, one can expect that the hole spin relaxation in such a symmetric complex with compensated electron spins is slow. Also, a SFRS mechanism based on the admixture of the triplet trion states to the singlet ones can be excluded for magnetic fields smaller than 20 T [182], since at low B -fields they are separated in energy by more than 2 meV. Furthermore, the specific polarization property, i.e. the pronounced σ^- polarization of the scattered light, of the e-SFRS line in Faraday geometry most probably reflects the equilibrium spin polarization of the resident electrons.

In the negative trion the electron-SFRS (in Faraday geometry) originates from two

intermediate scattering processes, as illustrated in the Fig. 3-12 (b). Firstly, the resident and photocreated electrons flip their spins via direct exchange interaction. In analogy to the Hamiltonian $\hat{H}_d^{\text{h-rh}}$, the flip-flop of the electron spins is described by the Hamiltonian

$$\hat{H}_d^{\text{e-re}} = J_{\text{e-re}} (\sigma_x^{\text{e}} \sigma_x^{\text{re}} + \sigma_y^{\text{e}} \sigma_y^{\text{re}}). \quad (3.9)$$

After the direct exchange interaction the photo-electron occupies the energetically lowest state $|+1/2\rangle$. Secondly, an anisotropic flip-stop-like exchange interaction between the photogenerated electron and hole changes the hole from $|\Psi_{\text{h}}^+\rangle = |3/2\rangle - \beta|-1/2\rangle$ to the energetically equivalent virtual state $|-3/2\rangle$. It is proposed that the virtual state has mainly heavy-hole character, since the final annihilation of the photo-exciton results in σ^- polarized light only. The Hamiltonian $\hat{H}_{\text{xch}}^{\text{e-hh}}$ is similar to that given in the Eq. (3.6). It transforms the $|\Psi_{\text{h}}^{\pm}\rangle$ states into the hh-states $|\mp 3/2\rangle$.

Finally, the angle-dependent reduction in the e-SFRS intensity will be discussed. An increase in the tilting angle θ leading to a smaller in-plane magnetic confinement reduces the localization of the electron and thus its SFRS line intensity. However, a tilting of the magnetic field direction with respect to the QW growth axis also enhances the mixing of the spin states. Therefore, one can expect a strong increase in the SFRS intensity, as it is shown for, e.g., (In,Ga)As quantum dots in Subsection 4.1.1. For the studied CdTe QW, at the T^+ trion resonance (without above-barrier illumination) the e-SFRS line disappears for tilting angles exceeding 25° . The line intensity of the e-SFRS probed at the exciton resonance also decreases with increasing angle, compare the Figs. 3-2 (a) and 3-7 (a). The disappearance of the e-SFRS can be attributed to the angle-dependent attenuation of the anisotropic electron-hole exchange interaction. The exchange interaction can be described as a transfer of the longitudinal and transverse spin polarizations between the electron and hole. The effective field which is produced by the one carrier due to its Larmor precession around the magnetic field direction, is felt by the other carrier, and vice versa. If the g factors of both carriers are identical, the time-dependent probability of spin exchange is proportional to $\sin^2(J_{\text{xch}}t/2)$, where J_{xch} marks the exchange constant [195]. In the case of different g factors the longitudinal and transverse spin exchanges deviate from each other. Thus, the probability of an exchange interaction process is scaled by the Larmor frequencies $\omega_{\text{L}} = g\mu_{\text{B}}B/\hbar$ of the electron and hole. The probability p_{xch} for the e-h exchange interaction is then given by [196]

$$p_{\text{xch}} \approx \hbar^2/(\mu_{\text{B}}B)^2 \left(\frac{J_{\text{xch}}}{g_{\text{e}} - g_{\text{h}}} \right)^2. \quad (3.10)$$

Since at larger angles θ the hole g factor considerably deviates from the isotropic electron g factor, the e-h exchange interaction becomes less probable. Accordingly, the intensity of the e-SFRS line decreases for resonant excitation of both the trion as well as exciton. In contrast to the e-SFRS at the T^+ resonance, the stronger localization potential of the exciton makes the e-SFRS observable in Voigt geometry, as shown by the black curve in the Fig. 3-7 (a). Therefore, the decrease of p_{xch} accounts for the angle-dependent disappearance of the e-SFRS. Note, its intensity is recovered and enhanced by the above-barrier illumination at the T^- resonance. It results from the optically induced increase in the resident electron concentration. Due to the larger number of resident electrons, the formation of negative trions and thus the electron-SFRS become more probable.

3.5 Conclusion

The spin-flip Raman scattering of electrons and heavy-holes is studied for resonant excitation of neutral and charged excitons in a CdTe/Cd_{0.63}Mg_{0.37}Te quantum well. The mechanisms of the spin-flip scattering are discussed by means of their polarization characteristics as well as angular and magnetic field dependencies. Model schemes of electric dipole allowed spin-flip Raman processes in the exciton complexes are compared to the experimentally determined scattering mechanisms, which originate from a reduced quantum well potential symmetry, the mixing between the light-hole and heavy-hole states, and mixed electron spin states in a tilted magnetic field geometry. At the exciton resonance anisotropic flip-stop-like exchange interactions induce the electron and heavy-hole spin-flip scattering processes. The electron spin-flip scattering in a spatially asymmetric exciton is established via an acoustic phonon interaction accompanied by an anisotropic flip-stop-like exchange between the electron and hole. The latter leaves the electron spin invariant, while the hole spin state is changed. The heavy-hole-SFRS is realized by a resident heavy-hole being in spatial vicinity of the photogenerated exciton. The strength of the anisotropic exchange interaction between the photogenerated and resident heavy-hole is about one order of magnitude smaller than that of the electron-hole exchange.

In resonance with the positively charged exciton the heavy-hole spin-flip scattering is based on a two-stage process (absorption and emission) governed by the mixing of conduction and valence band levels. It is demonstrated that the positive trion complex is spherical symmetric, on the contrary to the negative trion. The resonant excitation of the spatially asymmetric negative (singlet) trion yields an electron spin-flip scattering which is provided by direct spin exchange between both electrons and anisotropic electron-hole exchange interaction. The application of above-barrier illumination can considerably enhance the efficiency of the electron-SFRS. The variations in the resonant excitation energy and lattice temperature indicate that the spin-flip Raman scattering strongly depends on the spatial symmetry of the electron and heavy-hole wave functions, and also on the localization degree of the resident electrons and heavy-holes. The variation in the intensity of the electron spin-flip scattering in tilted geometries reveals an angular dependence of the anisotropic electron-hole exchange interaction. Its probability is inversely proportional to the squared difference of the electron and hole g factors.

Chapter 4

Spin-Flip Raman Scattering in (In,Ga)As/GaAs Quantum Dots

Semiconductor quantum dots (QDs) have aroused remarkable interests in most diverse scientific fields, as they open new opportunities particularly in spintronics and quantum information technology [197, 198, 199]. A major possibility of implementing solid-state quantum information applications is offered by electron spins in ensembles of QDs [23]. However, different kinds of mechanisms compete against robust electron spin coherence, such as the hyperfine electron-nuclear interaction [200, 201, 202]. A further loss of coherence among the phases of the electron spins can result from spin-nonconserving coupling between ground and excited electron states [203]. Apart from the electron-nuclear interactions, the study of possible impacts of excited spins on ground state processes in semiconductor QDs is essential.

In the Section 4.2, the involvement of excited electron states in the electron spin-flip Raman scattering (SFERS) is studied in singly charged (In,Ga)As/GaAs QD ensembles. In strong magnetic fields a first-excited electron state with nonzero orbital angular momentum is effectively coupled to an electron ground state. An incident photon creates a ground-state exciton and additionally excites the resident electron under spin reversal to a first-excited state. The SFERS of the resident electron is observed, its spin is flipped via isotropic exchange interaction with the photogenerated electron. This resonantly induced electron-exciton interaction shows similarities to the combined exciton-cyclotron resonance that has been observed in quantum wells [204]. It depends on the interplay between the spatial and magnetic field confinement in the QDs. Strong shifts of the SFERS resonance profiles in dependence on the orientation as well as strength of the external magnetic field reveal the coupling of the ground and excited electron states. Numerical calculations of the angle-dependent Fock-Darwin states affirm the novel electron-SFERS process.

It is well known that the SFERS technique provides the immediate measurement of the g factor of a carrier and the analysis of carrier-carrier and carrier-phonon interactions. In the Section 4.3, it is shown that also the optically induced electron-nuclear hyperfine interaction in an ensemble of (In,Ga)As QDs can be studied by using two-color SFERS. The Raman shift of the electron-SFERS line serves as direct indicator of the Overhauser shift. Not only the study of nuclei effects in ensembles of QDs is rather limited, also the application of the SFERS technique itself to characterize the QD s-shell is missing so

far. Hitherto, only Puls et al. have presented a spectrum with an electron-SFRS line in CdSe quantum dots [137]. In the first Section of the Chapter, the basic properties of the electron-SFRS in three (In,Ga)As/GaAs QD samples are discussed. The intensity of the electron-SFRS strongly depends on the magnetic field orientation with respect to the QD growth axis. The magnetic field dependence of the Raman shift reveals the existence of electron spin-flip scattering in undoped and singly charged QDs. Both SFRS mechanisms require the magnetic field induced mixing of the electron states in tilted geometries as well as light-heavy-hole mixing. The Section 4.1 is concluded by the discussion of the electron g factor dispersion across the inhomogeneously broadened QD ensembles.

Three samples with self-assembled (In,Ga)As/GaAs QDs, fabricated by molecular beam epitaxy on (001)-oriented GaAs substrates, were probed by the resonant SFRS technique. The samples contained 20 layers of lens-shaped QDs with 60 nm separation between adjacent layers and a density of 10^{10} dots per cm^2 . A charging by about one electron per QD was provided by n-modulation doping with Si-dopants 20-nm-below each layer. After the growth the samples were annealed at different temperatures of 900°C (#1), 945°C (#2), and 980°C (#3) leading to different QD sizes and composition profiles. Each sample, stress-free attached to the rotatable lens-based Raman-holder (see Sec. 2.2), was exposed to magnetic fields B up to 10 T and a low temperature of $T = 6$ K. The QD ensembles were excited by a tunable CW Ti:Sapphire laser with a typical power density of 5 W/cm^2 . The laser spot diameter was approximately 0.5 mm. The scattered light was analyzed by the triple-spectrometer operating in the subtractive mode which was equipped with a liquid-nitrogen cooled CCD camera. The backscattered SFRS experiments were performed in the Faraday and Voigt geometries as well as in tilted geometries, where the magnetic field vector \mathbf{B} and QD growth axis \mathbf{z} enclose an angle $0^\circ < \theta < 90^\circ$.

4.1 Characterization of Electron Spin-Flip Raman Scattering

4.1.1 Symmetry-Dependent Scattering Mechanism

The exciton photoluminescence (PL) spectra of the studied (In,Ga)As/GaAs QD ensembles are shown in the Fig. 4-1 (a). The PL was excited at an energy of 1.54 eV exceeding the wetting-layer band gap. The power density was about 0.12 W/cm^2 . The PL peaks of each QD ensemble are attributed to s-shell excitons, and the high-energy shoulders belong to the p-shell excitons. Both PL contributions are marked by arrows in the Fig. 4-1 (a). The s-shell peak energies for the samples #1, #2, and #3 are 1.341, 1.396, and 1.439 eV, respectively. The QD PL of the samples, which were annealed at higher temperatures T_{an} , is shifted to higher energies. The blue-shifting of the PL is caused by the diffusion of gallium atoms from the barrier material into the QDs during the post-growth annealing thus increasing the band gap energy*. The annealing also results in a more homogeneous distribution of QD sizes indicated by a narrowing of the PL line

*The band gap energy of the $\text{In}_x\text{Ga}_{1-x}\text{As}$ QDs is given by $E_g^\Gamma = 0.417x + 1.519(1-x) - 0.477x(1-x)$ [205]. By using the s-shell peak energy as approximation of the band gap energy, the average indium concentration x in the three samples #1, #2, and #3 is estimated to 0.12, 0.08, and 0.05, respectively.

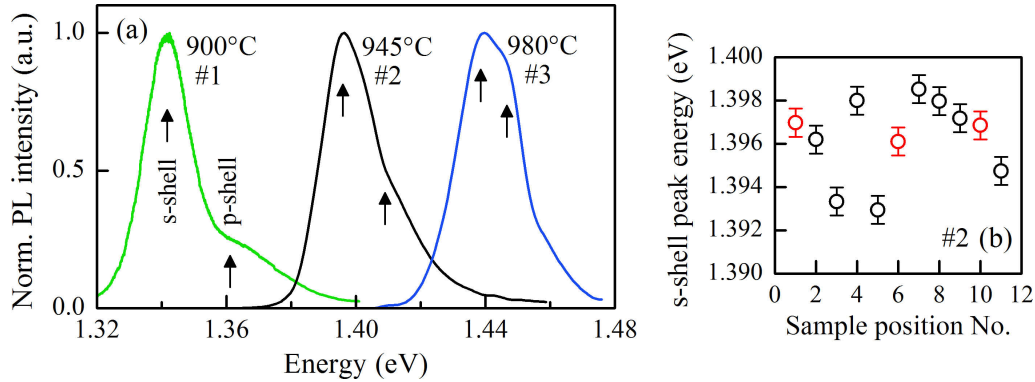


Figure 4-1: (a) PL spectra of the studied (In,Ga)As/GaAs QD samples measured at $T = 6$ K and $B = 0$ T. The arrows mark the s- and p-shell peaks. (b) s-shell peak energy in dependence on the illumination of different sample-#2-positions. The red-colored circles were measured for probing the same central area of the sample, the laser spot diameter did not exceed 0.5 mm.

width. Moreover, the increase in the annealing temperature leads to an increase in the effective QD diameter. It corresponds to a shallowing of the QD confinement potential and, in turn, to a reduction in the lateral confinement. The lateral confinement energy $\hbar\omega_0$ is evaluated from the transition spacing, i.e., the energy difference between the s- and p-shell peaks. The energies $\hbar\omega_0$ for the samples #1, #2, and #3 are given by 19.8, 13.1, and 9.8 meV, respectively.

As illustrated in the Fig. 4-1 (b) for sample #2, the probing of different sample areas causes shifts in the s-shell peak energy of about ± 2 meV. The variation in the peak energy across the sample is due to the spatial inhomogeneity of the QD size distributions and composition profiles. Hence, the experiments require a monitoring of the laser spot position on the sample surface. The adjustment of the sample and laser spot positions by checking the intermediate image of the sample surface, see description in Sec. 2.2, reduces the PL energy variation by one order of magnitude to ± 0.2 meV[†]. The reproducibility of the probing of the same sample position is depicted by the red-colored circles in the Fig. 4-1 (b). Note, the data presented in the following were acquired for definite sample positions.

In the Fig. 4-2 SFRS Stokes-spectra of the samples #2 and #3 are shown for different geometries. In the Faraday geometry ($\theta = 0^\circ$) a SFRS process is absent in both QD samples, only a PL background is observed as it can be seen in the Figs. 4-2 (a) and 4-2 (b). By tilting the magnetic field direction with respect to the QD growth axis a SFRS line becomes apparent. In the case of sample #2, see Fig. 4-2 (c), it is shifted by $|\Delta E_{\text{sf}}| = 0.34$ meV from the laser line. The Raman shift corresponds to a g factor of $|g| = |\Delta E_{\text{sf}}|/(\mu_B B) = 0.58$, where μ_B is the Bohr magneton. For the high-temperature annealed sample #3 the g factor is estimated to $|g| = 0.53$. The g factors are attributed to the Zeeman splitting of the electron states with opposite spin momentum projections, since the heavy-hole g factor is smaller than the electron one and strongly anisotropic

[†]The PL energy variation of ± 0.2 meV approximately corresponds to the average error derived from the fittings of the different PL lines.

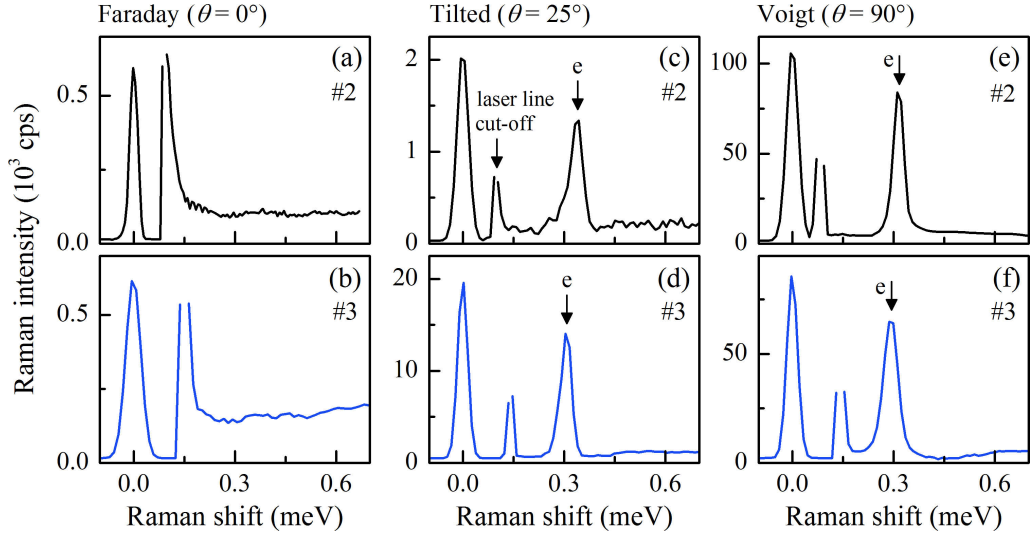


Figure 4-2: Electron-SFRS Stokes-spectra of the samples #2 and #3 measured in different geometries at $B = 10$ T and $T = 6$ K, the excitation energies were in resonance with the s-shell peaks. In the Faraday geometry SFRS is absent in both samples, as evidenced in (a) and (b). The intensities of the e-SFRS lines (marked by arrows) in the tilted geometry with $\theta = 25^\circ$, see (c) and (d), are significantly smaller than that in the Voigt geometry shown in (e) and (f). The Raman shift decreases with increasing tilting angle. The laser line cut-off is exemplarily indicated in panel (c).

[206]. A further tilting into the Voigt geometry, shown in the panels (e) and (f), leads to a reduction in the Raman shift. Hence, the electron g factor is slightly anisotropic ($|g_e^\parallel| > |g_e^\perp|$). Moreover, the intensities of the SFRS lines increase strongly. For sample #2 the intensity is enhanced by a factor of 50 from the tilted geometry with $\theta = 25^\circ$ to the Voigt geometry. The SFRS intensity for sample #3 already increases by varying the angle from 0° to 25° ; it amounts to about 1.3×10^4 counts per second at $\theta = 25^\circ$, and exceeds the e-SFRS intensity for sample #2 by one order of magnitude. In the Voigt geometry the SFRS lines for both samples have similar intensities. On the contrary, the SFRS line widths are independent of the geometry; they are mainly limited by the laser line width.

Besides the angular dependence of the energy shift and intensity of the electron-SFRS line, its polarization properties provide information on the scattering mechanism. The SFRS spectra of sample #2 in the co-polarized (σ^+, σ^+) and (σ^-, σ^-) as well as cross-polarized (σ^+, σ^-) and (σ^-, σ^+) configurations are depicted in the Fig. 4-3 (a). They were measured at $B = 10$ T, $T = 6$ K, and a tilting angle $\theta = 15^\circ$. The electron-SFRS is dominant for the (σ^+, σ^-) polarization in the Stokes regime, while in the anti-Stokes regime it has the highest intensity in the (σ^-, σ^+) configuration. The co-polarized spectra demonstrate weak e-SFRS lines in both regimes. How can the dominant SFRS line in the (σ^+, σ^-) configuration be described? The creation and annihilation of an exciton is governed by the electric dipole selection rules, as discussed in the Sections 1.2 and 3.4. In the Faraday geometry and for a high crystal symmetry of D_{2d} , the bright excitons with total angular momentum projections $j_z = \pm 1$ are excited by σ^\pm polarized light. Accordingly, an incident σ^+ polarized photon creates an exciton in the

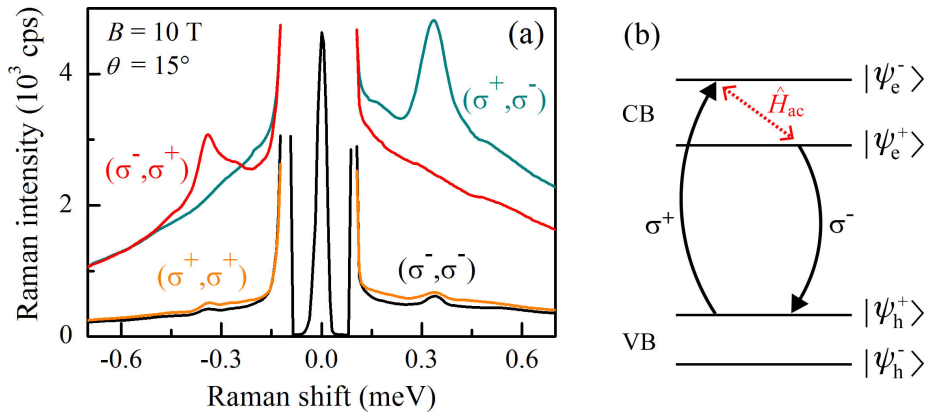


Figure 4-3: (a) Circularly cross- and co-polarized SFRS spectra of sample #2, excited at $E_R = 1.396$ eV. The most intensive e-SFRS lines are observed in the crossed polarized configurations; the (σ^+, σ^-) configuration is dominant in the Stokes regime. (b) Single-particle scheme of the electron spin-flip mechanism for σ^+ excitation. In undoped dots the electron-SFRS is based on acoustic phonon scattering marked by the Hamiltonian \hat{H}_{ac} (see Subsec. 3.4.1). The σ^- polarized scattering light is governed by the light-hole admixture to the hole wave function. In a negative singlet trion, formed in a singly charged dot, the two electrons occupy the levels $|\psi_e^+\rangle$ and $|\psi_e^-\rangle$.

state $|+1\rangle$ with a spin-down electron $s_{z,e} = -1/2$ and a spin-up heavy-hole $j_{z,hh} = 3/2$. For an e-SFRS only the electron flips its spin from $-1/2$ to $+1/2$, and thus the exciton $|+2\rangle = |1/2, 3/2\rangle$ becomes dark. However, the scattered light is mainly σ^- polarized, hence, the experimentally observed electron-SFRS cannot be explained on the basis of such a high symmetry.

The spin-flip Raman scattering of the electron depends on the tilting angle θ evidenced by both the Raman shift as well as intensity. While the dependence of the Raman shift on the angle indicates a spatial anisotropy of the electron g factor, the angular dependent SFRS intensity demonstrates that a reduction in the QD symmetry is necessary to observe the e-SFRS. As illustrated by the SFRS spectra in the Fig. 4-3 (a) which were measured at $\theta = 15^\circ$, the e-SFRS appears in oblique orientations of the magnetic field. Here, its nonzero in-plane component leads to a mixing of confined states thus enabling a lifting of the angular momentum conservation. An increase in the tilting angle which corresponds to an enhanced state mixing is accompanied by an increase in the SFRS intensity.

The electron-SFRS can be related to two different processes: (i) in the negative trion complex the e-SFRS is simply established via a two-stage process consisting of photon absorption and emission, or (ii) in the case of undoped QDs the spin of the electron in the neutral photo-exciton is scattered via an acoustic phonon. Both cases will principally be allowed in the Faraday geometry if the light-hole (lh) and heavy-hole (hh) states are mixed. In absence of lh-hh mixing the case (i) is not observable, while the case (ii) can be realized by anisotropic flip-stop-like exchange interaction between the electron and heavy-hole. The different transverse g factors of the electron and heavy-hole reduce the efficiency of that electron-hole exchange interaction, as discussed in the Section 3.4. Moreover, the carrier wave functions are rather spatially isotropic thus minimizing the probability of the anisotropic flip-stop-like exchange interaction. However, in tilted geometries the

magnetic field induced mixing of the electron spin states relative to the growth axis lifts the selection rules for both e-SFRS processes. The light-hole states are mixed with the heavy-hole subband due to, e.g., strain or asymmetries in the QD shape. It is exhibited by a nonzero transverse heavy-hole g factor; according to Ref. [206] it takes the value $|g_{\text{hh}}^{\perp}| = 0.15 \pm 0.05$. Therefore, the magnetic field couples to the nonzero in-plane magnetic momentum of both the electron as well as the heavy-hole. The splitting of the electron and heavy-hole states in the magnetic field $\mathbf{B} = (B_x, 0, B_z)^T$ can be described by the following Hamiltonian which includes linear Zeeman terms and cubic terms reflecting the symmetry of the Kohn-Luttinger Hamiltonian [207, 208]:

$$\begin{aligned} \hat{H}_B &= \frac{1}{2}\mu_B \left(g_e^{\parallel} \sigma_z B_z + g_e^{\perp} \sigma_x B_x \right) + \\ &+ g_0 \mu_B \left[\kappa_{\text{KL}} (J_x B_x + J_z B_z) + q_1 (J_x^3 B_x + J_z^3 B_z) + q_2 (J_y^3 B_x) \right]. \end{aligned} \quad (4.1)$$

Here, g_0 is the free electron g factor, $\sigma_{x,z}$ are the Pauli matrices, \mathbf{J} is the hole angular momentum operator, and κ_{KL} and $q_{1,2}$ are Kohn-Luttinger parameters [138]. The spatially anisotropic J^3 -term with the coefficient q_2 , which is present in low symmetries like C_{2v} , takes only into account the coupling of in-plane components. Both the Zeeman terms and the relatively weak cubic terms exhibit that an oblique magnetic field enhances the superposition of the electron spin states and lh-hh mixing.

The magnetic field $\mathbf{B} = (B_x, 0, B_z)^T = B(\sin \theta, 0, \cos \theta)^T$ introduces a mixing of the pure electron states $|s_{z,e} = \pm 1/2\rangle$. The mixed wave functions can be expressed as $|\Psi_e^{\pm}\rangle = \cos(\theta/2)|\pm 1/2\rangle \pm \sin(\theta/2)|\mp 1/2\rangle$, see also Eq. (3.8). In accordance with Eq. (3.5), the hole wave functions can be written in the form $|\Psi_h^{\pm}\rangle = \alpha(\theta)|\pm 3/2\rangle - \beta(\theta)|\mp 1/2\rangle$. Here, $\alpha(\theta)$ and $\beta(\theta)$ account for the angle-dependent coupling with the magnetic field and are functions of the coefficients κ_{KL} , q_1 , and q_2 . By means of these definitions the second- and third-order SFRS processes of the electron can be discussed. The electron spin-flip Stokes scattering is schematically illustrated within the single-particle picture in Fig. 4-3 (b). The processes are initiated by a σ^+ polarized photon. It creates (i) a negative trion in the state $|\Psi_e^-, \Psi_e^+, \Psi_h^+\rangle$, see also Section 3.4, or (ii) a $|\Psi_e^-, \Psi_h^+\rangle$ exciton in an undoped QD. In the case (i), an intermediate scattering state is not necessary, since both electrons form a singlet state and become indistinguishable. Accordingly, the trion annihilates under emission of a σ^- polarized photon, whereby, an electron in the state $|\Psi_e^-\rangle$ is left[‡]. In the case (ii), the electron interacts with an acoustic phonon thus changing its spin state from $|\Psi_e^-\rangle$ to $|\Psi_e^+\rangle$. The annihilation of the $|\Psi_e^+, \Psi_h^+\rangle$ exciton (and also of the singlet trion) is expected to result in elliptically polarized light due to the superposition of both electron states and the admixture of the $j_{z,\text{lh}} = -1/2$ light-hole to the $j_{z,\text{hh}} = 3/2$ heavy-hole. The experimental SFRS spectra demonstrate a strong σ^- polarization of the scattered light. Therefore, the outgoing resonance of the SFRS is defined by the light-hole part of the mixed hole wave function. One can also argue that the circular polarization of the scattered photon follows the equilibrium spin polarization of the resident electron. Accordingly, the final exciton recombination is not characterized by the typical probability (ratio of 1:3) of the lh- and hh-transitions. Nevertheless, a microscopic theory is required to give a unique picture of the SFRS in quantum dots. Note, the weak SFRS lines in the co-polarized Stokes and anti-Stokes spectra, shown in

[‡]Note, in the traditional Raman scattering, see Subsection 1.2.1 for details, an isotropic exchange interaction between both electrons would act as intermediate scattering process.

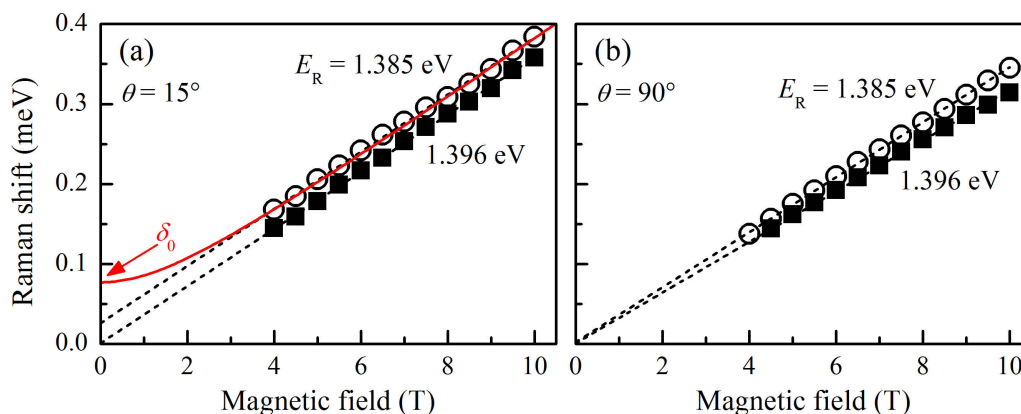


Figure 4-4: Raman shift of the e-SFRS line in dependence on the magnetic field for sample #2 in tilted geometry with $\theta = 15^\circ$ (a) and Voigt geometry (b). For the low-energy excitation at 1.385 eV and $\theta = 15^\circ$ the Raman shift tends to a zero-field offset. A fitting (red-colored curve) based on Eq. (4.2) shows that the offset corresponds to the exciton exchange energy δ_0 . The respective e-SFRS is performed in neutral excitons in undoped dots. Linear extrapolations (dashed lines) tending to zero at zero magnetic field indicate e-SFRS in negative trions. The error in the Raman shift does not exceed the symbol size.

the Fig. 4-3 (a), could stem from an anisotropic exchange interaction provided by a slight spatial asymmetry of the wave functions of the paired electrons also with regard to the hole wave function. However, these SFRS lines rather originate from a weakly elliptical polarization of the incident light[§].

4.1.2 Magnetic Field Dependence of the Raman Shift

In the following the observation of the electron spin-flip scattering in both neutral and negatively charged excitons will be discussed. In the Figs. 4-4 (a) and (b) the Raman shift of the electron-SFRS line is shown as a function of the magnetic field strength for a tilted geometry with $\theta = 15^\circ$ and the Voigt geometry. According to the electron Zeeman splitting, the Raman shift ΔE_{sf} linearly follows the magnetic field from $B = 10$ T down to 4 T. Below 4 T the stray-light suppression limit of the detection system is reached. Therefore, the experimental data are linearly extrapolated to the zero field, as demonstrated by the dashed lines. In the Voigt geometry the Raman shift tends to zero independent of the excitation energy. On the contrary, in the tilted geometry the extrapolations for both excitation energies differ from each other; for $E_R = 1.385$ eV the Raman shift deviates from zero at zero magnetic field. In exact and tilted Faraday geometries the exciton exchange energy δ_0 exceeds the Zeeman energy at low magnetic fields. The exciton exchange energy is defined as the splitting between the optically bright and dark exciton states in the neutral exciton [209, 210]. Accordingly, the Raman

[§]The presented results were obtained with the lens-based Raman-holder where a small silver mirror directs the laser beam onto the sample, compare Fig. 2-4. It has been found out that the circularly polarized incident light becomes slightly elliptical (about 5%) after its reflection at the mirror surface.

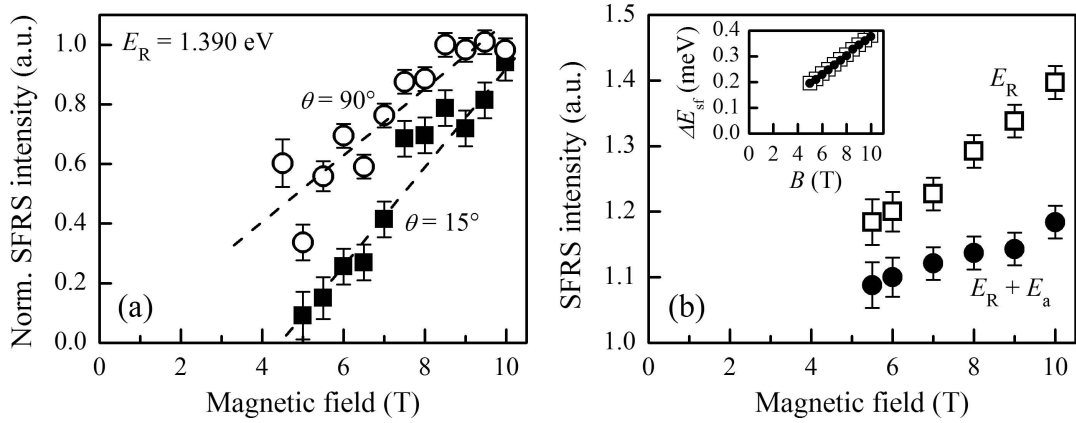


Figure 4-5: (a) Magnetic field dependence of the normalized e-SFRS intensity for $\theta = 15^\circ$ and 90° at $T = 6$ K, sample #2 has been excited at 1.390 eV. The dashed lines are guides for the eye. (b) SFRS intensity in relation to the PL background for resonant s-shell excitation only (open squares) and resonant excitation combined with above-wetting-layer illumination (full circles). The additional illumination with photon energy $E_a = 2.54$ eV and power density $P_a = 12$ W/cm² reduces the relative intensity of the e-SFRS. As illustrated in the inset, the Raman shift ΔE_{sf} and its magnetic field dependence are not affected by E_a .

shift is described by δ_0 and the Zeeman energy:

$$\Delta E_{sf} = \sqrt{\delta_0^2 + (\mu_B g_e B)^2}. \quad (4.2)$$

The red-colored solid line in the Fig. 4-4 (a) displays the fitting of the experimental data using $|g_e| = 0.64$. It provides $\delta_0 = (80 \pm 5)$ μ eV which is in agreement with values reported in previous publications [206, 209]. This zero-field offset identifies it as electron-SFRS in undoped QDs. On the contrary, the magnetic field dependent Raman shift for the excitation energy of 1.396 eV tends to zero. It determines electron-SFRS in negative trions. Since in the negative trion the total spin of the electrons is zero in the ground state [211], the exciton exchange interaction and, correspondingly, the Raman-shift offset vanish. Hence, in the intentionally n-doped (In,Ga)As/GaAs QDs the electron-SFRS takes place in neutral and negatively charged excitons. Note, one could conjecture that lower resonant excitation energies excite neutral excitons, while at higher energies the singly charged QDs are probed. It contradicts the typical assignment for QDs where the charging of a QD with an electron leads to a red-shift of the exciton transition energy due to a negative Coulomb-shift term [212]. Since such significantly shifted SFRS lines, as demonstrated in the Fig. 4-4 (a), have been observed rarely, a systematic dependence of the charge state of the QDs, i.e., the e-SFRS mechanism, on the excitation energy cannot be evaluated. In most cases the magnetic field dependence of the Raman shift tends to zero, hence, negatively charged QDs are predominant.

The dependence of the SFRS intensity on the magnetic field is depicted in the Fig. 4-5 (a) for resonant excitation at 1.390 eV of the sample #2. For the tilting angles $\theta = 15^\circ$ and 90° the intensity I_{sf} of the e-SFRS line is approximately a linear function of B , as marked by the dashed lines. In the tilted geometry with $\theta = 15^\circ$ the magnetic field dependent increase of I_{sf} is more pronounced than in the Voigt geometry. The magnetic

field dependence of the SFRS intensity depends on several parameters like the competition between the Coulomb interaction and correlation effects which are, in turn, scaled by the QD and magnetic confinement. Nevertheless, the intensity enhancement can be explained by the increase in the in-plane localization strength of the carriers involved in the scattering process. At higher magnetic fields the magnetic confinement exceeding the QD confinement potential contributes to the spatial shrinkage of the trion wave function probability. Correspondingly, the carrier wave functions overlap more strongly, the oscillator strength increases and the electron-hole recombination becomes more probable. The enhanced localization could also lead to a stronger isotropic exchange interaction. Since the scattering amplitude would be proportional to the square of the exchange constant, the electron spin-flip scattering could become more efficient.

The intensity of the electron-SFRS line is influenced by the application of above-wetting-layer illumination ($E_a = 2.54$ eV) in addition to the resonant excitation of the QDs. As shown in the Fig. 4-5 (b), the additional illumination with a power density of 12 W/cm^2 reduces the SFRS line intensity with respect to the PL background, see the full circles. Under resonant excitation only, illustrated by the open squares, the ratio between the SFRS and PL intensities is larger. Both relations show comparable dependencies on the magnetic field strength. However, the absolute intensity of the SFRS line under both illuminations is two times larger over the whole magnetic field range (not shown here). By comparison, the additional illumination does not affect the Raman shift, as it is demonstrated in the inset of Fig. 4-5 (b). On the one hand, the above-wetting-layer illumination heats the sample. Due to the high sensitivity of the Raman scattering efficiency to the lattice temperature, the SFRS intensity is reduced more strongly than the QD PL. On the other hand, the additional illumination can affect the resident carriers by either turning singly charged to empty dots, or creating doubly charged dots thus preventing the electron-SFRS. Consequently, the PL background increases at the expense of the SFRS intensity. By comparison, the increase in the absolute SFRS intensity can be caused by the optical charging of undoped dots with a single electron which forms a trion complex with the resonantly excited electron-hole pair.

4.1.3 Electron g Factor Dispersion

The dispersion of the electron g factor across the QD ensembles of the three samples is depicted in the Fig. 4-6 for tilted and Voigt geometry at a magnetic field of 8 T. According to Ref. [206] the sign of the electron g factor has been chosen negative. Three observations can be drawn from the experimental data: (i) the slopes of the energy dependencies of the electron g factor are similar for both geometries. The gradient of $g_e(E)$ is rather independent of the tilting angle. (ii) The angular dependent difference between the absolute values indicates an anisotropy of the g factor tensor. (iii) The g factor dispersions measured for the different samples can be linked together continuously. The energy-dependent evolution of g_e is mainly related to the change in the effective band gap energy caused by the dispersion in the vertical and lateral QD confinement [213]. It can be principally described by the Roth-Lax-Zwerdling equation $g_e = g_0 \{1 - E_p \Delta_{so} / [3E_g(E_g + \Delta_{so})]\}$, see Subsec. 1.1.3 for details. Here, E_g is the fundamental gap renormalized by the spatial confinement which is equal to the excitation energy for resonantly probing QDs with different sizes. For the samples #1 and #2 the equation is plotted as red-colored dashed line in the Fig. 4-6. The split-off energy Δ_{so} and Kane

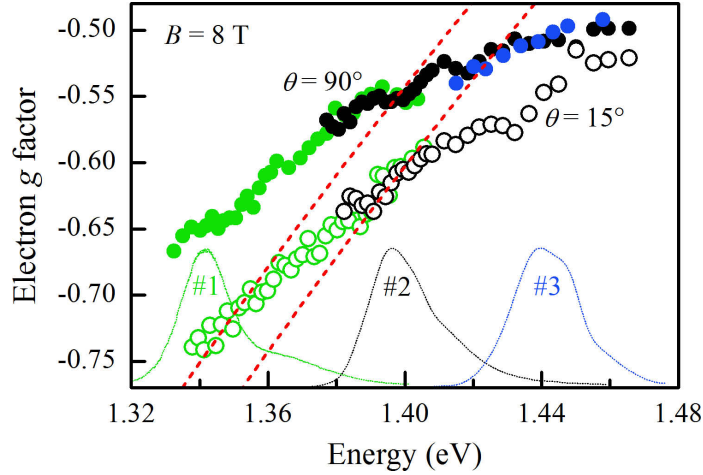


Figure 4-6: Dispersions of the electron g factor across the QD ensembles of the studied samples at $B = 8$ T and $T = 6$ K for tilted and Voigt geometry. The PL of the respective QD sample is shown for comparison. The plots of the Roth-Lax-Zwerdling equation (dashed lines) are based on the parameter sets ($\Delta_{so} = 0.345$ eV, $E_p = 27.0$ eV) for sample #1 and ($\Delta_{so} = 0.341$ eV, $E_p = 27.9$ eV) for sample #2. Each plot deviates from the experimental data at high energies.

parameter E_p have been estimated with regard to the different In concentrations in the samples. At low energies belonging to the s-shell peak the Roth-Lax-Zwerdling equation models the experimentally obtained g factors well, while in the high-energy range it does not describe the flattening of the g factor dispersion. The flattening can be attributed to the probing of excited QD states which resemble the wetting-layer states. In this case, only shallow QDs in the ensemble are excited and g_e reaches an average value being similar to the g factor of the wetting-layer electrons. Another possible explanation of the g factor flattening is related to hot trions which can induce the spin-flip of the resident electrons in their lowest state. Hence, a constant averaged value of the resident electron g factor can be expected. Since hot trions are generated in all samples for a high-energy excitation, the flattening should be observed for all samples. However, the electron g factor dispersion of sample #1 does not show a pronounced flattening.

In conclusion, the Roth-Lax-Zwerdling equation describes the g factor of the ground-state electron in the (In,Ga)As/GaAs QD samples by using the bulk parameters Δ_{so} and E_p . In order to characterize the g factors of excited electrons the Roth-Lax-Zwerdling equation must be extended. The above equation does not consider, e.g., the contributions Δg from remote bands, see Subsection 1.1.3. Moreover, band-mixing effects on the g factor are not taken into account. For instance, the flattening of the g factor dispersion can be simulated by the Roth-Lax-Zwerdling equation with higher polynomial order or with a smaller ratio between E_p and Δ_{so} .

4.2 Coupling of Ground and Excited Electron States

Studies in the low-dimensional semiconductor physics usually focus on phenomena related to the ground states of the confined carriers. Nevertheless, contributions from

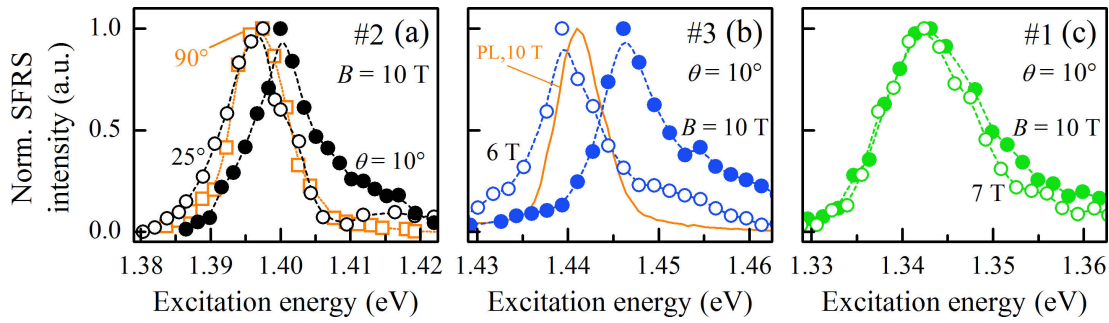


Figure 4-7: Normalized electron-SFRS resonance profiles measured at different magnetic fields and in various geometries at $T = 6$ K for the (In,Ga)As/GaAs QD samples. (a) Sample #2: angular dependent SFRS intensity at $B = 10$ T, at the small tilting angle of 10° the resonance profile is shifted to higher energies. (b) Sample #3: magnetic field dependent SFRS intensity for $\theta = 10^\circ$, the maximum of the profile at $B = 10$ T strongly deviates from the s-shell PL peak. (c) Sample #1: due to the strong lateral QD confinement compared to the magnetic confinement the resonance profiles do not significantly shift in their spectral positions. The absolute errors of the SFRS intensity and excitation energy do not exceed the symbol size.

excited states to ground state processes can raise major drawbacks for the carrier spin dynamics. In the following it will be shown that in the singly charged (In,Ga)As/GaAs QDs an excited negative trion acts as intermediate scattering state for the spin-flip of the resident electron. This optical resonance excitation in QDs, which shows similarities to the exciton-cyclotron resonance in quantum wells, is based on the direct exchange interaction of a pair of electrons occupying the ground and excited state, respectively. It requires the regime of strong magnetic confinement exceeding the lateral QD confinement. The intensity of the corresponding spin-flip scattering is highly sensitive to the orientation and strength of the magnetic field.

The SFRS resonance profiles for the studied samples are shown in the Fig. 4-7. A resonance profile describes the intensity of the electron-SFRS line as a function of the excitation energy across the inhomogeneously broadened QD ensemble. As illustrated in the Fig. 4-7 (a), the e-SFRS resonance profiles for the sample #2 depend on the tilting angle θ at $B = 10$ T. In the Voigt and tilted geometry with $\theta = 25^\circ$ the profiles become maximal at the energy $E_{\text{peak}}^{\text{sf}} = (1.3969 \pm 0.0001)$ eV. At a smaller angle of 10° the profile is blue-shifted to the energy of (1.4004 ± 0.0002) eV. Not only the orientation of the magnetic field with respect to the QD growth axis, but also the magnetic field strength influences the spectral distribution of the SFRS intensity. In the panel (b), the resonance profiles measured at $B = 6$ T and 10 T for a fixed angle $\theta = 10^\circ$ are compared to the PL acquired at 10 T. The increase in B leads to a strong shift of the resonance profile; the maxima of both profiles differ in energy by (6.5 ± 0.2) meV. Moreover, the peak of the resonance profile at 10 T deviates from the s-shell PL peak; the SFRS intensity has its maximum at the high-energy edge of the PL. These results belong to the sample #3 which was annealed at the high temperature of 980°C . The resonance profiles of the sample #1 measured at $B = 7$ T and 10 T for $\theta = 10^\circ$ are illustrated in the Fig. 4-7 (c). The difference $E_{\text{peak}}^{\text{sf}}(10 \text{ T}) - E_{\text{peak}}^{\text{sf}}(7 \text{ T})$ in their peak energies is given by (0.3 ± 0.4) meV[¶];

[¶]The error of the peak energy difference is rather large due to the broad resonance profiles whose

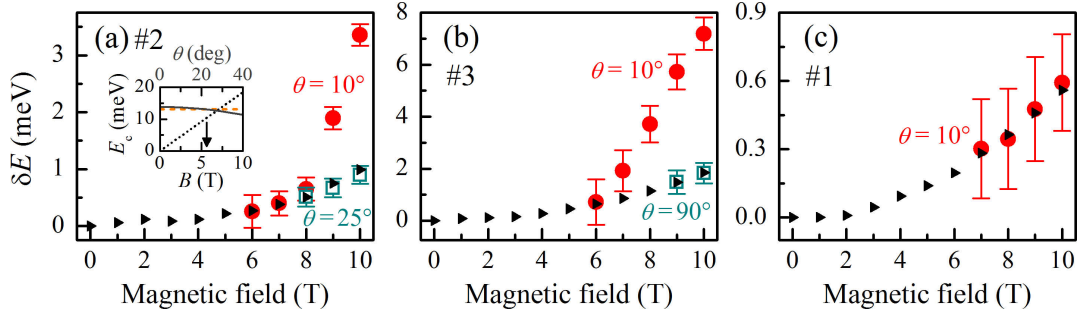


Figure 4-8: Magnetic field dependent differences δE in the peak positions of the SFRS resonance profiles (full circles and open squares) and of the s-shell PL (solid triangles) with respect to the zero-field energy value of the PL. (a) Sample #2: the shifts of the resonance profiles refer to $\theta = 10^\circ$ and 25° , while the PL was measured at 10° . In the inset the numerical estimations of E_c as a function of θ for $B = 7.1$ T (full curve) and of B for $\theta = 10^\circ$ (dotted curve) are shown, the constant lateral confinement energy $\hbar\omega_0$ is also depicted as orange-colored dashed line. In (b) and (c) the magnetic field dependencies of δE are demonstrated for the samples #3 and #1.

the resonance profiles are not considerably changed by the magnetic field strength. In contrast to the sample #3, the sample #1 was annealed at a relatively low temperature of 900°C , thus the QDs of sample #1 have much smaller sizes.

The e-SFRS resonance profiles depend on three parameters: the tilting angle θ , magnetic field strength B , and QD size. In order to specify these dependencies the peak energies of the resonance profiles and s-shell PL are depicted as a function of B and θ in the Fig. 4-8 for the studied samples. The profile peak energy $E_{\text{peak}}^{\text{sf}}$ and the s-shell PL peak energy E_{PL} are subtracted by the zero-field s-shell PL energy $E_{\text{PL}}(B = 0 \text{ T})$, these differences are denoted by δE . As shown for the sample #2 in Fig. 4-8 (a), at magnetic fields $B < 8$ T and in tilted geometry with $\theta = 10^\circ$ the energy difference $\delta E_{\text{peak}}^{\text{sf}}$, marked by the solid circles, corresponds to δE_{PL} (solid triangles). The resonance profile maximum follows the diamagnetic shift of the PL. At larger fields $B \geq 8$ T the SFRS intensity reaches its maximum at higher energies deviating from the PL peak energy by about 1.2 meV/T . On the contrary, the energies $E_{\text{peak}}^{\text{sf}}$ of the profiles measured at the angles of 25° , shown by the open squares, and 90° cannot be distinguished from the PL energy. Such a coincidence is also observed for the sample #3, as illustrated in the panel (b). Furthermore, at $\theta = 10^\circ$ the magnetic field dependent shift of the SFRS intensity maximum is more significant and differs from the PL energy at lower B -fields already. In contrast to the sample-#3-QDs with weak lateral confinement, the resonant excitation of small-sized QDs with large lateral confinement energies, provided by the sample #1, yields a coincidence of the SFRS resonance profile with the s-shell PL in the studied magnetic field range, see Fig. 4-8 (c). Hence, the interplay between the magnetic and lateral QD confinement influences the strength and initial occurrence of the SFRS resonance-profile deviation.

The shifts of the SFRS resonance profiles occur in the regime of strong magnetic field confinement where the magnetic confinement energy E_c exceeds the lateral confinement

widths are approximately two times larger than that of the samples #2 and #3.

energy $\hbar\omega_0$. This condition is assigned to small angles θ as far as the parabolic approximation of the lateral confinement is applicable. The magnetic confinement energy is described by

$$E_c(\theta, B) = \frac{\hbar e B}{m_e^*} (\cos \theta)^\beta, \quad (4.3)$$

where e is the elementary charge, and m_e^* is the in-plane effective mass of the electron. The impact of θ on the high-field resonance profile deviations can be well estimated by a $(\cos \theta)^\beta$ -dependence with $0.7 < \beta < 1$. A numerical estimation using the spatially isotropic value $m_e^* = 0.062m_0$ and $\beta = 0.8$ for sample #2 shows that the magnetic confinement dominates against the lateral QD confinement for angles smaller than approximately 20° at magnetic fields exceeding 7 T. The corresponding curves are illustrated in the inset of Fig. 4-8 (a). The estimated values are compatible with the experimentally detected SFRS resonance-profile shifts of sample #2.

How can the SFRS mechanism be explained? The SFRS of an electron in a negative singlet trion is always present due to the large dispersion of QDs with different transition energies. In the strong magnetic confinement regime an additional SFRS mechanism based on the ground-excited-state coupling becomes important. Since the magnetic confinement energy E_c exceeds $\hbar\omega_0$,^{||} the Fock-Darwin (FD) spectrum, see e.g. Eq. (1.16), becomes similar to the Landau level spectrum. Hence, it can be assumed that the resident electron conducts a cyclotron motion in the xy -plane of the QD perpendicular to \mathbf{B} . The cyclotron motion can resonantly absorb energy which coincides with E_c . The SFRS of the resident electron is performed via three stages with the involvement of the first-excited electron FD states having a nonzero orbital angular momentum ($l = -1$). The Stokes process for the (σ^+, σ^-) polarization is schematically shown in Fig. 4-9 (a) within the single-particle picture. In the following the three stages are described:

- (1) The energy of the incident photon exceeds the s-shell transition energy and is proposed to be in resonance with the excited FD state with the radial $n = 0$ and angular $l = -1$ momentum numbers. This state is characterized by $|\tilde{\Psi}_e^-\rangle = (\cos(\theta/2)|-1/2\rangle - \sin(\theta/2)|+1/2\rangle)|n = 0, l = -1\rangle$. The photon creates a $|\Psi_e^+, \Psi_h^+\rangle$ electron-hole pair, and simultaneously the resident electron is excited from $|\Psi_e^+\rangle$ to the state $|\tilde{\Psi}_e^-\rangle$. Its orbital angular momentum is reduced by -1 and its spin state is also changed. Note, in the tilted geometry the conservation of the angular momenta is lifted. In the anti-Stokes process the spin state of the resident electron is conserved. It is also possible within the coherent Raman process that the resident electron is excited into a virtual state whose energy differs from the real FD states with $l = -1$, while their spin state properties are equal. Therefore, the condition of the incident photon energy to be in (exact) resonance with one of the excited FD states can be relaxed.
- (2) This excited negative trion consists of electrons with s-type and p-type wave functions, compare the corresponding wave function probability densities in Subsection 1.1.2. Due to the orbital contribution the trion complex is not fully spherical symmetric, and one can differentiate between both electrons. Thus, in the excited negative trion the spin-flip scattering between the photogenerated electron (e) and

^{||}Correspondingly, the magnetic length which is scaled by $1/\sqrt{B}$ becomes smaller than the QD diameter.

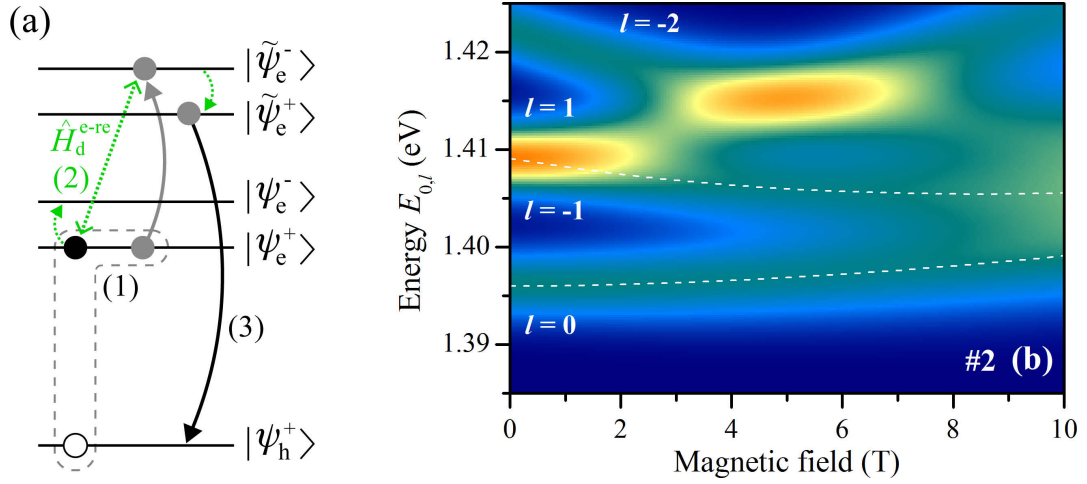


Figure 4-9: (a) Three-stage mechanism of the electron-SFRS in the regime of strong magnetic field confinement for a slightly tilted geometry. The incident photon excites an electron-hole pair (solid and open circles) and simultaneously the resident electron (gray-colored circle) to the mainly-spin-down Fock-Darwin state with $n = 0$ and $l = -1$. Thus, an excited negative trion complex is formed. The spin-flip scattering is performed via isotropic exchange interaction (green colored) between the ground- and excited-state electrons. (b) Calculated electron Fock-Darwin states $E_{0,l}$ for $\theta = 10^\circ$ and sample #2. Here, $g_e^\parallel \approx -0.60$ and $g_e^\perp = -0.55$ were used as longitudinal and transverse g factors. The Gaussian distributed density of Raman-active electron states defines the color of the image plot: blue indicates the minimum and orange the maximum density. For $B > 7$ T the confinement by the external magnetic field exceeds the lateral QD confinement giving rise to a Landau orbital formation.

resident electron (re) is performed via isotropic exchange interaction. In analogy to Eq. (3.9), the change in their spin states can be described by the Heisenberg-like Hamiltonian $\hat{H}_d^{e-re} = J_{e-re} \sigma_e \sigma_{re}$ with their Pauli matrices σ_e and σ_{re} . The exchange interaction does not change the orbital angular momentum. After the direct exchange the resident electron is in the state $|\tilde{\psi}_e^+\rangle$, and the $|\tilde{\psi}_e^-\rangle$ state is occupied by the photo-electron. As the symmetry of the excited trion complex is reduced by the spatially different s- and p-type wave functions of the photocreated and resident electrons, the e-re exchange interaction is also slightly anisotropic. Its contribution can be effectively estimated by a reduced isotropic coupling constant $J'_{e-re} < J_{e-re}$. It also leads to a weak elliptical polarization of the scattered light which can account for SFRS lines in the co-polarized configurations. However, the anisotropic contribution to an e-SFRS in Faraday geometry is insignificant due to a negligible degree of mixing between the conduction band states.

- (3) Finally, the electron-hole pair formed by the $|\Psi_h^+\rangle = \alpha(\theta)|3/2\rangle - \beta(\theta)|-1/2\rangle$ -photo-hole and the resident electron in the $|\tilde{\psi}_e^+\rangle = (\cos(\theta/2)|1/2\rangle + \sin(\theta/2)|-1/2\rangle)|0, -1\rangle$ state annihilates. The difference between the incident and scattered photon energies is equal to the Zeeman energy $|g_e| \mu_B B$. Hereby, the electron g factor is determined by the Zeeman splitting of both first-excited electron FD states. Due to the contributions from the $j_{lh} = -1/2$ light-hole and $s_e = -1/2$ electron the scattered light is mainly σ^- polarized, as in the case of the e-SFRS in the singlet trion.

The numerically evaluated electron FD spectrum in the limit of slightly tilted geometries ($\theta < 20^\circ$) underlines the high probability of ground-excited-state coupling at elevated magnetic field strengths. According to the Subsection 1.1.2, the electron FD states are written in the form $E_{n,l}(\theta) = E_0 + (2n + |l| + 1)\hbar\Omega + \frac{1}{2}l\hbar\omega_c \pm \frac{1}{2}g_e\mu_B B$ with $\Omega = \sqrt{(\omega_0^2 + \omega_c^2/4)}$. Aside from the in-plane parabolic confinement $\hbar\omega_0$ and magnetic field confinement energy $\hbar\omega_c = E_c(\theta)$, the energy $E_{n,l}(\theta)$ comprises the effective band gap energy E_0 , including the vertical confinement and the effective Coulomb interaction, and the Zeeman energy with the angular dependent g factor $g_e = [(g_e^\parallel \cos \theta)^2 + (g_e^\perp \sin \theta)^2]^{1/2}$. The calculated energetically-lowest FD states for sample #2 in consideration of an angle $\theta = 10^\circ$ are illustrated as an image plot in the Fig. 4-9 (b). The density of the Raman-active electron states defines the z -axis of the image plot. According to the line width of the s-shell PL, the density of states is estimated by a Gaussian distribution with a magnetic field dispersive width of $\Gamma = 5$ meV which increases by a factor of 0.05 per tesla. For $B > 7$ T the electron states $|\Psi_e\rangle$ and $|\tilde{\Psi}_e\rangle$ of differently sized QDs overlap, marked by the yellow-green color in Fig. 4-9 (b). Since the level spacing between the ground and first-excited states is reduced, as additionally indicated by the dashed curves, the isotropic exchange between both electrons is more probable. As a result, the SFRS intensity based on the ground-excited-state coupling is enhanced. The shift of the SFRS resonance profile mainly follows the magnetic field confinement energy E_c which is a linear function of B . Thus, the B -field evolution of the SFRS intensity maximum $I_{\text{peak}}^{\text{sf}}$ emphasizes the similarity to the exciton-cyclotron resonance in quantum wells. Alternatively, the magnetic field dependence of the SFRS resonance profile can be approximated by the derivative of the difference $E_{\text{diff}} = E_{0,-1} - E_{0,0}$ which is about linear in the studied magnetic field range: $I_{\text{peak}}^{\text{sf}} \sim dE_{\text{diff}}/dB$. Therefore, the linear shift of the SFRS resonance-profile maximum is a major feature to identify the participation of the excited electron states in the electron-SFRS in the singly charged (In,Ga)As QDs.

4.3 Optically Induced Electron-Nuclear Hyperfine Interaction

Besides the coupling between electrons in the ground and excited Fock-Darwin states, the electron-nuclear hyperfine interaction in semiconductor QDs is known to lead to electron spin decoherence. Due to the strong localization of an electron in a QD, its spin is highly coupled to the spins of the lattice nuclei [214]. By polarizing the nuclear spins via, e.g., optical pumping in a longitudinal magnetic field the random fluctuations of the effective nuclear magnetic field, which cause the loss of electron spin polarization, can be suppressed [215, 216]. The optical pumping of the nuclear spin system is explained by a two-stage process. Firstly, the electron spins become polarized by the absorption of circularly polarized photons in an external magnetic field \mathbf{B} applied along the QD growth axis (z -direction). In the second stage, the hyperfine interaction results in a transfer of the electron spin polarization to the nuclear spin system (dynamic nuclear polarization) [217]. An effective magnetic field that is proportional to the degree of the nuclear orientation acts back on the electron system, and energetically shifts the electron levels [218]. It is denoted as Overhauser shift [35]. The hyperfine interaction Hamiltonian $\hat{H}_{\text{hf}} \sim A_{\text{hf}}[\hat{I}_z\hat{s}_{z,e} + (\hat{I}_+\hat{s}_- + \hat{I}_-\hat{s}_+)/2]$ with raising and lowering operators \hat{I}_+ , \hat{s}_+ and \hat{I}_- , \hat{s}_- consists of the static term $\hat{I}_z\hat{s}_{z,e}$ which changes the energies of both spin systems, and

a dynamical part which describes the transfer of the angular momentum. The nuclear spin operator is given by \hat{I} and A_{hf} is the hyperfine constant. The change in the electron energy can be described by the Hamiltonian

$$\hat{H} = g_e \mu_B (B + B_N), \quad (4.4)$$

where the first term characterizes the electron Zeeman splitting, and the hyperfine interaction is expressed as an effective nuclear field

$$B_N = \frac{\langle A_{\text{hf}} I \rangle_z}{g_e \mu_B}.$$

The ensemble average $\langle A_{\text{hf}} I \rangle_z$ of the hyperfine interaction in z -direction represents the degree of nuclear spin polarization [218]. The hyperfine interaction mainly accounts for electrons [219], since the electron wave function is spherically symmetric and, in turn, strongly overlaps with the nuclear wave functions. By comparison, the hole experiences a negligible hyperfine interaction due to the p-orbital character of its wave function whose probability density vanishes at the nucleus site. The hole primarily loses its spin polarization because of the strong spin-orbit interaction. However, the holes interact with the nuclei via dipole-dipole interaction [166]. At high magnetic fields typically used for SFRS, the hole-nuclear and nucleus-nucleus dipolar interactions become negligible. Furthermore, the mixing between different nuclei spin states caused by nuclear quadrupole coupling is lifted at high magnetic fields. The electron-hole exchange interaction which suppresses the rate of nuclear polarization can also be neglected. Note, the probability of the electron-nuclear spin flip-flop defines the nuclear spin pumping efficiency. Therefore, a large Zeeman splitting of the electron states at a high magnetic field reduces this efficiency [220].

The orientation of the dynamically induced polarization of nuclei can be aligned either parallel or antiparallel to the external magnetic field B in Faraday geometry; it depends on the polarization of the incident light. In the case of σ^- circularly polarized light, the capture of a spin-up electron by a singly charged QD is blocked by Pauli's exclusion principle, since a resident electron already occupies the $|+1/2\rangle$ state. On the contrary, a σ^+ polarized excitation which generates spin-down electrons polarizes the nuclei thus giving rise to an Overhauser shift. In the SFRS experiment the Overhauser shift is induced by quasi-resonant excitation, additionally, the QDs are resonantly probed to detect the electron-SFRS. The Raman shift of the SFRS line can be expected to directly indicate the total electron Zeeman splitting.

In the Fig. 4-10 SFRS Stokes-spectra are shown for both circular polarizations and different power densities of the quasi-resonant excitation. The spectra were measured for the sample #2 at an absolute magnetic field strength of 8 T and a temperature $T = 6$ K in a tilted geometry with $\theta \approx 20^\circ$. The two-color excitation is established via two tunable CW Ti:Sapphire lasers, see details on the setup in the Fig. 2-4 (segment [ii]): one laser beam resonantly excites the QD ensemble with an energy of 1.401 eV and σ^+ polarization, the energy $E_a = 1.54$ eV of the second beam is tuned into quasi-resonance with the wetting layer**. When the quasi-resonant excitation is σ^- polarized

**The energy of the quasi-resonant excitation exceeds the band gap of the wetting layer (about 1.481 eV) and that of the GaAs substrate (1.51 eV). The dependence of the degree of the induced

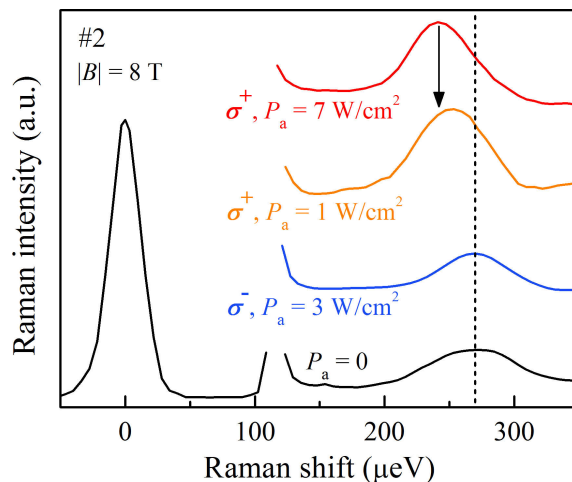


Figure 4-10: Electron-SFRS Stokes-spectra for different polarizations and power densities of the quasi-resonant excitation measured at $|B| = 8$ T, $T = 6$ K, and $\theta \approx 20^\circ$. The QDs were resonantly excited at $E_R = 1.401$ eV with $P_R = 5$ W/cm², the quasi-resonant excitation had the energy $E_a = 1.54$ eV. The power and polarization dependencies of the Raman shift demonstrate changes in the Overhauser shift of the electron states.

(blue curve) and when it is switched off (black curve), the Raman shifts of the e-SFRS lines are equal to $\Delta E_{sf} = (269 \pm 2)$ μeV , as marked by the dashed line. The application of σ^+ polarized quasi-resonant light leads to a decrease in the Raman shift. For a power density $P_a = 1$ W/cm² the Raman shift is reduced by about 17 μeV . Since the energy change is negative, the effective nuclear field B_N is aligned antiparallel to B . The total effective magnetic field is equal to $|B| - B_N$ and, in turn, the total electron Zeeman splitting is given by $g_e \mu_B (|B| - B_N)$. Without or with σ^- polarized optical pumping an Overhauser field is not induced. It has been shown that a linear-polarized excitation also results in a negligible Overhauser field ($B_N \approx 0$).

The electron-SFRS line depends on the power density of the quasi-resonant excitation, as illustrated by the red-colored curve and the vertical arrow in the Fig. 4-10. For $P_a = 7$ W/cm² the Raman shift amounts to $\Delta E_{sf} = (242 \pm 2)$ μeV . The power dependent reduction of the total electron Zeeman splitting is explained by the more efficient nuclear pumping at the higher rate of electron spin excitation^{††}. The Overhauser shift $\Delta E_{\text{OHS}} = 27$ μeV is used to estimate the nuclear spin polarization. According to the Table 1-1, the hyperfine constant of the In_{0.08}Ga_{0.92}As QDs is $\sum A_{\text{hf}} I = 147$ μeV which reflects the Overhauser shift of fully polarized nuclei. Thus, in the experiment a nuclear spin polarization of

$$\frac{\langle \hat{I} \rangle}{I} = \frac{\Delta E_{\text{OHS}}}{\sum A_{\text{hf}} I} \approx 18\%$$

nuclear spin polarization on the quasi-resonant excitation energy has not been studied yet. A resonant excitation of the wetting layer probably enhances the Overhauser shift.

^{††}An increase in the power density also leads to a PL background which interferes with the SFRS line. Therefore, the saturation regime of the nuclear spin polarization at higher pumping powers is probably not detectable in the studied QDs.

has been achieved. This value is smaller than reported values of about 40% for (In,Ga)As dots [221] or 65% for GaAs dots [216]. The low nuclear spin polarization can be ascribed to three aspects. (i) In the tilted geometry with $\theta \approx 20^\circ$ the transverse component of the external magnetic field leads to a fast relaxation of the nuclei spins. (ii) For $|B| \gg |B_N|$ the electron Zeeman splitting is large, hence, the spin flip-flop processes being necessary to polarize the nuclei are not energetically favorable [220, 221]. (iii) Due to the inhomogeneously broadened QD ensemble the experimentally observed Overhauser shift is an average value only.

The optically induced electron-nuclear coupling in an ensemble of (In,Ga)As QDs has been studied by the SFRS technique. The Raman shift of the electron-SFRS line directly indicates the dynamic polarization of the nuclei spins induced via optical pumping. The dependence of the Raman shift on the power density and polarization of the quasi-resonant excitation reveals the hyperfine interaction. As discussed in the Subsection 4.1.2, the application of highly energetic additional illumination with 2.54 eV does not change the Raman shift of the SFRS line within the accuracy of measurement. The impact of nuclear effects on the e-SFRS can be extended by further studies. Experiments at very low temperatures of about 1.8 K should be carried out. The temperature decrease from 6 to 1.8 K, which corresponds to a thermal energy change of about $360 \mu\text{eV}$, reduces the thermal heating of the nuclei thus avoiding spin depolarization, and the e-SFRS intensity increases. Furthermore, time-resolved two-color SFRS measurements could give insight into the dynamics of the nuclei. For instance, the measurement without optical pumping, which was done approximately 20 minutes after the measurement with σ^+ polarized excitation, did not show any effect of long-term nuclear spin polarization. Moreover, the SFRS technique can be combined with the application of a transverse magnetic field oscillating at radio-frequency (rf). When the latter is resonant with a nuclear Zeeman splitting, the corresponding nuclei can be depolarized effectively. Such a combination would provide an alternative to the electron-nuclear double resonance technique. For this technique an electron-paramagnetic and a nuclear-magnetic resonance transition must be implemented simultaneously. The combined rf-SFRS overcomes this limitation.

4.4 Conclusion

The electron spin-flip Raman scattering in singly charged (In,Ga)As/GaAs QD samples, postgrowth-annealed at different temperatures, strongly depends on the orientation of the magnetic field with respect to the QD growth axis. Only in a tilted geometry, where the in-plane component of the magnetic field vector induces a mixing of the conduction band as well as valence band states, the electron-SFRS becomes allowed by the electric dipole selection rules. The e-SFRS in a singlet trion based on a second-order Raman process is most intensive in the cross-circular polarization configuration. In the Voigt geometry the intensity of the e-SFRS line is enhanced by more than one order of magnitude compared to that in slightly tilted geometry. While strong magnetic fields enhance the e-SFRS efficiency due to a stronger localization of the carriers, additional high-energetic illumination heats the lattice and reduces the relative intensity of the electron spin-flip scattering line. The energy dispersion of the electron g factor deviates from the common Roth-Lax-Zwerdling expression, as it does not take into account tilting geometries and the excitation of excited states. Besides the dominant e-SFRS in singly charged dots, the

e-SFRS in undoped dots based on acoustic phonon scattering is revealed by the magnetic field dependence of the Raman shift: it demonstrates a zero-field offset which corresponds to the exciton exchange energy.

In the regime of Landau orbital formation, the resonant excitation of an excited negative trion under spin reversal of the resident electron is followed by the isotropic spin-flip-flop exchange scattering between the resident electron in a Fock-Darwin state with $l = -1$ and the photo-electron in the energetically lowest s-state. The coupling of the excited- to the ground-state electron leads to strongly shifted SFRS resonance profiles at high magnetic fields by more than 1 meV/T exceeding the diamagnetic shift of the PL. The shift of the resonance profile can be evaluated from the magnetic confinement energy which is a linear function of B scaled by the factor $\cos^\beta(\theta)$. In analogy to an exciton-cyclotron resonance, this optical resonance excitation observed in the e-SFRS process is only established in large-diameter QDs and close-to-Faraday geometries under application of high magnetic fields.

The Overhauser field optically induced in the (In,Ga)As QD ensemble is directly indicated by the Raman shift of the electron-SFRS in the negative singlet trion. For a σ^+ polarized optical pumping with a power density of 7 W/cm² a nuclear spin polarization of 18% is achieved for a sample temperature of 6 K. The polarization and power dependencies of the Raman shift measuring the total electron Zeeman splitting characterize the electron-nuclear hyperfine interaction. The nonzero transverse component of the external magnetic field and the large Zeeman splitting at $|B| = 8$ T reduce the nuclear spin polarization. Its relaxation takes place on a time scale faster than several minutes.

Chapter 5

Indirect Band-Gap (In,Al)As/AlAs Quantum Dots

While semiconductor quantum dots (QDs) have been established as efficient light emitters or detectors in optoelectronics [222], other applications are only perspective so far. A particular example in this respect is their implementation in spin electronics or quantum information technology. For that purpose, the QDs are typically loaded with resident carriers whose spins are rather well protected from relaxation by the three-dimensional confinement. In this context, exciton complexes have been used for manipulation of the spin of the resident carriers up to now, but are considered as less prospective as information carriers. This reservation is primarily related to their limited lifetime in the order of a nanosecond [223, 224, 225], which would most likely not allow enough coherent manipulations, either by microwave or optical techniques, to be of interest for quantum information. This situation may change if the exciton lifetime could be extended significantly.

Interesting, but technologically challenging in this respect is the placement of QDs in photonic crystals by which their radiative decay could be prevented [226, 227]. Another possibility is the realization of QDs with a band gap which is indirect in either real or momentum space or both. Here, the focus is placed on a novel type of structures: self-assembled (In,Al)As/AlAs quantum dots for which – dependent on the dot size – a crossover between the conduction-band ground states of the Γ -valley and X-valley occurs, as reflected by the lifetime of the lowest-energy exciton. This exciton is formed by a Γ_{hh} -valley heavy-hole and a mixed electron contributed by the Γ - and X-valley, whereby both carriers are located within the QD (type-I heterostructure) [228, 229]. The lifetime of this Γ -X mixed exciton lasts hundreds of μs , which may be sufficient for a large number of coherent manipulations in this time range.

The addressing of the properties of the X-valley electron and, in turn, indirect exciton by optical techniques poses a principle problem: the corresponding optical transitions are forbidden. This limitation can be bypassed by utilizing the state mixing of the direct and indirect conduction band minimum in the (In,Al)As/AlAs QDs. In the Section 5.1 the spin properties of the indirect exciton and its constituents are highlighted. The Γ -X mixing of the conduction band states particularly studied by the resonant spin-flip Raman scattering (SFRS) is described in Subsection 5.1.1. The SFRS spectroscopy is a suitable optical technique to probe the characteristics of spin structures as it enables the direct

measurement of the g factor of the particle under study. In the ensuing Subsections the fine structure of the Γ -X mixed exciton, namely its g factor tensor components are characterized. The Section is concluded by the simulation of a SFRS spectrum emphasizing the different contributions from the indirect and direct quantum levels with respect to the Γ -X mixing.

The recombination dynamics of the indirect exciton are described in detail in Section 5.2. The exciton lifetime distribution is experimentally studied by time-resolved photoluminescence (PL) in different ensembles of (In,Al)As/AlAs QDs. With support of numerical calculations it is shown that the lifetime of the indirect exciton considerably depends on the sharpness of the heterointerface between the (In,Al)As QD and the AlAs barrier matrix. The Section 5.3 addresses the polarization properties of the indirect exciton PL: besides stationary results on the magnetic field induced circular polarization, the magnetic field and temperature dependencies of the longitudinal spin relaxation time are demonstrated. The fundamental features of the indirect exciton including its fine structure as well as its recombination and spin lifetimes are summarized in Section 5.4.

5.1 Fine Structure of Γ -X Mixed Exciton

The g factor tensor components of the indirect exciton and its constituents of an X-valley electron and a Γ_{hh} -valley heavy-hole are determined in an undoped (In,Al)As/AlAs QD ensemble, where both direct and indirect band-gap QDs coexist. The mixing of the Γ - and X-electron ground states granting access to the fine structure of the indirect exciton is studied by photoluminescence and resonant SFRS. The magnetic field and angular dependencies of the Raman shifts reveal the isotropy of the X-valley electron g factor being equal to the free electron Landé factor. A theoretical calculation demonstrates that the Γ -X mixing manifests itself in spectrally separated SFRS lines of the electron related to its direct and indirect g factors. In the experiment only the X-valley contribution is observed; the short lifetime of the Γ -state and the broad dispersion in the QD sizes reduce the probability of SFRS in the conduction band at the Γ -point. A spectral study of the magnetic field induced circular PL polarization presents changes in the sign of the exciton g factor across the ensemble of direct and indirect band-gap QDs. The mechanism of the SFRS is explained by the involvement of dark exciton states in third-order Raman scattering with acoustic phonons. The observation of SFRS in the QDs requires the tilting of the magnetic field with respect to the QD growth axis lowering the QD symmetry. The angle dependence of the exciton levels is numerically modeled.

An ensemble of self-assembled $\text{In}_{0.3}\text{Al}_{0.7}\text{As}/\text{AlAs}$ QDs (#2890) has been studied. The sample was grown by molecular beam epitaxy on a (001)-oriented GaAs substrate [229]. The sample contained 20 layers of intentionally undoped QDs separated from each other by 20-nm-thick AlAs barriers, buffered by a 200-nm-thick GaAs layer. The QD layers had a nominal thickness of about 2.5 monolayers. The density of the lens-shaped QDs in each layer was about $3 \times 10^{10} \text{ cm}^{-2}$. The QDs were formed at a temperature of 525°C with an interruption time of the growth procedure of 30 s. A 5-nm-thick GaAs cap layer was grown on top of the structure in order to prevent oxidation of AlAs. For the SFRS measurements the sample, stress-free mounted at a rotatable mirror-based Raman-holder, was immersed in pumped liquid helium at a temperature of

$T = 1.8$ K and was exposed to magnetic fields* up to $B = 5$ T. The scattered light was analyzed by a 1-m double-spectrometer (Jobin Yvon, U1000) equipped with a cooled GaAs photomultiplier providing a spectral resolution of $\gtrsim 10 \mu\text{eV}$. For excitation a tunable continuous-wave Ti-Sapphire laser (Spectra-Physics, Matisse) was used with a power density of $P \leq 15 \text{ W/cm}^2$ at the sample. The SFRS spectra were measured in the backscattering geometry with crossed linear polarization. The angle θ between the magnetic field \mathbf{B} and the QD growth axis \mathbf{z} was varied between 0° (Faraday geometry) and 90° (Voigt geometry).

5.1.1 Γ -X Mixing of Conduction Band States

The dispersion in the QD size, shape, and material composition leads to the formation of (In,Al)As/AlAs QDs with different band energy structures. The energetically lowest electron state is transformed from the direct Γ - to the indirect X-valley of the conduction band. The transformation of the conduction band minimum is not accompanied by a type-I to type-II band alignment transition. Thus, both the photogenerated holes as well as electrons are spatially localized in the (In,Al)As QDs. The Γ - and X-valley levels of the electron and the heavy-hole level at the Γ_{hh} -point are schematically shown in the Fig. 5-1 (a) as a function of the QD diameter. According to an effective mass approximation including strain, deformation potential and a nonparabolic electron energy dispersion [229], the lowest electron level stems from the X-valley in small-diameter (< 8 nm) QDs having a strong quantum confinement in growth direction. When the QD diameter increases the electron ground state at the Γ -valley shifts to lower energies more strongly than the X-level due to a smaller effective mass of the electrons belonging to the Γ -valley [230]. For QDs with specific diameters the Γ - and X-electron levels intersect. The corresponding crossing energy $E_{\Gamma\text{X}}$ is marked in the Fig. 5-1 (a). Note, the quantum confinement lifts the twofold degenerate electron states at the X-point into the X_{xy} -state perpendicular to the growth axis and the X_z -state parallel to the z -axis. In accordance with Ref. [229] and in analogy to Ref. [231], the X_{xy} -state lies lower in energy. In the following this state is simply designated as X-electron state.

In the small-sized (In,Al)As/AlAs QDs the conduction band minimum is around the X-point, while the valence band maximum is at the Γ -point. In QDs the momentum is no longer a good quantum number. The wave function is distributed in momentum space over a range of \mathbf{k} -vectors that is inversely proportional to the QD size. This extension is smaller than the separation between the Γ - and the X-point in the k -space, hence, the indirect character of the band gap is maintained. Consequently, direct band-to-band transitions of electrons resulting in the emission of photons are suppressed. The radiative exciton recombination requires either the involvement of acoustic phonons, or the scattering of the electron at the heterointerface between the (In,Al)As QD and AlAs matrix, as it will be described in the Section 5.2, or the mixing of the Γ - and X-electron states. The latter two cases describe zero-phonon transitions: while the scattering at the interface provides the needed momentum $\Delta\mathbf{k} = \mathbf{k}_X - \mathbf{k}_\Gamma$ for the recombination of the electron and heavy-hole at the Γ -point [232], the admixture of the direct electron state to the indirect one makes the momentum transfer needless and thus the Γ -X mixed exciton is quasidirect [231, 233]. Note, in strong spatial confinement regimes (very small QDs) the

*A few experiments were performed with the 10 T-cryostat and triple-spectrometer in Dortmund.

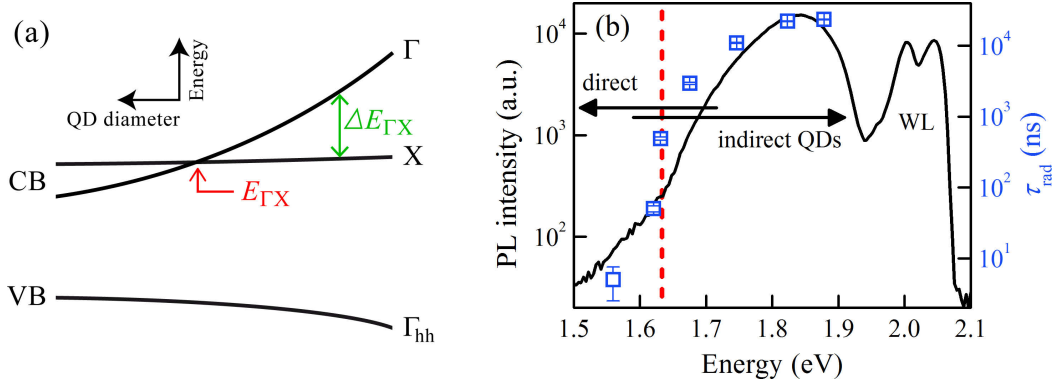


Figure 5-1: (a) Energetically lowest electron and heavy-hole levels dependent on the QD diameter, shown in real space. The energy difference $\Delta E_{\Gamma X}$ between the electron levels, and the crossing energy $E_{\Gamma X}$ are marked. (b) PL spectrum of the ensemble of direct and indirect band-gap (In,Al)As/AlAs QDs, measured at $T = 1.8$ K with an excitation at $E_a = 2.33$ eV above the wetting layer (WL). The exciton recombination times τ_{rad} across the QD ensemble are designated by the blue squares. The dashed line indicates the Γ -X-crossing energy.

uncertainty of the crystal momentum can increase in such a way that quasidirect optical transitions are allowed where neither phonons nor interface scattering nor energetically specific Γ -X mixing are necessary [234].

In the regime of the Γ -X mixing the matrix element of an electric dipole transition between the conduction and valence band can be written in the form [235, 236]:

$$M_{e,\text{hh}} = \frac{\langle \Psi_e^X | V_{\Gamma X} | \Psi_e^\Gamma \rangle \langle \Psi_e^\Gamma | \hat{p} | \Psi_{\text{hh}}^\Gamma \rangle}{\Delta E_{\Gamma X}}. \quad (5.1)$$

The dipole operator is given by \hat{p} and the Γ -X mixing is described by the potential $V_{\Gamma X}$. The matrix element is nonzero if the electron wave function Ψ_e consists of a Γ -part. Then, the wave function can be expressed as the superposition

$$\Psi_e = \gamma |\Gamma\rangle + \chi |X\rangle, \quad (5.2)$$

where $|\Gamma\rangle$ and $|X\rangle$ are the Bloch functions and γ and χ are the envelope functions of the Γ - and X -valley, respectively [237]. The oscillator strength f_{osc} of the Γ -X mixed exciton can be estimated by $M_{e,\text{hh}}^2$ which, in turn, is inversely proportional to the square of the Γ -X-energy difference: $f_{\text{osc}} \propto \Delta E_{\Gamma X}^{-2}$. The oscillator strength has its maximum at the Γ -X-crossing energy. In the case of a phonon-assisted transition or heterointerface scattering the potential $V_{\Gamma X}$ in Eq. (5.1) must be replaced by the electron-phonon interaction Hamiltonian or the interface scattering operator, respectively.

How can the type of the band alignment and band gap be determined experimentally? A typical property of a type-II band alignment is a blue-shift[†] of the PL as the excitation

[†]Due to the Coulomb interaction between the spatially separated electrons and holes the conduction and valence bands are bent in a different way. At high excitation powers corresponding to high carrier concentrations, the electron and hole levels are shifted to higher energies because of the band bending and, in turn, an enhanced confinement. As a result, the transition energies are increased.

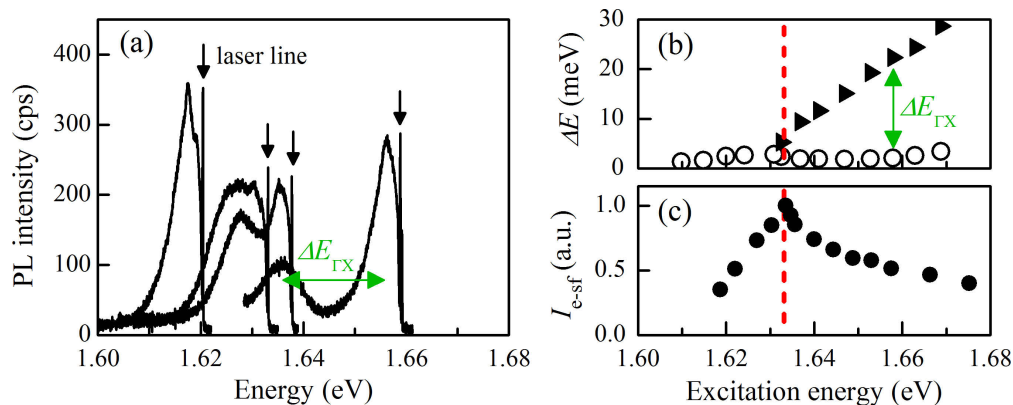


Figure 5-2: (a) Resonantly excited PL of the direct and Γ -X mixed excitons for $B = 0$ T. The laser line positions are marked by vertical arrows. (b) Energy difference between the laser line and peak position of either the direct (open circles) or the mixed (closed triangles) exciton PL. (c) SFRS resonance profile in Voigt geometry which illustrates the intensity I_{e-sf} of the electron-SFRS line as a function of the excitation energy, $B = 4$ T. The errors of ΔE and I_{e-sf} are not larger than the respective symbol sizes.

power increases [238, 239]. It has been shown that the spectral position of the PL of the (In,Al)As QDs is not influenced by the optical power density [228]. Hence, a type-II band alignment is excluded. By comparison, the coexistence of QDs with direct and indirect band gaps is evidenced by the radiative exciton recombination times τ_{rad} . The indirect QDs are characterized by long τ_{rad} in the microsecond range, which corresponds to a weak oscillator strength of the indirect exciton. On the contrary, in the direct band-gap dots the excitons recombine within a few nanoseconds. In the region of the Γ -X mixing the exciton PL decay is determined by both timescales. The spectral ranges, in which direct and/or indirect band-gap QDs are present, are indicated by horizontal arrows in the Fig. 5-1 (b). The indirect QDs mainly contribute to the PL, only a small fraction of the low-energy PL is attributed to the direct dots. Depending on QD parameters, the crossing energy $E_{\Gamma X}$ of the Γ - and X-level is spread over an energy range between 1.6 and 1.7 eV. In the following the regime of the Γ -X mixing across the inhomogeneously broadened QD ensemble will be specified.

In comparison to the above-wetting-layer excitation used for the measurement of the PL spectrum shown in the Fig. 5-1 (b), the PL for resonant QD excitation at zero magnetic field is illustrated in the Fig. 5-2 (a). The excitation energy E_R was varied from 1.61 to 1.68 eV, and the temperature was kept at $T = 5$ K. The resonant excitation leads to a reduction of the inhomogeneous broadening of the luminescence, thus, the contributions from the direct and Γ -X mixed exciton can be identified. For the excitation at low energy with $E_R < E_{\Gamma X}$ only the largest dots are probed giving rise to a spectrally narrow PL line. When the excitation energy exceeds the Γ -X-crossing energy $E_{\Gamma X}$, a broad PL line appears. In the Fig. 5-2 (b) the energy shifts ΔE of the narrow and broad PL lines with regard to the laser line are depicted as a function of the excitation energy. The narrow PL line follows E_R with a constant shift of $\Delta E = (2.2 \pm 0.1)$ meV, as indicated by the open circles. The broad PL linearly shifts from the laser line with increasing excitation energy. According to the band structure scheme shown in the

Fig. 5-1 (a), the energy of the direct exciton recombination is expected to follow the resonant excitation energy equidistantly. Due to the flat dispersion of the X-valley level the linearly shifted PL can be attributed to the Γ -X mixed exciton. As illustrated by the green-colored double-headed arrows in the Figs. 5-2 (a) and (b), the difference between the energy shifts of the direct and mixed exciton corresponds to $\Delta E_{\Gamma X}$ which, in turn, is a linear function of E_R in the regime of the Γ -X mixing. Moreover, the total integral intensity of both PL lines does not depend on the excitation energy, only the ratio of their intensities changes. Around the Γ -X-crossing point both intensities are similar, while at higher energies the direct exciton PL dominates. On the one hand, the redistribution of the PL intensities at $E_{\Gamma X}$ reflects the superposition of the Γ - and X-valley parts of the electron wave function. On the other hand, the rather strong decrease in the PL intensity of the mixed exciton demonstrates a strong dependence of its oscillator strength on the excitation energy. Since the oscillator strength is proportional to $\Delta E_{\Gamma X}^{-2}$ and $\Delta E_{\Gamma X}$ is linked to E_R , it can be assumed that $f_{osc} \propto (E_{\Gamma X} - E_R)^{-2}$. This estimation is valid for the quasidirect Γ -X mixed exciton. The quasidirect character of the mixed exciton is also confirmed by the resonant PL which does not show any phonon replica.

A possibility to accurately determine the Γ -X-crossing energy is provided by the SFRS technique. In Fig. 5-2 (c) the intensity I_{e-sf} of the electron-SFRS line is shown in dependence on the excitation energy. The SFRS experiment was measured in Voigt geometry at $B = 4$ T and $T = 5$ K. This SFRS resonance profile of the X-valley electron (see the next Subsection for details) has an asymmetric shape: the low-energy side is steep, while the intensity rather smoothly decreases at higher energies. The energy of the intensity maximum is comparable to the point where both PL lines have similar peak energies. The corresponding energy of 1.633 eV is taken as the definition of the crossing energy $E_{\Gamma X}$. The peak of the resonance profile indicates the maximum of the oscillator strength of the Γ -X mixed exciton. At higher excitation energies f_{osc} decreases, while the lifetime of the mixed exciton becomes dominated by the X-valley part of the electron wave function leading to a lower reduction in I_{e-sf} . Furthermore, the total width of the SFRS resonance profile can be considered as estimation of the energy range in which the Γ -X mixed exciton can be excited. The corresponding width amounts to about 60 meV, it is two times smaller than the full width at half maximum of the QD PL. The Γ -X-mixing regime is at the low-energy edge of the PL where the PL intensity is already reduced by a factor of 50 in comparison to the PL maximum.

5.1.2 SFRS on Γ -X Mixed Exciton

The crossing point of the Γ - and X-valley electron levels determined by the resonant PL has unambiguously been approved by the resonance profile of the electron-SFRS. The resonant SFRS further allows to define the carriers participating in the Raman scattering processes as well as the energies of the resonance states. The SFRS technique applied to the (In,Al)As dots is assumed to identify the direct and indirect excitons by measuring their g factors. As described in the Section 3.4, one can expect the spin-flip of each exciton in the Faraday geometry due to the interaction with an acoustic phonon. Hereby, the electron and heavy-hole of the bright exciton flip their spins simultaneously and, in turn, the exciton with the total angular momentum projection of $j_z = 1$ or -1 is scattered into the opposite state $|-1\rangle$ or $|+1\rangle$, respectively. According to the electric dipole selection rules the exciton-SFRS line should appear in crossed circular polarization. Note, the

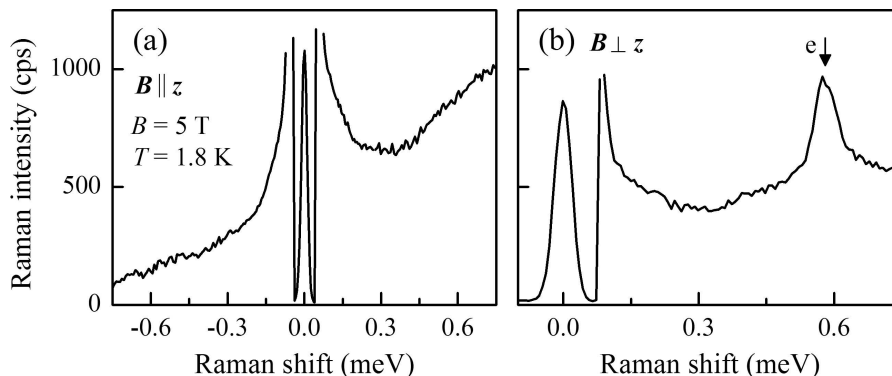


Figure 5-3: SFRS spectra for the (In,Al)As/AlAs QD sample in the Faraday (a) and Voigt (b) geometry. The excitation power density is about 12 W/cm^2 . In the Faraday geometry ($\mathbf{B} \parallel \mathbf{z}$) the spectrum was measured in the (σ^+, σ^-) polarization configuration, while in the Voigt geometry ($\mathbf{B} \perp \mathbf{z}$) the polarization is crossed linear. The SFRS line in the Voigt geometry belongs to the X-valley electron.

exciton-SFRS does not require the mixing between light-hole and heavy-hole states.

In the Fig. 5-3 (a) an exemplary SFRS spectrum measured in the Faraday geometry at $B = 5 \text{ T}$ and $T = 1.8 \text{ K}$ is depicted. The QD ensemble was excited at $E_R = 1.636 \text{ eV}$. Both in the Stokes and anti-Stokes regime a SFRS line is absent, only a PL background and elastically scattered light have been detected. Neither a variation in the excitation energy, nor the application of larger B -fields up to 10 T , nor using different polarization configurations lead to the appearance of an exciton-SFRS line. By comparison, for similar conditions a SFRS line is detected in the Voigt geometry, as shown in the Fig. 5-3 (b). Its Raman shift is about 0.58 meV which corresponds to a g factor of 2.0 . It will be demonstrated that this SFRS line originates from the X-valley electron. Neither in the Faraday nor Voigt geometry the SFRS of an exciton can be observed. It points out that the longitudinal g factor of the Γ -X mixed exciton (Ex) and probably direct exciton is close to zero and thus the respective SFRS line cannot be distinguished from the laser line. Since the band structure calculations for the (In,Al)As QDs have demonstrated that the splitting between the light-hole (lh) and heavy-hole (hh) states at the Γ -point exceeds several tens of meV [229], a lh-hh mixing is negligible in both geometries. Accordingly, the transverse g factor of the Γ_{hh} -valley hh is supposedly equal to zero. Therefore, in the Voigt geometry the Γ -X mixed exciton g factor is equal to the electron one and, in turn, their SFRS lines are shifted by the same energy from the laser line. Principally, the SFRS line detected in the Voigt geometry cannot be identified immediately. In order to separate and characterize the SFRS lines, their angular dependencies have to be studied. Before turning to the experimental results, the spin scattering mechanisms of the different carriers are described.

Assuming a tilted geometry with $\theta \neq 0^\circ$, the in-plane component $B_x = B \sin \theta$ of the magnetic field $\mathbf{B} = B(\sin \theta, 0, \cos \theta)^T$ leads to a mixing of the conduction band states due to the nonzero transverse magnetic moment of the electron. Since the light-holes and heavy-holes are not mixed – at least at the Γ -point – and QD shape anisotropies are negligible, the symmetry of the QDs is not lower than D_{2d} . The corresponding magnetic

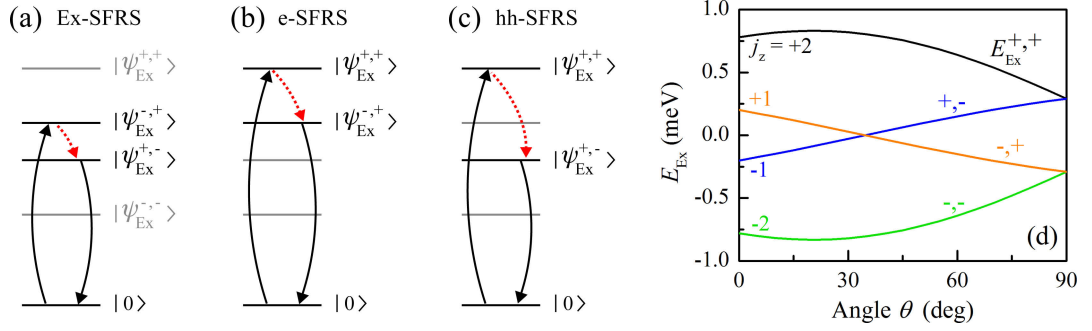


Figure 5-4: Stokes-SFRS mechanisms in the two-particle picture for a tilted geometry with $\theta < 35^\circ$. The spin of the exciton (a), electron (b), and heavy-hole (c) is scattered via an acoustic phonon. The corresponding spin-flip transitions are marked by the red-colored dashed arrows, the black-colored solid arrows designate the electric dipole allowed transitions. (d) Numerically calculated angular dependence of the exciton energies using the Eqs. (5.4) and (5.5), $B = 5$ T. E_{Exc} represents the energy changes induced by the magnetic field coupling. In the Faraday geometry the dark and bright excitons are described by the total angular momentum projections $j_z = \pm 2$ and ± 1 , respectively. The increase in the angle θ leads to a mixing between dark and bright exciton states.

Hamiltonian takes the following form, compare Eq. (4.1):

$$\hat{H}_B = \frac{1}{2}\mu_B \left(g_e^\parallel \sigma_z B_z + g_e^\perp \sigma_x B_x \right) + g_0 \mu_B \left(\kappa_{\text{KL}} J_z B_z + q_{\text{KL}} J_z^3 B_z \right). \quad (5.3)$$

The transverse and longitudinal electron g factors are g_e^\perp and g_e^\parallel , g_0 is the free electron g factor, $\sigma_{x,z}$ are the Pauli matrices, J_z is the z -component of the hh angular momentum operator, and μ_B is the Bohr magneton. The non-Zeeman term of the heavy-hole has the symmetry of the Kohn-Luttinger Hamiltonian [207, 208], it contains the parameters κ_{KL} and q_{KL} whose values can be found in the Table 1-1. Only the second electron Zeeman term introduces an off-diagonal coupling between the electron states $|\pm 1/2\rangle$. In analogy to Eq. (3.8), the eigenstates are then superpositions of the type $|\Psi_e^\pm\rangle = \cos(\theta/2)|\pm 1/2\rangle \pm \sin(\theta/2)|\mp 1/2\rangle$. These spin states are used to describe both the Γ - as well as X-valley electron. The angular dependent mixing of the electron spin states allows the spin-flip scattering of the electron and heavy-hole. The heavy-hole spin states are given by $|\Psi_{\text{hh}}^\pm\rangle = |\pm 3/2\rangle$. The confined exciton states can be factorized into the product of the electron and heavy-hole ones: $|\Psi_{\text{Exc}}^{\pm,\pm}\rangle = |\Psi_e^\pm\rangle \cdot |\Psi_{\text{hh}}^\pm\rangle$. As an example, the $|\Psi_{\text{Exc}}^{-,+}\rangle$ exciton consists of an electron in the state $|\Psi_e^-\rangle$ and a $j_z = +3/2$ heavy-hole.

The schemes of the exciton, electron, and heavy-hole spin-flips are illustrated in the Figs. 5-4 (a)-(c) for a tilted geometry. Since the polarization degrees of the incident and scattered light are not well defined in tilted geometries, they are not taken into account in the following. In consideration of Stokes scattering, the Ex-SFRS is initiated by an incident photon creating an exciton in the state $|\Psi_{\text{Exc}}^{-,+}\rangle$. The spin of the exciton is scattered by an acoustic phonon. Thus, the exciton-SFRS is described by the transition from $|\Psi_{\text{Exc}}^{-,+}\rangle$ to $|\Psi_{\text{Exc}}^{+,-}\rangle$, as it is shown in the Fig. 5-4 (a). The exciton annihilates (transition from $|\Psi_{\text{Exc}}^{+,-}\rangle$ to $|0\rangle$) under emission of a photon whose energy is reduced by $|g_{\text{hh}} - g_e|\mu_B B$ in comparison to the incident photon energy. Hereby, the exciton exchange energy δ_0

is neglected, see corresponding discussion in one of the following paragraphs. On the contrary, the electron- and heavy-hole-SFRS processes are initiated by the excitation of the $|\Psi_{\text{Ex}}^{+,+}\rangle$ exciton. The transition $|0\rangle \rightarrow |\Psi_{\text{Ex}}^{+,+}\rangle$ is optically addressable due to the admixture of the $s_{z,e} = -1/2$ electron state. The electron spin-flip yields the exciton into the state $|\Psi_{\text{Ex}}^{-,+}\rangle$, see Fig. 5-4 (b). In the case of the heavy-hole spin-flip the exciton is scattered into the state $|\Psi_{\text{Ex}}^{+,-}\rangle$, as depicted in the Fig. 5-4 (c). The subsequent annihilations give rise to Raman shifts which are specified by the electron or, respectively, heavy-hole Zeeman splitting.

In knowledge of the magnetic Hamiltonian and the scattering mechanisms, the dependence of the exciton states on the angle θ varied from the Faraday to the Voigt geometry will be discussed. The different exciton energies based on the Eq. (5.3) are illustrated in the Fig. 5-4 (d) for $B = 5$ T. They are given by

$$E_{\text{Ex}}^{+,+} = -E_{\text{Ex}}^{-,-} = \frac{1}{2}\mu_{\text{B}}B \left[g_{\text{e}} (\cos \theta + \sin \theta) + 3g_0 \cos \theta \left(\kappa_{\text{KL}} + \frac{9}{4}q_{\text{KL}} \right) \right], \quad (5.4)$$

$$E_{\text{Ex}}^{+,-} = -E_{\text{Ex}}^{-,+} = \frac{1}{2}\mu_{\text{B}}B \left[g_{\text{e}} (\cos \theta + \sin \theta) - 3g_0 \cos \theta \left(\kappa_{\text{KL}} + \frac{9}{4}q_{\text{KL}} \right) \right]. \quad (5.5)$$

An isotropic electron g factor of $g_{\text{e}} = 2$ is used, and the Kohn-Luttinger parameters are estimated to $\kappa_{\text{KL}} = 0.49$ and $q_{\text{KL}} = 0.033^{\ddagger}$. The angular dependence demonstrates a crossing of the exciton states $|\Psi_{\text{Ex}}^{+,-}\rangle$ and $|\Psi_{\text{Ex}}^{-,+}\rangle$ at about 35° . Here, the excitonic Raman shift vanishes. Also, at this crossing point the exciton g factor changes its sign. In the Voigt geometry the dark and bright exciton states are fully mixed and can be expressed by $|\Psi_{\text{Ex}}^{+,+}\rangle + |\Psi_{\text{Ex}}^{+,-}\rangle$ and $|\Psi_{\text{Ex}}^{-,-}\rangle + |\Psi_{\text{Ex}}^{-,+}\rangle$. As evaluated from the simulated dependence $E_{\text{Ex}}(\theta)$, all three SFRS lines should be observable at an angle of about 75° .

SFRS spectra measured at the magnetic fields of 4 and 5 T in a tilted geometry with an angle $\theta = 75^\circ$ are shown in the Fig. 5-5 (a) for resonant excitation at the Γ -X crossover. Three SFRS lines are spectrally separated both in the Stokes and anti-Stokes regime. The lines energetically shift with changes in the magnetic field strength. Their field-dependent shifts are depicted in the Fig. 5-5 (b). The Raman shifts ΔE_{sf} which correspond to transitions between exciton spin-sublevels are well described by linear Zeeman terms. A zero-field offset indicating the exciton exchange energy δ_0 cannot be detected, in contrast to the results on the undoped (In,Ga)As/GaAs QDs illustrated in Subsection 4.1.2. Since the heavy-hole spin-flip within the photogenerated exciton is the main reason for breaking the e-hh exchange coupling [240], it can be assumed that the spin relaxation time $\tau_{s,\text{hh}}$ of the heavy-hole is much faster than \hbar/δ_0 due to the admixture of the bright and dark exciton states in the strongly tilted geometry. The electron spin attempts to follow the precession of the heavy-hole spin whose orientation is stable for a long spin lifetime in unperturbed cases ($\tau_{s,\text{hh}} > \hbar/\delta_0$). Here, the heavy-hole spin and correspondingly its effective magnetic field vary very fast, hence, the electron experiences the external magnetic field only, and the exciton exchange energy does not contribute to the Raman shift. The solid lines, shown in the Fig. 5-5 (b), represent linear fits leading to the g factor values $|g_{\text{e}}^\theta| = 2.000 \pm 0.005$, $|g_{\text{hh}}^\theta| = 0.747 \pm 0.005$, and $|g_{\text{Ex}}^\theta| = 1.24 \pm 0.01$

[‡]The parameter q_{KL} is derived from the equation $x q_{\text{KL}}^{\text{InAs}} + (1-x) q_{\text{KL}}^{\text{AlAs}}$ with $x = 0.3$. The parameter κ_{KL} has been modified to simulate the experimental angle dependence of the SFRS. Thus, κ_{KL} used for the (In,Al)As QDs is about five times smaller than the value of 2.3 evaluated from the bulk parameters listed in the Table 1-1.

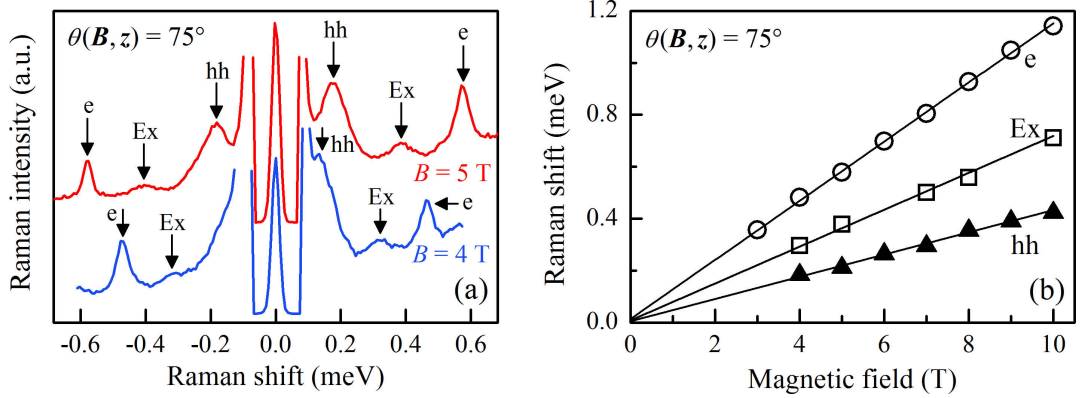


Figure 5-5: Magnetic field dependence of the SFRS of the X-valley electron, Γ_{hh} -valley heavy-hole, and mixed exciton, measured in a tilted geometry with $\theta = 75^\circ$ and at a temperature of 1.8 K. (a) Stokes and anti-Stokes SFRS spectra for magnetic fields of 4 and 5 T and resonant excitation of the Γ -X-level crossing at 1.636 eV. (b) Linear dependencies of the Raman shifts on the magnetic field strength. The error in the Raman shift does not exceed the symbol size.

for $\theta = 75^\circ$. According to the previous discussion including the numerical simulation the g factors can be attributed to the X-valley electron, Γ_{hh} -valley heavy-hole, and the Γ -X mixed exciton. The value of 2.000 ± 0.005 is consistent with the g factor of the electron at the X-valley reported for indirect band-gap structures [241, 242].

In what follows, the widths and intensities of the SFRS lines are shortly discussed. The minimum width of a SFRS line is defined by the spectral width of the laser line. The full width at half maximum (FWHM) taken from the Gaussian fit of the electron-SFRS line for $B = 5$ T amounts to $w_e = \sqrt{\ln 4} w_{\text{gauss}} \approx 0.03$ meV. It is similar to the laser line FWHM. The FWHM of 0.08 meV of the hh-SFRS line is about twice larger, while w_{Ex} is estimated to 0.06 meV. The difference in the line widths is caused by the different g factor dispersions. Nevertheless, the lifetime of the intermediate scattering state which is defined by the carrier-phonon interaction can be approximated. The lifetimes are $\tau_{hh} = \hbar/w_{hh} \approx 8$ ps and $\tau_e \approx 21$ ps. The small difference between them coincides with the theoretically predicted trend that the hh-phonon scattering is more efficient at high magnetic fields, see Subsection 1.2.2.

The temperature of the photogenerated electron and heavy-hole can be estimated from the intensity ratio of the Stokes I_{sf}^s and anti-Stokes $I_{\text{sf}}^{\text{as}}$ SFRS lines. For the single phonon process of the electron or heavy-hole spin-flip, the SFRS intensity ratio is proportional to the statistical factors $n(\Delta E_{\text{sf}}) + 1$ and $n(\Delta E_{\text{sf}})$. Here, n is the phonon occupation number which is governed by the Bose-Einstein distribution function [175]. The intensity ratio is then given by

$$\frac{I_{\text{sf}}^s}{I_{\text{sf}}^{\text{as}}} = \exp\left(\frac{\Delta E_{\text{sf}}}{k_B T_{e, hh}}\right). \quad (5.6)$$

Considering the SFRS spectrum for $B = 5$ T excited with a laser power density of about 12 W/cm^2 , the temperatures are evaluated from fits of the hh- and e-SFRS line intensities to $T_e = (5.6 \pm 0.4)$ K and $T_{hh} = (9.1 \pm 0.9)$ K. Both temperature values deviate from the temperature of the superfluid helium (1.8 K) surrounding the sample. The higher photo-

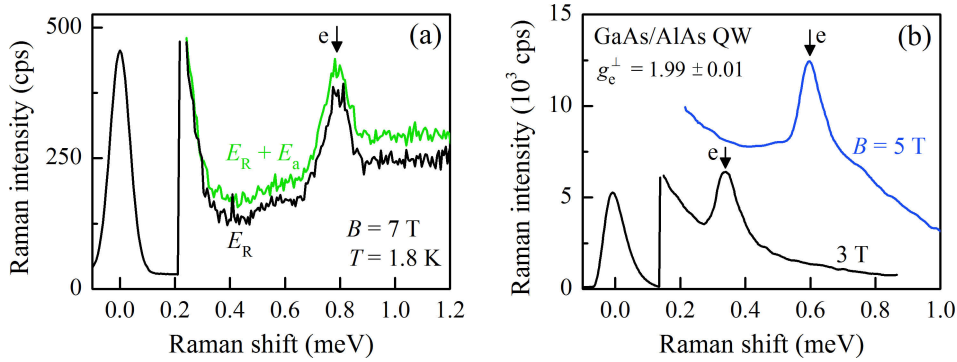


Figure 5-6: (a) SFRS spectra at $\theta = 75^\circ$ and $B = 7$ T for resonant excitation ($E_R = 1.632$ eV) of the (In,Al)As/AlAs QD ensemble and for resonant excitation with additional above-wetting-layer illumination with a photon energy $E_a = 2.33$ eV. The electron-SFRS line is not influenced by the above-wetting-layer illumination, only the PL background is slightly enhanced. (b) X-valley electron-SFRS in a GaAs/AlAs quantum well (QW) structure in Voigt geometry, $T = 5$ K and $E_R = 1.831$ eV.

hh temperature demonstrates that its way into thermal equilibrium with the lattice is limited by the short lifetime compared to the case of the photo-electron. Note, a strong laser power can also lead to an increase in the local lattice temperature. Since the SFRS is typically very sensitive to the lattice temperature, a local heating reduces the SFRS intensity. Thus, an increase in the optical power density is not directly linked to an enhancement of the SFRS intensity[§].

How does above-wetting-layer illumination influence the electron-SFRS in the (In,Al)As QDs? In the case of the CdTe/(Cd,Mg)Te quantum well the SFRS intensity can be increased by at least one order of magnitude, while in the (In,Ga)As/GaAs dots the e-SFRS intensity is reduced relative to the PL background. The impact of the above-wetting-layer illumination with $E_a = 2.33$ eV on the SFRS intensity of the X-valley electron is shown in the Fig. 5-6 (a). The SFRS intensity for only resonant excitation (black curve) is equal to the one for resonant excitation combined with the additional illumination (green curve) where the PL background is slightly increased. Due to the above-wetting-layer illumination hot electrons from continuum states relax into the intentionally undoped QDs. It can be assumed that these electrons can heat the lattice thus reducing the e-SFRS intensity. According to the insensitivity of the e-SFRS line to the above-wetting-layer illumination the power density of the additional illumination might be too weak to influence the phonon-assisted e-SFRS process. Note, in order to demonstrate a heating effect the intensity ratios I_{sf}^s/I_{sf}^{as} measured with and without additional illumination must be compared.

Before discussing the angular dependencies of the g factors in the (In,Al)As/AlAs QDs, a second example of measuring the X-valley electron g factor in a low-dimensional

[§]An accurate determination of the carrier temperature via the intensity ratio requires a stable laser power during the acquisition of the SFRS spectrum. The ratio of the Stokes and anti-Stokes e-SFRS intensities for $B = 4$ T, shown by the blue curve in the Fig. 5-5 (a), leads to a negative temperature. Here, the laser power was most probably unstable.

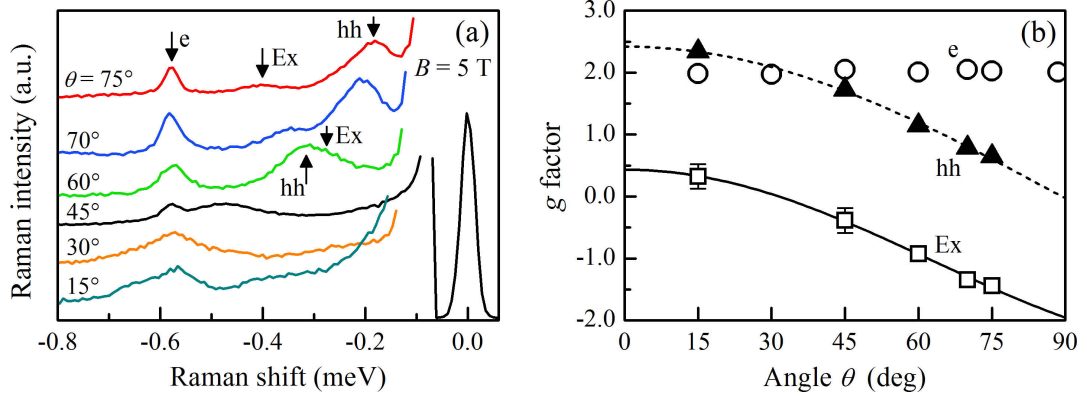


Figure 5-7: Angular dependent SFRS of the mixed exciton, X-valley electron, and Γ_{hh} -valley heavy-hole. (a) SFRS spectra at $B = 5$ T and $T = 1.8$ K for different tilting angles θ . The excitation energy is in resonance with the Γ -X-crossing point. (b) g factors as a function of θ . While the electron g factor does not show any angle dependence, the values of g_{hh} and g_{Ex} are approximated by $\cos\theta$ -equations (dashed and full lines). At $\theta = 30^\circ$ the hh-SFRS can only be identified as background of the e-SFRS line. In Voigt geometry the narrow SFRS line is attributed to the electron. The exciton g factors for $\theta = 15^\circ$ and 45° have been evaluated from spectra (not shown here) measured with very narrow spectrometer slits to strongly suppress the stray light. Their errors exceed the symbol size.

semiconductor by the SFRS technique is presented. In the Fig. 5-6 (b) two SFRS spectra for a GaAs/AlAs quantum well structure with type-II band alignment are depicted. They were measured at 3 and 5 T, and a temperature of 5 K in Voigt geometry. The excitation energy of 1.831 eV (Tekhnoscan, Dye-Laser Ametist-FD-08 with DCM solution) was tuned into resonance with the quantum well photoluminescence. The magnetic field dependent shift of the intensive line demonstrates its SFRS origin. Its Raman shift corresponds to a transverse g factor of 1.99 ± 0.01 . It can be attributed to the electron localized at the X-minimum of the conduction band in the AlAs layer [84]. Like in the (In,Al)As/AlAs QD ensemble, the g factor of the X-valley electron is very similar to that of the free electron.

5.1.3 Characteristics of the g Factors

The results discussed in the previous Subsection have demonstrated that in the Faraday geometry an exciton-SFRS is not detected due to its small longitudinal g factor. However, at a tilting angle $\theta = 75^\circ$ the SFRS lines of the Γ -X mixed exciton, Γ_{hh} -valley heavy-hole, and X-valley electron are present, and in the Voigt geometry only the X-valley electron-SFRS is observed. In the Fig. 5-7 (a) SFRS anti-Stokes spectra for different tilted geometries are shown. They were measured at $B = 5$ T, $T = 1.8$ K, and an excitation energy $E_R = 1.636$ eV. The SFRS spectra allow to trace the Raman shifts of the electron, heavy-hole and exciton with varying angle θ . The angular dependence of the corresponding g factors is illustrated in the Fig. 5-7 (b).

The SFRS line shift of the X-valley electron is not influenced by changes of the sample orientation in the xz -plane with respect to the magnetic field direction. Its g factor is

given by

$$g_e = g_e^{\parallel} = g_e^{\perp} = 2.00 \pm 0.01. \quad (5.7)$$

The isotropy of g_e and its large absolute value unambiguously indicate that the e-SFRS line is attributed to the spin-flip of the X-valley electron. It is consistent with electron g factor studies in indirect band-gap Si- or AlAs-based structures [84, 241, 242]. Note, the g factor of the X-valley electron also maintains its magnitude across the Γ -X-mixing range, evaluated from the SFRS lines of the resonance profile which has been shown in Fig. 5-2 (c). In general, the electron g factor is expressed as $g_e = g_0 - \Delta g$. The similarity of g_e to the free electron g factor g_0 originates from a negligibly small Δg , and thus from a negligible contribution from the orbital part of the X-valley electron wave function[¶]. According to the Roth-Lax-Zwerdling equation, see Eq. (1.21) for details, the g factor deviation Δg is roughly proportional to $(E_p \Delta_{so}/E_g^2)$. At the X-point the band gap E_g between the conduction and valence band is large. In AlAs, for example, the energy gap between the X_{6c} -level and the valence band level X_{7v} is 4.79 eV [243]. The energy E_p related to the momentum matrix element between the conduction and valence band is also reduced. Furthermore, spin-orbit corrections to the g factor are insignificant for the X-valley electron [244]. Therefore, its g factor coincides with g_0 , and is about 40 times larger than values of $g_e^* \approx 0.05$ for a Γ -valley electron localized in a quantum well where the energy of the lowest optical transition approaches 1.63 eV [245].

Besides the isotropic g factor of the X-valley electron, the angular dependent g factors, see Figs. 5-7 (a) and (b), are assigned to the Γ_{hh} -valley heavy-hole and the Γ -X mixed exciton. The g factor tensor components of the Γ_{hh} -valley hh are defined by the common expression $g_{hh}(\theta) = [(g_{hh}^{\parallel} \cos \theta)^2 + (g_{hh}^{\perp} \sin \theta)^2]^{1/2}$. In the present case the heavy-hole g factor mainly follows a cosine dependence, thus only g_{hh}^{\parallel} significantly differs from zero [246]. The longitudinal and transverse values of g_{hh} are estimated to

$$g_{hh}^{\parallel} = 2.42 \pm 0.05 \quad \text{and} \quad g_{hh}^{\perp} = 0.03 \pm 0.05. \quad (5.8)$$

The deviation of the transverse hh g factor from zero is not significant due to the large absolute error. Therefore, the lh-hh mixing at the Γ -point is absent in the (In,Al)As/AlAs QDs, since lh-hh mixing typically increases the in-plane hh g factor(s). Also, an anisotropy of the localization potential of the heavy-hole is negligible, and changes in g_{hh}^{\perp} induced by a \mathbf{k} -dependent admixture of light-holes or spin-orbit splitting can be ruled out. The small magnitude of g_{hh}^{\perp} is further evidenced by the Kohn-Luttinger parameter that has been used for the previously discussed simulation. For $q_{KL} = 0.033$ the transverse hh g factor takes the value $g_{hh}^* = 3q_{KL} \approx 0.1$.

In consideration of an isotropic electron g factor and a positive longitudinal heavy-hole g factor the equation $g_{Ex}(\theta) = g_{hh}^{\parallel} \cos \theta - g_e$ is valid for the Γ -X mixed exciton. This expression well describes the experimentally obtained exciton g factors, as illustrated by the solid line in the Fig. 5-7 (b). The g factor tensor components of the mixed exciton read

$$g_{Ex}^{\parallel} = 0.43 \pm 0.08 \quad \text{and} \quad g_{Ex}^{\perp} = -1.95 \pm 0.08. \quad (5.9)$$

The absolute value of the transverse g factor is similar to the one of the electron, while the

[¶]Since the wave functions of the X_{xy} and X_z electron states are spherically symmetric (s-like), the electron g factor is equal to 2.0 and isotropic in both cases.

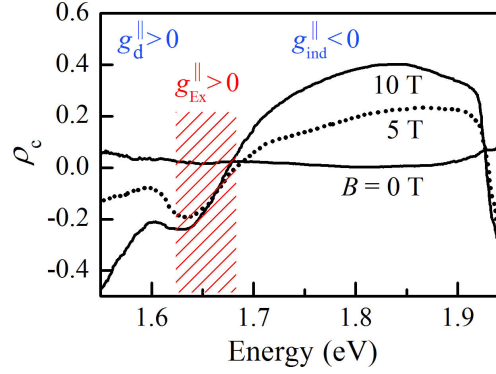


Figure 5-8: Magnetic field induced circular polarization degree ρ_c of the QD PL, excited by $E_a = 2.33$ eV at $T = 1.8$ K in the Faraday geometry. The Γ -X-crossing region is marked by the dashed area. Here, the contribution to ρ_c from the indirect exciton becomes important. The deviation of ρ_c from zero at $B = 0$ T for $E < 1.6$ eV is due to weak PL, compare the spectrum in Fig. 5-1 (b). For energies larger than 1.9 eV the wetting layer changes the sign of ρ_c .

longitudinal g factor deviates from zero considerably, as distinguished from the initial prediction. Nevertheless, the rather small g factor combined with a relatively weak intensity and broad line width makes it impossible to detect the Ex-SFRS in longitudinal magnetic fields of $B \leq 5$ T^{||}. It should be noted that the g factors in Eq. (5.9) actually belong to the indirect exciton, since they are explained by the X-valley electron and Γ_{hh} -valley heavy-hole g factors probed at energies belonging to the Γ -X-mixing regime. The sign of the longitudinal exciton g factor is analyzed in detail in the next paragraph. Moreover, for the Γ -X mixed exciton, whose wave function consists of the superposed electron wave functions, an average electron and, in turn, exciton g factor could be expected. In the Subsection 5.1.4, this aspect will be studied theoretically.

The positive sign of the longitudinal g factor of the indirect exciton probed at energies ranging about $E_{\Gamma X}$ is evidenced by the magnetic field induced circular polarization degree ρ_c of the QD ensemble PL. In the Fig. 5-8 the circular polarization degree is spectrally resolved for different magnetic field strengths in the Faraday geometry. The circular polarization degree $\rho_c = (I^+ - I^-)/(I^+ + I^-)$ is evaluated from the intensities I^+ and I^- of the σ^+ and σ^- polarized exciton PL, respectively. A positive ρ_c means that the exciton state $|+1\rangle$ is lower in energy than that of the $j_z = -1$ exciton and, in turn, the exciton g factor is negative. Hence, the sign of ρ_c allows to define the exciton g factor sign. As shown in the Fig. 5-8, the circular polarization degree changes its sign across the ensemble of the direct and indirect band-gap QDs. In the case of direct QDs at low energies, ρ_c is negative and thus the g factor of the Γ -exciton is $g_d^{\parallel} > 0$. This is consistent with results on the exciton g factor in self-assembled InAs-based QDs with direct band gap [206], and with the assumption of a small electron g factor ($|g_e^*| \ll |g_{hh}|$) for quantum structures with an effective band gap energy of about 1.63 eV [245]. In the Γ -X-crossing region, marked by the dashed area in the Fig. 5-8, ρ_c is provided by the emission of the mixed excitons. While the direct exciton contribution prevails, the

^{||}The application of larger B -fields was only possible with another experimental setup providing a comparable spectral resolution, but less stray light rejection.

increase in ρ_c already indicates the contribution of the indirect excitons. Nevertheless, the negative sign shows a positive g factor in accordance with the SFRS results measured in the Γ -X-mixing regime. In the spectral region of indirect band-gap QDs the circular polarization degree becomes positive. Here, the longitudinal Landé factor $g_{\text{ind}}^{\parallel}$ of the indirect exciton is negative. Since the exciton g factor is governed by $g_{\text{ind}} = g_{\text{hh}} - g_e$, the relation $|g_{\text{hh}}| < |g_e|$ is valid for $E > 1.68$ eV, and thus the hh g factor decreases with increasing energy. In conclusion, the discussion of the carrier g factor properties combined with the sign determination of $g_{\text{Ex}}^{\parallel}$ ascertains and completes the assignment of the SFRS line origins.

5.1.4 Theoretical Simulation of SFRS Spectrum

In the experiments Raman scattering induced spin-flips of the photocreated Γ -X mixed exciton, X-valley electron and Γ_{hh} -valley heavy-hole have been observed. Only the resonant excitation at energies where QDs in the ensemble have Γ -X mixing allows the optical access to the indirect electron. In the Γ -X-crossing region the electron state is a mixed state composed of the Γ - and X-valley, as described by Eq. (5.2): the electron wave function is defined as the superposition $|\Psi_e\rangle = \gamma|\Gamma\rangle + \chi|X\rangle$. It has been assumed that the change in the tilting angle affects their spin states in the same way, see Subsection 5.1.2 for details. Although the Γ -valley electron enables via its admixture to the X-valley electron the observation of the X-electron-SFRS as a sharp line in the spectrum, its own SFRS could not be detected. Besides the spin-flip scattering of the Γ -valley electron, one may also expect a SFRS line whose shift is defined by a mixed g factor of the direct and indirect electrons. A wide dispersion and small absolute magnitude of the Γ -valley electron g factor were previously given as reasons for its absence in the SFRS spectra. In the following the SFRS spectrum of an ensemble of a two-level quantum system will theoretically be described**. The model will be used to simulate the SFRS spectrum of the electron with both the Γ - and X-valley contributions. The simulation will prove the reasons above and provide further explanations.

An ensemble of a two-level quantum system can be defined by the wave function

$$|\Psi\rangle = C_1|1\rangle + C_2|2\rangle,$$

where $|j\rangle$ ($j = 1, 2$) are two orthonormalized basic states in an individual two-level quantum system characterized by the unperturbed eigenenergies E_j . For the lowest level, which will only be taken into account, the coefficients C_j are given by

$$C_1^2 = \frac{1}{2} \left(1 + \frac{\Delta}{\sqrt{\Delta^2 + \delta^2}} \right) \quad \text{and} \quad C_2^2 = \frac{1}{2} \left(1 - \frac{\Delta}{\sqrt{\Delta^2 + \delta^2}} \right).$$

Here, $\Delta = E_2 - E_1$ and δ is the modulus of the matrix element of the coupling of the states $|1\rangle$ and $|2\rangle$ due to some perturbation, e.g., due to mixing between Γ - and X-states in a QD. The g factor of a two-level quantum system is defined by

$$g \equiv g(\Delta) = g_1 C_1^2 + g_2 C_2^2, \quad (5.10)$$

**This theoretical part has been developed by E. L. Ivchenko from the Ioffe-Institute in St. Petersburg.

where g_j is the g factor in the basic state $|j\rangle$. The Eq. (5.10) can be written as

$$g \equiv g(\Delta) = \bar{g} - \tilde{g} \frac{\Delta}{\sqrt{\Delta^2 + \delta^2}} \quad (5.11)$$

with $\bar{g} = (g_1 + g_2)/2$ and $\tilde{g} = (g_2 - g_1)/2$. Note, for the (In,Al)As/AlAs QDs the relation $g_1 \ll g_2$ is valid.

The spectral line of the spin-flip Raman scattering is described by

$$I(\Omega) \propto \int F(\Delta) C_1^2 \delta[\Omega - g(\Delta)] d\Delta, \quad (5.12)$$

where the function $F(\Delta)$ denotes the distribution of the quantum systems over the energy Δ , and the δ -function depends on $g(\Delta)$ and on the frequency difference $\Omega = \omega_i - \omega_s$ with the incident ω_i and scattered ω_s light frequencies. The product $\mu_B B$ is set to unity. In what follows, it is assumed that the modulus δ of the coupling matrix element is smaller than the dispersion of the Δ -values. By taking into account the first derivative

$$\frac{dg(\Delta)}{d\Delta} = -\tilde{g} \frac{\delta^2}{(\Delta^2 + \delta^2)^{3/2}}$$

the spectral line of the SFRS takes the form

$$I(\Omega) \propto \frac{F(\Delta)}{|\tilde{g}|\delta^2} C_1^2 (\Delta^2 + \delta^2)^{3/2} = \frac{F(\Delta)}{2|\tilde{g}|\delta^2} \left(\sqrt{\Delta^2 + \delta^2} + \Delta \right) (\Delta^2 + \delta^2). \quad (5.13)$$

The difference Δ in the energies of the two states $|1\rangle$ and $|2\rangle$ is related to the frequency difference Ω (Raman shift) by the identity $\Omega = g(\Delta)$. The square of Δ can then be expressed as

$$\Delta^2 = \delta^2 \frac{(\Omega - \bar{g})^2}{\tilde{g}^2 - (\Omega - \bar{g})^2}.$$

In order to demonstrate the explicit dependence of Eq. (5.13) on both g factors, the sum $\Delta^2 + \delta^2$ is written as

$$\Delta^2 + \delta^2 = \delta^2 \frac{\tilde{g}^2}{\tilde{g}^2 - (\Omega - \bar{g})^2} = \delta^2 \frac{\tilde{g}^2}{(g_2 - \Omega)(\Omega - g_1)}. \quad (5.14)$$

It is obvious that $I(\Omega)$ is not zero for positive $\tilde{g}^2 - (\Omega - \bar{g})^2$. For the two cases of $\Omega \approx g_2$ and, respectively, $\Omega \approx g_1$ the sum (5.14) takes the following form resulting from a zero-order Taylor approximation:

$$\Delta^2 + \delta^2 \Big|_{\Omega \approx g_2} \approx \delta^2 \frac{\tilde{g}/2}{g_2 - \Omega}, \quad \Delta^2 + \delta^2 \Big|_{\Omega \approx g_1} \approx \delta^2 \frac{\tilde{g}/2}{\Omega - g_1}.$$

In consideration of systems with a negligible energy spacing $\Delta \approx 0$, the frequency shift is given by $\Omega = \bar{g}$ with the minimum intensity

$$I_{\min}(\Omega) \propto \delta. \quad (5.15)$$

The systems with negative Δ , which corresponds to the range of energies exceeding the Γ -X-crossing point, satisfy the inequality $\delta \ll |\Delta|$ and contribute to the peak at $\Omega \approx g_2$.

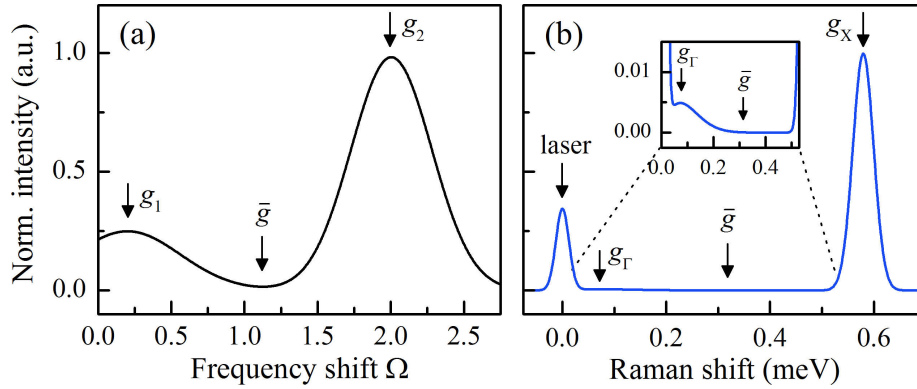


Figure 5-9: (a) Simulated SFRS spectrum of an ensemble of two-level quantum systems for $|\Delta| \gg \delta$. The spectrum contains two SFRS lines whose shifts correspond to the Landé factors $g_2 = g_0$ and $g_1 = g_2/10$. The line $I(g_1)$ of the direct state is rather weak and its frequency shift is small. For the mixed g factor $\bar{g} = (g_1 + g_2)/2$ the spectral intensity is minimal. The widths of the spectral lines indicate the dispersion in the g factor values. (b) Simulated SFRS spectrum for $B = 5$ T with modified parameters to fit the experimentally observed SFRS. The dispersion in the direct electron g factor and the short lifetime of the Γ -state reduce the SFRS intensity of the Γ -valley electron. The inset demonstrates the weak intensity of its line, and the vanishing intensity at \bar{g} . Only the SFRS of the X-valley electron appears as a rather narrow line in the spectrum. In contrast to the simulation shown in panel (a), for the calculation of the modified density distributions F the following parameters have been used: $w_{g_\Gamma} = 5w_{g_X} = 10w_L$ and $A_{0,g_\Gamma} = 0.5$.

The spectral line is described by

$$I(\Omega \approx g_2) \propto F(\Delta)|\Delta|. \quad (5.16)$$

The scattering peak near $\Omega = g_1$ adopts the equivalent intensity in that model without making assumptions on the density of states or the line broadening. If the density distribution $F(\Delta)$ is a smooth function, the maximum intensity will be achieved at $\Delta_m = F(\Delta_m)/F'(\Delta_m)$. The peak frequency shift is then equal to $\Omega_m = g_2 - \tilde{g}(\delta/\Delta_m)^2$. Overall, the spin-flip scattering spectrum has two peaks at $\Omega \approx g_1$ and $\Omega \approx g_2$, and reaches a minimum at $\Omega \approx \bar{g}$.

For the simulation of a SFRS spectrum the density distribution F is described in terms of the frequency shift Ω by the Gaussian function $F_j(\Omega) = A_0/(w\sqrt{\pi/2}) \exp[-2(\Omega - g_j)^2/w^2]$ with an amplitude $A_0 = 1$. The value of the width w is linked to the condition that the spectral intensity is minimal at \bar{g} . In order to take into account the relation $g_2 \gg g_1$ it is assumed that both g factors differ from each other by one order of magnitude, whereby g_2 is set to the free electron g factor g_0 thus marking the X-valley electron. The corresponding SFRS spectrum is shown in the Fig. 5-9 (a). The theoretical simulation demonstrates that for an ensemble of two-level quantum systems two spectrally broad lines at the frequency shifts belonging to the g factors of both levels appear in the SFRS spectrum. The large width of the spectral lines displays the dispersion in the g factor values of the mixed state. At the average g factor $\bar{g} = (g_1 + g_2)/2$ the intensity takes its minimum value. Despite the same density distribution function, the intensity of the line at $\Omega = g_2$ is four times larger than $I(\Omega = g_1)$ and about two orders of mag-

nitude larger than the intensity at \bar{g} . Concerning the (In,Al)As QDs it means that for a typical SFRS intensity $I(g_2)$ of 500 counts per second the intensity I_{\min} falls below 10 counts per second thus becoming indistinguishable from the PL background. Moreover, not only the rather weak intensity of the line $I(g_1)$ but also its close vicinity to the zero frequency shift (laser line) due to its small g factor account for the disappearance of the Γ -valley electron-SFRS in the spectra. Bear in mind that in direct band-gap GaAs-based quantum wells with an effective band gap energy of about 1.63 eV the electron g factor ranges about 0.05 [245].

In the following, features of the theoretical simulation are adapted to experimental parameters in order to highlight further reasons for the absence of the Γ -valley electron-SFRS. In the Fig. 5-9 (b) the modified SFRS spectrum is depicted, the model parameters are listed in the caption. Only the SFRS line of the X-valley electron is pronounced, while the SFRS contribution from the Γ -valley electron is strongly suppressed. As illustrated in the inset of panel (b), its line intensity is more than two orders of magnitude smaller than $I(g_x)$, while at the average g factor the intensity vanishes. Moreover, the Γ -valley e-SFRS line overlaps with the laser line. Which model parameters have been changed to closely simulate the experimental SFRS? Mainly, the width of $I(g_r)$ has been increased by five times with respect to the width of $I(g_x)$ which has been approximated by twice the typical width $w_L = 0.02$ meV of the laser line. It accounts for the broad dispersion of the Γ -valley electron g factor following the strong variation in QD sizes. Furthermore, the SFRS process with a Γ -electron is inefficient at an excitation energy exceeding the Γ -X-crossing point. It is attributed to the short lifetime τ_d of the Γ -valley electron which effectively relaxes to the X-valley. Owing to the proportionality $I_{sf} \propto \tau$, the short lifetime attenuates the intensity of the spectral line. The amplitude of $I(g_r)$ has only been bisected in value, although the Γ -electron lifetime is considerably smaller than that of the X-valley electron. Principally, the line intensity also depends on the concentration of the QDs excited at a certain energy within the Γ -X-mixing range, see Subsection 5.1.1 for details. Hereby, the SFRS intensities of both the direct and indirect electron are affected in the same manner. Only for resonant excitation of the direct dots, its small concentration of 2% further reduces the SFRS line intensity. According to these reasons, it is not possible to detect the SFRS line of the Γ -valley electron. As evidenced by the theoretical derivation and illustrated by the simulated SFRS spectra, the SFRS line related to a mixed g factor has the minimum intensity. Note, the application of very high magnetic fields ($B \gg 5$ T) perpendicular to the QD growth axis could enhance the SFRS intensity of the Γ -valley electron so strongly that it could be detected with an efficient detection system.

5.2 Recombination Dynamics of the Indirect Exciton

The kinetics of the exciton recombination in semiconductor QDs is often analyzed in terms of an exponential decay with one characteristic recombination time [247]. However, the luminescence decay in QDs is typically nonexponential [247, 248, 249], for which there are several reasons, such as the contribution of dark excitons to the emission or the influence of Coulomb correlation effects. Nevertheless, for a single QD in the strong confinement regime the bright exciton PL is found to decay monoexponentially [248, 250]. For an ensemble of such QDs, on the other hand, nonexponential decays are typical and

a statistical analysis of the time-resolved emission demonstrates that this behavior can be attributed to a dispersion of radiative and/or nonradiative lifetimes of QD confined excitons [249]. This ensemble decay at a specific energy results from the superposition of monoexponential PL decays of excitons that are localized in QDs having different sizes, shapes, and compositions [251]. In the case of continuously distributed lifetimes τ of excitons, characterized by the same recombination energy, their PL decay can be described by a distribution function $G(\tau)$.

As shown in the Subsection 5.1.1, a long exciton recombination time evaluated from the nonexponential PL decay is characteristic of indirect band-gap (In,Al)As/AlAs QDs with type-I band alignment. Here, the conduction band minimum is around the X-valley, while the valence band maximum is around the Γ -point. Since only indirect band-gap QDs are probed at energies deviating from the Γ -X-mixing regime ($E \gg E_{\Gamma X}$), a radiative recombination requires a momentum transfer via either a phonon or a scattering process at the heterointerface between the (In,Al)As QD and AlAs matrix, as demonstrated, for instance, in indirect band-gap GaAs/AlAs and InAs/AlAs quantum wells [252, 253]. For the indirect (In,Al)As/AlAs QDs it has been ascertained that the radiative exciton recombination is mainly caused by the scattering at the (In,Al)As/AlAs heterointerface [229]. Hence, the exciton recombination dynamics, namely the recombination time τ and the lifetime distribution $G(\tau)$, can yield valuable information on this interface.

In the following the dynamics of the exciton recombination in ensembles of indirect band-gap (In,Al)As/AlAs QDs with varying sharpness of the QD-matrix interface is studied by time-resolved PL. It will be illustrated that the radiative lifetime of the exciton that is indirect in momentum space is strongly influenced by this sharpness. The PL decay is well described by a power-law function $I(t) \sim (1/t)^\alpha$ which, in turn, is based on a phenomenological distribution function $G(\tau)$ depending on a single fitting parameter.

5.2.1 Sample Characteristics

The studied self-assembled (In,Al)As QDs, embedded in an AlAs matrix, were grown by molecular beam epitaxy on semi-insulating (001)-oriented GaAs substrates. The structures had one QD sheet sandwiched between 50-nm-thick AlAs layers grown on top of a 200-nm-thick GaAs buffer layer. The nominal amount of deposited InAs was about 2.5 monolayers. A 20-nm-thick GaAs cap layer protected the AlAs layer against oxidation.

The diameter, density, and composition of the intentionally undoped (In,Al)As/AlAs QDs are determined by the growth conditions such as the substrate temperature T_g , growth interruption time t_{gi} , and postgrowth annealing temperature T_{an} . The three structures S1 (#1474), S2 (#1498, as-grown), and S3 (#1379), which were grown under the conditions listed in the Table 5-1, have different (In,Al)As QD alloy compositions. Despite the effect of intermixing on the QD composition profile during the epitaxy, as-grown self-assembled QDs have a sharp QD-matrix interface [254]. The reason for the sharp interface formation arises from the Stranski-Krastanov growth mode. The intermixing during the dot formation determines the QD composition due to mass transfer along the wetting layer [255, 256]. The interfaces of the QDs which are independent of their composition are given by stable crystallographic planes thus minimizing the interface energy. These planes provide interface stability against the intermixing with the matrix material during the overgrowth of the QDs. Nevertheless, the sharpness of the

Table 5-1: Growth parameters and basic properties of the studied (In,Al)As/AlAs QDs. The average diameter d_{av} , diameters corresponding to the smaller d_s or larger d_l half width of the QD size distribution, the size dispersion S_d , and the average fraction x_{InAs} of InAs in the QDs are listed. Additionally, the exponent α of the PL decay curve, and the parameter τ_0 of the exciton lifetime distribution described by the Eq. (5.19) are specified. The QD densities are within the same range of $(7 \pm 3) \times 10^{10} \text{ cm}^{-2}$. For the structure S2 the diameter $d_l = 18.5 \text{ nm}$ refers to direct band-gap QDs. In order to address indirect band-gap QDs in S2 the smaller diameter $d_l^* = 17 \text{ nm}$, marked in Fig. 5-10, is chosen. The corresponding parameter value τ_0/α for S2 belongs to the QD ensemble with the characteristic diameter d_l^* .

| Sample | T_g/t_{gi} (°C/s) | T_{an} (°C) | d_s (nm) | d_{av} (nm) | d_l (nm) | S_d (%) | x_{InAs} | $\tau_0 (\mu\text{s})/\alpha$ | | |
|--------|------------------------|------------------|---------------|------------------|---------------|--------------|------------|-------------------------------|-------------------|----------------|
| | | | | | | | | $I_{1/2}(d_s)$ | $I_{max}(d_{av})$ | $I_{1/2}(d_l)$ |
| S1 | 450/10 | - | 4.3 | 5.5 | 7 | 40 | 0.99 | 0.13/1.75 | 0.10/1.75 | 0.07/1.30 |
| S2 | 460/60 | - | 9 | 13.8 | 17* | 60 | 0.80 | 0.24/1.95 | 0.13/1.55 | 0.06/1.25 |
| S3 | 510/60 | 700 | 15 | 18.3 | 22 | 52 | 0.47 | 2.3/1.75 | 2.1/1.50 | 0.7/1.35 |
| S4 | 460/60 | 800 | 12 | 19.6 | 28 | 75 | 0.35 | 5.4/2.45 | 5.2/2.40 | 4.0/2.08 |

(In,Al)As/AlAs interface can be smeared out by means of high-temperature postgrowth annealing. The structures S3 and S4 (#1498) were annealed at elevated temperatures T_{an} , as marked in the Table 5-1. The sample S4 is designated as annealed S2 structure, since they only differ in the postgrowth annealing.

The QD sizes and densities are studied by transmission electron microscopy (TEM). In Fig. 5-10 TEM plane-view images (illustrating the lateral QD sizes only, not their cross sections) and the respective histograms of the QD diameter distribution are shown for the four structures. The average diameters d_{av} and the diameters corresponding to the larger d_l and smaller d_s half widths of the QD size distributions are summarized in the Table 5-1. Additionally, the size dispersion S_d is listed, which is defined as the ratio of the difference between the half widths d_l and d_s to the average diameter: $S_d = 100\% \times (d_l - d_s)/d_{av}$. Note, from TEM cross-section images it has been evaluated that the (In,Al)As QDs are lens shaped with a typical aspect ratio (height to diameter) of 1:4 [228].

The unannealed structure S1 has a relatively narrow distribution ($S_d = 40\%$) around a small QD diameter of $d_{av} = 5.5 \text{ nm}$, as depicted in the Fig. 5-10. The structures S2, S3, and S4 contain QDs with larger diameters, which are also distributed over broader ranges. The largest lateral QD sizes are found for the structure S4 which was annealed at the highest temperature of 800°C . The comparison between the annealed structure S4 and the unannealed structure S2 indicates that postgrowth annealing leads to broadening of the QD diameter and its distribution. The average QD diameter increases from 13.8 to 19.6 nm and the size dispersion S_d from 60% to 75% . The increase in the diameter is caused by the InAs diffusion from the QD into the surrounding AlAs matrix. Accordingly, a diffused $\text{In}_x\text{Al}_{1-x}\text{As}$ layer around the QD-matrix interface is the result of the annealing. It is obvious that the thickness of this $\text{In}_x\text{Al}_{1-x}\text{As}$ layer depends on the annealing temperature and duration. Hereby, the sharpness of the interface is defined as the degree of spatial separation between the different materials of (In,Al)As and AlAs. Therefore, the sharpness of the QD-matrix interface can be described by the thickness of this diffused layer: a sharp (blurred) interface corresponds to a thin (thick) $\text{In}_x\text{Al}_{1-x}\text{As}$ layer. Hence, the structures S1-S4 represent a set of QD ensembles having different diameters and interface sharpnesses.

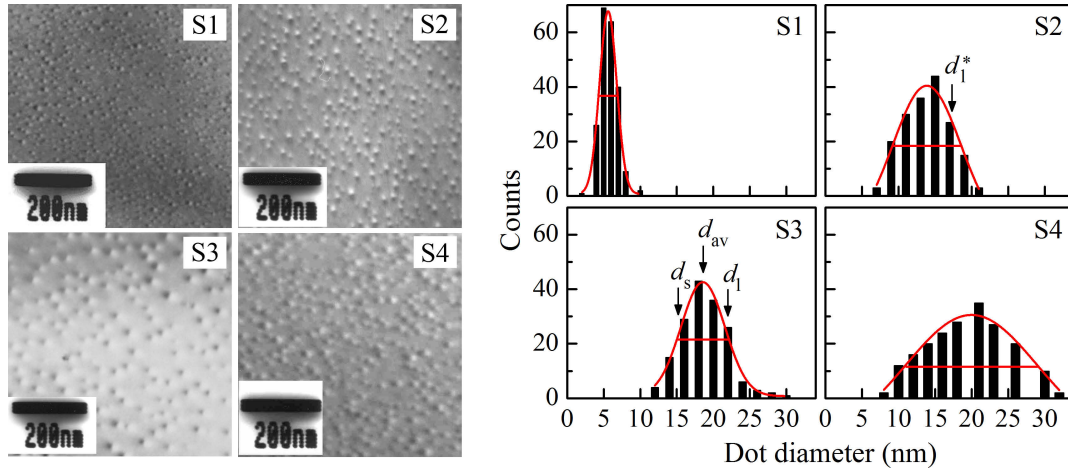


Figure 5-10: TEM plane-view images (panels on the left), and histograms of the QD diameter distribution (panels on the right) including the size dispersion fitted by Gaussian curves for the structures S1-S4. A histogram shows the incidences of finding a QD with a specific diameter in the TEM image within an area ranging from 0.3 to $0.5 \mu\text{m}^2$. The half width of a QD size distribution is marked by the horizontal line. The average diameter d_{av} and the large d_l and small d_s diameters defined by the half width of the QD size distribution are exemplarily indicated for the structure S3. For the structure S2, d_1^* is taken as the diameter corresponding to indirect band-gap QDs, see the caption of the Table 5-1.

It should be noted that the characterization of the heterointerface is based on the assumption of a nonuniform QD composition profile. Since the interface sharpness is expressed as the degree of the spatial separation between the two different kinds of materials, it can be described in terms of their concentrations. A nonuniform composition profile means that the concentration of the QD material gradually decreases from the InAs core to the edge of the core-surrounding (In,Al)As diffusion layer which, in turn, is bordered on the AlAs matrix layer. A thick diffusion layer corresponds to a small gradual change in the concentration. The material intermixing and/or strain transfer can change the profile of the (In,Al)As concentration and, correspondingly, the interface sharpness [257]. By the variation of the thickness of the (In,Al)As QD layer the influence of the interdiffusion and the finite strain field on the carriers can be controlled, since the carrier wave function is mainly localized at the center of the QD, see Subsection 1.1.2 for details. For instance, the decrease in the diffusion layer thickness enhances the strain energy and the InAs-AlAs intermixing. This kind of nonuniform profile describes a radial distribution of the concentration [258, 259]. It can be used to delineate the composition profiles of the studied QD structures.

In addition to the TEM images, the photoluminescence of the QD ensembles provides information on the heterointerface. Normalized PL spectra of the studied structures are illustrated in the Fig. 5-11. The PL spectra were measured at the temperature $T = 5$ K, and were excited by a He-Cd laser with a photon energy of 3.81 eV. Two PL bands DQD and IQD are observed in the spectra which result from the exciton recombination in QDs with direct and indirect band gaps, respectively. As shown in the Subsection 5.1.1, the intensity of the DQD emission band decays during a few nanoseconds, while the decay time of the IQD band amounts to hundreds of microseconds. These two types of QDs

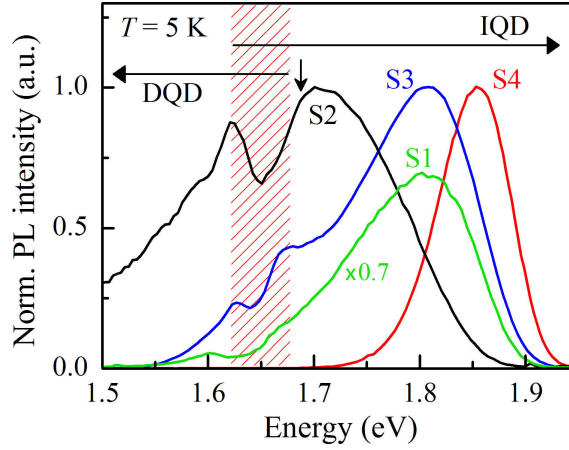


Figure 5-11: Normalized PL spectra of the different (In,Al)As/AlAs QD structures S1-S4 at $B = 0$ T, excited by a He-Cd laser with a power density of 10 W/cm^2 . The PL intensity of the S1 structure is multiplied by 0.7 for better visibility. The dashed area marks the Γ -X-mixing region. The vertical arrow indicates the energy of the exciton recombination in QDs with the typical diameter d_1^* for S2, see the caption of Table 5-1.

coexist in the ensembles of the (In,Al)As/AlAs QDs. The DQD PL band of the S1, S2, and S3 structures is at energies below 1.65 eV. This energy is similar to the Γ -X-crossing energy which has been evaluated from the electron-SFRS resonance profile of the sample #2890, see the Fig. 5-2 (c). At this energy the oscillator strength of the Γ -X mixed exciton has its maximum; the Γ -X-mixing region is marked by the dashed area in the Fig. 5-11. Strictly speaking, the Γ -X-crossing energy designates the boundary between the direct and indirect band-gap (In,Al)As/AlAs QDs.

Since the shape of the PL emission reflects the distribution of QD sizes, a relation between the parameters characterizing the spectra and the geometric quantities of the average diameter d_{av} and size dispersion S_d can be established. This relation has the following features:

- The increase in d_{av} and S_d for the as-grown structures S1 and S2 leads to a red-shift from 1.8 to 1.7 eV and an increase in the full width at half maximum (FWHM) of the IQD band from 130 to 170 meV. Moreover, the intensity of the DQD band is enhanced by about one order of magnitude in S2 compared to S1.
- The increase in d_{av} and S_d , resulting from the high-temperature annealing of S2 and its transformation to the S4 structure, gives rise to a blue-shift of the IQD band from 1.7 to 1.85 eV and a decrease in the FWHM from 170 to 75 meV. The annealing also causes a reduction in the DQD band intensity for the S3 structure and the disappearance of this band for S4.

In order to explain these results the following aspects characterizing the energy of the optical transitions must be taken into account: (i) the quantum confinement energy which decreases with increasing QD size, and (ii) the band gap energy of the (In,Al)As layer in the QD which increases with a decreasing InAs fraction. In lens-shaped QDs the QD height mainly defines the confinement energy. The average QD composition can

be evaluated from a comparison of the IQD band energy position with results of model calculations*. The determined concentrations of InAs are collected in the Table 5-1. The red-shift and broadening of the IQD band, going from the S1 to the S2 structure, are caused by a weaker quantum confinement and larger size dispersion S_d . The QD composition is not changed remarkably. In comparison to the S2 structure, the IQD band of S4 shifts to higher energies due to a larger band gap energy of the (In,Al)As layer with a small InAs fraction in the QD alloy composition. This compensates for the decrease in the quantum confinement energy owing to the annealing induced increase in the QDs height based on a fixed aspect ratio. Moreover, one would expect that the thermal annealing leads to a more homogeneous QD size distribution and thus to a reduction in the PL line width. However, the FWHM of the IQD band decreases with larger size dispersions S_d . This narrowing is explained by the shift of the QD energy levels toward the level of the wetting layer. It can be described by a shallow quantum well which is only slightly influenced by changes in the width or height [260].

The energy separation between the optical transitions of the direct and indirect excitons weakly depends on the QD size, shape, and composition [228, 229]. Therefore, the change in the intensity of the DQD band relative to that of the IQD band reflects the change in the relative layer density of the direct band-gap QDs. This density is a function of the QD size and composition. The disappearance of the DQD band in the emission of the S4 structure results from the lower InAs fraction in the QD alloy composition. This, in turn, gives rise to a conversion of the band gap from a direct to an indirect one.

5.2.2 Time-Resolved Photoluminescence

The study of the exciton recombination dynamics and its dependence on the interface sharpness requires that the exciton population does not exceed one exciton per QD. In order to avoid an accumulation of electron-hole pairs and a formation of multiexciton complexes in the indirect band-gap QDs with long exciton lifetimes the optical excitation has to be carefully chosen. The number of excitons, which are photogenerated in the QD surrounding matrix and captured in the QDs per laser pulse, is mainly determined by the pulse energy density. However, it is independent of the QD band gap structure because the relaxation from the excited Γ -state to the X-valley ground state is very fast. The repetition frequency of the excitation pulses should be reduced to a level that there is sufficient time for the excitons to recombine between subsequent pulses, so that multiexciton complexes are not created. Since the lifetime of the indirect excitons exceeds that of the direct ones by up to five orders of magnitude, the pulse repetition frequency as well as the average excitation density should decrease correspondingly[†]. Hence, the

*The recombination energy of a QD exciton depends on the QD size, while the emission at a certain spectral energy is contributed by QDs with similar sizes. Thus, the PL band maximum corresponds to recombinations in QDs characterized by the average diameter. The comparison between the measured energy of the PL maximum and the calculated optical transition energies in QDs with known average sizes allows to determine the average composition of these QDs. The calculation of the confined energy levels of QDs with different diameters as a function of the QD composition, and the determination of the InAs fraction in the (In,Al)As QDs as a function of growth parameters are given in Ref. [229].

[†]As an example, for direct band-gap (In,Ga)As/GaAs QDs with typical exciton lifetimes of about 1 ns, which are excited by picosecond pulses (at 13.2 ns pulse separation), the average exciton population per dot is smaller than 0.15, when an average excitation density of 8 W/cm² with an energy density of 100 nJ/cm² per pulse is used [248].

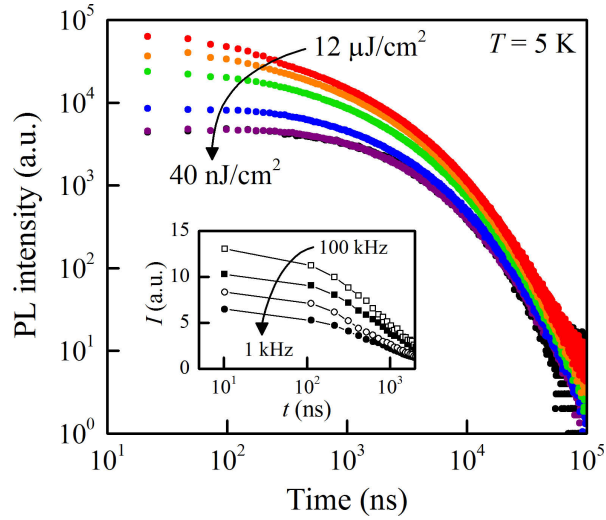


Figure 5-12: Low-temperature PL kinetics obtained at the maximum of the IQD band at 1.856 eV of the S4 structure using different energy densities of the excitation pulse, presented in double-logarithmic scale. The excitation pulse ends at $t = 10$ ns. The pulse repetition frequency is 1.5 kHz, which is sufficiently low to monitor a PL intensity decrease by five orders of magnitude between successive laser pulses. The excitation pulse densities P (given in nJ/cm^2) are, from top to bottom, 1.2×10^4 , 4×10^3 , 1.2×10^3 , 400, 120, and 40. The inset demonstrates the PL kinetics measured at $P = 900 \text{ nJ}/\text{cm}^2$ for different pulse repetition frequencies, from top to bottom (in kHz): 100, 30, 10, and 1. While for the time axis a logarithmic scale is chosen, the intensity axis is scaled linearly in order to underline the changes in the PL decay.

recombination dynamics of single excitons in the (In,Al)As/AlAs QDs can be studied.

The time-resolved PL experiments were established by the third harmonic (3.49 eV) of a Q-switched Nd:YVO₄ laser with a pulse duration of 5 ns. The pulse repetition frequency was varied from 1 to 100 kHz and the pulse energy density was chosen between 0.04 and $12 \mu\text{J}/\text{cm}^2$. The emitted light was dispersed by the third stage of the triple-spectrometer and detected by the GaAs photomultiplier operating in the time-correlated photon-counting mode. In order to monitor the PL decay in a wide temporal range up to 0.5 ms the time resolution of the detection system was varied between 1.6 and 200 ns. Details on the experimental setup can be found in the Section 2.3.

The Fig. 5-12 shows the low-temperature PL kinetics measured at the IQD band maximum of the S4 structure for different excitation pulse energy densities. The power-dependent behavior of the kinetics of the other structures is similar to the one presented. The transient PL data are plotted on a double-logarithmic scale which is convenient to illustrate the nonexponential character of the decay over a wide range of times and PL intensities. The recombination kinetics demonstrates two distinctive stages: (i) a rather flat PL decay immediately after the excitation pulse up to approximately $1 \mu\text{s}$ and, subsequently, (ii) a reduction in the PL intensity which can be described by a power-law function $I(t) \sim (1/t)^\alpha$. In the case of the stage (i) a high-power excitation results in a fast decay of the exciton PL. It can be assigned to the recombination of multiexciton complexes [250]. By decreasing the power down to $P = 120 \text{ nJ}/\text{cm}^2$ the decay decelerates, and below this value the power does not affect the decay times. Here, the regime of single

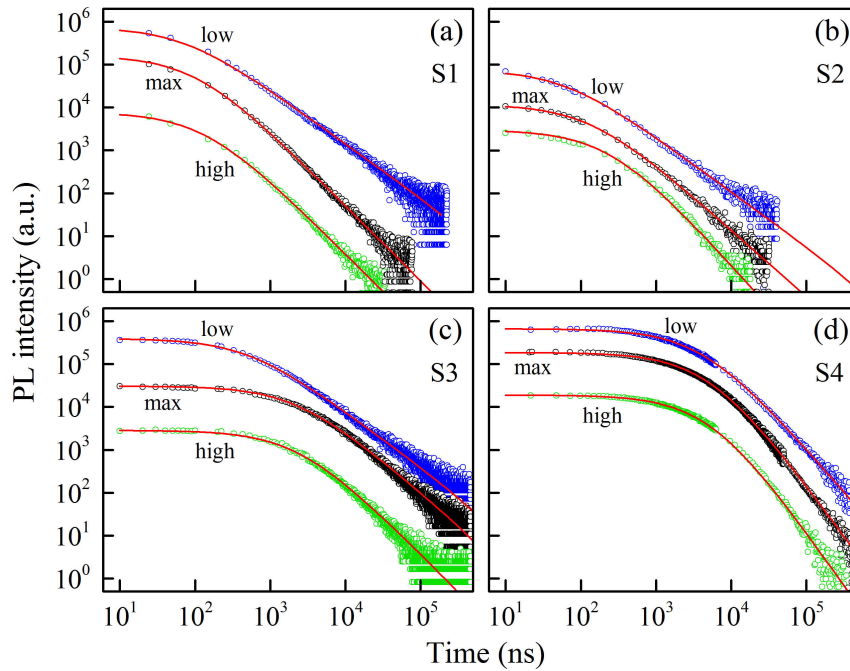


Figure 5-13: PL kinetics for the structures S1-S4 at the intensity maximum (max) and at half of this maximum on either the high-energy (high) or low-energy (low) side of the IQD emission band, $T = 5$ K and $P = 40$ nJ/cm². The pulse repetition frequency is 1.5 kHz, and the excitation pulse ends at 10 ns. The PL intensities are scaled by the factors 10 (low) and 0.1 (high) for better visualization. The red-colored solid lines show the modeled results with the distribution $G(\tau)$ described by the Eq. (5.19) and the parameters listed in the Table 5-1. For S2 the curve, marked by low, corresponds to the exciton recombination in QDs with the diameter d_1^* .

exciton recombination is reached. Considering the absorption coefficient α_{abs} for the laser light in the AlAs matrix [261] together with the QD density and average diameter, the average number of excitons captured in a QD per pulse is estimated to about 0.3^\ddagger for $P = 120$ nJ/cm². An increase in the repetition rate of the excitation pulses at fixed pulse power also results in an acceleration of the initial kinetics stage, as shown in the inset of Fig. 5-12. Since each pulse should excite the sample when it has reached its equilibrium state, for the following studies P is chosen to 40 nJ/cm². It corresponds to an average QD exciton population of 0.1 per pulse at a repetition frequency of 1.5 kHz which is equal to a time interval of 670 μ s between subsequent pulses.

In the Fig. 5-13 the PL decays for the structures S1-S4 are illustrated for different detection energies. The selection of these energies provides information on the exciton recombination in QDs with different characteristic sizes in the ensemble. The energy of the intensity maximum of the IQD band (the curves are labeled by max) corresponds to the recombination in QDs with the diameter d_{av} . The energies of the half maxima (curves denoted by high and low) refer to the recombinations in QDs with the diameters d_s and d_l , respectively. The PL decays show the following features: (i) the second decay

[‡]The average number of excitons $\langle N \rangle = (\alpha_{\text{abs}} d_{\text{av}} / d_{\text{QD}}) P / E_{\text{exc}}$ includes the absorption cross section which takes the value of $6 \times 10^4 \text{ cm}^{-1} \cdot 19.6 \times 10^{-7} \text{ cm} / (8.5 \times 10^{10} \text{ cm}^{-2}) = 1.4 \times 10^{-12} \text{ cm}^2$.

stage starts 100 ns after the end of the excitation pulse in the unannealed structures S1 and S2, while for the annealed structures S3 and S4 it begins a few microseconds after the pulse. (ii) For each structure the exponent α of the power-law decay is determined by fitting the second stage of the decay curves with the form $I(t) \sim (1/t)^\alpha$. The exponent α increases across the IQD band from the low- to the high-energy side. The PL decay obviously depends on sample characteristics; as will be shown in the next Subsection, it is affected by both the typical QD size in the ensemble and the interface sharpness. In order to quantitatively describe the effect of the dot size and interface sharpness on the lifetime of the indirect exciton in the (In,Al)As/AlAs QD ensembles, the distribution function $G(\tau)$, which controls the observed PL kinetics, will be evaluated.

5.2.3 Exciton Lifetime Distribution

Nonexponential decays of the exciton PL intensity $I(t)$ are frequently described by stretched exponentials of the form $I(t) \propto \exp[-(t/\tau)^\beta]$, including a constant lifetime τ and a dispersion factor β [262, 263]. The stretch parameter $0 < \beta \leq 1$ qualitatively defines the underlying distribution function $G(\tau)$: a broad distribution results from $\beta \ll 1$, while for a narrow one β is about 1. However, the evaluation of the lifetime distribution on the basis of the stretched-exponential model is mathematically complicated and feasible for specific β -values only, see Ref. [249] and references therein. Alternatively, the distribution $G(\tau)$ can be determined by the equation

$$I(t) = \int_0^\infty G(\tau) \exp\left(-\frac{t}{\tau}\right) d\tau. \quad (5.17)$$

Here, $G(\tau)$ is established via either the numerical solution of the integral equation (5.17) [264], or an assumed analytical expression of $G(\tau)$ with a set of fitting parameters. Among different analytical expressions such as normal and Lorentzian distributions, the distribution $G(\tau)$ in a QD ensemble can be modeled by a log-normal function which is additionally scaled with $1/\tau^2$:

$$G(\tau) = \frac{A}{\tau^2} \exp\left[-\frac{\ln^2(\tau_0/\tau)}{w^2}\right], \quad (5.18)$$

where A is a constant, τ_0 characterizes the maximum of the exciton lifetime distribution, and w is a dimensionless parameter specifying the distribution width. The log-normal distribution was used to describe the nonexponential decay of the exciton PL intensity over two to three orders of magnitude for different QD systems with a continuous distribution of direct exciton lifetimes. Among them are ensembles of CdSe/ZnSe colloidal QDs [265], and dye molecules embedded in photonic crystals [266].

In the (In,Al)As/AlAs QDs the excitons predominantly recombine via radiative recombination[§]. Therefore, the dispersion of the radiative recombination times in the ensemble causes the nonexponential PL decay. In order to derive the exciton lifetime

[§]The long exciton lifetimes in the (In,Al)As/AlAs QDs indicate that carriers captured in the QDs predominantly recombine through photon emission. A small fraction of QDs containing nonradiative centers of about 5% would decrease the PL decay time down to a few μ s due to the long-distance transfer of the exciton energy to the nonradiative centers [267].

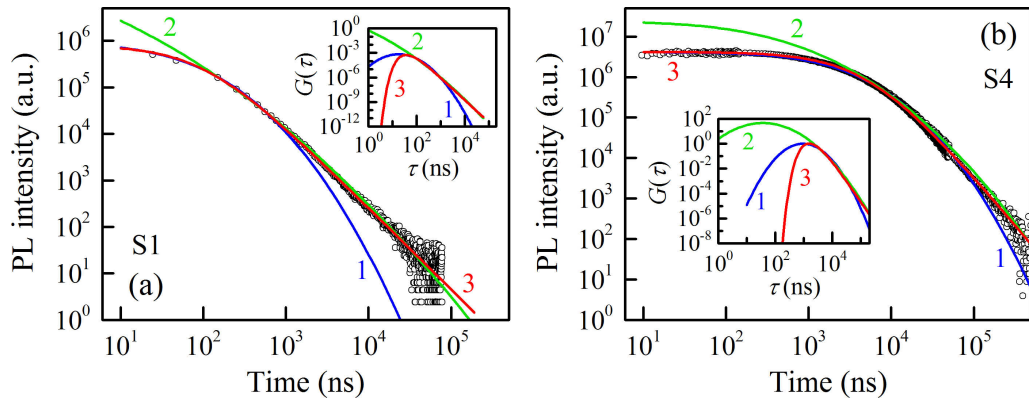


Figure 5-14: Experimental and simulated PL decays of the (In,Al)As/AlAs QDs for the samples S1 and S4, measured at the IQD band maximum for $T = 5$ K. The excitation density is $P = 40$ nJ/cm², and the pulse repetition frequency is 1.5 kHz. The end of the excitation pulse corresponds to a time of 10 ns. The modeling of the experimental PL decays (open circles) by the log-normal-like and phenomenological distribution functions $G(\tau)$ is shown by the lines. The corresponding distribution functions are depicted in the insets. (a) Structure S1: curves 1 and 2 are based on model calculations using the log-normal-like distribution of the Eq. (5.18) with the parameter sets $(\tau_0 = 0.2 \mu\text{s}, w = 1.55)$ and $(\tau_0 = 0.05 \mu\text{s}, w = 3.50)$, respectively. The curve 3 is for $G(\tau)$ of the Eq. (5.19) with the parameters $\tau_0 = 0.1 \mu\text{s}$ and $\gamma = 2.75$. (b) Structure S4: curves 1 and 2 are also modeled by $G(\tau)$ of the Eq. (5.18) with the parameter sets $(\tau_0 = 5.8 \mu\text{s}, w = 1.35)$ and $(\tau_0 = 3.0 \mu\text{s}, w = 2.10)$, respectively. Curve 3 is given by the phenomenological $G(\tau)$ with $\tau_0 = 5.2 \mu\text{s}$ and $\gamma = 3.40$.

distribution $G(\tau)$ the PL kinetics are fitted by the Eq. (5.17) using the log-normal-like distribution of the Eq. (5.18). As illustrated in the Figs. 5-14 (a) and (b), this distribution only fits either the initial stage (curves 1) or the long-time stage (curves 2) of the temporal PL evolution, probed at the maximum intensity of the IQD band of S1 and S4. Hereby, different sets of parameters (τ_0, w) have been used, their values can be found in the caption of Fig. 5-14. Nevertheless, the log-normal distribution does not allow to describe the PL decay over the whole temporal range.

In order to describe the exciton PL decay for the studied structures over the whole dynamical range of five orders of magnitude the asymmetric distribution

$$G(\tau) = \frac{C}{\tau^\gamma} \exp\left(-\frac{\tau_0}{\tau}\right) \quad (5.19)$$

is proposed. Here, C is a constant, the exciton lifetime distribution has its maximum at τ_0/γ , and the parameter γ is defined as $\alpha + 1$. This phenomenological distribution suitably models power-law decays of the form $I(t) \sim (1/t)^\alpha$. By use of a double-logarithmic scale the power-law decay $(1/t)^\alpha$ represents a line with a slope α . Note, in knowledge of the exponent α of the experimental decay curve, only the free parameter τ_0 is required to describe the PL decay by the phenomenological $G(\tau)$. The red-colored decay curves, shown in the Fig. 5-14 and labeled by 3, are evaluated from the Eq. (5.19). The experimentally determined α -values, see Table 5-1, yield the parameters $\gamma = 2.75$ and 3.40 for the structures S1 and S4, respectively. The calculations fit the experimental data over the whole temporal range from the low-nanosecond to the high-microsecond region. The

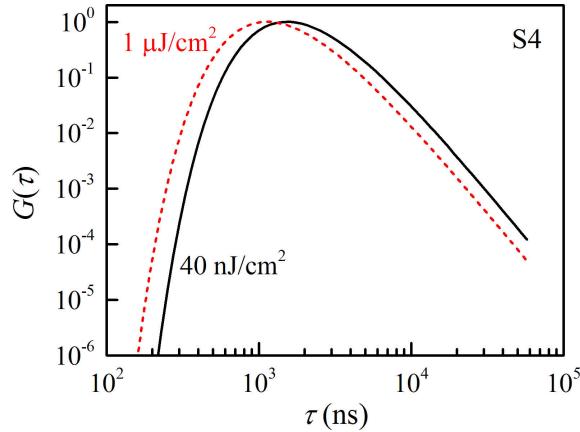


Figure 5-15: Normalized distribution functions $G(\tau)$ for QDs with the same average diameter $d_{av} = 19.6$ nm in structure S4. The two dependencies result from the fittings of the recombination kinetics belonging to the different excitation energy densities of 40 nJ/cm² (solid line) and 1 μ J/cm² (dashed line).

fits are obtained for the distributions $G(\tau)$ which are depicted in the insets of Fig. 5-14 by the red-colored lines. Hereby, the fit parameters $\tau_0 = 0.1$ μ s for S1 and $\tau_0 = 5.2$ μ s for S4 have been taken into account. The phenomenological distribution function strongly deviates from the log-normal one for lifetimes smaller than τ_0 . However, this difference hardly influences the modeling of the initial stage ($t \leq \tau_0$) of the PL decays. One can conjecture that the decay curves are mainly contributed by the recombination of excitons with lifetimes exceeding the average lifetime τ_0 . In turn, the parameter γ which is the exponent of the long-lifetime tail of $G(\tau)$ can be used as a qualitative measure of the effective width of the phenomenological $G(\tau)$. Hereby, an increase in γ reduces the dispersion of the τ -values.

It should finally be noted that the filling of the QDs with multiexciton complexes at high excitation densities distorts $G(\tau)$. The Fig. 5-15 illustrates the distribution functions $G(\tau)$ obtained via fitting of two different recombination kinetics of S4: in the case of $P = 40$ nJ/cm² the average number of excitons $\langle N \rangle$ in a single QD is smaller than one, while for 1 μ J/cm² multiexciton complexes ($\langle N \rangle \approx 2.5$) have to be taken into account. The distribution maximum is shifted to shorter times due to multiexciton QD occupation. Thus and as it has initially been postulated, the determination of $G(\tau)$, which is intrinsic for the ensemble of indirect band-gap QDs, requires an average exciton population in the dots being less than unity.

5.2.4 Impact of Interface Sharpness

The exciton lifetime distributions $G(\tau)$ for the four structures S1-S4 are evaluated from the fitting of the decay curves, presented in Fig. 5-13, by using the Eqs. (5.17) and (5.19). The values of the fit parameters $\gamma = \alpha + 1$ and τ_0 are collected in the Table 5-1. The fit results are illustrated by the solid lines in the Fig. 5-13. In what follows, the features that allow to distinguish between the effect of the QD size and interface sharpness on the exciton lifetime will be highlighted.

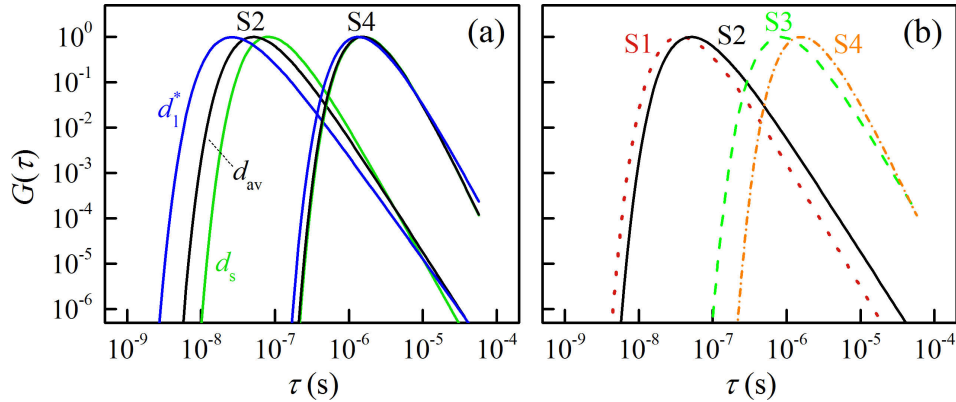


Figure 5-16: Distributions $G(\tau)$ in dependence on QD diameters. (a) $G(\tau)$ for QDs with the diameters $d_1^* = 17$ nm, $d_{av} = 13.8$ nm, and $d_s = 9$ nm (from left to right) for the structure S2 and for QDs with diameters $d_1 = 28$ nm, $d_{av} = 19.6$ nm, and $d_s = 12$ nm for structure S4. (b) Comparison of $G(\tau)$ for QDs with average diameters in the different samples. The distributions are shown for $d_{av} = 5.5$ nm (S1), 13.8 nm (S2), 18.3 nm (S3), and 19.6 nm (S4).

The relative change in τ_0 and γ by varying the QD diameter from d_s to d_1 is larger in the as-grown structures S1 and S2 than in the annealed structures S3 and S4. This is illustrated by the Fig. 5-16 (a) for the structures S2 (with smaller size dispersion $S_d = 60\%$) and S4 (with larger size dispersion $S_d = 75\%$). Moreover, the decrease of τ_0 and γ with increasing QD diameter is a common feature for each structure. Despite the large difference in the QD diameter d_{av} for S1 and S2, these structures have similar distributions of the exciton lifetime, as depicted in the Fig. 5-16 (b). However, the comparison of $G(\tau)$ in the QD ensembles with similar diameters ($d_1^* = 17$ nm, $d_{av} = 18.3$ nm, and $d_{av} = 19.6$ nm for the structures S2, S3, and S4, respectively) highlights a strong increase in the exciton lifetime by about two orders of magnitude with decreasing interface sharpness. Thus, the interface sharpness considerably affects the exciton lifetime in the indirect band-gap (In,Al)As/AlAs QDs, while the dependence of τ on the QD size is much weaker. Nevertheless, the decrease of τ_0 with rising QD diameter from d_s to d_1 for each of the studied structures indicates that the effect of the QD size on the recombination time cannot fully be neglected.

In the following a relation between the lifetime τ of the indirect exciton and the thickness D of the (In,Al)As diffusion layer at the QD-matrix interface will be derived. The wave function of the QD exciton can be written as the product of the electron and hole wave functions:

$$\Psi(\mathbf{r}_e, \mathbf{r}_h) = \Psi_e^X(\mathbf{r}_e) \Psi_h^\Gamma(\mathbf{r}_h) V_C(\mathbf{r}_e - \mathbf{r}_h), \quad (5.20)$$

where \mathbf{r}_e and \mathbf{r}_h are the coordinate vectors of the electron and hole, and $V_C(\mathbf{r}_e - \mathbf{r}_h)$ describes the electron-hole Coulomb interaction. The exciton recombination rate is proportional to $V_C^2(0) |\langle \Psi_e^X \nabla \Psi_h^\Gamma \rangle|^2$. The wave functions can be decomposed into the products of the Bloch waves and envelope wave functions $\chi_e(\mathbf{r})$ and $\gamma_h(\mathbf{r})$. Assuming that ∇ only acts on the Bloch amplitudes, the exciton recombination rate is proportional to the square

of the modulus of the convolution of the envelopes:

$$\tau_{\text{Ex}}^{-1} = \int \chi_e(\mathbf{r}) \gamma_h^*(\mathbf{r}) d^3r. \quad (5.21)$$

To estimate this integral the following form of the envelopes in the vicinity of the QD-matrix interface at $z = 0$ is proposed:

$$\begin{aligned} \chi_e(z) &= \exp(iqz) \sum_k A(k) \exp(ikz), \\ \gamma_h(z) &= \sum_p B(p) \exp(ipz), \end{aligned}$$

where $q = \pi/a$, a is the lattice constant, and A as well as B are coefficients which can be evaluated from the boundary conditions. They are constants in the infinite crystal, but depend on the electron and hole momenta \mathbf{k} and \mathbf{p} in the QDs. The summation of these values spreads over $k, p \sim 1/L$, where $L \gg a$ is the dot size (for the studied lens-shaped QDs L is the height of the QD). Thus, it can be assumed that $k, p \ll q$ and the value of the exciton recombination rate at the QD-matrix interface is determined by the integral:

$$\tau_{z,\text{Ex}}^{-1} = \int \exp[i(p - k + q)z] dz, \quad (5.22)$$

which is zero far from the interface due to the oscillating factor $\exp(iqz)$. At a sharp interface ($p \approx k$), $\tau_{z,\text{Ex}}^{-1}$ can be estimated to

$$\tau_{z,\text{Ex}}^{-1} \sim \frac{1}{iq} \sim \frac{ia}{\pi}. \quad (5.23)$$

For the integration over the dot interface, $\tau_{z,\text{Ex}}^{-1}$ can be approximated by the ratio between the number of atoms located at the interface and the total number of atoms in the QD. At a diffused interface, p and k smoothly vary with the position inside the interface layer: $p(z) = \sqrt{2m_h^*[E - V_{\text{di}}(z)]}$ and $k(z) = \sqrt{2m_e^*[E - V_{\text{di}}(z)]}$, where $V_{\text{di}}(z)$ is the potential profile of the diffused interface, and m_h^* as well as m_e^* are the effective masses of the hole and electron, respectively. Then the recombination rate takes the form

$$\tau_{z,\text{Ex}}^{-1} = \int_{-\infty}^{+\infty} \exp\{i[p(z) - k(z) + q]z\} dz. \quad (5.24)$$

Considering the integrand in the Eq. (5.24) as a function of the complex variable z , the integration contour can be displaced from the real axis into the upper half plane up to the nearest singularity z_p of the potential $V_{\text{di}}(z)$. This value is about iD , where D is the characteristic thickness of the diffused interface. For

$$V_{\text{di}}(z) = \frac{V_0}{1 + \exp(-z/D)}$$

the value of z_p is given by $i\pi D$; the actual value of z_p depends on the model for the interface. Therefore, the integral in the Eq. (5.24) contains the exponential factor $\exp(iqz_p) \sim \exp(qD)$. In analogy to Eq. (7) in Ref. [268], the integral in the Eq. (5.24)

is evaluated to

$$\tau_{z,\text{Ex}}^{-1} \sim \frac{\exp(-qD)}{q} \sim \frac{a}{\pi} \exp\left(-\frac{D}{a}\right). \quad (5.25)$$

Note, the estimations in Eqs. (5.22)-(5.24) suppose a large size of the QD. A decrease in the QD size, e.g., in its height, causes an increase in the electron energy and a reduction in the hole energy. It is due to the size quantization and the nonzero value of the electron and hole momenta which is about $\pi\hbar/L$. Taking into account this fact, π/L must be added to the exponent in the Eq. (5.24), i.e., q is substituted by $q+\pi/L$ in the Eqs. (5.24) and (5.25). Finally, the Eq. (5.25) adopts the form

$$\tau_{z,\text{Ex}}^{-1} \sim \frac{a}{\pi} \exp\left[-\frac{D}{a}\left(1 + \frac{a}{L}\right)\right], \quad (5.26)$$

and the lifetime of the indirect exciton can be described by

$$\tau \sim \exp\left(\frac{D}{a} + \frac{D}{L}\right). \quad (5.27)$$

Thus, an increase in the thickness D of the diffusion layer at the QD-matrix interface results in an exponential enhancement of the lifetime of the indirect exciton due to its momentum scattering at the interface. It is reasonable to assume that the ratio $D/a \geq 1$ weakly changes with the QD size for a particular structure type. Hence, the exciton lifetime is characterized by the second term $D/L < 1$, and decreases with increasing QD size. It is in agreement with the experimental results, see, for example, the data for structure S2 shown in the Fig. 5-16 (a). Furthermore, for a large ratio $D/a \gg 1$, i.e., for a very smooth interface, the exciton lifetime is not determined by the scattering at the heterointerface, but by phonon scattering processes. When the rate of the non-phonon recombination becomes smaller than that of the phonon emission, the exciton recombination is mainly defined by the phonon scattering. For instance, in the case of a very high annealing temperature of 950°C, which leads to a very smooth QD-matrix interface, phonon replicas appear in the spectrum of the QD PL [260].

Finally, the impact of the interface sharpness on the effective width of the $G(\tau)$ -distribution will be qualitatively discussed. Due to momentum scattering at the QD-matrix interface the exciton lifetime is proportional to $\exp(D/a + D/L)$. Therefore, the argument $D/a + D/L$ varying for different QDs should define the width of the lifetime distribution. Since the dispersion of a varying quantity is inversely proportional to the square root of its mean value, the width of $G(\tau)$ should decrease with increasing $D/a + D/L$. The experimental data tend to confirm this expectation: for QDs with similar sizes the effective width of $G(\tau)$, which behaves like $1/\gamma \sim 1/\tau_0$, becomes narrower with increasing thickness of the diffused layer, as depicted in the Fig. 5-16 (b). On the contrary, for $D/a \approx \text{const.}$ an increase in the ratio D/L for larger QDs reduces $D/a + D/L$ and broadens $G(\tau)$. A corresponding decrease in the value γ is shown in the Table 5-1.

5.3 Spin Dynamics of the Indirect Exciton

The fine structure of the indirect exciton revealed by the SFRS via Γ -X mixing of the conduction band levels as well as its recombination dynamics controlled by fundamental

material parameters have been highlighted in the previous Sections. It has been demonstrated that, for instance, the spin-orbit interaction for the X-valley electron is negligible, the light-hole and heavy-hole states at the Γ -point are not mixed, and the in-plane QD localization potential is isotropic. Furthermore, the lifetime of the exciton in the indirect band-gap (In,Al)As QDs with type-I band alignment can reach hundreds of microseconds. According to these properties the (In,Al)As/AlAs QD structure is regarded as promising candidate for quantum applications where long exciton lifetimes and an undisturbed carrier environment are necessary for coherent spin manipulations [269]. While such requirements of spin-based semiconductor applications have been proven to be fulfilled, this Section makes the first step toward the spin dynamics of the indirect exciton: the magnetic field induced circular polarization of the exciton PL in the stationary and time-resolved domain will be presented. The brief discussion[¶] includes the magnetic field and temperature dependence of the exciton spin relaxation time.

In the Fig. 5-17 (a) the magnetic field dependence of the circular polarization degree $\rho_c = (I^+ - I^-)/(I^+ + I^-)$ is illustrated for the structure S4 (#1498), see details on the sample in the Table 5-1. The experiment was performed in the Faraday geometry, and linearly polarized laser light with an energy of 3.33 eV was used for excitation. The circularly polarized PL intensities I^+ and I^- have been integrated over the range of ± 0.5 meV at $E_{\text{det}} = 1.85$ eV. This energy corresponds to the maximum of the indirect band-gap QD PL, which is depicted in the Fig. 5-11. The polarization degree ρ_c rather weakly increases for low magnetic field strengths, while at high magnetic fields the increase in ρ_c is stronger. By comparison, the magnetic field dependence of ρ_c for the sample #2890, shown in the panel (b), is strictly linear at $E_{\text{det}} = 1.82$ eV probing indirect band-gap QDs (corresponding PL spectrum is illustrated in Fig. 5-1 (b)). While the magnetic field dependent evolutions for both samples are different, the magnitudes of ρ_c at $B = 10$ T are comparable. On the contrary, at lower detection energy where direct excitons also contribute to the PL the circular polarization degree for sample #2890 saturates at high magnetic fields, as depicted by the solid squares in the Fig. 5-17 (b). The negative sign of ρ_c originates from a change in the exciton g factor sign, as discussed in Subsection 5.1.3. At low magnetic fields ρ_c shows a very similar slope independent of the detection energy. The impacts of the magnetic field and the exciton type on the stationary ρ_c are assumedly based on changes in the exciton spin relaxation.

The circular polarization degree can be described by the populations n^+ and n^- of the bright exciton levels $|+1\rangle$ and $|-1\rangle$ in the form $\rho_c = (n^+ - n^-)/(n^+ + n^-)$. The population of a state depends on the respective generation rate G of the exciting light. In the case of linearly polarized excitation ($G^+ = G^-$), both exciton states can be expected to be equally populated at $t = 0$. Both populations are reduced by the radiative exciton recombinations characterized by the average lifetime τ_0 . In comparison to the spin relaxation specified by the time τ_s from the upper to the lower level, the spin scattering from the lower to the upper level is scaled by the partial thermalization of excitons to the lower energy state [270]. It is taken into account by the Boltzmann factor $\exp[-g_{\text{ind}}^{\parallel} \mu_B B / (k_B T)]$ ensuring that the excitons achieve the thermal equilibrium. The longitudinal g factor $g_{\text{ind}}^{\parallel} = -0.8$ of the indirect exciton is chosen to be negative and twice larger than $g_{\text{Ex}}^{\parallel}$. Altogether, the time-dependent populations can be derived – in

[¶]Details on the exciton spin dynamics are expected to be presented in the dissertation of D. Dunker.

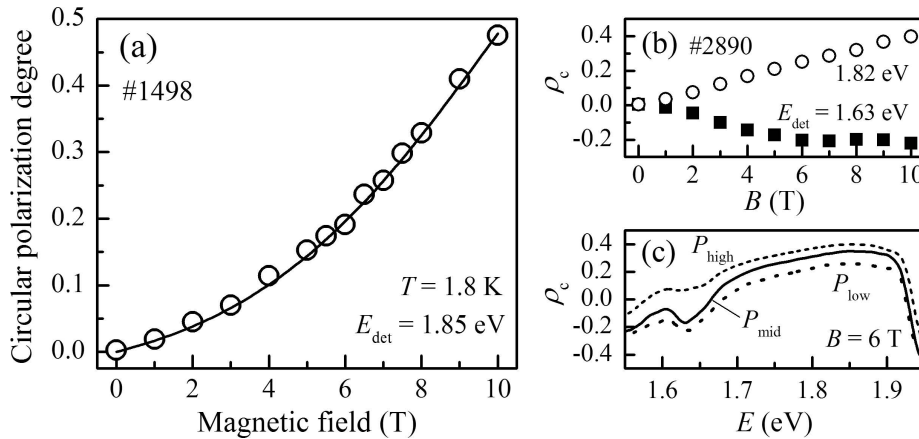


Figure 5-17: (a) and (b) Magnetic field dependence of the circular polarization degree ρ_c of the exciton PL for the samples #1498 (S4) and #2890. The temperature is $T = 1.8$ K, the above-wetting-layer excitation is linearly polarized and its power density is about $P_{\text{low}} = 1.2$ mW/cm². The error of ρ_c does not exceed the symbol size. For sample #1498: ρ_c is evaluated from the PL at the energy 1.85 eV. It is modeled by the Eq. (5.30) with $\tau_s = 100$ μ s. For sample #2890: the B -field behavior of ρ_c depends on the detection energy. At the Γ -X-crossing energy of 1.63 eV the polarization degree $\rho_c(B)$ saturates at about -21% . (c) Spectral dependence of ρ_c for three different excitation densities, measured at $B = 6$ T for sample #2890. At $P_{\text{high}} = 152$ mW/cm² the polarization degree is increased, particularly in the Γ -X-mixing region.

a simple form – from the following two-level rate equations [270, 271, 272]:

$$\frac{dn^+}{dt} = G^+ - \frac{n^+}{\tau_0} - \frac{n^+}{\tau_s} + \frac{n^-}{\tau_s} e^{-\frac{g_{\text{ind}}^{\parallel} \mu_B B}{k_B T}}, \quad (5.28)$$

$$\frac{dn^-}{dt} = G^- - \frac{n^-}{\tau_0} + \frac{n^+}{\tau_s} - \frac{n^-}{\tau_s} e^{-\frac{g_{\text{ind}}^{\parallel} \mu_B B}{k_B T}}. \quad (5.29)$$

It has experimentally been determined (not shown here) that the exciton lifetime is not changed by the magnetic field, i.e., $\tau_0(B)$ is constant. Considering the steady-state solution ($\frac{dn}{dt} = 0$) of Eqs. (5.28) and (5.29), the circular polarization degree is given by

$$\rho_c(\tau_s, B) = \frac{\exp\left(\frac{g_{\text{ind}}^{\parallel} \mu_B B}{k_B T}\right) - 1}{\left(\frac{\tau_s}{\tau_0} + 1\right) \exp\left(\frac{g_{\text{ind}}^{\parallel} \mu_B B}{k_B T}\right) + 1}. \quad (5.30)$$

The experimentally obtained $\rho_c(B)$ for sample #1498 can be described by the latter equation, as illustrated by the solid curve in Fig. 5-17 (a). The fitting yields a spin relaxation time of $\tau_s = 100$ μ s which considerably exceeds the average exciton lifetime $\tau_0 = 5.4$ μ s. A single spin relaxation time has been used for the description of the $\rho_c(B)$ -dependence. Nevertheless, the underlying exciton spin relaxation mechanism can be supposed to depend on the magnetic field strength. And, the nonlinear evolution of the circular polarization degree might be influenced by the interplay between the spin relaxation time and the exciton lifetime. By comparison, the circular polarization degree probed at $E_{\text{det}} = 1.63$ eV shows a saturation for $B > 6$ T. Since the energy corresponds

to the Γ -X-crossing energy, the saturation might be caused by the short lifetime of the direct exciton. Accordingly, a detailed study of the spectral dependence of the exciton spin relaxation in the (In,Al)As/AlAs QDs is required.

A further aspect of study is the dependence of the circular polarization degree on the excitation power. The Fig. 5-17 (c) shows $\rho_c(E)$ at $B = 6$ T and $T = 1.8$ K for three different power densities $P_{\text{low}} = 1.2$ mW/cm², $P_{\text{mid}} = 7.5$ mW/cm², and $P_{\text{high}} = 152$ mW/cm². The sample #2890 was excited at $E_a = 2.33$ eV. The increase in the power density leads to an enhancement of ρ_c . For instance, at the Γ -X-mixing energy the circular polarization degree of the exciton PL changes from -22% at P_{low} to $+7\%$ at P_{high} . Also, at the energy of 1.82 eV ρ_c increases from 25% at P_{low} to 39% at P_{high} . The rise in the absolute value of ρ_c can be attributed to an enhancement of the spin relaxation time at high power densities. While inelastic exciton-phonon scattering is not expected to depend on the density of the excited excitons, the momentum scattering via exciton-exciton collisions becomes more efficient [273]. Due to this elastic scattering the \mathbf{k} -vector of the exciton is frequently changed and, in turn, its Larmor frequency direction $\mathbf{\Omega}_{\mathbf{k}}$ changes randomly fast. Principally, the spin relaxation due to spin splitting can be suppressed by processes changing the direction of \mathbf{k} . Accordingly, the spin relaxation time, given by $\tau_s \propto (\mathbf{\Omega}_{\mathbf{k}}^2 \tau_p)^{-1}$, increases in that regime of $|\mathbf{\Omega}_{\mathbf{k}}| \ll \tau_p^{-1}$ dominated by collisions [59], where τ_p denotes the momentum relaxation time of the exciton. Bear in mind that the latter explanation is strictly valid for free excitons only. In the Γ -X-mixing region the contribution of the indirect excitons seems to dominate thus giving rise to a sign inversion of ρ_c . Since the lifetime of the indirect exciton is reduced by multiexciton formation, as demonstrated in Fig. 5-15, the impact of multiexciton complexes on the exciton spin relaxation in the indirect band-gap QDs should be clarified in future experiments.

In what follows, the direct measurements of the spin relaxation time of the indirect exciton are discussed. The circular polarization degree as a function of time and magnetic field is depicted in the Fig. 5-18 (a), obtained at $T = 1.8$ K for sample #1498. After the excitation pulse with a duration of 5 ns^{||}, ρ_c increases until it reaches an equilibrium value in the μs -time range. The evolution of $\rho_c(t)$ is nonlinear, and is characterized by $\rho_c(0) \neq 0$. The nonzero value at $t = 0$ can be attributed to an initial spin polarization due to a background doping with one type of carriers. The magnitude $\rho_c(0)$ then reflects the spin polarization of the resident carriers [274]. The time-dependence of ρ_c can be described by a two-level spin system including the exciton lifetime distribution $G(\tau)$. Accordingly, the circularly polarized PL intensities are expressed as

$$I^{\pm} = \int_{\tau_{\text{min}}}^{\tau_{\text{max}}} n^{\pm}(t, \tau, \tau_s, \Delta E_Z) G(\tau) d\tau. \quad (5.31)$$

Here, ΔE_Z is the Zeeman splitting energy of the bright exciton states, and the exciton spin relaxation time τ_s is the fitting parameter. Its magnetic field dependence is shown in Fig. 5-18 (b). At $B = 4$ T the spin relaxation time is about 200 μs , while it decreases to about 1 μs at 10 T. A $\tau_s \propto B^{-5}$ relation (see solid curve) describes the evaluated spin relaxation times well. As demonstrated in Subsection 1.2.2 by the Eq. (1.43), such a

^{||}The capture time of carriers in the (In,Al)As QDs, estimated by the rise time of the PL, is shorter than the used time resolution of about 1 ns. Details on the experimental setup can be found in Sec. 2.3.

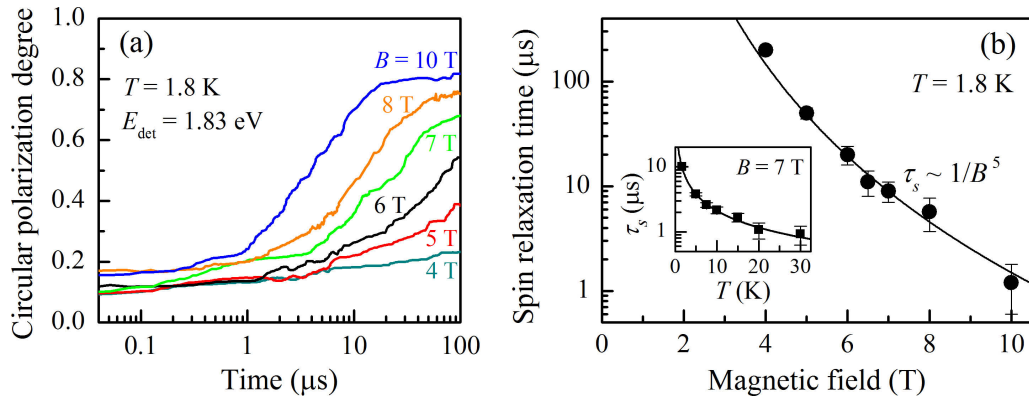


Figure 5-18: (a) Circular polarization degree ρ_c of the indirect exciton PL as a function of time for different magnetic fields. The sample #1498 was excited by a pulse of linearly polarized laser light with a width of 5 ns, the photon energy was 3.49 eV. The power density was chosen to excite less than one exciton per QD. (b) Dependence of τ_s on the magnetic field strength for $T = 1.8$ K. The spin relaxation times have been evaluated from fittings of $\rho_c(t)$ by means of the Eq. (5.31). The τ_s -values can be modeled by a $1/B^5$ -relation. The temperature behavior of τ_s for $B = 7$ T is depicted in the inset. The fitting curve is given by $\tau_s \sim T^{-0.85}$.

$\tau_s(B)$ -dependence is characteristic of acoustic phonon scattering which induces electron spin-flip transitions by mixing the electron Zeeman levels via spin-orbit interaction [275]. One could conjecture that this kind of single-phonon scattering mechanism accounts for the spin relaxation of the indirect exciton in the (In,Al)As QDs.

In addition to that, the exciton spin relaxation time is rather robust against an increase in the lattice temperature**. As illustrated in the inset of Fig. 5-18 (b), τ_s still ranges about $1 \mu\text{s}$ at $T = 30$ K for $B = 7$ T. It decreases as a function of $T^{-0.85}$. The temperature dependence is consistent within the picture of the one-phonon scattering [134]: the increase in the temperature leads to an increase in the phonon number. Hence, the exciton-phonon scattering and, correspondingly, the spin-flip transition probability are enhanced. If the spin scattering mechanism is based on the spin-orbit interaction mediated by single phonons, it can further be expected that the spin coherence time T_2 approaches the theoretical limit $T_2 \leq 2\tau_s$ [276]. In low magnetic fields the longitudinal spin relaxation time τ_s and, in turn, the spin coherence time T_2 may even reach the millisecond range. Note, for small B -fields the hyperfine interaction and exchange-induced spin scattering become significant thus introducing spin decoherence. These preliminary results have to be extended by systematic studies and evidenced by theoretical derivations which should also consider the Γ -X mixing in the (In,Al)As/AlAs QDs.

5.4 Conclusion

The mixing of the Γ - and X-valley electron states in the indirect band-gap (In,Al)As/AlAs QDs with type-I band alignment is revealed by the resonant spin-flip Raman scattering.

** Also, the average exciton lifetime τ_0 does not change with increasing temperature up to 30 K (not shown here).

By optically addressing the Γ -X mixed exciton, whose oscillator strength is inversely proportional to the square of the relative detuning of the excitation energy from the Γ -X-mixing energy, the s-shell fine structure of the indirect exciton is characterized. The longitudinal and transverse g factors of the indirect exciton, Γ_{hh} -valley heavy-hole, and X-valley electron are determined. The small value $g_{\text{hh}}^{\perp} = 0.03 \pm 0.05$ of the transverse heavy-hole g factor indicates that the light-hole and heavy-hole states are not mixed and suggests a spatial isotropy of the hole localization potential. The isotropic X-valley electron g factor is equal to 2.00 ± 0.01 due to the large band gap at the X-point and negligible spin-orbit interaction. The longitudinal g factor of the indirect exciton is $g_{\text{Ex}}^{\parallel} = 0.43 \pm 0.08$ probed at energies within the Γ -X-mixing regime. Its positive sign is evidenced by the spectral dependence of the magnetic field induced circular PL polarization. The spin-flip of an exciton, electron, or a hole is induced by the resonant scattering with an acoustic phonon. Hereby, the tilting of the magnetic field direction with respect to the QD growth axis leads to a mixing of the electron spin states thus allowing the SFRS processes of the electron and heavy-hole. The angular dependence of the exciton energies is evaluated from the linear Zeeman terms and the J_z^3 -term of the magnetic Hamiltonian using slightly modified Kohn-Luttinger bulk parameters. The theoretical description of an ensemble of two-level quantum systems shows that the SFRS spectrum principally contains the SFRS lines of both the direct and indirect level, while the SFRS line attributed to the Γ -X mixed state with average g factor has the lowest intensity. However, the SFRS of the Γ -valley electron cannot be observed experimentally because of its short lifetime and the broad dispersion of its g factor corresponding to the strong variation in the QD sizes. Besides the detection of the exciton- and heavy-hole-SFRS in QDs for the first time, the resonant SFRS has turned out to be a suitable technique to study properties of the electron and exciton that are indirect in momentum space.

The maximal radiative lifetime of the exciton, that is indirect in momentum space, in the (In,Al)As/AlAs QD ensembles approaches several hundreds of microseconds. The momentum of the indirect exciton is mainly scattered at the QD-matrix interface, accordingly, the exciton lifetime is determined by the sharpness of the diffused (In,Al)As layer at the heterointerface, while it weakly depends on the QD size. A high-temperature postgrowth annealing of the QD sample leads to a smooth heterointerface and thus to an enhancement of the exciton lifetimes. On the contrary, a large QD diameter reduces the exciton lifetime. Also, the formation of multiexcitons in a QD at high excitation power densities shortens the recombination kinetics of the indirect exciton. Due to the QD-matrix interface sharpness and the different dot sizes, multiple monoexponential PL decays with different lifetimes are superposed. As a result, the exciton recombination dynamics shows a nonexponential decay behavior that can be described by a power-law function. A phenomenological distribution function $G(\tau)$ of the radiative exciton recombination times in such QD ensembles models the power-law PL decay over five orders of magnitude.

In addition to the characterizations of the spin-level structure and the radiative recombination dynamics of the indirect exciton, its spin dynamics is studied via the stationary and time-resolved circular polarization degree ρ_c of the nonresonantly excited PL. The experimentally obtained temporal evolutions $\rho_c(t)$ are described by two-level rate equations combined with the exciton lifetime distribution $G(\tau)$. The exciton spin relaxation time τ_s exceeds $100 \mu\text{s}$ at low magnetic fields ($B \leq 4 \text{ T}$) for $T = 1.8 \text{ K}$. Since the dependence of τ_s on the magnetic field follows a $1/B^5$ -relation, the exciton-

phonon scattering is proposed as spin relaxation mechanism. It is further confirmed by the temperature dependence of $\tau_s \propto 1/T^{0.85}$ which is typical of phonon induced spin-flip transitions. The circular polarization degree sensitively responds to the excitation power density, the presence of resident carriers, and the type of the exciton in the (In,Al)As/AlAs QDs.

Chapter 6

Summary

By means of the resonant spin-flip Raman scattering (SFRS) technique fundamental spin interactions of carriers confined in low-dimensional semiconductors, their dependence on the local structure symmetry as well as the type and excitation state of the carrier complex are characterized – compare the conclusions in the corresponding Chapters. The scattering of the electron, hole, and exciton spins depends on the symmetry of the crystal lattice, quantum confinement potential, and magnetic field confinement. A Raman scattering process of a single spin requires that the carrier is localized in a potential whose symmetry is reduced by a perturbation. It defines the restrictions imposed by the angular momentum conservation, the electric dipole selection rules govern the optical transitions. The spin-flip scattering in semiconductor quantum wells and quantum dots is shown to be frequently based on the mixing between light-hole and heavy-hole states, induced by strain, well width fluctuations and/or shape anisotropies, as well as the level mixing resulting from the coupling of a tilted magnetic field to a nonzero in-plane magnetic moment of the electron and/or heavy-hole. In the case of spatially shifted localization centers of the carriers involved in the scattering the anisotropic exchange interaction can provide the spin-flip scattering process. The probability of anisotropic exchange between the photogenerated electron and hole is found to sensitively depend on the difference between their g factor values. In addition to that, the strength of the anisotropic exchange interaction – also between identically charged carriers – is estimated by the in-plane localization energy of the carriers. While in the quantum well structure the anisotropic exchange interaction is present, the isotropic exchange interaction and the carrier scattering via an acoustic phonon represent the main SFRS mechanisms in the studied quantum dots.

Aside from the spatial symmetry of the scattering complex, the spin-flip Raman scattering is also dependent on the type of carrier complex: it must be distinguished between the resonant excitation of a neutral exciton and charged exciton complexes where Pauli's exclusion principle becomes relevant. In singly charged quantum dots a novel optical resonance excitation is observed where an incident photon excites an electron-hole pair and simultaneously the resident electron to an excited Fock-Darwin state; in this excited carrier complex the electrons mutually change their spin states thus yielding an electron-SFRS. Since strong magnetic fields, close-to-Faraday geometries, and large-diameter quantum dots are necessary to initiate that process, it can be compared to the quantum well phenomenon of an exciton-cyclotron resonance. The SFRS technique fur-

ther provides a direct identification of electron-nuclear hyperfine interaction in quantum dot ensembles. Moreover, a resonant SFRS experiment combined with a nonresonant laser excitation allows to study effects of the carriers additionally injected into the quantum structure on the intermediate scattering state giving rise to an enhancement or a quenching of the SFRS intensity. By using that two-color SFRS method carrier-carrier interactions in a quantum well are described.

Novel indirect band-gap quantum dots are demonstrated as promising low-dimensional semiconductor structures for spintronic applications. The quantum dots with indirect band-gap and type-I band alignment possess a rather high symmetry: the light-hole and heavy-hole states are not mixed, and at the X-point in the momentum space spin-orbit corrections are negligible. The fine structure of the indirect exciton consisting of a Γ -valley heavy-hole and X-valley electron is determined by the measurement of the g factor tensor components using the SFRS technique. Hereby, the electron spin-flip indicates the regime of mixing between the conduction band levels at the Γ - and X-point. A theoretical model evaluates the contributions of the Γ - and X-valley states and their mixing to the spectral intensity distribution of the SFRS spectrum. The remarkable features of these quantum dots are the long radiative recombination time and long and temperature-robust longitudinal spin relaxation time of the indirect exciton, revealed by time-resolved circularly polarized photoluminescence. Due to the coexistence of direct and indirect band-gap dots in a single sample comparisons between the dynamics of the direct and indirect excitons can immediately be drawn. A model is proposed to describe the exciton lifetime distribution on the basis of the sharpness of the quantum dot-matrix interface which, in turn, depends on the composition profile and size of the quantum dots. The combination of that kind of radiative lifetime distribution and two-level rate equations allows to model the spin dynamics of the indirect exciton.

Chapter 7

Outlook: SFRS and Beyond

The spin-flip Raman scattering of an exciton in Faraday geometry has not been observed in either the quantum well structure or the InAs-based quantum dots, although the optical selection rules do not forbid the spin-flip of the bright exciton. The absence of a corresponding SFRS line in the spectra has been attributed to the relatively small and dispersive g factors of the studied excitons. Nevertheless, one may raise the question whether the SFRS of an exciton also requires a reduced symmetry established by, e.g., a tilting of the magnetic field direction with respect to the structure growth axis. Apart from the pursuit of an answer on that question of principle, aspects of further studies on the direct and indirect band-gap InAs-based QDs will be suggested in the following. The outlook reaches from the investigation of excited exciton complexes and inter-dot coupling in (In,Ga)As dots to the extension of the indirect exciton spin dynamics and nuclei effects in the (In,Al)As QDs. In the last Section, an alternative structure for spintronic applications is presented: negatively charged nitrogen-vacancy centers in diamond.

7.1 Many-Body Effects and Inter-Dot Coupling in Direct Band-Gap QDs

Some results presented in the Chapter 4 are gathered for the resonant excitation of excited states in the direct band-gap (In,Ga)As/GaAs QDs: the electron g factor dispersion becomes flattened at large excitation energies, and the electron-SFRS resonance profiles are strongly shifted in energy. In both cases the p-shell electrons participate in the spin-flip scattering processes. Actually, the features of excited exciton complexes and many-body effects in highly charged QDs are rarely studied. The SFRS technique can be used to characterize the g factors of electrons and holes in excited states, the interplay between the Coulomb interactions of the carriers and the QD confinement, as well as the impact of symmetry of the crystal lattice and QD shape on the exciton fine structure [277]. Hereby, the relevance of inter-valley Γ -X coupling might be studied in the

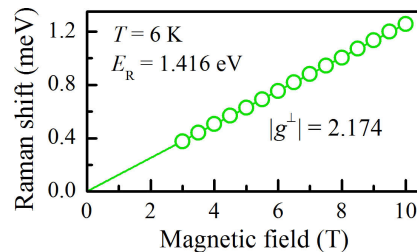


Figure 7-1: Magnetic field dependence of the Raman shift of a SFRS line measured for a highly n-doped (In,Ga)As QD sample (#11652) in Voigt geometry.

indirect band-gap (In,Al)As QDs. Since the confined holes do not follow the Aufbau principle [278], the SFRS is suggested to probe their open-shell configurations. Moreover, the longitudinal and transverse spin relaxation times of excited states and their temperature dependencies are unknown; it is possible to reveal them by means of time-resolved PL and pump&probe spectroscopy. For that purposes, structures containing QDs that are located in the vicinity of a two-dimensional carrier gas are equipped with gate electrodes in order to control the filling of the QDs and to prepare many-carrier states. As an example, the magnetic field dependence of the Raman shift of a SFRS line observed in highly n-doped (In,Ga)As/GaAs QDs is shown in the Fig. 7-1. The transverse g factor is $|g^\perp| = 2.174$. The origin of the SFRS line with such a large Raman shift is unknown; it might be attributed to excited electron states, but it is also possible that a carrier bound to a residual defect is involved in the spin-flip scattering process.

Another open question refers to the inter-dot coupling in an ensemble of QDs. It is possible that, for instance, the resonantly excited electron in one QD changes its spin state via exchange interaction with an electron confined in another dot. The isotropic exchange interaction between two spins separated by a distance of 30 nm has been approximated to about 0.2 meV [279, 280]. Anisotropic exchange interactions can be expected to exceed this value [167]. Hereby, the spin exchange can be performed between dots in the lateral plane, but also between dots located in different layers along the growth axis. The recently proposed optical RKKY interaction is too weak (1 μ eV) to account for spin-flips of electrons exposed to strong external magnetic fields [281]. In order to experimentally estimate the relevance of such inter-dot spin exchange, single QDs can be studied by micro-SFRS. The excitation of a single QD and collection of the scattered light using microscope objectives would result in low SFRS line intensities. Aside from that technical aspect, the micro-SFRS on a single dot of a pair of closely neighbored QDs may give insight into spin-based inter-dot coupling mechanisms.

It has been demonstrated that an optically induced Overhauser field is evaluated from the Raman shift of the electron-SFRS line. Electron-nuclear hyperfine interactions in QD ensembles can also be expected to be studied by the SFRS combined with an applied transverse magnetic field oscillating at radio-frequency. The depolarization of the nuclear spin system via that transverse B -field can then be monitored by the electron-SFRS line. As mentioned in Chapter 4, such a combination would provide an alternative to the electron-nuclear double resonance technique. Furthermore, the question whether the nuclei spins affect the excited carrier states with open-shell configurations in charged QDs might also be explored.

A time-resolved SFRS is possible in the case of a two-color experiment: the intensity dynamics of the spin-flip Raman line can be monitored in dependence on the additional pulsed laser illumination, while the SFRS itself is induced by CW laser light. A single beam time-resolved SFRS directly following the spin-flip scattering dynamics is rather impossible. Temporally short laser pulses in the picosecond range with spectrally narrow widths less than approximately 0.2 meV would be necessary in order to excite the Zeeman split exciton states separately. The light gathering efficiency would be a further problem. Nevertheless, a time-resolved two-color SFRS experiment could be useful to investigate dynamics of carrier-carrier spin interactions.

7.2 Spin Dynamics and Valley Mixing in (In,Al)As/AlAs Quantum Dots

The spin dynamics of the indirect exciton in the indirect band-gap (In,Al)As/AlAs QDs has been proven to be prospective for spintronic applications due to the long and rather temperature-robust longitudinal spin relaxation time. The determination of the spin coherence time is missing so far, also the influence of background doping is unclear. Due to the broad resonance of the indirect excitons, spin beats in time-resolved Kerr-rotation experiments are probably not observable. Moreover, the indirect exciton should be characterized in zero magnetic field thus studying nuclei effects by, for instance, Hanle measurements. In that context, one should check if the X-valley-electron–nuclear spin system can be used as long-lived spin memory. Additionally, in absence of an external magnetic field a rather high optical orientation degree of the indirect exciton PL has been found, as shown in Fig. 7-2. For quasi-resonant excitation the PL spectrum in circularly co-polarized configuration has a pronounced multi-peak structure. At a temperature of 1.8 K the maximum degree of the optical orientation approaches 50% depending on the laser power. The explanation of the remarkable optical orientation, its spectral dependence, as well as possible impact factors have to be clarified, and should be evidenced by a microscopic theory.

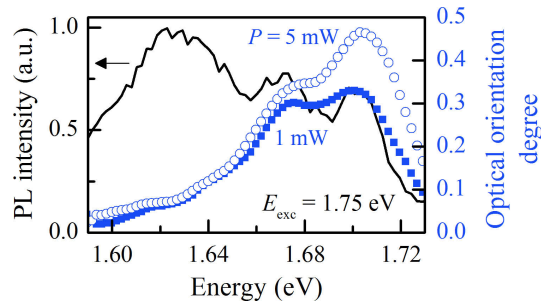


Figure 7-2: PL spectrum and degree of optical orientation at $B = 0$ T for sample #2890.

Furthermore, the studies on the mixed exciton can be extended to indirect band-gap (In,Al)As/AlAs QDs where the conduction band minimum is located at the L-point. The L-valley electron probably has an anisotropic g factor. The characteristics of the Γ -X and Γ -L mixed excitons can be compared with respect to their oscillator strengths and binding energies, for example. Also, it should be tried to detect the SFRS of the Γ -valley electron in a sample with a large concentration of direct band-gap QDs at very high B -fields in order to complete the electron g factor dispersion.

7.3 NV⁻ Centers in Diamond

Over the past years the negatively charged nitrogen-vacancy (NV⁻) center in diamond whose optical properties are comparable to that of a semiconductor QD has been studied due to its possible application in spintronics. Its density can be tailored that a single NV⁻ center is optically addressable. Furthermore, the trigonal crystal field lifts the degeneracy of the triplet ground state and forms a two-level quantum system which can be used as a qubit; long spin coherence times of a few milliseconds have been reported [282]. While the spin-triplet structure has been revealed in recent time [283], details on the spin-singlet states are missing so far. It is probable to gather information on the singlet-level structure by means of the spin-flip Raman scattering technique. Moreover, most of the studies are performed on single NV⁻ centers, whereas ensembles of nitrogen vacancies are rarely considered. The polarization-dependent magneto-optical characterization of

the NV^- center is also incomplete. In what follows, a brief outlook on the magneto-photoluminescence of an ensemble of NV^- centers in diamond is presented.

The NV^- center consists of a nitrogen atom that is associated with a vacancy in an adjacent lattice site possessing C_{3v} symmetry [284]. The nitrogen atom and the three carbon atoms surrounding the vacancy provide six electrons to the NV^- center [285]. The unpaired electrons form the spin-triplet ground state $|^3A_2\rangle$. It is characterized by a zero orbital angular momentum projection along the NV^- axis, the corresponding orbital state is denoted by $|E_0\rangle$. The spin momentum projection takes the value 0, +1, or -1. Accordingly, the ground states can be described by $|^3A_{20}\rangle = |E_0\rangle|0\rangle$ and

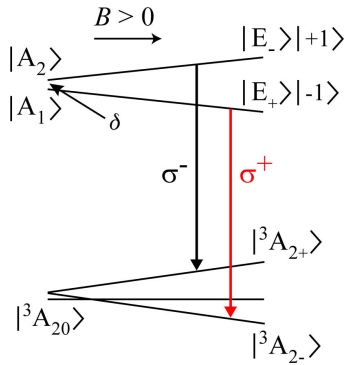


Figure 7-3: Level scheme for zero phonon lines of the NV^- center in diamond depending on the B -field.

$|^3A_{2±}\rangle = |E_0\rangle|\pm 1\rangle$. The optical transitions from the excited state $|A_2\rangle = 1/\sqrt{2}(|E_-\rangle + 1\rangle + |E_+\rangle - 1\rangle)$ with nonzero orbital angular momentum to one of the ground states $|^3A_{2±}\rangle$ define zero phonon lines at energies of about 1.946 eV [286]. Hereby, photons with opposite circular polarizations σ^\mp are emitted, since the change in the electronic orbital angular momentum determines the photon polarization degree while the spin is conserved. The selection rules for the optical transitions from $|A_2\rangle$ and $|A_1\rangle = 1/\sqrt{2}(|E_-\rangle + 1\rangle - |E_+\rangle - 1\rangle)$ are the same. As illustrated in the Fig. 7-3, under application of an external magnetic field the excited states split into the two levels $|E_-\rangle + 1\rangle$ and $|E_+\rangle - 1\rangle$. The energy difference between these levels is given by a zero-field splitting δ and the Zeeman term $(g_s - g_l)\mu_B B$ with the spin and orbital g factors. The ground states with nonzero spin momentum projections are split on

account of the Landé factor $g_s = 2.0$. The orbital g factor is about 0.1 [287]. The splitting between the states $|E_-\rangle + 1\rangle$ and $|E_+\rangle - 1\rangle$ can be expected to be acquired via the SFERS for resonant excitation thus determining the value of g_l precisely.

Alternatively, the effective orbital contribution to the Zeeman splitting of the differently circular-polarized zero phonon lines can be evaluated from magneto-photoluminescence measurements. In the Fig. 7-4 zero phonon transitions at a magnetic field of 10 T and a temperature of 6 K are shown for a synthetic diamond crystal with a density of nitrogen vacancies of about $2.5 \times 10^{16} \text{ cm}^{-3}$. The energy difference between the σ^- and σ^+ polarized lines amounts to $\delta + g_l\mu_B B = 0.16 \text{ meV}$ which corresponds to $g_l = 0.26$ for a zero-field offset $\delta \approx 0.01 \text{ meV}$ [285]. The considerable deviation of that g factor from 0.1 has not been explained yet. Furthermore, the σ^- polarized zero phonon line for a diamond crystal with higher NV^- center concentration of $1 \times 10^{17} \text{ cm}^{-3}$ is illustrated as dashed curve in the Fig. 7-4. Its width is much larger due to the higher defect concentration which, in turn, causes a broader g factor dispersion and/or shorter electron lifetimes. It resembles the PL of an inhomogeneously broadened QD ensemble. Moreover, the difference in the PL intensities (solid curves) indicates a circular polarization degree of $\rho_c = -0.045$. The depen-

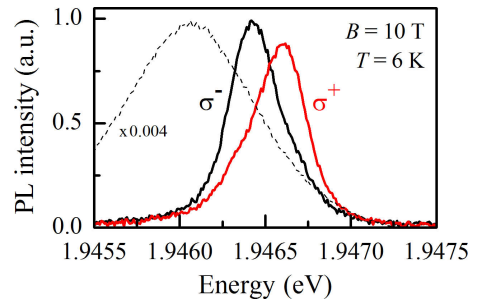


Figure 7-4: PL spectra of the zero phonon lines of NV^- centers in diamond at $B = 10 \text{ T}$, excited at 2.2 eV.

dence of the triplet and singlet states of the NV⁻ center in diamond on strong external magnetic fields has not yet been demonstrated either experimentally or theoretically. Also, the experimental determination of the energetic hierarchy of the spin-singlet states is missing so far. The SFRS technique would be useful for that purpose.

Bibliography

- [1] O. Stern's quotation written from memory by D. R. Herschbach. *Molecular Dynamics of Elementary Chemical Reactions (Nobel Lecture)*. *Angew. Chem. Int. Ed. Engl.* **26**, 1221 (1987).
- [2] W. Gerlach and O. Stern. Der experimentelle Nachweis der Richtungsquantelung im Magnetfeld. *Z. Phys.* **9**, 349 (1922).
- [3] P. Zeeman. The effect of magnetisation on the nature of light emitted by a substance. *Nature* **55**, 347 (1897).
- [4] W. Pauli. Über den Einfluß der Geschwindigkeitsabhängigkeit der Elektronenmasse auf den Zeemaneffekt. *Z. Phys.* **31**, 373 (1925).
- [5] G. E. Uhlenbeck and S. Goudsmit. Ersetzung der Hypothese vom unmechanischen Zwang durch eine Forderung bezüglich des inneren Verhaltens jedes einzelnen Elektrons. *Naturwiss.* **13**, 953 (1925).
- [6] P. A. M. Dirac. Quantum Mechanics of Many-Electron Systems. *Proc. R. Soc. Lond. A* **123**, 714 (1929).
- [7] W. Pauli. The Connection Between Spin and Statistics. *Phys. Rev.* **58**, 716 (1940).
- [8] J. Bardeen. Surface States and Rectification at a Metal Semi-Conductor Contact. *Phys. Rev.* **71**, 717 (1947).
- [9] D. Hisamoto, W.-C. Lee, J. Kedzierski, H. Takeuchi, K. Asano, C. Kuo, E. Anderson, T.-J. King, J. Bokor, and C. Hu. FinFET – A Self-Aligned Double-Gate MOSFET Scalable to 20 nm. *IEEE Trans. Electron Devices* **47**, 2320 (2000).
- [10] J. Cartwright. Intel enters the third dimension. *Nature News*, doi:10.1038/news.2011.274 (2011).
- [11] G. E. Moore. Progress in digital integrated electronics. *IEEE Int. Electron Devices Meeting* **21**, 11 (1975).
- [12] M. N. Baibich, J. M. Broto, A. Fert, F. Nguyen Van Dau, F. Petroff, P. Eitenne, G. Creuzet, A. Friederich, and J. Chazelas. Giant Magnetoresistance of (001)Fe/(001)Cr Magnetic Superlattices. *Phys. Rev. Lett.* **61**, 2472 (1988).
- [13] G. Binasch, P. Grünberg, F. Saurenbach, and W. Zinn. Enhanced magnetoresistance in layered magnetic structures with antiferromagnetic interlayer exchange. *Phys. Rev. B* **39**, 4828 (1989).
- [14] S. Datta and B. Das. Electronic analog of the electro-optic modulator. *Appl. Phys. Lett.* **56**, 665 (1990).

- [15] V. Cerletti, W. A. Coish, O. Gywat, and D. Loss. Recipes for spin-based quantum computing. *Nanotechnology* **16**, R27 (2005).
- [16] K. C. Hall and M. E. Flatté. Performance of a spin-based insulated gate field effect transistor. *Appl. Phys. Lett.* **88**, 162503 (2006).
- [17] D. D. Awschalom and M. E. Flatté. Challenges for semiconductor spintronics. *Nature Physics* **3**, 153 (2007).
- [18] R. I. Dzhioev, B. P. Zakharchenya, V. L. Korenev, and M. N. Stepanova. Spin diffusion of optically oriented electrons and photon entrainment in *n*-gallium arsenide. *Phys. Solid State* **39**, 1765 (1997).
- [19] J. M. Kikkawa, I. P. Smorchkova, N. Samarth, and D. D. Awschalom. Room-Temperature Spin Memory in Two-Dimensional Electron Gases. *Science* **277**, 1284 (1997).
- [20] P. Maletinsky, M. Kroner, and A. Imamoglu. Breakdown of the nuclear-spin-temperature approach in quantum-dot demagnetization experiments. *Nature Physics* **5**, 407 (2009).
- [21] C. Kammerer, C. Voisin, G. Cassabois, C. Delalande, Ph. Roussignol, F. Klopff, J. P. Reithmaier, A. Forchel, and J. M. Gérard. Line narrowing in single semiconductor quantum dots: Toward the control of environment effects. *Phys. Rev. B* **66**, 041306(R) (2002).
- [22] M. Anderlini, P. J. Lee, B. L. Brown, J. Sebby-Strabley, W. D. Phillips, and J. V. Porto. Controlled exchange interaction between pairs of neutral atoms in an optical lattice. *Nature* **448**, 452 (2007).
- [23] A. Greulich, D. R. Yakovlev, A. Shabaev, Al. L. Efros, I. A. Yugova, R. Oulton, V. Stavarache, D. Reuter, A. Wieck, and M. Bayer. Mode Locking of Electron Spin Coherences in Singly Charged Quantum Dots. *Science* **313**, 341 (2006).
- [24] D. Press, T. D. Ladd, B. Zhang, and Y. Yamamoto. Complete quantum control of a single quantum dot spin using ultrafast optical pulses. *Nature* **456**, 218 (2008).
- [25] K. De Greve, P. L. McMahon, D. Press, T. D. Ladd, D. Bisping, C. Schneider, M. Kamp, L. Worschech, S. Höfling, A. Forchel, and Y. Yamamoto. Ultrafast coherent control and suppressed nuclear feedback of a single quantum dot hole qubit. *Nature Physics* **7**, 872 (2011).
- [26] I. Malajovich, J. J. Berry, N. Samarth, and D. D. Awschalom. Persistent sourcing of coherent spins for multifunctional semiconductor spintronics. *Nature* **411**, 770 (2001).
- [27] X. Qian, X.-H. Peng, D. O. Ansari, Q. Yin-Goen, G. Z. Chen, D. M. Shin, L. Yang, A. N. Young, M. D. Wang, and S. Nie. *In vivo* tumor targeting and spectroscopic detection with surface-enhanced Raman nanoparticle tags. *Nature Biotechnology* **26**, 83 (2008).
- [28] M. Mu, S. Osswald, Y. Gogotsi, and K. I. Winey. An *in situ* Raman spectroscopy study of stress transfer between carbon nanotubes and polymer. *Nanotechnology* **20**, 335703 (2009).

- [29] I. A. Akimov, R. I. Dzhioev, V. L. Korenev, Yu. G. Kusrayev, V. F. Sapega, D. R. Yakovlev, and M. Bayer. Optical Orientation of Mn^{2+} Ions in GaAs in Weak Longitudinal Magnetic Fields. *Phys. Rev. Lett.* **106**, 147402 (2011).
- [30] O. Gywat, H. J. Krenner, and J. Berezovsky. *Spins in Optically Active Quantum Dots*. Wiley-Vch Verlag, Weinheim (2010).
- [31] D. Bimberg (Ed.). *Semiconductor Nanostructures*. Springer-Verlag, Berlin (2008).
- [32] M. I. Dyakonov and V. I. Perel. Spin relaxation of conduction electrons in non-centrosymmetric semiconductors. *Sov. Phys. Solid State* **13**, 3023 (1972).
- [33] M. I. Dyakonov and V. Yu. Kachorovskii. Spin relaxation of two-dimensional electrons in noncentrosymmetric semiconductors. *Sov. Phys. Semicond.* **20**, 110 (1986).
- [34] Yu. A. Bychkov and E. I. Rashba. Properties of a 2D electron gas with lifted spectral degeneracy. *JETP Lett.* **39**, 78 (1984).
- [35] F. Meier and B. P. Zakharchenya (Eds.). *Optical Orientation*. North-Holland, Amsterdam (1984).
- [36] P. Y. Yu and M. Cardona. *Fundamentals of Semiconductors – Physics and Materials Properties*. Springer-Verlag, Berlin (2010).
- [37] G. F. Koster, J. O. Dimmock, R. G. Wheeler, and H. Statz. *Properties of the thirty-two point groups*. M.I.T. Press, Cambridge (1963).
- [38] C. Klingshirn. *Semiconductor Optics*. Springer-Verlag, Berlin (2005).
- [39] E. Wigner. Über die Operation der Zeitumkehr in der Quantenmechanik. *Nachr. v. d. Ges. d. Wiss. zu Göttingen*, 546 (1932).
- [40] A. G. Thompson, M. Cardona, K. L. Shaklee, and J. C. Woolley. Electroreflectance in the GaAs-GaP Alloys. *Phys. Rev.* **146**, 601 (1966).
- [41] E. L. Ivchenko and G. E. Pikus. *Superlattices and Other Heterostructures*. Springer-Verlag, Berlin (1997).
- [42] R. Singh and G. Bester. Lower Bound for the Excitonic Fine Structure Splitting in Self-Assembled Quantum Dots. *Phys. Rev. Lett.* **104**, 196803 (2010).
- [43] F. Bloch. Über die Quantenmechanik der Elektronen in Kristallgittern. *Z. Phys.* **52**, 555 (1928).
- [44] W. Heisenberg. Über den anschaulichen Inhalt der quantentheoretischen Kinematik und Mechanik. *Z. Phys.* **43**, 172 (1927).
- [45] M. Fox. *Optical Properties of Solids*. Oxford University Press, Oxford (2010).
- [46] W. Que. Excitons in quantum dots with parabolic confinement. *Phys. Rev. B* **45**, 11036 (1992).
- [47] L. E. Brus. Electron-electron and electron-hole interactions in small semiconductor crystallites: The size dependence of the lowest excited electronic state. *J. Chem. Phys.* **80**, 4403 (1984).

- [48] G. W. Bryant. Excitons in quantum boxes: Correlation effects and quantum confinement. *Phys. Rev. B* **37**, 8763 (1988).
- [49] T. Takagahara. Effects of dielectric confinement and electron-hole exchange interaction on excitonic states in semiconductor quantum dots. *Phys. Rev. B* **47**, 4569 (1993).
- [50] W. Kohn. Cyclotron Resonance and de Haas-van Alphen Oscillations of an Interacting Electron Gas. *Phys. Rev.* **123**, 1242 (1961).
- [51] F. M. Peeters. Magneto-optics in parabolic quantum dots. *Phys. Rev. B* **42**, 1486 (1990).
- [52] F. B. Pedersen and Y.-C. Chang. Energy levels of one and two holes in parabolic quantum dots. *Phys. Rev. B* **53**, 1507 (1996).
- [53] L. Jacak, P. Hawrylak, and A. Wojs. *Quantum Dots*. Springer-Verlag, Berlin (1998).
- [54] M. Valin-Rodriguez, A. Puente, and L. Serra. Quantum dots based on spin properties of semiconductor heterostructures. *Phys. Rev. B* **69**, 153308 (2004).
- [55] A. Schliwa, M. Winkelkemper, and D. Bimberg. Impact of size, shape, and composition on piezoelectric effects and electronic properties of In(Ga)As/GaAs quantum dots. *Phys. Rev. B* **76**, 205324 (2007).
- [56] A. Wojs, P. Hawrylak, S. Fafard, and L. Jacak. Electronic structure and magneto-optics of self-assembled quantum dots. *Phys. Rev. B* **54**, 5604 (1996).
- [57] G. Bester and A. Zunger. Compositional and size-dependent spectroscopic shifts in charged self-assembled $\text{In}_x\text{Ga}_{1-x}\text{As}/\text{GaAs}$ quantum dots. *Phys. Rev. B* **68**, 073309 (2003).
- [58] J. I. Climente, A. Bertoni, and G. Goldoni. Photoluminescence spectroscopy of trions in quantum dots: A theoretical description. *Phys. Rev. B* **78**, 155316 (2008).
- [59] E. L. Ivchenko. *Optical Spectroscopy of Semiconductor Nanostructures*. Alpha Science International Ltd., Harrow (2005).
- [60] A. Wojs and P. Hawrylak. Negatively charged magnetoexcitons in quantum dots. *Phys. Rev. B* **51**, 10880 (1995).
- [61] I. Saidi, K. Sellami, M. Yahyaoui, C. Testelin, and K. Boujdaria. Electron and hole energy levels in InAs/GaAs quantum dots: Size and magnetic field effects. *J. Appl. Phys.* **109**, 033703 (2011).
- [62] M. Bayer, O. Stern, A. Kuther, and A. Forchel. Spectroscopic study of dark excitons in $\text{In}_x\text{Ga}_{1-x}\text{As}$ self-assembled quantum dots by a magnetic-field-induced symmetry breaking. *Phys. Rev. B* **61**, 7273 (2000).
- [63] O. Voskoboynikov, C. P. Lee, and O. Tretyak. Spin-orbit splitting in semiconductor quantum dots with a parabolic confinement potential. *Phys. Rev. B* **63**, 165306 (2001).
- [64] C. F. Destefani, S. E. Ulloa, and G. E. Marques. Spin-orbit coupling and intrinsic spin mixing in quantum dots. *Phys. Rev. B* **69**, 125302 (2004).

- [65] D. Pfannkuche and R. R. Gerhardts. Quantum-dot helium: Effects of deviations from a parabolic confinement potential. *Phys. Rev. B* **44**, 13132 (1991).
- [66] N. A. Bruce and P. A. Maksym. Quantum states of interacting electrons in a real quantum dot. *Phys. Rev. B* **61**, 4718 (2000).
- [67] V. Fock. Bemerkung zur Quantelung des harmonischen Oszillators im Magnetfeld. *Z. Phys.* **47**, 446 (1928).
- [68] C. G. Darwin. The Diamagnetism of the Free Electron. *Math. Proc. Cambridge Philos. Soc.* **27**, 86 (1931).
- [69] S. Raymond, S. Studenikin, A. Sachrajda, Z. Wasilewski, S. J. Cheng, W. Sheng, P. Hawrylak, A. Babinski, M. Potemski, G. Ortner, and M. Bayer. Excitonic Energy Shell Structure of Self-Assembled InGaAs/GaAs Quantum Dots. *Phys. Rev. Lett.* **92**, 187402 (2004).
- [70] P. A. Maksym and T. Chakraborty. Quantum Dots in a Magnetic Field: Role of Electron-Electron Interactions. *Phys. Rev. Lett.* **65**, 108 (1990).
- [71] P. A. Maksym, L. D. Hallam, and J. Weis. Models of quantum dots. *Physica B* **212**, 213 (1995).
- [72] G. Bester and A. Zunger. Cylindrically shaped zinc-blende semiconductor quantum dots do not have cylindrical symmetry: Atomistic symmetry, atomic relaxation, and piezoelectric effects. *Phys. Rev. B* **71**, 045318 (2005).
- [73] M. Grundmann, O. Stier, and D. Bimberg. InAs/GaAs pyramidal quantum dots: Strain distribution, optical phonons, and electronic structure. *Phys. Rev. B* **52**, 11969 (1995).
- [74] A. A. Sirenko, T. Ruf, M. Cardona, D. R. Yakovlev, W. Ossau, A. Waag, and G. Landwehr. Electron and hole g factors measured by spin-flip Raman scattering in CdTe/Cd_{1-x}Mg_xTe single quantum wells. *Phys. Rev. B* **56**, 2114 (1997).
- [75] A. A. Kiselev, E. L. Ivchenko, and U. Rössler. Electron g factor in one- and zero-dimensional semiconductor nanostructures. *Phys. Rev. B* **58**, 16353 (1998).
- [76] C. E. Pryor and M. E. Flatté. Landé g Factors and Orbital Momentum Quenching in Semiconductor Quantum Dots. *Phys. Rev. Lett.* **96**, 026804 (2006).
- [77] M. J. Snelling, G. P. Flinn, A. S. Plaut, R. T. Harley, A. C. Tropper, R. Eccleston, and C. C. Phillips. Magnetic g factor of electrons in GaAs/Al_xGa_{1-x}As quantum wells. *Phys. Rev. B* **44**, 11345 (1991).
- [78] B. Kowalski, P. Omling, B. K. Meyer, D. M. Hofmann, C. Wetzel, V. Härle, F. Scholz, and P. Sobkowicz. Conduction-band spin splitting of type-I Ga_xIn_{1-x}As/InP quantum wells. *Phys. Rev. B* **49**, 14786 (1994).
- [79] B. Odom, D. Hanneke, B. D'Urso, and G. Gabrielse. New Measurement of the Electron Magnetic Moment Using a One-Electron Quantum Cyclotron. *Phys. Rev. Lett.* **97**, 030801 (2006).
- [80] C. Hermann and C. Weisbuch. $\vec{k} \cdot \vec{p}$ perturbation theory in III-V compounds and alloys: a reexamination. *Phys. Rev. B* **15**, 823 (1977).

- [81] L. M. Roth, B. Lax, and S. Zwerdling. Theory of Optical Magneto-Absorption Effects in Semiconductors. *Phys. Rev.* **114**, 90 (1959).
- [82] N. J. Traynor, R. J. Warburton, M. J. Snelling, and R. T. Harley. Highly nonlinear Zeeman splitting of excitons in semiconductor quantum wells. *Phys. Rev. B* **55**, 15701 (1997).
- [83] A. A. Kiselev, K. W. Kim, and E. Yablonovitch. In-plane light-hole g factor in strained cubic heterostructures. *Phys. Rev. B* **64**, 125303 (2001).
- [84] H. W. van Kesteren, E. C. Cosman, W. A. J. A. van der Poel, and C. T. Foxon. Fine structure of excitons in type-II GaAs/AlAs quantum wells. *Phys. Rev. B* **41**, 5283 (1990).
- [85] E. A. Chekhovich, A. B. Krysa, M. S. Skolnick, and A. I. Tartakovskii. Direct Measurement of the Hole-Nuclear Spin Interaction in Single InP/GaInP Quantum Dots Using Photoluminescence Spectroscopy. *Phys. Rev. Lett.* **106**, 027402 (2011).
- [86] S. Adachi, T. Yokoi, H. Sasakura, S. Muto, H. Kumano, and I. Suemune. Dynamic nuclear polarization in a self-assembled InAlAs quantum dot. *Phys. stat. sol. (c)* **2**, 3838 (2005).
- [87] I. Vurgaftman, J. R. Meyer, and L. R. Ram-Mohan. Band parameters for III-V compound semiconductors and their alloys. *J. Appl. Phys.* **89**, 5815 (2001).
- [88] M. Nawrocki and A. Twardowski. Oscillatory Magnetoabsorption in CdTe. *Phys. stat. sol. (b)* **97**, K61 (1980).
- [89] A. Fleszar and W. Hanke. Electronic structure of II^B-VI semiconductors in the GW approximation. *Phys. Rev. B* **71**, 045207 (2005).
- [90] L. S. Dang, G. Neu, and R. Romestain. Optical detection of cyclotron resonance of electron and holes in CdTe. *Solid State Commun.* **44**, 1187 (1982).
- [91] C. Weisbuch and C. Hermann. Optical detection of conduction-electron spin resonance in GaAs, Ga_{1-x}In_xAs, and Ga_{1-x}Al_xAs. *Phys. Rev. B* **15**, 816 (1977).
- [92] J.-M. Jancu, R. Scholz, E. A. de Andrada e Silva, and G. C. La Rocca. Atomistic spin-orbit coupling and k-p parameters in III-V semiconductors. *Phys. Rev. B* **72**, 193201 (2005).
- [93] S. Tsoi, I. Miotkowski, S. Rodriguez, A. K. Ramdas, H. Alawadhi, and T. M. Pekarek. Resonant electron spin-flip Raman scattering in CdTe and the diluted magnetic semiconductor Cd_{1-x}V_xTe. *Phys. Rev. B* **69**, 035209 (2004).
- [94] M. F. Doty, M. Scheibner, I. V. Ponomarev, E. A. Stinaff, A. S. Bracker, V. L. Korenev, T. L. Reinecke, and D. Gammon. Electrically Tunable g Factors in Quantum Dot Molecular Spin States. *Phys. Rev. Lett.* **97**, 197202 (2006).
- [95] L. W. Molenkamp, R. Eppenga, G. W. 't Hooft, P. Dawson, C. T. Foxon, and K. J. Moore. Determination of valence-band effective-mass anisotropy in GaAs quantum wells by optical spectroscopy. *Phys. Rev. B* **38**, 4314 (1988).
- [96] M.-Z. Huang and W. Y. Ching. A minimal basis semi-*ab initio* approach to the band structures of semiconductors. *J. Phys. Chem. Solids* **46**, 977 (1985).

-
- [97] C. R. Pidgeon, D. L. Mitchell, and R. N. Brown. Interband Magnetoabsorption in InAs and InSb. *Phys. Rev.* **154**, 737 (1967).
- [98] C. Klingshirn (Ed.). 4.1 General properties in Landolt-Börnstein – Group III Condensed Matter, Vol. 34C1: Optical Properties. Springer-Verlag, Berlin (2011).
- [99] Ch. Neumann, A. Nöthe, and N. O. Lipari. Two-photon magnetoabsorption of ZnTe, CdTe, and GaAs. *Phys. Rev. B* **37**, 922 (1988).
- [100] C. V. Raman. A new radiation. *Indian J. Phys.* **2**, 387 (1928). Available online: *Proceedings Mathematical Sciences* **37**, 333 (1953).
- [101] C. V. Raman and K. S. Krishnan. A New Type of Secondary Radiation. *Nature* **121**, 501 (1928).
- [102] C. V. Raman and K. S. Krishnan. The Production of New Radiations by Light Scattering - Part I. *Proc. R. Soc. Lond. A* **122**, 23 (1929).
- [103] G. Landsberg and L. Mandelstam. Eine neue Erscheinung bei der Lichtstreuung in Krystallen. *Naturwiss.* **16**, 557 (1928).
- [104] G. Landsberg and L. Mandelstam. Über die Lichtzerstreuung in Kristallen. *Z. Phys.* **50**, 769 (1928).
- [105] E. L. Feinberg. The forefather (about Leonid Isaakovich Mandelstam). *Phys.-Usp.* **45**, 81 (2002).
- [106] L. D. Landau and E. M. Lifshitz. *Mechanics (Course of theoretical physics - Vol. 1)*. Butterworth-Heinemann, Oxford (2000).
- [107] E. Noether. Invariante Variationsprobleme. *Nachr. v. d. Ges. d. Wiss. zu Göttingen*, 235 (1918).
- [108] R. P. Feynman, R. B. Leighton, and M. Sands. *The Feynman Lectures on Physics – Quantum Mechanics*. Addison-Wesley, Reading (2005).
- [109] J. P. Eisenstein, H. L. Störmer, V. Narayanamurti, A. C. Gossard, and W. Wiegmann. Effect of Inversion Symmetry on the Band Structure of Semiconductor Heterostructures. *Phys. Rev. Lett.* **53**, 2579 (1984).
- [110] P. Busch. The Time-Energy Uncertainty Relation, Chap. 3 in *Time in Quantum Mechanics - Vol. 1*, edited by J. G. Muga, R. Sala Mayato, and I. L. Egusquiza. Springer-Verlag, Berlin (2008).
- [111] H. P. Robertson. The Uncertainty Principle. *Phys. Rev.* **34**, 163 (1929).
- [112] H. Maassen and J. B. M. Uffink. Generalized Entropic Uncertainty Relations. *Phys. Rev. Lett.* **60**, 1103 (1988).
- [113] W. H. Weber and R. Merlin (Eds.). *Raman Scattering in Materials Science*. Springer-Verlag, Berlin (2000).
- [114] M. Beye, F. Hennies, M. Deppe, E. Suljoti, M. Nagasono, W. Wurth, and A. Föhlisch. Dynamics of Electron-Phonon Scattering: Crystal- and Angular-Momentum Transfer Probed by Resonant Inelastic X-Ray Scattering. *Phys. Rev. Lett.* **103**, 237401 (2009).

- [115] Al. L. Efros. Luminescence polarization of CdSe microcrystals. *Phys. Rev. B* **46**, 7448 (1992).
- [116] S. S. Jha and J. W. F. Woo. Theory of Nonlinear Light Scattering from Phonons in Crystals. *Il Nuovo Cimento B* **2**, 167 (1971).
- [117] P. A. M. Dirac. The Quantum Theory of the Emission and Absorption of Radiation. *Proc. R. Soc. Lond. A* **114**, 243 (1927).
- [118] T. Kato. Fundamental Properties of Hamiltonian Operators of Schrödinger Type. *Trans. Amer. Math. Soc.* **70**, 195 (1951).
- [119] D. Belkic. Principles of Quantum Scattering Theory. Institute of Physics Publishing, Bristol (2004).
- [120] F. J. Dyson. Heisenberg Operators in Quantum Electrodynamics - I. *Phys. Rev.* **82**, 428 (1951).
- [121] B. A. Lippmann and J. Schwinger. Variational Principles for Scattering Processes - I. *Phys. Rev.* **79**, 469 (1950).
- [122] M. Balkanski, J. Reydillet, C. Hirlimann, and M. Kanehisa. Resonant Light Scattering. *J. Lum.* **18**, 665 (1979).
- [123] T. Takagahara (Ed.). Quantum Coherence, Correlation and Decoherence in Semiconductor Nanostructures. Academic Press, London (2003).
- [124] Y. R. Shen. Distinction between resonance Raman scattering and hot luminescence. *Phys. Rev. B* **9**, 622 (1974).
- [125] C. Trallero-Giner, T. Ruf, and M. Cardona. Theory of one-phonon resonant Raman scattering in a magnetic field. *Phys. Rev. B* **41**, 3028 (1990).
- [126] C. Schüller. Inelastic Light Scattering of Semiconductor Nanostructures. Springer-Verlag, Berlin (2006).
- [127] S. Rudin, T. L. Reinecke, and B. Segall. Temperature-dependent exciton linewidths in semiconductors. *Phys. Rev. B* **42**, 11218 (1990).
- [128] G. L. Bir and G. E. Pikus. Theory of the deformation potential for semiconductors with a complex band structure. *Sov. Phys. Solid State* **2**, 2039 (1960).
- [129] X. B. Zhang, T. Taliercio, S. Kolliakos, and P. Lefebvre. Influence of electron-phonon interaction on the optical properties of III nitride semiconductors. *J. Phys.: Condens. Matter* **13**, 7053 (2001).
- [130] G. Piacente and G. Q. Hai. Electron-acoustic-phonon scattering and electron relaxation in two-coupled quantum rings. *J. Appl. Phys.* **101**, 124308 (2007).
- [131] L. M. Woods, T. L. Reinecke, and Y. Lyanda-Geller. Spin relaxation in quantum dots. *Phys. Rev. B* **66**, 161318 (2002).
- [132] L. M. Woods, T. L. Reinecke, and R. Kotlyar. Hole spin relaxation in quantum dots. *Phys. Rev. B* **69**, 125330 (2004).
- [133] A. Dargys. Luttinger-Kohn Hamiltonian and coherent excitation of the valence-band holes. *Phys. Rev. B* **66**, 165216 (2002).

- [134] J. L. Cheng, M. W. Wu, and C. Lü. Spin relaxation in GaAs quantum dots. *Phys. Rev. B* **69**, 115318 (2004).
- [135] M. Sugawara. Magnetic-field-induced enhancement of exciton oscillator strength in $\text{In}_{0.53}\text{Ga}_{0.47}\text{As}/\text{InP}$ quantum wells. *Phys. Rev. B* **45**, 11423 (1992).
- [136] T. C. Damen, S. P. S. Porto, and B. Tell. Raman Effect in Zinc Oxide. *Phys. Rev.* **142**, 570 (1966).
- [137] J. Puls, M. Rabe, H.-J. Wünsche, and F. Henneberger. Magneto-optical study of the exciton fine structure in self-assembled CdSe quantum dots. *Phys. Rev. B* **60**, R16303 (1999).
- [138] G. E. Pikus and F. G. Pikus. The mechanism of heavy and light hole mixing in GaAs/AlAs superlattices. *Solid State Commun.* **89**, 319 (1994).
- [139] G. Sallen, B. Urbaszek, M. M. Glazov, E. L. Ivchenko, T. Kuroda, T. Mano, S. Kunz, M. Abbarchi, K. Sakoda, D. Lagarde, A. Balocchi, X. Marie, and T. Amand. Dark-Bright Mixing of Interband Transitions in Symmetric Semiconductor Quantum Dots. *Phys. Rev. Lett.* **107**, 166604 (2011).
- [140] Y. Léger, L. Besombes, L. Maingault, and H. Mariette. Valence-band mixing in neutral, charged, and Mn-doped self-assembled quantum dots. *Phys. Rev. B* **76**, 045331 (2007).
- [141] V. F. Sapega, M. Cardona, K. Ploog, E. L. Ivchenko, and D. N. Mirlin. Spin-flip Raman scattering in $\text{GaAs}/\text{Al}_x\text{Ga}_{1-x}\text{As}$ multiple quantum wells. *Phys. Rev. B* **45**, 4320 (1992).
- [142] V. F. Sapega, T. Ruf, M. Cardona, K. Ploog, E. L. Ivchenko, and D. N. Mirlin. Resonant Raman scattering due to bound-carrier spin flip in $\text{GaAs}/\text{Al}_x\text{Ga}_{1-x}\text{As}$ quantum wells. *Phys. Rev. B* **50**, 2510 (1994).
- [143] W. Greulich (Ed.). *Lexikon der Physik - Band 1*. Spektrum Akademischer Verlag, Heidelberg (1998).
- [144] M. Atatüre, J. Dreiser, A. Badolato, A. Högele, K. Karrai, and A. Imamoglu. Quantum-Dot Spin-State Preparation with Near-Unity Fidelity. *Science* **312**, 551 (2006).
- [145] D. G. Thomas and J. J. Hopfield. Spin-Flip Raman Scattering in Cadmium Sulfide. *Phys. Rev.* **175**, 1021 (1968).
- [146] B. D. Moore, L. Stevenson, A. Watt, S. Flitsch, N. J. Turner, C. Cassidy, and D. Graham. Rapid and ultra-sensitive determination of enzyme activities using surface-enhanced resonance Raman scattering. *Nature Biotechnology* **22**, 1133 (2004).
- [147] M. Born and E. Wolf. *Principles of optics*. Pergamon Press Ltd., Oxford (1986).
- [148] J. Satterly. The Physical Properties of Solid and Liquid Helium. *Rev. Mod. Phys.* **8**, 347 (1936).
- [149] A. Winter. Transformation region of glass. *J. Am. Ceram. Soc.* **26**, 189 (1943).

- [150] W. R. C. Coode-Adams. The Refractive Index of Quartz. *Proc. R. Soc. Lond. A* **117**, 209 (1927).
- [151] J. S. Blakemore. Semiconducting and other major properties of gallium arsenide. *J. Appl. Phys.* **53**, R123 (1982).
- [152] J.-Q. Xi, M. F. Schubert, J. K. Kim, E. F. Schubert, M. Chen, S.-Y. Lin, W. Liu, and J. A. Smart. Optical thin-film materials with low refractive index for broad-band elimination of Fresnel reflection. *Nature Photon.* **1**, 176 (2007).
- [153] TriVista System Manual - Version 1.A. Princeton Instruments, Trenton (2005).
- [154] J. Eichler and H. J. Eichler. *Laser - Bauformen, Strahlführung, Anwendungen*. Springer-Verlag, Berlin (2006).
- [155] M. Czerny and A. F. Turner. Über den Astigmatismus bei Spiegelspektrometern. *Z. Phys.* **61**, 792 (1930).
- [156] T. Dieing, O. Hollricher, and J. Toporski (Eds.). *Confocal Raman Microscopy*. Springer-Verlag, Berlin (2010).
- [157] R. Petit (Ed.). *Electromagnetic Theory of Gratings*. Springer-Verlag, Berlin (1980).
- [158] Technical Manual - Ramanor U1000 Monochromator, Version 3. Jobin Yvon (1988).
- [159] T&D-scan laser system - Instruction manual. Tekhnoscan Laser Systems, Novosibirsk (2010).
- [160] C. Palmer and E. Loewen. *Diffraction Grating Handbook*. Newport Corporation, New York (2005).
- [161] A. K. Zvezdin and V. A. Kotov. *Modern Magneto-optics and Magneto-optical Materials*. Institute of Physics Publishing, Bristol (1997).
- [162] J. Berezovsky, M. H. Mikkelsen, N. G. Stoltz, L. A. Coldren, and D. D. Awschalom. Picosecond Coherent Optical Manipulation of a Single Electron Spin in a Quantum Dot. *Science* **320**, 349 (2008).
- [163] D. Heiss, V. Jovanov, F. Klotz, D. Rudolph, M. Bichler, G. Abstreiter, M. S. Brandt, and J. J. Finley. Optically monitoring electron spin relaxation in a single quantum dot using a spin memory device. *Phys. Rev. B* **82**, 245316 (2010).
- [164] C. Phelps, T. Sweeney, R. T. Cox, and H. Wang. Ultrafast Coherent Electron Spin Flip in a Modulation-Doped CdTe Quantum Well. *Phys. Rev. Lett.* **102**, 237402 (2009).
- [165] H. Kosaka, H. Shigyou, Y. Mitsumori, Y. Rikitake, H. Imamura, T. Kutsuwa, K. Arai, and K. Edamatsu. Coherent Transfer of Light Polarization to Electron Spins in a Semiconductor. *Phys. Rev. Lett.* **100**, 096602 (2008).
- [166] M. I. Dyakonov (Ed.). *Spin Physics in Semiconductors*. Springer-Verlag, Berlin (2008).

- [167] K. V. Kavokin. Anisotropic exchange interaction of localized conduction-band electrons in semiconductors. *Phys. Rev. B* **64**, 075305 (2001).
- [168] K. V. Kavokin. Symmetry of anisotropic exchange interactions in semiconductor nanostructures. *Phys. Rev. B* **69**, 075302 (2004).
- [169] L. P. Gor'kov and P. L. Krotkov. Spin relaxation and antisymmetric exchange in n -doped III-V semiconductors. *Phys. Rev. B* **67**, 033203 (2003).
- [170] N. E. Bonesteel, D. Stepanenko, and D. P. DiVincenzo. Anisotropic Spin Exchange in Pulsed Quantum Gates. *Phys. Rev. Lett.* **87**, 207901 (2001).
- [171] M. Q. Weng and M. W. Wu. Spin dephasing in n -type GaAs quantum wells. *Phys. Rev. B* **68**, 075312 (2003).
- [172] N. J. Harmon, W. O. Putikka, and R. Joynt. Theory of electron spin relaxation in n -doped quantum wells. *Phys. Rev. B* **81**, 085320 (2010).
- [173] R. I. Dzhioev, K. V. Kavokin, V. L. Korenev, M. V. Lazarev, B. Ya. Meltser, M. N. Stepanova, B. P. Zakharchenya, D. Gammon, and D. S. Katzer. Low-temperature spin relaxation in n -type GaAs. *Phys. Rev. B* **66**, 245204 (2002).
- [174] K. V. Kavokin. Spin relaxation of localized electrons in n -type semiconductors. *Semicond. Sci. Technol.* **23**, 114009 (2008).
- [175] A. A. Sirenko, V. I. Belitsky, T. Ruf, M. Cardona, A. I. Ekimov, and C. Trallero-Giner. Spin-flip and acoustic-phonon Raman scattering in CdS nanocrystals. *Phys. Rev. B* **58**, 2077 (1998).
- [176] A. V. Koudinov, Yu. G. Kusrayev, B. P. Zakharchenya, D. Wolverson, J. J. Davies, T. Wojtowicz, G. Karczewski, and J. Kossut. Spin-flip Raman scattering in semi-magnetic quantum wells with in-plane anisotropy: Analysis of the intermediate states. *Phys. Rev. B* **67**, 115304 (2003).
- [177] A. A. Kiselev, E. L. Ivchenko, A. A. Sirenko, T. Ruf, M. Cardona, D. R. Yakovlev, W. Ossau, A. Waag, and G. Landwehr. Electron and hole g factor anisotropy in CdTe/CdMgTe quantum wells. *J. Crystal Growth* **184**, 831 (1998).
- [178] R. Shen, K. Oto, K. Muro, G. Karczewski, T. Wojtowicz, J. Kossut, and S. Takeyama. High-resolution spin-flip Raman scattering in CdTe quantum wells at ^3He temperature. *Phys. Rev. B* **80**, 125312 (2009).
- [179] E. A. Zhukov, D. R. Yakovlev, M. Gerbracht, G. V. Mikhailov, G. Karczewski, T. Wojtowicz, J. Kossut, and M. Bayer. Spin coherence of holes and electrons in undoped CdTe/(Cd,Mg)Te quantum wells. *Phys. Rev. B* **79**, 155318 (2009).
- [180] G. V. Astakhov, V. P. Kochereshko, D. R. Yakovlev, W. Ossau, J. Nürnbergger, W. Faschinger, G. Landwehr, T. Wojtowicz, G. Karczewski, and J. Kossut. Optical method for the determination of carrier density in modulation-doped quantum wells. *Phys. Rev. B* **65**, 115310 (2002).
- [181] G. V. Astakhov, D. R. Yakovlev, V. P. Kochereshko, W. Ossau, J. Nürnbergger, W. Faschinger, G. Landwehr. Charged excitons in ZnSe-based quantum wells. *Phys. Rev. B* **60**, R8485 (1999).

- [182] G. Bartsch, M. Gerbracht, D. R. Yakovlev, J. H. Blokland, P. C. M. Christiaenen, E. A. Zhukov, A. B. Dzyubenko, G. Karczewski, T. Wojtowicz, J. Kossut, J. C. Maan, and M. Bayer. Positively versus negatively charged excitons: A high magnetic field study of CdTe/Cd_{1-x}Mg_xTe quantum wells. *Phys. Rev. B* **83**, 235317 (2011).
- [183] G. V. Astakhov, D. R. Yakovlev, V. P. Kochereshko, W. Ossau, W. Faschinger, J. Puls, F. Henneberger, S. A. Crooker, Q. McCulloch, D. Wolverson, N. A. Gippius, and A. Waag. Binding energy of charged excitons in ZnSe-based quantum wells. *Phys. Rev. B* **65**, 165335 (2002).
- [184] M. Bayer, S. N. Walck, T. L. Reinecke, and A. Forchel. Exciton binding energies and diamagnetic shifts in semiconductor quantum wires and quantum dots. *Phys. Rev. B* **57**, 6584 (1998).
- [185] E. A. Zhukov, D. R. Yakovlev, M. Bayer, M. M. Glazov, E. L. Ivchenko, G. Karczewski, T. Wojtowicz, and J. Kossut. Spin coherence of a two-dimensional electron gas induced by resonant excitation of trions and excitons in CdTe/(Cd,Mg)Te quantum wells. *Phys. Rev. B* **76**, 205310 (2007).
- [186] A. V. Kavokin. Exciton oscillator strength in quantum wells: From localized to free resonant states. *Phys. Rev. B* **50**, 8000 (1994).
- [187] X. Marie, T. Amand, P. Le Jeune, M. Paillard, P. Renucci, L. E. Golub, V. D. Dymnikov, and E. L. Ivchenko. Hole spin quantum beats in quantum-well structures. *Phys. Rev. B* **60**, 5811 (1999).
- [188] P. Redliński. Binding energy of negative trions in a CdTe quantum well at high magnetic fields. *J. Appl. Phys.* **99**, 063702 (2006).
- [189] D. N. Krizhanovskii, A. Ebbens, A. I. Tartakovskii, F. Pulizzi, T. Wright, M. S. Skolnick, and M. Hopkinson. Individual neutral and charged In_xGa_{1-x}As-GaAs quantum dots with strong in-plane optical anisotropy. *Phys. Rev. B* **72**, 161312(R) (2005).
- [190] Private correspondence with D. R. Yakovlev, E. A. Zhukov, and E. L. Ivchenko.
- [191] E. L. Ivchenko. Exchange interaction and scattering of light with reversal of the hole angular momentum at an acceptor in quantum-well structures. *Sov. Phys. Solid State* **34**, 254 (1992).
- [192] A. V. Koudinov, Yu. G. Kusrayev, D. Wolverson, L. C. Smith, J. J. Davies, G. Karczewski, and T. Wojtowicz. Giant modulation of resonance Raman scattering from (Cd,Mn)Te quantum wells by secondary illumination. *Phys. Rev. B* **79**, 241310(R) (2009).
- [193] M. A. Herman, D. Bimberg, and J. Christen. Heterointerfaces in quantum wells and epitaxial growth processes: Evaluation by luminescence techniques. *J. Appl. Phys.* **70**, R1 (1991).
- [194] N. El-Kadry, A. Ashour, and S. A. Mahmoud. Structural dependence of d.c. electrical properties of physically deposited CdTe thin films. *Thin Solid Films* **269**, 112 (1995).

- [195] A. I. Burshtein. Kinetics of the relaxation induced by a sudden potential change. *Sov. Phys. JETP* **22**, 939 (1966).
- [196] Yu. N. Molin, K. M. Salikhov, and K. I. Zamaraev. *Spin Exchange*. Springer-Verlag, Berlin (1980).
- [197] A. G. Curto, G. Volpe, T. H. Taminiau, M. P. Kreuzer, R. Quidant, and N. F. van Hulst. Unidirectional Emission of a Quantum Dot Coupled to a Nanoantenna. *Science* **329**, 930 (2010).
- [198] A. Kholi, B. W. Lovett, S. C. Benjamin, and T. M. Stace. All-Optical Measurement-Based Quantum-Information Processing in Quantum Dots. *Phys. Rev. Lett.* **97**, 250504 (2006).
- [199] H. Kosaka, T. Inagaki, Y. Rikitake, H. Imamura, Y. Mitsumori, and K. Edamatsu. Spin state tomography of optically injected electrons in a semiconductor. *Nature* **457**, 702 (2009).
- [200] A. V. Khaetskii, D. Loss, and L. Glazman. Electron Spin Decoherence in Quantum Dots due to Interaction with Nuclei. *Phys. Rev. Lett.* **88**, 186802 (2002).
- [201] Y. G. Semenov and K. W. Kim. Effect of an external magnetic field on electron-spin dephasing induced by hyperfine interaction in quantum dots. *Phys. Rev. B* **67**, 073301 (2003).
- [202] D. Gammon, S. W. Brown, E. S. Snow, T. A. Kennedy, D. S. Katzer, and D. Park. Nuclear Spectroscopy in Single Quantum Dots: Nanoscopic Raman Scattering and Nuclear Magnetic Resonance. *Science* **277**, 85 (1997).
- [203] Y. G. Semenov and K. W. Kim. Phonon-Mediated Electron-Spin Phase Diffusion in a Quantum Dot. *Phys. Rev. Lett.* **92**, 026601 (2004).
- [204] D. R. Yakovlev, V. P. Kochereshko, R. A. Suris, H. Schenk, W. Ossau, A. Waag, G. Landwehr, P. C. M. Christianen, and J. C. Maan. Combined Exciton-Cyclotron Resonance in Quantum Well Structures. *Phys. Rev. Lett.* **79**, 3974 (1997).
- [205] T. Nakaoka, T. Saito, J. Tatebayashi, and Y. Arakawa. Size, shape, and strain dependence of the g factor in self-assembled In(Ga)As quantum dots. *Phys. Rev. B* **70**, 235337 (2004).
- [206] I. A. Yugova, A. Greulich, E. A. Zhukov, D. R. Yakovlev, M. Bayer, D. Reuter, and A. D. Wieck. Exciton fine structure in InGaAs/GaAs quantum dots revisited by pump-probe Faraday rotation. *Phys. Rev. B* **75**, 195325 (2007).
- [207] A. V. Koudinov, I. A. Akimov, Yu. G. Kusrayev, and F. Henneberger. Optical and magnetic anisotropies of the hole states in Stranski-Krastanov quantum dots. *Phys. Rev. B* **70**, 241305(R) (2004).
- [208] Y. G. Semenov and S. M. Ryabchenko. Effects of photoluminescence polarization in semiconductor quantum wells subjected to an in-plane magnetic field. *Phys. Rev. B* **68**, 045322 (2003).
- [209] M. Bayer, G. Ortner, O. Stern, A. Kuther, A. A. Gorbunov, A. Forchel, P. Hawrylak, S. Fafard, K. Hinzer, T. L. Reinecke, S. N. Walck, J. P. Reithmaier, F. Klopff, and F. Schäfer. Fine structure of neutral and charged excitons in self-assembled In(Ga)As/(Al)GaAs quantum dots. *Phys. Rev. B* **65**, 195315 (2002).

- [210] J. G. Tischler, A. S. Bracker, D. Gammon, and D. Park. Fine structure of trions and excitons in single GaAs quantum dots. *Phys. Rev. B* **66**, 081310(R) (2002).
- [211] I. A. Akimov, K. V. Kavokin, A. Hundt, and F. Henneberger. Electron-hole exchange interaction in a negatively charged quantum dot. *Phys. Rev. B* **71**, 075326 (2005).
- [212] D. V. Regelman, E. Dekel, D. Gershoni, E. Ehrenfreund, A. J. Williamson, J. Shumway, A. Zunger, W. V. Schoenfeld, and P. M. Petroff. Optical spectroscopy of single quantum dots at tunable positive, neutral, and negative charge states. *Phys. Rev. B* **64**, 165301 (2001).
- [213] A. Schwan, B.-M. Meiners, A. B. Henriques, A. D. B. Maia, A. A. Quivy, S. Spatzek, S. Varwig, D. R. Yakovlev, and M. Bayer. Dispersion of electron g -factor with optical transition energy in (In,Ga)As/GaAs self-assembled quantum dots. *Appl. Phys. Lett.* **98**, 233102 (2011).
- [214] R. V. Cherbunin, K. Flisinski, I. Ya. Gerlovin, I. V. Ignatiev, M. S. Kuznetsova, M. Yu. Petrov, D. R. Yakovlev, D. Reuter, A. D. Wieck, and M. Bayer. Resonant nuclear spin pumping in (In,Ga)As quantum dots. *Phys. Rev. B* **84**, 041304(R) (2011).
- [215] D. Paget, G. Lampel, B. Sapoval, and V. I. Safarov. Low field electron-nuclear spin coupling in gallium arsenide under optical pumping conditions. *Phys. Rev. B* **15**, 5780 (1977).
- [216] D. Gammon, Al. L. Efros, T. A. Kennedy, M. Rosen, D. S. Katzer, D. Park, S. W. Brown, V. L. Korenev, and I. A. Merkulov. Electron and Nuclear Spin Interactions in the Optical Spectra of Single GaAs Quantum Dots. *Phys. Rev. Lett.* **86**, 5176 (2001).
- [217] K. Flisinski, I. Ya. Gerlovin, I. V. Ignatiev, M. Yu. Petrov, S. Yu. Verbin, D. R. Yakovlev, D. Reuter, A. D. Wieck, and M. Bayer. Optically detected magnetic resonance at the quadrupole-split nuclear states in (In,Ga)As/GaAs quantum dots. *Phys. Rev. B* **82**, 081308(R) (2010).
- [218] S. W. Brown, T. A. Kennedy, D. Gammon, and E. S. Snow. Spectrally resolved Overhauser shifts in single GaAs/Al_xGa_{1-x}As quantum dots. *Phys. Rev. B* **54**, R17339 (1996).
- [219] T. Yokoi, S. Adachi, H. Sasakura, S. Muto, H. Z. Song, T. Usuki, and S. Hirose. Polarization-dependent shift in excitonic Zeeman splitting of self-assembled In_{0.75}Al_{0.25}As/Al_{0.3}Ga_{0.7}As quantum dots. *Phys. Rev. B* **71**, 041307(R) (2005).
- [220] J. Skiba-Szymanska, E. A. Chekhovich, A. E. Nikolaenko, A. I. Tartakovskii, M. N. Makhonin, I. Drouzas, M. S. Skolnick, and A. B. Krysa. Overhauser effect in individual InP/Ga_xIn_{1-x}P dots. *Phys. Rev. B* **77**, 165338 (2008).
- [221] P.-F. Braun, B. Urbaszek, T. Amand, X. Marie, O. Krebs, B. Eble, A. Lemaitre, and P. Voisin. Bistability of the nuclear polarization created through optical pumping in In_{1-x}Ga_xAs quantum dots. *Phys. Rev. B* **74**, 245306 (2006).
- [222] P. Michler (Ed.). *Single Semiconductor Quantum Dots*. Springer-Verlag, Berlin (2009).

- [223] H. Yu, S. Lycett, C. Roberts, and R. Murray. Time resolved study of self-assembled InAs quantum dots. *Appl. Phys. Lett.* **69**, 4087 (1996).
- [224] F. Adler, M. Geiger, A. Bauknecht, D. Haase, P. Ernst, A. Dörnen, F. Scholz, and H. Schweizer. Self-assembled InAs/GaAs quantum dots under resonant excitation. *J. Appl. Phys.* **83**, 1631 (1998).
- [225] K. Hennessy, A. Badolato, M. Winger, D. Gerace, M. Atatüre, S. Gulde, S. Fält, E. L. Hu, and A. Imamoglu. Quantum nature of a strongly coupled single quantum dot-cavity system. *Nature* **445**, 896 (2007).
- [226] P. Michler, A. Kiraz, C. Becher, W. V. Schoenfeld, P. M. Petroff, L. Zhang, E. Hu, and A. Imamoglu. A Quantum Dot Single-Photon Turnstile Device. *Science* **290**, 2282 (2000).
- [227] J. Vuckovic and Y. Yamamoto. Photonic crystal microcavities for cavity quantum electrodynamics with a single quantum dot. *Appl. Phys. Lett.* **82**, 2374 (2003).
- [228] T. S. Shamirzaev, A. V. Nenashev, and K. S. Zhuravlev. Coexistence of direct and indirect band structures in arrays of InAs/AlAs quantum dots. *Appl. Phys. Lett.* **92**, 213101 (2008).
- [229] T. S. Shamirzaev, A. V. Nenashev, A. K. Gutakovskii, A. K. Kalagin, K. S. Zhuravlev, M. Larsson, and P. O. Holtz. Atomic and energy structure of InAs/AlAs quantum dots. *Phys. Rev. B* **78**, 085323 (2008).
- [230] J.-W. Luo, A. Franceschetti, and A. Zunger. Quantum-size-induced electronic transitions in quantum dots: Indirect band-gap GaAs. *Phys. Rev. B* **78**, 035306 (2008).
- [231] G. H. Li, A. R. Goni, K. Syassen, O. Brandt, and K. Ploog. State mixing in InAs/GaAs quantum dots at the pressure-induced Γ - X crossing. *Phys. Rev. B* **50**, 18420 (1994).
- [232] M. S. Hybertsen. Absorption and Emission of Light in Nanoscale Silicon Structures. *Phys. Rev. Lett.* **72**, 1514 (1994).
- [233] M. Nakayama, K. Imazawa, K. Suyama, I. Tanaka, and H. Nishimura. Γ - X mixing effects on pseudodirect exciton transitions in GaAs/AlAs type-II superlattices. *Phys. Rev. B* **49**, 13564 (1994).
- [234] D. Kovalev, H. Heckler, M. Ben-Chorin, G. Polisski, M. Schwartzkopff, and F. Koch. Breakdown of the k -Conservation Rule in Si Nanocrystals. *Phys. Rev. Lett.* **81**, 2803 (1998).
- [235] M. S. Skolnick, G. W. Smith, I. L. Spain, C. R. Whitehouse, D. C. Herbert, D. M. Whittaker, and L. J. Reed. Phonon coupling and X - Γ mixing in GaAs-AlAs short-period superlattices. *Phys. Rev. B* **39**, 11191 (1989).
- [236] M.-H. Meynadier, R. E. Nahory, J. M. Worlock, M. C. Tamargo, J. L. de Miguel, and M. D. Sturge. Indirect-Direct Anticrossing in GaAs-AlAs Superlattices Induced by an Electric Field: Evidence of Γ - X Mixing. *Phys. Rev. Lett.* **60**, 1338 (1988).

- [237] Y. Fu, M. Willander, E. L. Ivchenko, and A. A. Kiselev. Valley mixing in GaAs/AlAs multilayer structures in the effective-mass method. *Phys. Rev. B* **47**, 13498 (1993).
- [238] F. Hatami, N. N. Ledentsov, M. Grundmann, J. Böhrer, F. Heinrichsdorff, M. Beer, D. Bimberg, S. S. Ruvimov, P. Werner, U. Gösele, J. Heydenreich, U. Richter, S. V. Ivanov, B. Ya. Meltser, P. S. Kop'ev, and Zh. I. Alferov. Radiative recombination in type-II GaSb/GaAs quantum dots. *Appl. Phys. Lett.* **67**, 656 (1995).
- [239] T. Baier, U. Mantz, K. Thonke, R. Sauer, F. Schäffler, and H.-J. Herzog. Type-II band alignment in Si/Si_{1-x}Ge_x quantum wells from photoluminescence line shifts due to optically induced band-bending effects: Experiment and theory. *Phys. Rev. B* **50**, 15191 (1994).
- [240] M. Dyakonov, X. Marie, T. Amand, P. Le Jeune, D. Robart, M. Brousseau, and J. Barrau. Coherent spin dynamics of excitons in quantum wells. *Phys. Rev. B* **56**, 10412 (1997).
- [241] C. F. Young, E. H. Poindexter, G. J. Gerardi, W. L. Warren, and D. J. Keeble. Electron paramagnetic resonance of conduction-band electrons in silicon. *Phys. Rev. B* **55**, 16245 (1997).
- [242] E. E. Vdovin, Yu. N. Khanin, L. Eaves, M. Henini, and G. Hill. Spin splitting of X-valley-related donor impurity states in an AlAs barrier. *Phys. Rev. B* **71**, 195320 (2005).
- [243] N. Fraj, I. Saidi, S. Ben Radhia, and K. Boujdaria. Band structures of AlAs, GaP, and SiGe alloys: A 30 k×p model. *J. Appl. Phys.* **102**, 053703 (2007).
- [244] F. A. Baron, A. A. Kiselev, H. D. Robinson, K. W. Kim, K. L. Wang, and E. Yablonovitch. Manipulating the *L*-valley electron *g* factor in Si-Ge heterostructures. *Phys. Rev. B* **68**, 195306 (2003).
- [245] I. A. Yugova, A. Greilich, D. R. Yakovlev, A. A. Kiselev, M. Bayer, V. V. Petrov, Yu. K. Dolgikh, D. Reuter, and A. D. Wieck. Universal behavior of the electron *g* factor in GaAs/Al_xGa_{1-x}As quantum wells. *Phys. Rev. B* **75**, 245302 (2007).
- [246] I. Toft and R. T. Phillips. Hole *g* factors in GaAs quantum dots from the angular dependence of the spin fine structure. *Phys. Rev. B* **76**, 033301 (2007).
- [247] A. F. van Driel, G. Allan, C. Delerue, P. Lodahl, W. L. Vos, and D. Vanmaekelbergh. Frequency-Dependent Spontaneous Emission Rate from CdSe and CdTe Nanocrystals: Influence of Dark States. *Phys. Rev. Lett.* **95**, 236804 (2005).
- [248] T. Berstermann, T. Auer, H. Kurtze, M. Schwab, D. R. Yakovlev, M. Bayer, J. Wiersig, C. Gies, F. Jahnke, D. Reuter, and A. D. Wieck. Systematic study of carrier correlations in the electron-hole recombination dynamics of quantum dots. *Phys. Rev. B* **76**, 165318 (2007).
- [249] A. F. van Driel, I. S. Nikolaev, P. Vergeer, P. Lodahl, D. Vanmaekelbergh, and W. L. Vos. Statistical analysis of time-resolved emission from ensembles of semiconductor quantum dots: Interpretation of exponential decay models. *Phys. Rev. B* **75**, 035329 (2007).

- [250] V. Zwiller, M.-E. Pistol, D. Hessman, R. Cederström, W. Seifert, and L. Samuelson. Time-resolved studies of single semiconductor quantum dots. *Phys. Rev. B* **59**, 5021 (1999).
- [251] T. Bartel, M. Dworzak, M. Strassburg, A. Hoffmann, A. Strittmatter, and D. Bimberg. Recombination dynamics of localized excitons in InGaN quantum dots. *Appl. Phys. Lett.* **85**, 1946 (2004).
- [252] T. S. Shamirzaev, A. M. Gilinsky, A. K. Kalagin, A. V. Nenashev, and K. S. Zhuravlev. Energy spectrum and structure of thin pseudomorphic InAs quantum wells in an AlAs matrix: Photoluminescence spectra and band-structure calculations. *Phys. Rev. B* **76**, 155309 (2007).
- [253] L. S. Braginsky, M. Yu. Zaharov, A. M. Gilinsky, V. V. Preobrazhenskii, M. A. Putyato, and K. S. Zhuravlev. Kinetics of exciton photoluminescence in type-II semiconductor superlattices. *Phys. Rev. B* **63**, 195305 (2001).
- [254] P. Offermans, P. M. Koenraad, J. H. Wolter, K. Pierz, M. Roy, and P. A. Maksym. Atomic-scale structure and photoluminescence of InAs quantum dots in GaAs and AlAs. *Phys. Rev. B* **72**, 165332 (2005).
- [255] E. Placidi, F. Arciprete, M. Fanfoni, F. Patella, E. Orsini, and A. Balzarotti. InAs/GaAs(001) epitaxy: kinetic effects in the two-dimensional to three-dimensional transition. *J. Phys.: Condens. Matter* **19**, 225006 (2007).
- [256] Ch. Heyn and W. Hansen. Ga/In-intermixing and segregation during InAs quantum dot formation. *J. Cryst. Growth* **251**, 140 (2003).
- [257] H. Lüth. *Solid Surfaces, Interfaces and Thin Films*. Springer-Verlag, Berlin (2001).
- [258] J. Tersoff. Enhanced Nucleation and Enrichment of Strained-Alloy Quantum Dots. *Phys. Rev. Lett.* **81**, 3183 (1998).
- [259] K. Muraki, S. Fukatsu, Y. Shiraki, and R. Ito. Surface segregation of In atoms during molecular beam epitaxy and its influence on the energy levels in InGaAs/GaAs quantum wells. *Appl. Phys. Lett.* **61**, 557 (1992).
- [260] T. S. Shamirzaev, A. K. Kalagin, A. I. Toropov, A. K. Gutakovskii, and K. S. Zhuravlev. Narrowing of ground energy level distribution in an array of InAs/AlAs QDs by post grown annealing. *Phys. stat. sol. (c)* **3**, 3932 (2006).
- [261] B. Monemar, K. K. Shih, and G. D. Pettit. Some optical properties of the $\text{Al}_x\text{Ga}_{1-x}\text{As}$ alloy system. *J. Appl. Phys.* **47**, 2604 (1976).
- [262] J. C. Phillips. Stretched exponential relaxation in molecular and electronic glasses. *Rep. Prog. Phys.* **59**, 1133 (1996).
- [263] O. Guillois, N. Herlin-Boime, C. Reynaud, G. Ledoux, and F. Huisken. Photoluminescence decay dynamics of noninteracting silicon nanocrystals. *J. Appl. Phys.* **95**, 3677 (2004).
- [264] C. Delerue, G. Allan, C. Reynaud, O. Guillois, G. Ledoux, and F. Huisken. Multi-exponential photoluminescence decay in indirect-gap semiconductor nanocrystals. *Phys. Rev. B* **73**, 235318 (2006).

- [265] I. S. Nikolaev, P. Lodahl, A. F. van Driel, A. F. Koenderink, and W. L. Vos. Strongly nonexponential time-resolved fluorescence of quantum-dot ensembles in three-dimensional photonic crystals. *Phys. Rev. B* **75**, 115302 (2007).
- [266] R. A. L. Vallée, K. Baert, B. Kolaric, M. Van der Auweraer, and K. Clays. Non-exponential decay of spontaneous emission from an ensemble of molecules in photonic crystals. *Phys. Rev. B* **76**, 045113 (2007).
- [267] T. S. Shamirzaev, A. M. Gilinsky, A. K. Kalagin, A. I. Toropov, A. K. Gutakovskii, and K. S. Zhuravlev. Strong sensitivity of photoluminescence of InAs/AlAs quantum dots to defects: evidence for lateral inter-dot transport. *Semicond. Sci. Technol.* **21**, 527 (2006).
- [268] E. M. Baskin and L. S. Braginsky. Short-wavelength phonon emission from a metal-semiconductor interface. *Phys. Rev. B* **50**, 12191 (1994).
- [269] R. Hanson and D. D. Awschalom. Coherent manipulation of single spins in semiconductors. *Nature* **453**, 1043 (2008).
- [270] S. Mackowski, T. A. Nguyen, H. E. Jackson, L. M. Smith, J. Kossut, and G. Karczewski. Exciton spin relaxation time in quantum dots measured by continuous-wave photoluminescence spectroscopy. *Appl. Phys. Lett.* **83**, 5524 (2003).
- [271] C. D. Poweleit, A. R. Hodges, T.-B. Sun, L. M. Smith, and B. T. Jonker. Exciton spin thermalization in strained and relaxed $\text{Zn}_{1-x}\text{Mn}_x\text{Se}$ epilayers. *Phys. Rev. B* **59**, 7610 (1999).
- [272] T. Uenoyama and L. J. Sham. Carrier relaxation and luminescence polarization in quantum wells. *Phys. Rev. B* **42**, 7114 (1990).
- [273] S. Pfalz, R. Winkler, T. Nowitzki, D. Reuter, A. D. Wieck, D. Hägele, and M. Oestreich. Optical orientation of electron spins in GaAs quantum wells. *Phys. Rev. B* **71**, 165305 (2005).
- [274] S. Cortez, O. Krebs, S. Laurent, M. Senes, X. Marie, P. Voisin, R. Ferreira, G. Bastard, J.-M. Gérard, and T. Amand. Optically Driven Spin Memory in *n*-Doped InAs-GaAs Quantum Dots. *Phys. Rev. Lett.* **89**, 207401 (2002).
- [275] M. Kroutvar, Y. Ducommun, D. Heiss, M. Bichler, D. Schuh, G. Abstreiter, and J. J. Finley. Optically programmable electron spin memory using semiconductor quantum dots. *Nature* **432**, 81 (2004).
- [276] V. N. Golovach, A. Khaetskii, and D. Loss. Phonon-Induced Decay of the Electron Spin in Quantum Dots. *Phys. Rev. Lett.* **93**, 016601 (2004).
- [277] M. Ediger, G. Bester, B. D. Gerardot, A. Badolato, P. M. Petroff, K. Karrai, A. Zunger, and R. J. Warburton. Fine Structure of Negatively and Positively Charged Excitons in Semiconductor Quantum Dots: Electron-Hole Asymmetry. *Phys. Rev. Lett.* **98**, 036808 (2007).
- [278] D. Reuter, P. Kailuweit, A. D. Wieck, U. Zeitler, O. Wibbelhoff, C. Meier, A. Lorke, and J. C. Maan. Coulomb-Interaction-Induced Incomplete Shell Filling in the Hole System of InAs Quantum Dots. *Phys. Rev. Lett.* **94**, 026808 (2005).
- [279] G. Burkard, D. Loss, and D. P. DiVincenzo. Coupled quantum dots as quantum gates. *Phys. Rev. B* **59**, 2070 (1999).

- [280] C. Piermarocchi, P. Chen, L. J. Sham, and D. G. Steel. Optical RKKY Interaction between Charged Semiconductor Quantum Dots. *Phys. Rev. Lett.* **89**, 167402 (2002).
- [281] S. Spatzek, A. Greilich, S. E. Economou, S. Varwig, A. Schwan, D. R. Yakovlev, D. Reuter, A. D. Wieck, T. L. Reinecke, and M. Bayer. Optical Control of Coherent Interactions between Electron Spins in InGaAs Quantum Dots. *Phys. Rev. Lett.* **107**, 137402 (2011).
- [282] G. Balasubramanian, P. Neumann, D. Twitchen, M. Markham, R. Kolesov, N. Mizuochi, J. Isoya, J. Achard, J. Beck, J. Tissler, V. Jacques, P. R. Hemmer, F. Jelezko, and J. Wrachtrup. Ultralong spin coherence time in isotopically engineered diamond. *Nature Mater.* **8**, 383 (2009).
- [283] M. W. Doherty, N. B. Manson, P. Delaney, and L. C. L. Hollenberg. The negatively charged nitrogen-vacancy centre in diamond: the electronic solution. *New J. Phys.* **13**, 025019 (2011).
- [284] A. Batalov, V. Jacques, F. Kaiser, P. Siyushev, P. Neumann, L. J. Rogers, R. L. McMurtrie, N. B. Manson, F. Jelezko, and J. Wrachtrup. Low Temperature Studies of the Excited-State Structure of Negatively Charged Nitrogen-Vacancy Color Centers in Diamond. *Phys. Rev. Lett.* **102**, 195506 (2009).
- [285] E. Togan, Y. Chu, A. S. Trifonov, L. Jiang, J. Maze, L. Childress, M. V. G. Dutt, A. S. Sorensen, P. R. Hemmer, A. S. Zibrov, and M. D. Lukin. Quantum entanglement between an optical photon and a solid-state spin qubit. *Nature* **466**, 730 (2010).
- [286] J. R. Maze, A. Gali, E. Togan, Y. Chu, A. Trifonov, E. Kaxiras, and M. D. Lukin. Properties of nitrogen-vacancy centers in diamond: the group theoretic approach. *New J. Phys.* **13**, 025025 (2011).
- [287] J. P. D. Martin. Fine structure of excited 3E state in nitrogen-vacancy centre of diamond. *J. Lumin.* **81**, 237 (1999).

Symbols and Abbreviations

| Symbol | Meaning |
|----------------------------|--|
| \hat{a}, \hat{a}^\dagger | Annihilation and creation operators for an electron |
| a_B | Bohr radius |
| A_{hf} | Hyperfine constant |
| Al | Aluminum |
| As | Arsenic |
| a.u. | Arbitrary units |
| \hat{b}, \hat{b}^\dagger | Annihilation and creation operators for a phonon |
| \mathbf{B} | Magnetic field vector |
| B_N | Effective nuclear field |
| c | Speed of light in vacuum, 2.9979×10^8 m/s |
| \hat{c}, \hat{c}^\dagger | Annihilation and creation operators for a photon |
| CB | Conduction band |
| CCD | Charge-coupled device |
| Cd | Cadmium |
| cm^{-1} | Inverse centimeter (unit), $1 \text{ cm}^{-1} \approx 123.9841 \mu\text{eV}$ |
| cps | Counts per second |
| CW | Continuous wave |
| d | Quantum dot diameter |
| δ_0 | Exciton exchange energy |
| $\Delta_{\text{hh-lh}}$ | Splitting between heavy-hole and light-hole band |
| Δ_{so} | Split-off energy |
| ΔE_{OHS} | Overhauser shift |
| ΔE_{sf} | Spin-flip Raman scattering line shift (Raman shift) |
| det | Detection |
| e | Electron |
| e | Elementary charge, 1.6022×10^{-19} C |
| \mathbf{e} | Polarization unit vector |
| E | Energy |
| E_a | Energy of above-barrier illumination |
| E_c | Magnetic confinement energy |
| E_g | Band gap energy |

| | |
|------------------|--|
| $E_{\Gamma X}$ | Γ -X-crossing energy |
| $E_{n,l}$ | Fock-Darwin energy |
| E_p | Kane parameter |
| ϵ | Activation energy |
| E_R | Resonant excitation energy |
| η_s | Scattering efficiency |
| eV | Electron volt (unit), 1.6022×10^{-19} J |
| Ex | Exciton |
| exc | Excitation |
| f | Focal length |
| FD | Fock-Darwin |
| FWHM | Full width at half maximum |
| g | Landé factor |
| g_0 | Free electron g factor, $g_0 \approx 2.0023$ |
| Ga | Gallium |
| γ_i | Kohn-Luttinger Hamiltonian parameter ($i = 1, 2, 3$) |
| Γ | Damping rate, or SFRS line width |
| Γ_i | Irreducible representation (point group specific) |
| $G(\tau)$ | Exciton lifetime distribution |
| h | Hole |
| \hbar | Reduced Planck constant, $\hbar = \frac{h}{2\pi} \approx 6.5821 \times 10^{-16}$ eVs |
| $\hbar\omega_0$ | Lateral confinement energy |
| hh | Heavy-hole |
| \hat{H}_{ac} | Acoustic phonon scattering operator |
| \hat{H}_d | Direct exchange interaction operator |
| \hat{H}_{e-ph} | Electron-phonon interaction operator |
| \hat{H}_{e-R} | Electron-radiation interaction operator |
| \hat{H}_s | Scattering operator |
| \hat{H}_{xch} | Anisotropic exchange interaction operator |
| \hat{I} | Nuclear spin operator |
| I_{bg} | PL background intensity |
| In | Indium |
| I^+, I^- | σ^+ , σ^- polarized PL intensity |
| I_s | Scattering intensity |
| I_{sf} | Spin-flip Raman scattering intensity |
| $j; j_z$ | Total angular momentum; its projection along z -axis |
| κ | Photon wave vector |
| \mathbf{k} | Wave vector |
| k_B | Boltzmann constant, 8.6173×10^{-5} eV/K |
| κ_{KL} | Kohn-Luttinger parameter |

| | |
|----------------------|---|
| l | Orbital angular momentum |
| λ | Wavelength |
| l_0 | Confinement length |
| l_c | Magnetic length |
| l_Ω | Effective length of QD system |
| lh | Light-hole |
| m_0 | Free electron mass, 9.1094×10^{-31} kg |
| m^* | Effective mass |
| M_{fi} | Scattering matrix between initial and final states |
| Mg | Magnesium |
| μ_B | Bohr magneton, 5.7884×10^{-5} eV/T |
| n | Radial quantum number |
| N_A | Numerical aperture |
| N_f | f -number |
| ν | Refractive index |
| NV ⁻ | Negatively charged nitrogen vacancy |
| ω | Frequency |
| Ω | Frequency of an elementary excitation (e.g. phonon) |
| ω_c | Cyclotron frequency |
| P | Laser power (density) |
| ϕ | Azimuthal coordinate |
| PL | Photoluminescence |
| PMT | Photomultiplier tube |
| Ψ | Wave function |
| \mathbf{q} | Wave vector of an elementary excitation |
| q_{KL} | Kohn-Luttinger parameter |
| QD | Quantum dot |
| QW | Quantum well |
| \mathbf{r} | Position vector in Cartesian coordinates x, y, z |
| R | Quantum dot radius |
| ρ | Radial coordinate |
| ρ_c | Circular polarization degree |
| ρ_m | Density of mass |
| RKKY | Ruderman-Kittel-Kasuya-Yosida (interaction) |
| $R_{n,l}(\rho)$ | Radial wave function |
| $s; s_z$ | Spin quantum number; its projection along z -axis |
| σ | Pauli spin matrix |
| σ^+, σ^- | Right-handed, left-handed circular polarization |
| SAQD | Self-assembled quantum dot |

| | |
|-----------------|--|
| SFRS | Spin-flip Raman scattering |
| t | Time |
| T^+, T^- | Positive trion, negative trion |
| T | Temperature |
| T_{an} | Postgrowth annealing temperature |
| τ | (Exciton) Lifetime |
| τ_0 | Average exciton lifetime |
| τ_s | Exciton spin relaxation time |
| τ_s | Scattering time |
| Te | Tellurium |
| θ | Angle between magnetic field and growth axis |
| V | Volume, or potential (with index) |
| VB | Valence band |
| v_{ph} | Sound velocity |
| VTI | Variable temperature insert |
| w_{fi} | Scattering rate between initial and final states |
| \mathcal{V} | Solid angle |
| ζ | Scattering cross section |

List of Figures

| | | |
|------|--|----|
| 1-1 | Electronic band structures for different point group symmetries | 6 |
| 1-2 | Fock-Darwin states of a single electron in an (In,Ga)As quantum dot | 10 |
| 1-3 | Probability distributions of electron and heavy-hole wave functions | 12 |
| 1-4 | Calculated energy dependence of g_e for an InAs/GaAs heterostructure ... | 15 |
| 1-5 | Feynman diagram of a Stokes scattering process | 18 |
| 1-6 | Calculated rates for e- and hh-spins scattered by acoustic phonons | 23 |
| | | |
| 2-1 | Schematic overview of experimental parameters for SFRS | 30 |
| 2-2 | Comparison between the standard- and Raman-holder | 31 |
| 2-3 | Exemplary simulated SFRS spectra | 34 |
| 2-4 | Scheme of SFRS setup including different segments | 36 |
| 2-5 | Scheme of time-resolved PL setup | 38 |
| | | |
| 3-1 | B -field dependence of PL energy and circular polarization degree | 44 |
| 3-2 | SFRS Stokes-spectra for parallel and crossed circular polarizations | 46 |
| 3-3 | SFRS anti-Stokes spectra at Ex- and T^- -resonances | 48 |
| 3-4 | Magnetic field dependence of Raman shifts and intensities | 49 |
| 3-5 | SFRS resonance profiles of electron and heavy-hole | 50 |
| 3-6 | Angular dependence of Raman shifts at $B = 7$ T and $T = 1.8$ K | 52 |
| 3-7 | SFRS spectra in Voigt and tilted geometry without and with E_a | 53 |
| 3-8 | Temperature dependence of e- and hh-SFRS intensities | 54 |
| 3-9 | Dependence of SFRS and PL intensities on power density | 55 |
| 3-10 | Model schemes of SFRS processes in three exciton complexes | 57 |
| 3-11 | Schemes of e- and hh-SFRS Stokes-processes at Ex-resonance | 61 |
| 3-12 | Schemes of hh- and e-SFRS Stokes-processes in T^+ and T^- trions | 65 |
| | | |
| 4-1 | PL spectra of (In,Ga)As/GaAs QD samples | 71 |
| 4-2 | e-SFRS spectra for samples #2 and #3 in different geometries | 72 |
| 4-3 | Circularly polarized SFRS spectra for sample #2, and SFRS scheme | 73 |
| 4-4 | Raman shift of e-SFRS line in dependence on B and θ | 75 |
| 4-5 | Magnetic field dependence of e-SFRS intensity | 76 |
| 4-6 | Dispersion of electron g factor across the ensembles of QDs | 78 |

| | | |
|------|---|-----|
| 4-7 | e-SFRS resonance profiles as a function of B and θ | 79 |
| 4-8 | Magnetic field dependence of the shifts δE | 80 |
| 4-9 | Scheme of e-SFRS for $E_c > \hbar\omega_0$, and FD spectrum | 82 |
| 4-10 | e-SFRS Stokes-spectra indicating Overhauser shifts | 85 |
| | | |
| 5-1 | Band structure at Γ -X-mixing point, PL of direct and indirect QDs | 92 |
| 5-2 | Γ -X-crossing energy measured by resonant PL and SFRS | 93 |
| 5-3 | SFRS spectra in Faraday and Voigt geometry | 95 |
| 5-4 | Schemes of SFRS mechanisms, and calculation of $E_{\text{Ex}}(\theta)$ | 96 |
| 5-5 | B -field dependence of e-, hh-, and Ex-SFRS | 98 |
| 5-6 | e-SFRS for E_R and $E_R + E_a$, e-SFRS in a GaAs/AlAs QW | 99 |
| 5-7 | Angle-dependent SFRS of mixed exciton, X-electron, and Γ -hh | 100 |
| 5-8 | Magnetic field induced circular polarization degree of QD PL | 102 |
| 5-9 | Simulated SFRS spectra of two-level quantum systems | 105 |
| 5-10 | TEM plane-view images and histograms of QD diameters | 109 |
| 5-11 | PL spectra of (In,Al)As/AlAs QD structures S1-S4 at $B = 0$ T | 110 |
| 5-12 | PL kinetics of S4 as a function of excitation pulse power | 112 |
| 5-13 | PL kinetics for S1-S4 at different energies of IQD emission band | 113 |
| 5-14 | PL decays of S1 and S4 modeled by $G(\tau)$ | 115 |
| 5-15 | $G(\tau)$ in dependence on optical power density | 116 |
| 5-16 | Distributions $G(\tau)$ in dependence on QD diameters | 117 |
| 5-17 | B -field dependence of ρ_c for samples S4 and #2890 | 121 |
| 5-18 | $\rho_c(t)$ of indirect exciton PL as a function of B and T | 123 |
| | | |
| 7-1 | SFRS line shift as a function of B for highly n-doped (In,Ga)As QDs ... | 129 |
| 7-2 | PL spectrum and optical orientation at $B = 0$ T for sample #2890 | 131 |
| 7-3 | Level scheme for zero phonon lines of NV^- center in diamond | 132 |
| 7-4 | PL spectra of zero phonon lines at $B = 10$ T | 132 |

List of Tables

| | | |
|-----|--|-----|
| 1-1 | Material parameters for bulk GaAs, AlAs, InAs, and CdTe | 16 |
| 2-1 | Typical experimental parameters for SFRS experiments | 37 |
| 3-1 | Properties of SFRS lines for resonant excitation of Ex- and T-states | 58 |
| 5-1 | Growth parameters for (In,Al)As/AlAs QD samples | 108 |

Curriculum Vitae

Jörg Debus

born on 20/09/1983 in Witten, Germany

Qualification:

- 2003 - 2008 Diploma in Physics (with highest distinction), TU Dortmund University, Germany.
Since 2008 PhD student in Physics, TU Dortmund University, Germany.

Research Interests:

- Optical study of semiconductor nanostructures (quantum wells and quantum dots):
- characterization of spin interactions and spin-level structures by means of spin-flip Raman scattering technique,
 - spin dynamics of carriers and magnetic ions,
 - optical resonance detection using radio-frequency or microwave radiation.

Scientific Awards:

Polish-German Young Researcher Prize 2011 – founded by the Polish Academy of Sciences (PAN) and the Consulate General of the Republic of Poland in Cologne.

Research Visits:

- Feb/Mar-08 Introduction into optically-detected magnetic resonance experiments on (Zn,Mn)Se quantum wells, invited by Dr. V. Yu. Ivanov, IFPAN, Warsaw, Poland.
Sep/Oct-10 Spin-flip Raman scattering measurements on (In,Al)As quantum dots, invited by Prof. Dr. V. F. Sapega, Ioffe-Institute, St. Petersburg, Russia.

Invited Presentations:

- Sep-10 **Seminar talk**, invited by Prof. Dr. Yu. G. Kusrayev, Ioffe-Institute, St. Petersburg, Russia. *Accelerating the magnetization dynamics in diluted magnetic semiconductors.*
Oct-10 **Seminar talk**, invited by Prof. Dr. E. A. Zhukov, Faculty of Physics, M. V. Lomonosov Moscow State University, Moscow, Russia. *Accelerating the magnetization dynamics in diluted magnetic semiconductors.*

- Oct-10 **Seminar talk**, invited by Prof. Dr. A. A. Maksimov, Institute of Solid State Physics, Chernogolovka, Russia. *Spin-flip Raman scattering in self-assembled InAs quantum dots.*
- Jul-12 **Advanced seminar talk**, International Summer School of Spintronics (ISSO-2012), St. Petersburg, Russia. *Spin-flip Raman scattering in type-I quantum dots with direct and indirect band structure.*

Conference Presentations:

- Sep-08 **Regular talk**, Summer School on Semiconductor Spinelectronics, Goslar, Germany. *Acceleration of the spin-lattice relaxation in (Zn,Mn)Se/(Zn,Be)Se quantum wells by cross-relaxation of Mn cluster spin-levels.*
- Mar-09 **Regular talk**, DPG Spring Meeting of the Condensed Matter Section, Dresden, Germany. *Accelerated, two-staged spin-lattice relaxation in (Zn,Mn)Se quantum wells.*
- Jul-09 **Poster**, Spintech V - 5th International School and Conference on Spintronics and Quantum Information Technology, Krakow, Poland. *Intrinsic resonances in Mn²⁺ ion spin clusters in (Zn,Mn)Se/(Zn,Be)Se quantum wells.*
- Aug-09 **Poster**, 14th International Conference on II-VI Compounds, St. Petersburg, Russia. *Relaxation of magnetization controlled by spin diffusion in (Cd,Mn)Te quantum wells.*
- Mar-10 **Regular talk**, DPG Spring Meeting of the Condensed Matter Section, Regensburg, Germany. *Spin-flip Raman scattering in (In,Ga)As/GaAs quantum dots.*
- Apr-10 **Poster**, 6th International Conference on Quantum Dots, Nottingham, UK. *Spin-flip Raman scattering in (In,Ga)As/GaAs quantum dots.*
- Jul-10 **Regular talk**, 30th International Conference on the Physics of Semiconductors, Seoul, Korea. *Dynamical control of Mn spin system cooling by photogenerated carriers in a (Zn,Mn)Se/BeTe heterostructure.*
- Aug-11 **Regular & Late-News Talk**, 15th International Conference on II-VI Compounds, Mayan Riviera, Mexico. *Dynamical control of Mn spin system cooling by photogenerated carriers in a (Zn,Mn)Se/BeTe heterostructure & Variety of exchange interactions providing spin-flip Raman scattering in CdTe/(Cd,Mg)Te quantum wells.*
- Sep-11 **Poster**, 12th International Conference on Optics of Excitons in Confined Systems, Paris, France. *Fine structure of Γ -X mixed exciton states in indirect band-gap (In,Al)As/AlAs quantum dots measured by spin-flip Raman scattering.*

List of released and yet unpublished papers:

- (1) A. A. Maksimov, D. R. Yakovlev, J. Debus, I. I. Tartakovskii, A. Waag, G. Karczewski, T. Wojtowicz, J. Kossut, and M. Bayer.
Spin diffusion in the Mn²⁺ ion system of II-VI diluted magnetic semiconductor heterostructures.
Phys. Rev. B **82**, 035211 (2010).

-
- (2) J. Debus, A. A. Maksimov, D. Dunker, D. R. Yakovlev, I. I. Tartakovskii, A. Waag, and M. Bayer.
Dynamical control of Mn spin-system cooling by photogenerated carriers in a (Zn,Mn)Se/BeTe heterostructure.
Phys. Rev. B **82**, 085448 (2010).
- (3) T. S. Shamirzaev, J. Debus, D. S. Abramkin, D. Dunker, D. R. Yakovlev, D. V. Dmitriev, A. K. Gutakovskii, L. S. Braginsky, K. S. Zhuravlev, and M. Bayer.
Exciton recombination dynamics in an ensemble of (In,Al)As/AlAs quantum dots with indirect band-gap and type-I band alignment.
Phys. Rev. B **84**, 155318 (2011).
- (4) D. V. Azamat, J. Debus, D. R. Yakovlev, V. Yu. Ivanov, M. Godlewski, M. Fanciulli, and M. Bayer.
Electron paramagnetic resonance and magneto-optical spectroscopy of the iron centers in ZnO.
Phys. Rev. B, submitted.
- (5) J. Debus, T. S. Shamirzaev, V. F. Sapega, D. Dunker, D. R. Yakovlev, K. S. Zhuravlev, and M. Bayer.
Fine structure of Γ -X mixed exciton states in indirect band-gap (In,Al)As/AlAs quantum dots measured by spin-flip Raman scattering.
Phys. Rev. Lett., submitted.
- (6) J. Debus, D. Dunker, V. F. Sapega, D. R. Yakovlev, G. Karczewski, T. Wojtowicz, J. Kossut, and M. Bayer.
Spin-flip Raman scattering on neutral and charged excitons in a CdTe/(Cd,Mg)Te quantum well.
Phys. Rev. B, submitted.
- (7) J. Debus, D. Dunker, V. F. Sapega, D. R. Yakovlev, D. Reuter, A. D. Wieck, and M. Bayer.
Optical resonance-excitation involved in the Raman-scattering induced electron spin-flip in singly charged (In,Ga)As/GaAs quantum dots.
Phys. Rev. Lett., submitted.
- (8) J. Debus, V. Yu. Ivanov, A. A. Maksimov, D. R. Yakovlev, S. M. Ryabchenko, Y. G. Semenov, M. Godlewski, A. Waag, and M. Bayer.
Intrinsic resonances in Mn²⁺ ion spin clusters in (Zn,Mn)Se/(Zn,Be)Se quantum wells.
In preparation for submission to Phys. Rev. Lett.

- (9) J. Debus, D. Dunker, V. F. Sapega, D. R. Yakovlev, D. Reuter, A. D. Wieck, and M. Bayer.
Electron spin-flip Raman scattering affected by nuclei-hyperfine-coupling in an ensemble of singly charged (In,Ga)As/GaAs quantum dots.
In preparation for submission to Phys. Rev. B.
- (10) J. Debus, D. Dunker, A. A. Maksimov, I. I. Tartakovskii, D. R. Yakovlev, G. Karczewski, T. Wojtowicz, J. Kossut, A. Waag, and M. Bayer.
Spin diffusion efficiency of the Mn spin system after laser-pulse heating in (Zn,Mn)Se/(Be,Mn)Te quantum wells.
In preparation for submission to Appl. Phys. Lett.
- (11) D. Dunker, T. S. Shamirzaev, J. Debus, D. R. Yakovlev, K. S. Zhuravlev, and M. Bayer.
Long and temperature-robust exciton spin lifetime in indirect band-gap (In,Al)As/AlAs quantum dots.
In preparation for submission to Appl. Phys. Lett.
- (12) E. A. Zhukov, Yu. G. Kusrayev, J. Debus, A. Schwan, I. A. Akimov, D. R. Yakovlev, G. Karczewski, T. Wojtowicz, J. Kossut, and M. Bayer.
Optical orientation and spin relaxation of magnetic polarons in (Cd,Mn)Te/(Cd,Mg,Mn)Te quantum wells.
In preparation for submission to Phys. Rev. Lett.
- (13) J. Debus, D. Dunker, V. L. Korenev, I. A. Akimov, A. Schwan, D. R. Yakovlev, and M. Bayer.
Polarization-dependent magneto-photoluminescence of negatively charged nitrogen-vacancy centers in diamond.
In preparation.
- (14) J. Debus, D. Dunker, V. F. Sapega, D. R. Yakovlev, D. Reuter, A. D. Wieck, and M. Bayer.
Spin-flip Raman scattering in differently doped InAs-based quantum dots.
In preparation.
- (15) J. Debus.
Raman studies on amorphous carbon layers – Raman-Untersuchungen von amorphen Kohlenstoffschichten.
Condensed Matter - Materials Science, arXiv:1203.0035 (2012).
- (16) J. Debus and D. Dunker.
Raman studies on a heavily distorted polycarbonate sample – Raman-Untersuchungen an einer stark deformierten Polycarbonat-Probe.
Condensed Matter - Materials Science, arXiv:1203.0064 (2012).

Acknowledgments

Firstly, I offer my regards to everybody without whom this dissertation would not have been realized at all.

I would like to thank Prof. Dr. Manfred Bayer for providing me the opportunity to carry out all the studies and for his ongoing and fruitful support. I greatly acknowledge Prof. Dr. Dmitri R. Yakovlev for his invaluable guidance and admirable help. I am grateful to Prof. Dr. Dietmar Fröhlich for giving unique advices on several experimental aspects. I am indebted and thankful to Prof. Dr. Victor F. Sapega for his outstanding support and excellent cooperation. Many thanks to Daniel Dunker not only for his irreplaceable help but also for patiently enduring me every day over the past years. I will never forget our nightly lab-sessions pushing us and the cryo to the limits. Thanks a lot!

I would like to thank Dr. Timur S. Shamirzaev for providing so many thrilling samples and ideas for experiments. It is a pleasure to thank Dr. Ilya A. Akimov and Prof. Dr. Volodya L. Korenev for fruitful discussions. I also appreciate the theoretical support from Prof. Dr. Eougenious L. Ivchenko. Further I like to thank very much Lukas Langer and Steffen Varwig for the proofreading. I am grateful to Dr. Gregor Bartsch for his willing to listen to my problems, his endless support and the great time in the office - thanks for everything!

How would be everyday life in the laboratory without Klaus Wieggers? Before getting lost in a bad nightmare, I would like to thank him for his excellent technical assistance and the little jokes on the side! It is a pleasure to thank Michaela Wäscher for her brilliant administrative work. Thanks to Lars Wieschollek and Thomas Stöhr for solving bunches of technical problems. Many thanks to Dr. Stefan Spatzek for the challenging table tennis matches and computer sessions, and, for sure, I would take the bus next time again. I would like to thank Dr. Marc A. Aßmann for the Inspiring Conversations and the gorgeous time in Korea. I am thankful to Alexander Schwan and Tillmann Godde for the nice conference stays in Mexico and Russia.

I would like to thank all E2-members for the pleasant atmosphere and lots of fun.

Great thanks to my friends for their tireless efforts to make me think about other stuff than physics.

Lastly, I owe my deepest gratitude to my parents Heidi and Wolfgang for their continuous support in every respect during the completion of my dissertation.